Acoustic solutions to the particle mixing problem in aqueous dispersions

Thomas Alexander Hazlehurst

University of Leeds

Department of Applied Mathematics

School of Food Science and Nutrition

Submitted in accordance with the requirements for the degree of

Doctor of Philosophy

September 2015

The candidate confirms that the work submitted is his own, except where work which has formed part of jointly-authored publications has been included. The contribution of the candidate and the other authors to this work has been explicitly indicated below. The candidate confirms that appropriate credit has been given within the thesis where reference has been made to the work of others.

Chapter four is based on the paper: *Hazlehurst, Harlen, Holmes and Povey "Multiple scattering in dispersions, for long wavelength thermoacoustic solutions", Journal of Physics: Conference Series 498:012005, 2014.* The candidate was the main author of the paper and was responsible for both the writing of the paper and performing all the calculations and figures presented in it. The other authors are all members of the supervisory team who provided comments on the work and on its presentation in the paper.

For mum & dad

Acknowledgements

I would like to first thank my supervisors, Oliver Harlen, Malcolm Povey and Mel Holmes. Not just for the continuous formal support that they have provided, but for the inspiration and encouragement that they have each given. I could not have asked for a better group of people to guide me through this journey.

This work was funded by EPSRC and P&G (supervised by Luis Martin de Juan) through a CASE award. The collaboration between academic and industrial partners was stimulating and motivating, and I am grateful to both for providing the financial support required for this work.

Throughout my studies I have met many friends and colleagues who I could have not made this journey with out. And I while I thank each and every one of you, there are a few people I would like to take a moment to thank individually. Nik Watson for his guidance as to the ways of an experimental laboratory to a clueless mathematician. Erin Crossland for distracting me from said experiments. Sonia Mills for distracting me with cats. The University of Leeds Handball Club for even more distractions! Andie Gill for being doomy. Matt Benatan for so many lunch dates. And Tim Furze for not trying hard enough to convince me not to do a PhD.

Lastly, I would like to thank my family for their unwavering support, in particular my mum and dad for their infinite amounts of patience. This would have not of been possible without them, and I can not even begin to thank them enough.

- Thomas Alexander Hazlehurst, 29th September 2015

Abstract

Colloidal dispersions are found in many modern product formulation processes, and one of the problems commonly occurring in these processes is characterising the particles within these systems. The existing theories for predicting acoustic scattering in these systems do not fully account for the interactions between neighbouring particles. Most importantly they do not account for the thermal interactions in thermoacoustic scattering.

In this thesis I develop an asymptotic solution in the small wave number limit to the multiple scattering problem. This is done by considering the thermoacoustic field interaction between two different sized particles close together, and applying this to a pair distribution probability function, giving an extra term in the far field scattering calculations. This provides a method of predicting attenuation in mono- and bi-disperse colloids, especially for those of higher concentrations.

This theory is compared to attenuation experimental data for a number of different colloidal systems, mono- and bi-disperse of increasing concentrations, where the thermal field overlap between particles is more prominent. Comparing these experiments with the new two particle thermoacoustic scattering theory give more consistent results than previous theories for volume concentrations up to 30%.

Further work, as part of a CASE studentship, on sedimentation detection in pipe flow using by monitoring the behaviour of pulses of ultrasound is also presented in this thesis.

Contents

List of Figures

List of Tables

Chapter 1

Introduction

> *"That's it! You people have stood in my way long enough. I'm going to clown college!" - Homer Simpson*

1.1 Colloidal Dispersions

A colloid, also known as a colloidal dispersion, is a suspension of particles, ranging from nano-metre to micro-metre in size. In a colloid these particles are dispersed evenly throughout the suspending medium, and do not settle (a degree of stirring is acceptable within this definition), hence the name colloidal dispersion. We call the particles the disperse phase, and the suspending media the continuous or suspending phase. Each of these phases can be a gas, liquid or solid, although in this thesis we will consider only the case where the continuous medium is a liquid and the dispersed phase is either a liquid or a solid.

In modern manufacturing, a huge number of products are, at one stage or another in their manufacture, colloids. Examples of these include foods, pharmaceuticals, cosmetics and paints. Colloidal suspensions are not always stable and can change depending on temperature, light or time. Mechanical disturbances, such as, stirring, pumping and vibrations can also affect the stability of a colloid. The particle sizes can also have an impact on stability. In general stability occurs when, either, all the particles are of the same size (mono-disperse), or they are of all different sizes (poly-disperse).

The ability to be able to measure whether a colloid is stable and whether it has been sufficiently mixed is a key issue for manufacturing. As technology advances, it is increasing important to be able to determine these properties for increasingly concentrated dispersions. The aim of this thesis is to develop the theoretical foundations of ultrasound measurements of colloids to enable it to be used to monitor particle size distribution.

1.1.1 Types of colloids

Colloids can be classed into four main types, [1], examples of which are given in table 1.1:

Sol: is defined as having a solid disperse phase in either a liquid or a solid continuous phase

Emulsion: is defined as having a liquid disperse and continuous phase

Foam: is defined as having a gas disperse phase in a liquid or solid continuous phase

Aerosol: is defined as having a liquid or solid disperse phase in a gas continuous phase

In this thesis the focus will be on emulsions and sols with a liquid continuous phase. However, this will not be limited to a single disperse phase as a colloid dispersion can contain more than one type of dispersed phase.

1.1.2 Light scattering

Colloids can traditionally be distinguished from true solutions, where components are are mixed at a molecular level, by the *Tyndall Effect* [1]. By passing a beam of light through a colloid, an observer viewing from a direction perpendicular to the direction of the beam of light observes the illumination due to the disperse phase scattering the light in all directions. However, if a beam of light passes through a true solution then an observer would not see any light as the light passes cleanly though the solution without being scattered, see figure 1.1. The Tyndall effect

Disperse Phase	Continuous Phase	Type	Examples
Solid	Liquid	Sol	Paint, colloidal silica, muddy water
Liquid	Liquid	Emulsion	Milk, oil in water
Gas	Liquid	Foam	Froth, soap suds, whipped cream
Solid	Gas	Aerosol	Smoke, dust
Liquid	Gas	Aerosol	Fog, mist, clouds
Solid	Solid	Solid sol	Ruby glass, pearls
Liquid	Solid	Solid Emulsion	Cheese, jelly, shoe polish
Gas	Solid	Solid Foam	Lava, pumice, aerated chocolate

Table 1.1

Different combinations of disperse and continuous phases create different types of colloids. Alongside these are examples of each type of colloid.

is wavelength dependent and visible light will scatter from particles with sizes down to about 80nm. Particles smaller than this will not scatter visible light and if shorter light wavelengths are not used then the Tyndall effect is not altogether a reliable indicator of the formation of a solution.

1.1.3 Ultrasound measurement of colloids

While light scattering can be a useful tool in the classification of colloids, it suffers from significant drawbacks. Since light cannot penetrate opaque materials, for example pipe walls, it cannot be used for in-line monitoring except by providing windows. Second, light scattering requires a low concentration of disperse phase, which, particularly in industry requires diluting the sample, which can change the particle structure. It is possible to use other forms of electromagnetic radiation, however these require ionising radiation, which could be of concern in some industries, particularly the food industry.

High frequency sound waves, usually called ultrasound can penetrate opaque

Figure 1.1

A red laser beam being pointed through water (left) and milk (right). In the left image, the beam passes cleanly through the water because it is not reflected as water is not a colloid. In the right image, the light is being reflected in all directions because milk is a colloid.

materials, which can be exploited in the pursuit of non-invasive and non-intrusive testing. Ultrasound, also does not require sample dilution in the measurement process. This makes ultrasound a potentially valuable tool for monitoring colloids. By exploiting the theory of ultrasound spectroscopy it is possible to avoid the need for calibration, provided the physical constants of the samples in question are known. Furthermore, the ability to be able to detect the phase, as well as the amplitude of ultrasound radiation provides valuable additional information. There are many examples of ultrasound being used to measure the concentration and size of particles [2, 3], and also to monitor processes, such as flocculation, crystallisation and creaming [4, 5]. However the existing theory of ultrasound particle sizing applies only to the limit of concentrations too low for acoustic multiple scattering to occur and one of the aims for this thesis is to increase the range of concentrations that can be accurately measured.

It is worth noting that acoustic theory is based on a completely different set of physical laws to electromagnetic propagation, although the mathematical apparatus deployed has many similarities in describing scattering phenomena. In particular, sound is the collective motion of many particles whilst light is carried by an elementary particle, the photon. This means that ultrasound and light techniques, provide complimentary information that can be used to characterise a colloidal system.

1.2 Theory of Acoustics

Ultrasound shares a historical time line (not surprisingly) with general acoustics. The idea that sound is a wave phenomenon originally grew from an analogy with water waves [6, 7]. The Greek philosopher Chrysippus (c.a. 240 B.C.) mentioned this idea, as did the Roman engineer and architect Vetruvius (c.a. 25 B.C.) and the Roman philosopher Boethius (A.D. 480-524). Aristotle (384-322 B.C.) was also known to promote this idea of waves. However, technological limitations prevented the exploitation of these ideas.

The first instance of sound being described as “pressure” pulses between adjacent fluid particles is in Newton’s (1642-1727) *Principia* (1686). The present classical theory of sound propagation has its foundations in the work of Euler

(1707-1783), Lagrange (1736-1813) and d'Alembert (1717-1738).

Ultrasound is defined as the range of sound frequencies above human hearing, typically above 16 kHz. In the application of ultrasound measurement of emulsion properties, low powered acoustic fields are generated, typically below 100 mW. As the power levels are low, the wave propagation does not cause any disruption to the particles or affect the samples, meaning that ultrasound is considered to be non-destructive. This also means that linear elastic theory can be applied to ultrasound measurement except at the high power levels associated with power ultrasound. Typical measurement power levels are of the order of 10 kWm^{-2} and this is further reduced by the fact that pulsed sound is used with a duty cycle (ratio of time on to time off) of 10^{-3} giving average power levels of 10 Wm^{-2}.

Sound waves are compressional oscillations in time and space occurring in extended material bodies. In figure 1.2 the wave is a time-varying and space-varying signal. The frequency f characterises the time variation, and the wavelength λ characterises the space variation. These are related through the velocity of sound,

$$c = f\lambda. \tag{1.1}$$

In this thesis, propagation is assumed to be *adiabatic* in homogeneous media [8]. This means that despite the temperature fluctuations due to the changes in pressure, the effects of thermal diffusion are negligible, so that the compression may be assumed to be adiabatic. Pierce [6] shows that this assumption holds for values approaching $f \to 0$. It is also shown that the dissipation of heat falls as the wavelength increases. However, this assumption fails above 10^{12} Hz in water, and when the media is inhomogeneous. The propagation may become closer to the isothermal conditions near the boundaries under these conditions. This is known as thermal scattering, which will be described in more detail in section 1.2.2.

Wood [9], describes how propagation through a material is dependent on a relationship between density and elasticity. This gives an expression for the speed of sound in a homogeneous fluid that depends upon the compressibility κ and the density ρ,

$$c^2 = \frac{1}{\kappa\rho}. \tag{1.2}$$

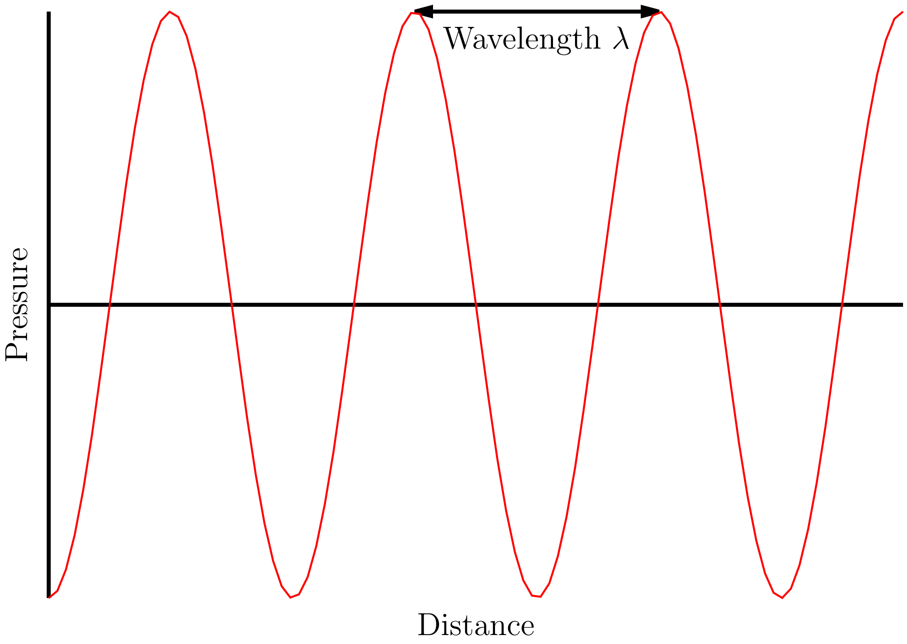

Figure 1.2

The relationship between wavelength, pressure and distance of a signal.

For the ideal case, this can be expanded to a non-scattering multi-phase system [10]. This equation is known as the *Urick equation*

$$c^2 = \frac{1}{\bar{\kappa}\bar{\rho}} \tag{1.3}$$

where

$$\bar{\kappa} = \sum_j \phi_j \kappa_j, \tag{1.4}$$

and

$$\bar{\rho} = \sum_j \phi_j \rho_j, \tag{1.5}$$

where $\bar{\kappa}$ and $\bar{\rho}$ are the effective adiabatic compressibility and density of the mixture and ϕ is the volume fraction of each phase.

For a two phase system such as an emulsion, this can be simplified to

$$\bar{\kappa} = \kappa'\phi + \kappa(1-\phi) \tag{1.6}$$

and

$$\bar{\rho} = \rho'\phi + \rho(1-\phi), \tag{1.7}$$

where the unprimed values are the continuous phase, and the primed values are the disperse phase.

1.2.1 Measurement of sound velocity and attenuation

The measurement of sound velocity is based on the method devised by Colladon and Sturm [11] and differs only through the development of more sophisticated technology. A signal is sent from one transducer, through the material to a receiver - a technique known as “pitch and catch”, or reflected and received again by the first transducer - referred to as “pulse echo”. The time between the sent signal and received signal is then used along with the distance travelled by the wave to calculate the speed.

In addition to the velocity of sound the other commonly measured quantity is the attenuation. Using the same apparatus as the velocity measurement, the amplitude of a single peak is monitored. The amplitude of a decaying wave is expressed as [9]

$$A_x = A_0 e^{-\alpha x}, \tag{1.8}$$

where x is the propagation distance, A_0 is the initial amplitude, and α is the attenuation coefficient. Thus it follows that the attenuation coefficient can be obtained by

$$\alpha = \frac{1}{x} \ln \left(\frac{A_0}{A_x} \right). \tag{1.9}$$

1.2.2 Thermal effects

The fluctuations in pressure associated with sound waves cause oscillations in temperature as well. The basic acoustic theory assumes that these temperature fluctuations are adiabatic, and that the effects of heat transfer are negligible. However as noted earlier, at high frequencies, heat transport can be important. This effect becomes more prevalent at the boundaries due to the sudden changes in thermal properties.

Generally, the term *thermoacoustics* can include any effects by temperature and entropy on acoustic propagation, however a more precise definition was created by Kirchhoff [12], from the theory of friction and heat conduction. This idea has been described fully by Lord Rayleigh [13].

While thermodynamics effects can be used to power engines, heat pumps and refrigerators [14], these use very high pressures to create large temperature changes. The relationship between temperature and pressure in a liquid medium of infinite extent is given by Edmonds [15] as

$$\Delta T = \frac{\Delta P}{\beta} \left(\xi - \frac{1}{\rho c^2} \right), \tag{1.10}$$

where ΔT is the change in the amplitude of the temperature perturbation, ΔP is the amplitude of the pressure perturbation, β is the thermal expansion coefficient and ξ is the isothermal expansion coefficient. In the systems involved in acoustic spectroscopy, a typical value for the temperature variation for a 10 kWm^{-2}, 1

MHz acoustic wave in water would be approximately 4 mK [16]. While it is tempting to assume this is negligible, as many have done, it is important to note that as a wave propagates across a boundary, the difference in specific heats mean that the pressure fluctuations give rise to different temperature perturbations. Consequently, if heat did not flow through this boundary layer there would be a discontinuity in temperature. Therefore, there must be heat flow through the boundary. This energy transport will heat and cool the region near the boundary, with an associated expansion and contraction of the boundary layer. This creates a secondary sound source. Thermoacoustic effects are particularly strong in oil-in-water colloids due to the contrast in specific heats.

1.2.3 Visco-inertial effects

Another secondary source of sound at a phase boundary is due to *visco-inertial* effects. Visco-inertial acoustic effects are similar to thermoacoustics in the sense that result from a difference in material properties, which in the case of visco-inertial effects is the difference in density between the phases. In the case of a particle, the oscillating forces in sound waves cause motion of the particle relative to the surrounding area. The surrounding medium resists this force and causes movement to counter balance this. This movement is a sound source as the medium around the particle compresses and rarefies. This creates a shear field that propagates away from the particle. This wave decays quickly from the source as a fluid cannot support shear waves to any significant extent.

1.3 Single Scattering Theory

The scattering of an acoustic wave is the term used to describe any energy loss from the wave, reducing the propagating acoustic field. The energy lost from the propagating field is scattered in all directions and also converts to thermal and viscous dissipations around each particle. In emulsions, the scattering arises at the boundaries of each of the suspended particles. In single scattering theory, it assumed that each of these particles are far apart, so that the scattering from each individual particle does not interact with any other particle.

1.3.1 History of acoustic scattering theory

The first theory for scattering of acoustic waves was developed by Lord Rayleigh [13, 17]. He considered propagation in the long wavelength limit, where the distance over which thermal diffusion and viscous diffusion take place within one cycle

$$ka \ll 1, \tag{1.11}$$

where $k = \frac{2\pi}{\lambda}$ is the wavenumber and a is the particle radius. This is known as the *Rayleigh limit* and also sometimes known as the *long wavelength limit*, and can be rewritten in terms of the wavelength

$$\frac{2\pi a}{\lambda} < \frac{1}{10}. \tag{1.12}$$

The ultrasound velocity and attenuation per wavelength vary with the parameter which is proportional to the thermal and the visco-inertial wave length in the long wavelength limit. The limit equation (1.11) can be written in terms of this parameter as

$$a\sqrt{f} < \sqrt{\frac{v}{20\pi}}\sqrt{a}, \tag{1.13}$$

where v is the sound velocity. This approximation is valid for the work in this thesis, as the measurements that will be made in the MHz region, with particles with radii around 1μm.

One of the most important theories Rayleigh considered was that attenuation is inversely proportional to the square of the frequency,

$$\alpha \propto f^2. \tag{1.14}$$

Lord Rayleigh investigated acoustic scattering off a spherical object. Following the work of Lord Rayleigh there have been attempts to improve and expand the theory to include thermal and visco-inertial effects, most notably by Epstein and Carhart, and Allegra and Hawley [18, 19]. This is the most widely used theory of ultrasound scattering and is referred to as *ECAH*.

1.3.2 Acoustic propagation in a viscous fluid

For acoustic wave propagation in a fluid, following the method of Epstein and Carhart [18], the governing equations are: conservation of momentum in the form of Navier-Stokes equations, conservation of mass, and conservation of energy. The effects of microstructural relaxation will be neglected, so that background temperature and pressure will remain constant as the system is in a quasi-steady state. The perturbations to these fields are assumed to be small, which implies that we can neglect the variability of coefficients of viscosity and heat conduction with temperature, thus they can be treated as constants. The compressional coefficient of viscosity will, on the other hand, be retained. In the form of a viscous stress tensor, P_{ij},

$$P_{ij} = \eta e_{ij} - \frac{2}{3}\left(\eta - \mu\right)\left(\nabla \cdot \mathbf{v}\right)\delta_{ij}, \tag{1.15}$$

where η and μ are the coefficients of shear viscosity and compressional viscosity respectively, $\mathbf{v}$ is the velocity, δ_{ij} is the Kronecker symbol ($\delta_{ij} = 1$ for $i = j$, otherwise $\delta_{ij} = 0$) and e_{ij} is the strain tensor defined by

$$e_{ij} = \frac{\partial v_i}{\partial x_j} + \frac{\partial v_j}{\partial x_i}. \tag{1.16}$$

The three conservation equations for mass, momentum and energy are [18]:

$$\frac{\partial \rho}{\partial t} + \nabla \cdot \left(\rho \mathbf{v}\right) = 0, \tag{1.17}$$

$$\rho \frac{\partial \mathbf{v}}{\partial t} + \rho\left(\mathbf{v} \cdot \nabla\right)\mathbf{v} = -\nabla p + N\eta\nabla\left(\nabla \cdot \mathbf{v}\right) - \eta\nabla \times \nabla \times \mathbf{v}, \tag{1.18}$$

where $N = \frac{4}{3}\left(1 + \frac{\mu}{2\eta}\right)$ and p is pressure, and

$$\rho \frac{\partial u}{\partial t} + \rho \mathbf{v} \cdot \nabla u + p\left(\nabla \cdot \mathbf{v}\right) - \Psi_\eta - \nabla \cdot \left(\tau \nabla T\right) = 0, \tag{1.19}$$

where $\Psi_\eta = \frac{1}{2} e_{ij} P_{ij}$ is the rate of viscous heating, τ is thermal conductivity, T is temperature and u is the specific internal energy. With a little rearrangement, using equation (1.17), the energy equation equation (1.19) can be rewritten in the form,

$$\rho \frac{Du}{Dt} + p\rho \frac{D}{Dt}\left(\frac{1}{\rho}\right) - \Psi_\eta - \nabla \cdot (\tau \nabla T) = 0, \tag{1.20}$$

where

$$\frac{D}{Dt} \equiv \frac{\partial}{\partial t} + \mathbf{v} \cdot \nabla \tag{1.21}$$

is the Lagrangian derivative. Note the correction of equation (1.20) from [18] with the extra ρ on the second component.

We now consider perturbations of the basic state, using the following substitutions into equations (1.17)–(1.19),

$$\begin{aligned} \rho &= \rho_0 + \rho_1, \qquad & p &= p_0 + p_1, \\ T &= T_0 + T_1, \qquad & u &= u_0 + u_1, \end{aligned} \tag{1.22}$$

where index 0 denotes the constant unperturbed values. Retaining only the first order terms in perturbed quantities, the linearised form of the conservation equations are,

$$\frac{\partial \rho_1}{\partial t} + \rho_0 \nabla \cdot \mathbf{v} = 0, \tag{1.23}$$

$$\rho_0 \frac{\partial \mathbf{v}}{\partial t} + \nabla p_1 - N\eta \nabla (\nabla \cdot \mathbf{v}) + \eta \nabla \times \nabla \times \mathbf{v} = 0, \tag{1.24}$$

$$\rho_0 \frac{\partial u_1}{\partial t} + p_0 (\nabla \cdot \mathbf{v}) - \tau \nabla^2 T_1 = 0, \tag{1.25}$$

assuming that τ is constant. The terms u_1, ρ_1 and p_1 are related through the thermal and caloric equations of state, writing the pressure and the internal energy in the form

$$p = p(\rho, T), \qquad u = u(\rho, T), \tag{1.26}$$

and using $\dot{u}$ to denote $\frac{\partial u}{\partial t}$ we have,

$$\dot{u} = \frac{\partial u}{\partial t} = \left(\frac{\partial u}{\partial \rho}\right)_T \dot{\rho} + \left(\frac{\partial u}{\partial T}\right)_\rho \dot{T}, \tag{1.27}$$

$$\nabla p = \left(\frac{\partial p}{\partial \rho}\right)_T \nabla \rho + \left(\frac{\partial p}{\partial T}\right)_\rho \nabla T, \tag{1.28}$$

which can be linearised about the basic state. From the definition of the adiabatic speed of sound c and the ratio $\gamma = \frac{C_p}{C_v}$, where C_p and C_v are specific heats, at constant pressure and constant volume respectively, we can write

$$\left(\frac{\partial p}{\partial \rho}\right)_T = \frac{c^2}{\gamma}. \tag{1.29}$$

Also, from the thermodynamic relations we have,

$$\left(\frac{\partial u}{\partial T}\right)_\rho = C_v, \tag{1.30}$$

$$\left(\frac{\partial p}{\partial T}\right)_\rho = \frac{\rho_0(\gamma - 1)C_v}{\beta T_0}, \tag{1.31}$$

where $\beta = -\frac{1}{\rho_0}\left(\frac{\partial \rho}{\partial T}\right)_p$. That can also be expressed as

$$\left(\frac{\partial p}{\partial T}\right)_\rho = -\left(\frac{\partial p}{\partial \rho}\right)_T \left(\frac{\partial \rho}{\partial T}\right)_p = \frac{c^2 \rho_0 \beta}{\gamma}. \tag{1.32}$$

This expression together with equation (1.31) implies,

$$\gamma(\gamma - 1)C_v = c^2 \beta^2 T_0. \tag{1.33}$$

Furthermore,

$$\rho_0^2 \left(\frac{\partial u}{\partial \rho}\right)_T = p_0 - T_0 \left(\frac{\partial p}{\partial T}\right)_\rho = \frac{p_0 - \rho_0\,(\gamma - 1)\,C_v}{\beta}. \tag{1.34}$$

Hence, by differentiating equations (1.23) and (1.28) with respect to time we obtain,

$$\dot{u} = -\rho_0 \left(\frac{\partial u}{\partial \rho}\right)_T \nabla \cdot \mathbf{v} + C_v \dot{T}, \tag{1.35}$$

$$\nabla \dot{p} = -\left(\frac{\rho_0 c^2}{\gamma^2}\right) \nabla \left(\nabla \cdot \mathbf{v}\right) + \left[\frac{\rho_0 \left(\gamma - 1\right) C_v}{\beta T_0}\right] \nabla \dot{T}. \tag{1.36}$$

Putting these two equations into equation (1.25) together with the derivative of equation (1.24) with respect to time,

$$\rho_0 \frac{\partial^2 \mathbf{v}}{\partial t^2} + \nabla \dot{p} - N\eta \nabla \left(\nabla \cdot \frac{\partial \mathbf{v}}{\partial t}\right) + \eta \nabla \times \nabla \times \frac{\partial \mathbf{v}}{\partial t} = 0. \tag{1.37}$$

Hence the equations of energy and momentum conservation can be written as

$$\gamma \sigma \nabla^2 T - \dot{T} = \frac{(\gamma - 1)}{\beta} \nabla \cdot \mathbf{v}, \tag{1.38}$$

$$\frac{\partial^2 \mathbf{v}}{\partial t^2} - \left(\frac{c^2}{\gamma}\right) \nabla \left(\nabla \cdot \mathbf{v}\right) - N\nu \nabla \left(\nabla \cdot \frac{\partial \mathbf{v}}{\partial t}\right) + \nu \nabla \times \nabla \times \frac{\partial \mathbf{v}}{\partial t} = -\left(\frac{\beta c^2}{\gamma}\right) \nabla \dot{T}, \tag{1.39}$$

where we have introduced the kinematic viscosity $\nu = \frac{\eta}{\rho_0}$ and the thermometric diffusivity $\sigma = \frac{\tau}{\rho_0 C_p}$.

1.3.3 Acoustic potentials

We now seek solutions to equations (1.38) and (1.39) in the form of harmonic waves with a time dependence $\exp(-i\omega t)$, where $\omega = 2\pi f$ is the angular frequency, so that time derivatives can be replaced by

$$\frac{\partial}{\partial t} = -i\omega. \tag{1.40}$$

Using this reduces equations (1.38) and (1.39) to the form,

$$\gamma \sigma \nabla^2 T + i\omega T \quad = \frac{\gamma - 1}{\beta} \nabla \cdot \mathbf{v}, \tag{1.41}$$

$$\omega^2 \mathbf{v} + \left(\frac{c^2}{\gamma} - i\omega N\nu\right) \nabla\left(\nabla \cdot \mathbf{v}\right) + i\omega\nu \nabla \times \nabla \times \mathbf{v} = -\left(\frac{i\omega c^2 \beta}{\gamma}\right) \nabla T. \qquad (1.42)$$

Clebsch's theorem states that a vector $\mathbf{v}$ can always be represented in terms of a scalar potential $\bar{\varphi}$ and a vector potential $\boldsymbol{\chi}$ as

$$\mathbf{v} = -\nabla \bar{\varphi} + \nabla \times \boldsymbol{\chi}, \qquad (1.43)$$

with $\nabla \cdot \boldsymbol{\chi} = 0$. Using Clebsch's theorem on equation (1.41),

$$\gamma \sigma \nabla^2 T + i\omega T + \frac{\gamma - 1}{\beta} \nabla^2 \bar{\varphi} = 0. \qquad (1.44)$$

Thus, T is a function of the scalar potential $\bar{\varphi}$ only. Applying the same substitution to equation (1.42) gives,

$$\nabla \left[\omega^2 \bar{\varphi} + \left(\frac{c^2}{\gamma} - i\omega N\nu\right) \nabla^2 \bar{\varphi} - \left(\frac{i\omega c^2 \beta}{\gamma}\right) T\right] = \nabla \times \left[\omega^2 \boldsymbol{\chi} + i\omega\nu \nabla \times \nabla \times \boldsymbol{\chi}\right]. \qquad (1.45)$$

We seek solutions in which both sides of this equation vanish independently, so recalling that $\nabla \cdot \boldsymbol{\chi}$, we have

$$\nu \nabla^2 \boldsymbol{\chi} + i\omega \boldsymbol{\chi} = 0, \qquad (1.46)$$

$$\beta T = -\left(\frac{i\omega\gamma}{c^2}\right) \bar{\varphi} - \left[\frac{i}{\omega} + \frac{N\nu\gamma}{c^2}\right] \nabla^2 \bar{\varphi}. \qquad (1.47)$$

Now, denoting $e = \frac{N\nu\omega}{c^2}$ and $h = \frac{\sigma}{\omega}\left(\frac{\omega}{c}\right)^2$ for simplicity and substituting equation (1.47) into equation (1.44), we obtain the following fourth order partial differential equation for $\bar{\varphi}$,

$$\bar{\varphi} + \left(\frac{c}{\omega}\right)^2 \left[1 - i\left(e + \gamma h\right)\right] \nabla^2 \bar{\varphi} - \left(\frac{c}{\omega}\right)^4 h\left(ih + e\gamma\right) \nabla^4 \bar{\varphi} = 0. \qquad (1.48)$$

This can be factorised in the form

$$\left(\nabla^2 + k_c^2\right)\left(\nabla^2 + k_T^2\right)\bar{\varphi} = 0, \tag{1.49}$$

where

$$\left.\begin{array}{c} \frac{1}{k_c^2} \\ \frac{1}{k_T^2} \end{array}\right\} = \frac{c^2}{2\omega^2}\left\{1 - i\left(e + \gamma h\right) \pm \left[1 - 2ie - 2ih\left(\gamma - 2\right) - \left(e - \gamma h\right)^2\right]^{\frac{1}{2}}\right\}. \tag{1.50}$$

Here k_c and k_T are referred to as the acoustic and thermal wave numbers respectively. Since $k_c \neq k_T$, the general solution of equation (1.49) can be written as

$$\bar{\varphi} = \varphi + \psi, \tag{1.51}$$

where,

$$\nabla^2\varphi + k_c^2\varphi = 0, \qquad \nabla^2\psi + k_T^2\psi = 0. \tag{1.52}$$

Thus the scalar potential can be written as the sum of two solutions of two different Helmholtz equations. These are joined by a vector potential $\boldsymbol{\chi}$, satisfying a third Helmholtz equation

$$\nabla^2\boldsymbol{\chi} + k_s^2\boldsymbol{\chi} = 0. \tag{1.53}$$

This shows that the media can support two kinds of longitudinal and one kind of transverse wave. The subscripts c, T and s represent the wave numbers for the compression, thermal and shear modes respectively. For frequencies ω such that e and h are small (as is the case for this thesis) the wave numbers k_c, k_T and k_s can be simplified as

$$k_c = \left(\frac{\omega}{c}\right)\left\{1 + i\left[N\nu + \left(\gamma - 1\right)\sigma\right]\frac{\omega}{c^2}\right\}, \tag{1.54}$$

$$k_T = \left(1 + i\right)\sqrt{\frac{\omega}{2\sigma}}, \tag{1.55}$$

$$k_s = (1+i)\sqrt{\frac{\omega}{2\nu}}. \tag{1.56}$$

The wave number k_c represents the acoustic wave propagation at speed c, but with an imaginary part that represents the small degree of attenuation from viscosity and thermal diffusion. Introducing the attenuation coefficient,

$$\alpha = \left[N\nu + (\gamma - 1)\sigma\right]\frac{\omega^2}{c^3}, \tag{1.57}$$

we can write equation (1.54) in the form

$$k_c = \left(\frac{\omega}{c}\right) + i\alpha. \tag{1.58}$$

The second two wave numbers are non-propagation waves due to thermoacoustic and visco-inertial effects that decay after a few wavelengths, due to them both being complex. Thus, these waves decay within distances of order $\sqrt{\frac{\sigma}{\omega}}$ and $\sqrt{\frac{\nu}{\omega}}$ respectively.

We can derive the temperature field from equation (1.38), as

$$\nabla \cdot \mathbf{v} = \nabla^2 \bar{\varphi} = -k_c^2\varphi - k_T^2\psi = \frac{i\beta}{\gamma - 1}\left(\omega - i\gamma\sigma\nabla^2 T\right), \tag{1.59}$$

which gives

$$T = \Gamma_c\varphi + \Gamma_T\psi, \tag{1.60}$$

where

$$\Gamma_c = \frac{-ik_c^2\left(\gamma - 1\right)}{\beta\left(\omega + i\gamma\sigma k_c^2\right)} \approx \frac{k_c^2\left(\gamma - 1\right)}{\beta\sigma k_T^2} = \frac{i\beta\omega T_0}{C_p} \tag{1.61}$$

and

$$\Gamma_T = \frac{-ik_T^2\left(\gamma - 1\right)}{\beta\left(\omega + i\gamma\sigma k_T^2\right)} \approx -\frac{1}{\beta\sigma}. \tag{1.62}$$

It is worth commenting that the ratio of the thermal factors,

$$\left|\frac{\Gamma_c}{\Gamma_T}\right| \approx \frac{k_c^2\left(\gamma - 1\right)}{k_T^2}, \tag{1.63}$$

is small, as $k_c^2 \ll k_T^2$, as noted by Pinfield [20]. This means the temperature changes are dominated by the thermal mode, ψ.

1.3.4 Boundary conditions

As discussed above scattering occurs at the boundaries between the phases. At a boundary where there is a change in the material properties there is a requirement for continuity of the velocity, temperature, heat flux and stress components: this means that

$$\mathbf{v} = \mathbf{v}', \tag{1.64a}$$

$$T = T', \tag{1.64b}$$

$$\tau \frac{\partial T}{\partial \mathbf{n}} = \tau' \frac{\partial T'}{\partial \mathbf{n}}, \tag{1.64c}$$

$$P_{ij} = P'_{ij}, \tag{1.64d}$$

where **n** is the normal unit vector facing outwards from the surface of the dispersed phase.

1.3.5 Sommerfeld radiation condition

An important concept to consider is what happens to an acoustic wave as it approaches infinity. Consider, Φ that satisfies the three-dimensional Helmholtz equation outside some finite sphere of radius a,

$$\nabla^2 \Phi + k^2 \Phi = 0. \tag{1.65}$$

Spherically symmetric solutions of equation (1.65) satisfy

$$\frac{1}{r^2} \frac{d}{dr} \left(r^2 \frac{d\Phi}{dr} \right) + k^2 \Phi = 0, \tag{1.66}$$

or, rewritten,

$$\frac{d^2}{dr} (r\Phi) + k^2 (r\Phi) = 0, \tag{1.67}$$

which has solutions

$$\Phi = \frac{e^{ikr}}{r} \text{ and } \frac{e^{-ikr}}{r}. \tag{1.68}$$

These solutions correspond to outgoing and ingoing waves to and from infinity respectively. In scattering problems it is required that sound waves traverse outwards towards infinity. This is imposed by the *Sommerfeld radiation conditions* [21]

$$|r\Phi| < k, \tag{1.69}$$

$$r\left(\frac{\partial \Phi}{\partial r} - ik\Phi\right) \to 0, \tag{1.70}$$

uniformly as $r \to \infty$, since

$$\frac{\partial}{\partial r}\left(\frac{e^{ikr}}{r}\right) = ik\Phi - \frac{1}{r^2}e^{ikr}, \tag{1.71}$$

which only the outgoing wave from equation (1.68) satisfies. It follows that we can calculate the far field scattering pattern,

$$\Phi(ka,\theta) = \frac{e^{ikr}}{r}\left\{\Phi(ka,\theta) + O\left(\frac{1}{kr}\right)\right\}, \tag{1.72}$$

as $r \to \infty$, where $\Phi(ka,\theta)$ is the scattered solution of equation (1.65).

1.3.6 Single particle solution

Let us consider a plane wave incident on a spherical particle of radius a, as in figure 1.3. The continuous phase, outside the sphere, and the disperse phase, inside the sphere, are composed of two different media. The continuous phase is denoted by unprimed and the disperse phase by primed variables. This is an axi-symmetric problem. This allows us to use spherical polar coordinates (r, θ and Ω) with the origin at the centre of the sphere. Since the problem is axi-symmetric, $v_\Omega = P_{r\Omega} = 0$. This leaves equation (1.64) with six boundary conditions.

The incident plane wave is of the form

$$\varphi_0 = \exp(-ikr\cos\theta), \tag{1.73}$$

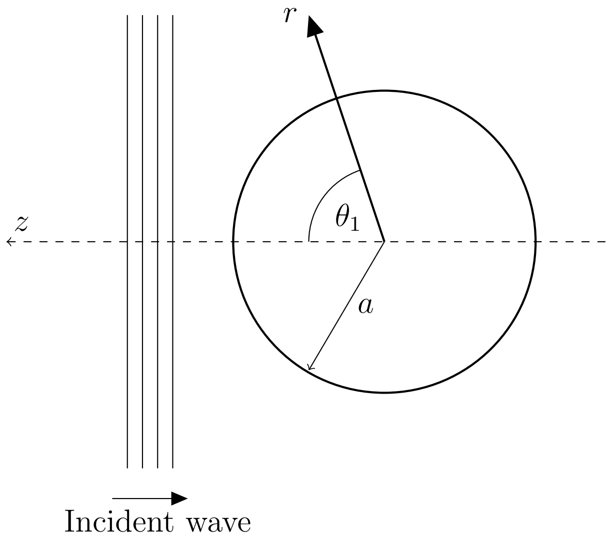

Figure 1.3

Geometry of single spherical object with a plain wave propagating towards it as described in the ECAH single scattering method.

which can be written as a sum of spherical waves in the form

$$\varphi_0 = \sum_{n=0}^{\infty} i^n (2n+1) j_n(kr) P_n(\cos\theta), \tag{1.74}$$

where j_n is the spherical Bessel's function of order n and P_n is the Legendre polynomial. The scattering from the sphere provides six additional waves to consider, three outside of the sphere, and three inside. The external velocity potential is given by

$$\varphi = \varphi_0 + \varphi_R + \psi + \chi, \tag{1.75}$$

where the subscript R represents the reflected compressional wave and ψ, the thermal wav. In addition, there is the vector potential, $\boldsymbol{\chi}$, however, due to axial symmetry, only the Ω component needs to be considered which is denoted by a scalar χ. Writing the solutions to Helmholtz equations (1.52) and (1.53) give,

$$\varphi_R = \sum_{n=0}^{\infty} i^n \left(2n+1\right) A_n h_n \left(k_c r\right) P_n \left(\cos\theta\right), \tag{1.76}$$

$$\psi = \sum_{n=0}^{\infty} i^n \left(2n+1\right) B_n h_n \left(k_T r\right) P_n \left(\cos\theta\right), \tag{1.77}$$

$$\chi = \sum_{n=0}^{\infty} i^n \left(2n+1\right) C_n h_n \left(k_s r\right) P_n^1 \left(\cos\theta\right), \tag{1.78}$$

where the h_n are the *spherical Hankel functions*, which means that the solution satisfies the Sommerfeld radiation conditions equations (1.69) and (1.70) Similarly for inside the sphere, the velocity potentials are given by $\varphi' = \varphi'_R + \psi' + \chi'$

$$\varphi'_R = \sum_{n=0}^{\infty} i^n \left(2n+1\right) A'_n j_n \left(k'_c r\right) P_n \left(\cos\theta\right), \tag{1.79}$$

$$\psi' = \sum_{n=0}^{\infty} i^n \left(2n+1\right) B'_n j_n \left(k'_T r\right) P_n \left(\cos\theta\right), \tag{1.80}$$

$$\chi' = \sum_{n=0}^{\infty} i^n \left(2n+1\right) C'_n j_n \left(k'_s r\right) P_n^1 \left(\cos\theta\right). \tag{1.81}$$

The coefficients A_n to C'_n are determined by applying the boundary conditions (1.64) on the surface of the sphere at $r = a$. Continuity of velocity gives

$$\begin{aligned} k_c j'_n \left(k_c a\right) + A_n k_c a h'_n \left(k_c a\right) + B_n k_T a h'_n \left(k_T a\right) - C_n n(n+1) h_n(k_s a) = \\ A'_n k'_c a j'_n \left(k'_c a\right) + B'_n k'_T a j'_n \left(k'_T a\right) - C'_n n(n+1) j_n \left(k'_c a\right) \end{aligned} \tag{1.82a}$$

and

$$\begin{aligned} j_n \left(k_c a\right) + A_n h_n \left(k_c a\right) + B_n h_n \left(k_T a\right) - C_n \left[h_n \left(k_s a\right) + k_s a h'_n \left(k_s a\right)\right] = \\ A'_n j_n \left(k'_c a\right) + B'_n j_n \left(k'_T a\right) - C'_n \left[j_n \left(k'_s a\right) + k'_s a h'_n \left(k'_s a\right)\right]. \end{aligned} \tag{1.82b}$$

On the surface of sphere $r = a$, continuity of temperature requires that

$$\begin{aligned} &\Gamma_c \left[j_n \left(k_c a \right) + A_n h_n \left(k_c a \right) \right] + \Gamma_T B_n h_n \left(k_T a \right) = \\ &\qquad \Gamma'_c A'_n j_n \left(k'_c a \right) + \Gamma'_T B'_n j_n \left(k'_T a \right) \end{aligned} \tag{1.82c}$$

and continuity of thermal flux that

$$\begin{aligned} &\tau \big\{ \Gamma_c \left[k_c a j'_n \left(k_c a \right) - A_n k_c a h'_n \left(k_c a \right) \right] + \Gamma_T B_n k_T a h'_n \left(k_T a \right) \big\} = \\ &\qquad \tau' \left\{ \Gamma'_c A'_n k'_c a j'_n \left(k'_c a \right) + \Gamma'_T B'_n k'_T a j'_n \left(k_T a \right) \right\}. \end{aligned} \tag{1.82d}$$

Finally the condition of continuity of stress components gives

$$\begin{aligned} &\eta \Big\{ \big[k_c a j'_n \left(k_c a \right) - j_n \left(k_c a \right) \big] + A_n \big[k_c a h'_n \left(k_c a \right) - h_n \left(k_c a \right) \big] \\ &+ B_n \big[k_T a h'_n \left(k_T a \right) - h_n \left(k_T a \right) \big] - \frac{1}{2} C_n \Big[\left(k_s a \right)^2 h''_n \left(k_s a \right) + \big(n^2 + n - 2 \big) h_n \left(k_s a \right) \Big] \Big\} \\ &= \eta' \Big\{ A'_n \big[k'_c a j'_n \left(k'_c a \right) - j_n \left(k'_c a \right) \big] + B'_n \big[k'_T a j'_n \left(k'_T a \right) - j_n \left(k'_T a \right) \big] \\ &\qquad - \frac{1}{2} C'_n \big[\left(k'_s a \right)^2 j''_n \left(k'_s a \right) + \big(n^2 + n - 2 \big) j_n \left(k'_s a \right) \big] \Big\} \end{aligned} \tag{1.82e}$$

and

$$\begin{aligned} &\eta \Big\{ \left[\left(k_s a \right)^2 j_n \left(k_c a \right) - 2 \left(k_c a \right)^2 j''_n \left(k_c a \right) \right] + A_n \left[\left(k_s a \right)^2 h_n \left(k_s a \right) - 2 \left(k_c a \right)^2 h''_n \left(k_c a \right) \right] \\ &\qquad + B_n \left[\left(1 - \frac{2\nu}{\sigma} \right) \left(k_c a \right)^2 h_n \left(k_T a \right) - 2 \left(k_T a \right)^2 h''_n \left(k_T a \right) \right] \\ &\qquad + 2n(n+1) C_n \left[k_s a h'_n \left(k_s a \right) - h_n \left(k_s a \right) \right] \Big\} \\ &\qquad = \eta' \Big\{ A'_n \left[\left(k'_s a \right)^2 j_n \left(k'_s a \right) - 2 \left(k'_c a \right)^2 j''_n \left(k'_c a \right) \right] \\ &\qquad + B'_n \left[\left(1 - \frac{2\nu}{\sigma} \right)' \left(k'_s a \right)^2 j_n \left(k_T a \right) - 2 \left(k'_T a \right)^2 j''_n \left(k'_T a \right) \right] \\ &\qquad + 2n \left(n + 1 \right) C'_n \left[\left(k'_s a \right) j'_n \left(k_s a \right) - j_n \left(k'_s a \right) \right] \Big\}. \end{aligned} \tag{1.82f}$$

These equations allow for the computation of the scattering coefficients. In the limit of $\mu', \mu \to 0, C_n$ and C'_n are negligible and our equations (1.82a)–(1.82f) reduce to four equations (1.82a)–(1.82d), ignoring the stress components. These form sets of six linear equations from which the coefficient A_n can be calculated numerically, to find the scattered acoustic field. This solution was first obtained by Epstein and Carhart [18] for emulsions and aerosols and later by Allegra and Hawley [19] generalised the solution to include solid particles (introducing a number of typographical errors in the equations in their paper which are corrected in Challis *et al.* [22], and hence this solution is referred to as *ECAH*.

1.3.7 Small wave number limit

While we can find an exact solution of the ECAH equations (1.82a)–(1.82f), Harlen *et al.* [23] showed, for the parameter values typical of ultrasound experiments, that these matrices have very high condition numbers, as seen in table 1.2. This causes the inversion of these problems to be numerically unstable. This is known as being ill-conditioned. These problems occur for $k_c a$ and $k'_c a \ll 1$, and arise from the divergence of the spherical Hankel functions as $k_c a \to 0$.

		Condition number		
$\lvert k_c a\rvert$	$\lvert k_T a\rvert$	A_0	A_1	A_2
8.47×10^{-8}	6.6×10^{-3}	1.5×10^{8}	2.9×10^{22}	5.9×10^{37}
4.2×10^{-3}	6.6	7.7×10^{4}	6.0×10^{8}	2.9×10^{14}

Table 1.2

Table from Harlen et al. *[23]. Calculated condition numbers for ECAH matrix generated by equations* (1.82a)–(1.82f) *for two combinations of wavenumbers k_c and k_T and particle radius a, for silicone oil. The material properties for silicone oil appear in section 2.2.*

For $|z| \ll 1$ the spherical Bessel and Hankel functions have the asymptotic properties [24]

$$j_n(z) \approx 2^2 z^2 \frac{n!}{(2n+1)!}, \tag{1.83a}$$

$$h_n(z) \approx -\frac{1}{2^n z^{n+1}} \frac{(2n)!}{n!} i, \tag{1.83b}$$

$$j_n'(z) \approx 2^n n z^{n-1} \frac{n!}{(2n+1)!}, \tag{1.83c}$$

$$h_n'(z) \approx \frac{n+1}{2^n z^{n+2}} \frac{(2n)!}{n!} i. \tag{1.83d}$$

For typical applications $k_c a \approx 10^{-3}$, this suggests that it should be possible to obtain appropriate solutions using the asymptotic equations (1.83). Kleinman [25] showed how to construct uniformly asymptotic solutions for the exterior scattering problem in the limit where $k_c a \ll 1$. The radiation condition at infinity satisfying Helmholtz equations have radiation solutions with the asymptotic form

$$\varphi(r,\theta,\Omega) = \frac{e^{ik_c r}}{r} \sum_{n=0}^{\infty} \frac{f_n(\theta,\Omega)}{r^n}, \tag{1.84}$$

where f_n are differentiable functions of k_c, and the polar angles θ and Ω. However, φ is not regular at infinity due to the presence of the e^{ikr} term. To be regular at infinity a function φ must satisfy the following two conditions:

$$\lim_{r\to\infty} |r\varphi| < \infty, \tag{1.85}$$

and

$$\lim_{r\to\infty} \left| r^2 \frac{\partial \varphi}{\partial r} \right| < \infty. \tag{1.86}$$

Thus to provide a regular problem, we introduce the variable

$$\tilde{\varphi} = e^{-ik_c(r-a)} \varphi, \tag{1.87}$$

where $\tilde{\varphi}$ satisfies

$$\nabla^2 \tilde{\varphi} = -\frac{2ik_c}{r} \frac{\partial}{\partial r}(r\tilde{\varphi}), \tag{1.88}$$

together with the boundary condition

$$\lim_{r\to\infty} r^2 \frac{\partial \tilde{\varphi}}{\partial r} = 0, \tag{1.89}$$

which implies that $\tilde{\varphi}$ is a regular function.

Using this form, there have been three different methods, each exploring a different limit of $|k_T a|$ with the limit of $|k_c a| \ll 1$, carried out in [23, 26, 27]. These works neglect the visco-inertial terms, as will we in the remainder of this thesis. Although, subsequent solutions using these methods including the shear mode have been carried out by Pinfield and Povey [28], in the exposition below we shall also neglect visco-inertial effects.

1.3.7.1 Low-frequency potential scattering

The first method, described by Harlen *et al.* [23], is based on the asymptotic solution when both $|k_c a|$ and $|k_T a| \ll 1$. This method is known as *Low Frequency potential scattering theory* or *LFPST*. We define functions in the exterior given by,

$$\tilde{\varphi} = e^{-ik_c r}\varphi \text{ and } \tilde{\psi} = e^{-ik_T r}\psi. \tag{1.90}$$

These are both regular at infinity and we can rewrite the Helmholtz equations (1.49) in the form

$$\nabla^2 \tilde{\varphi} = -\frac{2ik_c}{r}\frac{\partial}{\partial r}\left(r\tilde{\varphi}\right), \qquad \nabla^2 \tilde{\psi} = -\frac{2ik_T}{r}\frac{\partial}{\partial r}\left(r\tilde{\psi}\right). \tag{1.91}$$

In the thermoacoustic approximation, there are four boundary conditions corresponding to continuity of the normal component of velocity, pressure, temperature and thermal flux. Putting the substitutions (1.90) into these boundary conditions, we have

$$ik_c \cos\theta e^{ik_c a\cos\theta} + e^{ik_c a}\left(ik_c\tilde{\varphi} + \frac{\partial\tilde{\varphi}}{\partial r}\right) + e^{ik_T a}\left(ik_T\tilde{\psi} + \frac{\partial\tilde{\psi}}{\partial r}\right) = \frac{\partial}{\partial r}\left(\varphi' + \psi'\right), \tag{1.92}$$

$$e^{ik_c a\cos\theta} + e^{ik_c a}\tilde{\varphi} + e^{ik_T a}\tilde{\psi} = \hat{\rho}\left(\varphi' + \psi'\right), \tag{1.93}$$

$$\Gamma_c\left(e^{ik_c a\cos\theta} + e^{ik_c a}\tilde{\varphi}\right) + \Gamma_T e^{ik_T a}\tilde{\psi} = \Gamma'_c\varphi' + \Gamma'_T\psi', \tag{1.94}$$

$$\begin{aligned}&\Gamma_c\left(ik_c\cos\theta e^{ik_c\cos\theta} + \left(ik_c\tilde{\varphi} + \frac{\partial\tilde{\varphi}}{\partial r}\right)e^{ik_c a}\right)\\ &+\Gamma_T\left(ik_T\tilde{\psi} + \frac{\partial\tilde{\psi}}{\partial r}\right)e^{ik_T a} = \hat{\tau}\left(\Gamma'_c\frac{\partial}{\partial r}\varphi' + \Gamma'_T\frac{\partial}{\partial r}\psi'\right),\end{aligned} \tag{1.95}$$

where $\hat{\rho} = \rho'/\rho$and $\hat{\tau} = \tau'/\tau$. Since the functions $\tilde{\varphi}, \tilde{\psi}, \varphi'$ and ψ' are regular they can be expanded as Poincaré series in the form,

$$\tilde{\varphi} = \sum_{n=0}^{\infty}\left(ik_c\right)^n\tilde{\varphi}_n, \tag{1.96}$$

$$\tilde{\psi} = \sum_{n=0}^{\infty}\left(ik_T\right)^n\tilde{\psi}_n, \tag{1.97}$$

$$\varphi' = \sum_{n=0}^{\infty}\left(ik'_c\right)^n\varphi'_n, \tag{1.98}$$

$$\psi' = \sum_{n=0}^{\infty}\left(ik'_T\right)^n\psi'_n. \tag{1.99}$$

These series converge for $|k_c a| < \ln(2)$ and $|k_T a| < \ln(2)$, as shown by Kleinmann [25]. This perturbation approach exploits the cause of the ill-conditioning of ECAH. Furthermore, it can be shown, using LFPST, that the error is bounded by $O(|k_c a|^{m+1})$ if the solution to order-m is used. From equations (1.52) and (1.91) the terms in the Poincaré series are related by

$$\nabla^2\tilde{\varphi}_{n+1} = -\frac{2}{r}\frac{\partial}{\partial r}\left(r\tilde{\varphi}_n\right), \tag{1.100}$$

$$\nabla^2\varphi'_{n+2} = \varphi'_n, \tag{1.101}$$

$$\nabla^2 \tilde{\psi}_{n+1} = -\frac{2}{r}\frac{\partial}{\partial r}\left(r\tilde{\psi}_n\right) \tag{1.102}$$

and

$$\nabla^2 \psi'_{n+2} = \psi'_n. \tag{1.103}$$

Hence at order zero $\tilde{\varphi}_0, \tilde{\psi}_0$, φ'_0 and ψ'_0 satisfy Laplace's equation and so are given by,

$$\tilde{\varphi}_0 = \frac{e^{-ik_c a}}{r}\sum_{n=0}^{\infty}\frac{A_n^{(0)}}{r^n}P_n\left(\cos\theta\right), \tag{1.104}$$

$$\tilde{\psi}_0 = \frac{e^{-ik_T a}}{r}\sum_{n=0}^{\infty}\frac{B_n^{(0)}}{r^n}P_n\left(\cos\theta\right), \tag{1.105}$$

$$\varphi'_0 = \sum_{n=0}^{\infty}A_n^{'(0)}r^n P_n\left(\cos(\theta)\right), \tag{1.106}$$

$$\psi'_0 = \sum_{n=0}^{\infty}B_n^{'(0)}r^n P_n\left(\cos(\theta)\right), \tag{1.107}$$

where from the boundary conditions subsequent terms are found by solving the associated Poisson equations. The leading order contribution to the far field scattering is found in the second-order terms. Consequently, the effects of the thermal scattering are found to be proportional to $(k_T a)^2$ in the limit of $|k_T a| \ll 1$, so the term $\tilde{\psi}_2$ is of most interest to us.

1.3.7.2 Geometric theory of diffraction

The LFPST approximation is no longer valid once the particle size becomes comparable with the thermal length scale $\sqrt{\frac{\sigma}{\omega}}$. The second method, from Harlen *et al.* [26], relies, again, on the assumption that $|k_c a| \ll 1$, however this time, $|k_T a| \gg 1$. It is based on curves along which the terms of asymptotic expansions satisfy ordinary differential equations, known as rays. This will only be summarised briefly here, but there is a more in-depth discussion in [26]. The thermal component of the potential ψ satisfies an equation of the form,

$$\left(\nabla^2 + k_T^2 n^2(x)\right)\psi = 0, \tag{1.108}$$

where $n(x)$ is the effective refractive index of the media. If homogeneous, $n(x) = constant$, then plane wave solutions are obtained,

$$\psi = \tilde{\psi} e^{in(x)\mathbf{k_T}\cdot\mathbf{r}}, \tag{1.109}$$

where $\mathbf{k_T} = k_T \hat{k_T}$ is the propagation vector, $\hat{k_T}$ the unit vector. Solutions are sought on the basis of (1.109) in the form

$$\psi = \tilde{\psi} e^{ik_T s(x)}, \tag{1.110}$$

which when introduced in (1.108) gives

$$-k_T^2 \left\{ |\nabla s|^2 - n^2 \right\} \tilde{\psi} + 2ik_T \nabla s \cdot \nabla \tilde{\psi} + ik_T \tilde{\psi} \nabla^2 s + \nabla^2 \tilde{\psi} = 0. \tag{1.111}$$

The crucial difference with this method is that, since $k_T a$ is large, the expansion of inverse powers of $ik_T a$ are used in place of (1.97),

$$\tilde{\psi} = \sum_{m=0}^{\infty} (ik_T a)^{-m} \tilde{\psi}_m. \tag{1.112}$$

It follows from this that if $\tilde{\psi}_0 \neq 0$ then the Eiconal equation

$$|\nabla s|^2 = n^2(x) \tag{1.113}$$

is obtained. For $m = 0$,

$$2\nabla s \cdot \nabla \tilde{\psi}_0 + \tilde{\psi}_0 \nabla^2 s = 0, \tag{1.114}$$

and for $m = 1, 2, ...$,

$$2\nabla s \cdot \nabla \tilde{\psi}_m + \tilde{\psi}_m \nabla^2 s = -\nabla^2 \tilde{\psi}_{m-1}. \tag{1.115}$$

These two equations can be considered as analogous to equation (1.96) in the LF-PST case. For homogeneous media, it can be considered, for a spherical geometry, that

$$s(r) = \pm constant, \tag{1.116}$$

thus, equation (1.110) becomes,

$$\psi = \tilde{\psi} e^{\pm k_T r}. \tag{1.117}$$

Using this equation with boundary conditions, similar to the method in section 1.3.7.1, we define

$$\tilde{\varphi} = \sum_{n=0}^{\infty} \sum_{m=0}^{\infty} \frac{(ik_c a)^n}{(ik_T a)^m} \tilde{\varphi}_{nm}, \tag{1.118}$$

$$\varphi' = \sum_{n=0}^{\infty} \sum_{m=0}^{\infty} \frac{(ik'_c a)^n}{(ik'_T a)^m} \varphi'_{nm}, \tag{1.119}$$

$$\tilde{\psi} = \sum_{n=0}^{\infty} \sum_{m=0}^{\infty} \frac{(ik_c a)^n}{(ik_T a)^m} \tilde{\psi}_{nm}, \tag{1.120}$$

$$\psi' = \sum_{n=0}^{\infty} \sum_{m=0}^{\infty} \frac{(ik'_c a)^n}{(ik'_T a)^m} \psi'_{nm}. \tag{1.121}$$

By expanding these equations, it is shown that solutions with the order $(k_c a)^2 (k_T a)^{-1}$ describe the first interactions between the thermal and acoustic fields, the full solution has been solved by Harlen *et al.* [26].

1.3.7.3 Weak thermal scattering approximation

This third method, first described by Pinfield *et al.* [29] and later developed by Harlen *et al.* [27], is based on the assumptions, $|k_c a| \ll 1$, but with $|k_T a| \sim 1$. This allows the use of a perturbation power series in $ik_c a$, similar to LFPST but where $\tilde{\varphi}_n$ and $\tilde{\psi}_n$ remain dependent on k_T:

$$\tilde{\varphi} = \sum_{n=0}^{\infty} (ik_c a)^n \tilde{\varphi}_n, \tag{1.122}$$

$$\tilde{\psi} = \sum_{n=0}^{\infty} (ik_c a)^n \tilde{\psi}_n, \tag{1.123}$$

$$\varphi' = \sum_{n=0}^{\infty} (ik_c a)^n \varphi'_n, \tag{1.124}$$

$$\psi' = \sum_{n=0}^{\infty} (ik_c a)^n \psi'_n. \tag{1.125}$$

It can again be shown for $|k_c a| < \ln(2)$ that these series converge. The key observation is that in this limit the acoustic fields $\tilde{\varphi}$ and φ' make only a weak contribution to the temperature fields since $\Gamma_c \sim (k_c a)^2 \Gamma_T$, from equation (1.63). As a consequence, the thermal boundary conditions (1.64) link the $\tilde{\varphi}_{n+2}, \varphi'_{n+2}$ and $\tilde{\psi}_n, \psi'_n$, whereas velocity and pressure boundary conditions link $\tilde{\varphi}_n, \tilde{\psi}_n, \varphi'_n$ and ψ'_n. Following this, the solutions can be written as finite sums, as follows:

$$\tilde{\varphi}_n = \sum_{m=0}^{n} A_{mn} \frac{a^{m+1}}{r^{m+1}} P_m(\cos\theta) + I_n(r,\theta), \tag{1.126}$$

$$\varphi'_n = \sum_{m=0}^{n} A'_{mn} \frac{r^m}{a^m} P_m(\cos\theta) + I'_n(r,\theta), \tag{1.127}$$

which only contain the first n harmonics, and

$$\psi_n = \sum_{m=0}^{n-2} B_{nm} h_m(k_T r) P_m(\cos\theta), \tag{1.128}$$

$$\psi'_n = \sum_{m=0}^{n-2} B'_{nm} h_m(k'_T r) P_m(\cos\theta), \tag{1.129}$$

which only contain the first $n-2$ harmonics. Where I_n and I'_n are the associated particular integrals of the inhomogeneous equations, see [27] for more details. This gives the solution for order $n = 0$,

$$\tilde{\varphi}_0 = 0, \tag{1.130}$$

$$\varphi'_0 = \frac{1}{\hat{\rho}}, \tag{1.131}$$

which is just an increase in the internal acoustic field to balance the external field. At order $|k_c a|$, the leading terms give a dipole field:

$$\tilde{\varphi}_1 = A_{11}\frac{a^2}{r^2}\cos\theta, \tag{1.132}$$

$$\varphi'_1 = A'_{11}\frac{r}{a}\cos\theta, \tag{1.133}$$

where

$$A_{11} = \frac{\hat{\rho}-1}{1+2\hat{\rho}}, \quad A'_{11} = \frac{3}{1+2\hat{\rho}}. \tag{1.134}$$

At order $|k_c a|^2$, the leading order thermal field terms are produced,

$$\psi_2 = \frac{\hat{\tau}\left(\hat{\Gamma}G'_c - \hat{\rho}G_c\right)(k'_T a - \tan k'_T a)}{\hat{\rho}\left(\hat{\tau}k'_T a + (1-\hat{\tau}-ik_T a)\tan k_T a\frac{a}{r}e^{ik_T(r-a)}\right)}, \tag{1.135}$$

$$\tilde{\varphi} = A_{22}\frac{a^3}{r^3}P_2(\cos\theta) + A_{20}\frac{a}{r} - A_{11}\frac{a(r-a)}{r^2}\cos\theta, \tag{1.136}$$

where $\frac{\Gamma_c}{\Gamma_T} = -k_c^2 a^2 G_c$, $\frac{\Gamma'_c}{\Gamma'_T} = -k_c^2 a^2 G'_c$, $\hat{\Gamma} = \frac{\Gamma'_T}{\Gamma_T}$,

$$A_{22} = \frac{2(\hat{\rho}-1)}{3(2+3\hat{\rho})}, \tag{1.137}$$

$$A_{20} = \frac{\hat{\rho}-\hat{v}}{3\hat{\rho}} + \frac{(\hat{\Gamma}\hat{\tau}-1)(\hat{\Gamma}G'_c - \hat{\rho}G_c)\,(k'_T a - \tan k'_T a)\,(ik_T a - 1)}{\hat{\Gamma}\hat{\rho}\,(\hat{\tau}k'_T a + (1-\hat{\tau}-ik_T a)\tan k'_T a)}. \tag{1.138}$$

Note the correction from Harlen's original paper [27] in the denominator of equation (1.138).

1.3.8 Forward scattering

Now the results of the calculations in sections 1.3.7.1–1.3.7.3 can be used to predict the attenuation of a system of particles suspended in liquid. Epstein and Carhart [18], and Allegra and Hawley [19] obtained a calculation for the energy at large distances, so after the effects of the thermal and shear modes have disappeared. They simply assumed the total energy lost is proportional to the concentration of the particles, ϕ, as

$$\left(\frac{\tilde{k}_c}{k_c}\right)^2 = 1 + \frac{3\phi f(0)}{k_c^2 a^3}, \tag{1.139}$$

where $f(\theta)$ is the far field pattern, which has the form,

$$\varphi \sim \frac{e^{ik_c r}}{r} f(\theta) = \frac{e^{ik_c r}}{r} \sum_{n=0}^{\infty} (2n+1) A_n P_n(\cos\theta). \tag{1.140}$$

Also, $\tilde{k}_c$ is the effective wave number for the dispersion. It may also be written as

$$\tilde{k}_c = \frac{\omega}{\tilde{c}} + i\alpha_{tot}, \tag{1.141}$$

where $\tilde{c}$ is the effective sound speed in the dispersion, and α_{tot} is the total attenuation throughout the two separate phases and the scattering due to the spheres. So, subtracting the dispersed phase attenuation just leaves the scattered attenuation $\alpha = (\alpha_{tot} - \alpha_C(1-\phi) - \alpha_P)$, where α_C and α_P are the attenuation coefficients for the continuous phase and particle phase, respectively. This can be written as an attenuation coefficient

$$\alpha_P = -\frac{3\phi}{2k_c^2 a^3} \sum_{n=0}^{\infty} (2n+1) \operatorname{Re} A_n. \tag{1.142}$$

This is simply a summation of the attenuation of many single scatters as one particle is not considered to have an effect on any other particles.

A comparison of the three approximations, LFPST (section 1.3.7.1), geometric theory of diffraction (section 1.3.7.2) and weak thermal scattering (section 1.3.7.3), compared to the ECAH solution can be found in figure 1.4.

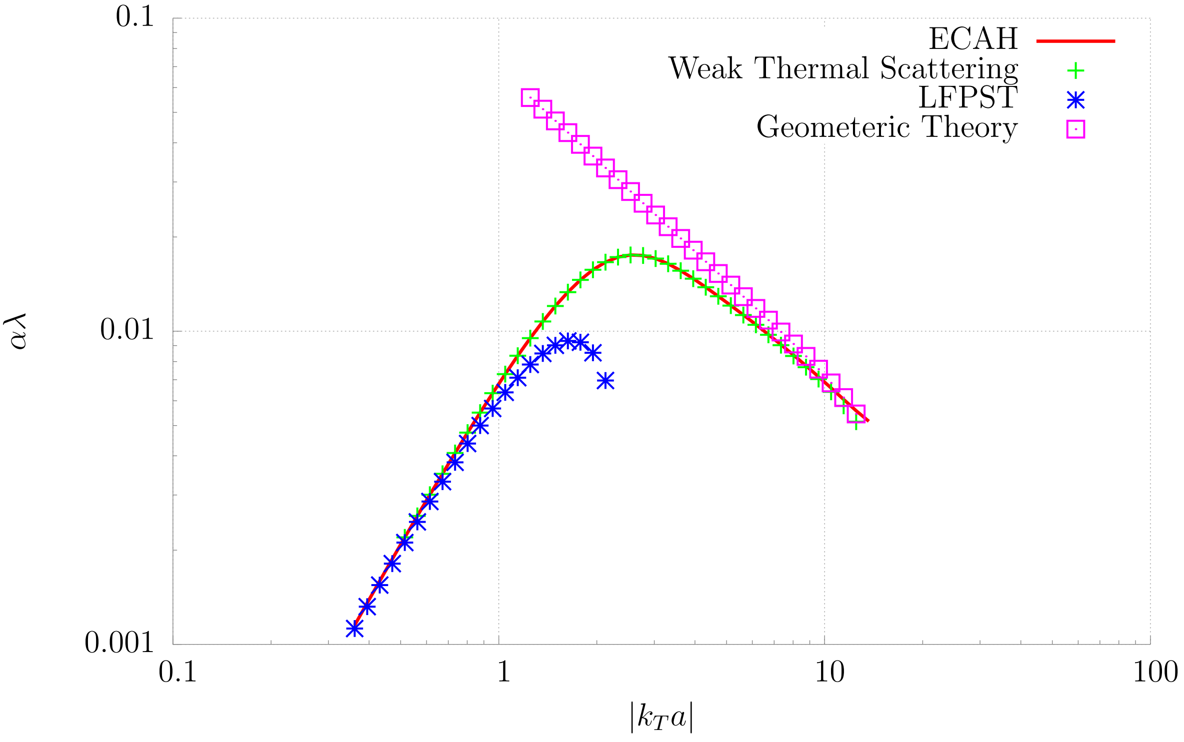

Figure 1.4

Thermal wavenumber and particle size against $|k_T a|$ *attenuation per wavelength for ECAH single scattering theory, with the three approximation limits for the different regions of the limits of* $|k_T a|$*, for a silicone oil-in-water emulsion with a 5% volume fraction. The blue line, LFPST described in section 1.3.7.1, approximates the ECAH prediction closely when* $|k_T a| < 1$ *but fails outside this region. Similarly the purple line, geometric theory of diffraction described in section 1.3.7.2, provides a close approximation for* $|k_T a| > 1$ *but again fails outside this region. The green line, weak thermal scattering described in section 1.3.7.3, provides a good approximation in the region* $|k_T a| \sim 1$*.*

1.4 Single Field Multiple Scattering Methods

There have been various methods over the years to devise a theory to compensate for multiple scattering effects. One of the early attempts was a model devised by Urick and Ament [30], which was based on a "thin slab approximation" to obtain an effective wavenumber for a single particle scattering system. The forward and back scattered wave amplitude were then calculated from a thin slice of the disperse phase less than a wavelength thick. The apparent wavenumber was determined by calculating the scattering coefficients by comparing the reflected and transmitted waves which would be obtained from a homogeneous slice of fluid with a given wavenumber. It was assumed that each particle in the slice experienced the same acoustic field, hence, transverse waves were neglected. They gave the result,

$$\left(\frac{\tilde{k}_c}{k_c}\right)^2 = \left(1 - \frac{3i\phi}{k_c^3 a^3} A_0\right)\left(1 - \frac{9i\phi}{k_c^3 a^3} A_1\right). \tag{1.143}$$

Two of the more common theories for the analysis of ultrasound measurements are by Waterman and Truell [31], Fikioris and Waterman [32], Lloyd [33, 34], and Lloyd and Berry [35]. They use the hierarchy method to determine the wavenumber of a dispersion and ensemble average to obtain the acoustic field, building on work by Foldy [36] and Lax [37, 38].

Waterman and Truell's first attempt [31] at solving the problem agreed with ECAH. However, a later calculation by Fikioris and Waterman [32], corrected an error and provided

$$\left(\frac{\tilde{k}_c}{k_c}\right)^2 = 1 - \frac{3i\phi}{k_c^3 a^3}\left(A_0 + 3A_1\right) - \frac{27\phi^2}{k_c^6 a^6}\left(A_0 A_1 + 2A_1^2\right). \tag{1.144}$$

Lloyd and Berry approached the problem from a different point of view. They took the point of view of the density energy states in a medium. This method is currently the most accepted solution to the multiple scattering problem. However, it is flawed as it deals with particles as points rather than spheres. The result that is presented here has been terminated at second order terms, however more can be calculated,

$$\left(\frac{\tilde{k_c}}{k_c}\right)^2 = 1 - \frac{3i\phi}{k_c^3 a^3}\left(\sum_{n=0}^{\infty}(2n+1)A_n\right) - \frac{27\phi^2}{k_c^6 a^6}\left(A_0A_1 + \frac{10}{3}A_0A_2 + 2A_1^2 + 11A_1A_2 + \frac{230}{21}A_2^2\right), \tag{1.145}$$

or in terms of the far-field,

$$\left(\frac{\tilde{k_c}}{k_c}\right)^2 = 1 + \frac{3\phi}{k_c^2 a^3}f(0) + \frac{9\phi^2}{4k_c^4 a^6}\left(f^2(\pi) - f^2(0) - \int_0^{\pi} d\theta \frac{1}{\sin(\theta/2)}\left(\frac{d}{d\theta}f^2(\theta)\right)\right), \tag{1.146}$$

upto $n = 1$. This result was also found later by Linton and Martin [39] by considering only the acoustic scattering off each sphere in a finite array of spheres, and taking the limit as the scatter size tends to zero.

1.4.1 Limitations of single field scattering theory

While single scattering theory can be effective in predicting the acoustic behaviour of a colloidal dispersions, it does suffer when the concentrations of the disperse phase increase. This can be explained by looking at the decay length of the thermal field around an oil droplet, which is given by [40] as

$$\delta_T = \sqrt{\frac{2\tau}{\rho C_p \omega}}. \tag{1.147}$$

At low enough concentrations the droplets are sufficiently far enough apart that these field do not interact. But now consider

$$\delta_T \geq \frac{d}{2}, \tag{1.148}$$

where d is the distance between the centre of neighbouring particles. Then the thermal fields of the two droplets must overlap. In figure 1.5, the decay length in water has been plotted against frequency. The decay length decreases as the frequency increases, thus there will be more thermal overlap at lower frequencies.

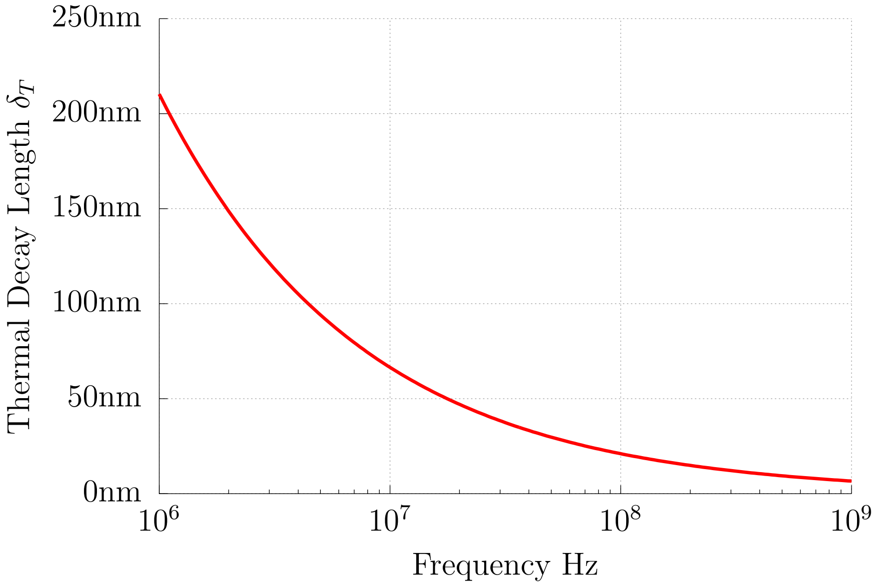

Figure 1.5

A comparison of thermal decay length against frequency from equation (1.147) *in water at* 25°C*. At lower frequencies the thermal decay length is higher, which leads to more overlaps with other particles' thermal fields.*

Thus we can define a critical concentration, ϕ_c, at which the thermal field of neighbouring particles begin to overlap. This critical volume fraction is given by [41]

$$\phi_c = \left(\frac{1}{1 + \frac{\delta_T}{a}} \right)^3 . \tag{1.149}$$

The critical volume fraction can be seen in figure 1.6 for varying particle sizes in water at 25°C at 1 MHz. It is notable that the critical volume fraction becomes more predominant as the particle size is reduced.

More recent approaches to overcome the limitations of single field scattering theory have been by Pinfield [42, 43] and Luppé *et al.* [44]. They consider the additional effects on multiple scattering caused by mode conversion two and from thermal waves. Building on the work by Waterman and Truell [31] and Waterman

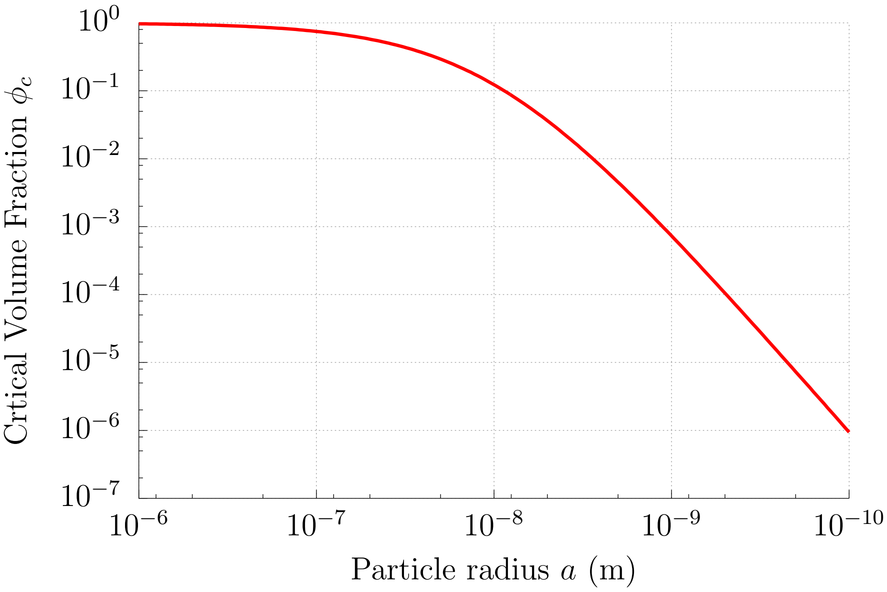

Figure 1.6

A comparison of critical volume fraction against particle radius in water at $25°C$ *at* 1 *MHz. As the particle size is reduced the amount of thermal overlap increases, which reduces the accuracy of current theories when measurements of concentrations greater than this are required.*

[45] the transition operator $T^{pq}(\mathbf{r})$ is introduced by defining a generalised far field scattering function

$$f^{qp}(\theta) = \sum_{n=0}^{\infty}(2n+1)T_n^{qp}P_n(\cos\theta), \tag{1.150}$$

where

$$T_n^{pq}(\mathbf{r})j_n(k_q r)P_n(\cos\theta) = T_n^{pq}(\mathbf{r})h_n(k_p r)P_n(\cos\theta). \tag{1.151}$$

The coefficients p and q represent either the thermal or the compressional waves, such that we can consider

$$T_n^{CC} \equiv A_n, \tag{1.152}$$

to be the compressional scattering coefficient from equation (1.76), and

$$T_n^{CT} \equiv B_n, \tag{1.153}$$

to be the thermal scattering coefficient from equation (1.77). This method assumed that the zero order coefficients of the compressional-thermal mode-conversion terms are retained, and thus allow the introduction of a thermal incident wave

$$\psi_T^{\text{inc}} = \sum_{n=0}^{\infty} i(2n+1)j_n(k_T r)P_n(\cos\theta). \tag{1.154}$$

This allows for T_0^{CT} thermal fields based on zero order compressional fields to be generated, but also T_0^{TC}, a scattered compressional field based on the zero-order thermal field. This has been used to account for multiple scattering of the thermal waves for higher concentration colloids, and produces an additional term to the Lloyd and Berry equation (1.146),

$$\begin{aligned}\Delta\left(\frac{\tilde{k}_c}{k_c}\right)^2 &= -\frac{27\phi^2}{k_c^6 a^6}\frac{k_c^3}{6k_T\left(k_c^2-k_T^2\right)}\left[\left(2ik_T a-1\right)j_0(2k_c a)\right.\\ &\left.-(2k_c a)j_0'(2k_c a)\right]\cdot\left\{T_0^{CT}h_0(k_T a)\right\}\left\{\frac{T_0^{TC}}{j_0(k_T a)}\right\}\left(1-e^{2ik_T a}\right).\end{aligned} \tag{1.155}$$

While this method does consider the thermal overlap between particles, it does not explicitly look at the interaction between two particles, which is what we aim to do in this thesis.

1.5 Aims and Outline of Thesis

The focus of this thesis is to increase understanding of inter-particle thermo-acoustic scattering in the pursuit of developing methods for increased accuracy in predicted attenuation profiles of high concentration colloidal suspensions, by developing a mathematical solution for thermo-acoustic scattering by a pair of spheres for different sizes. The first step towards this is using the Harlen *et al.* [27] weak thermal scattering method to treat the problem in the low frequency limit, which allows the use of perturbation power series to define the acoustic field about a sphere. This approach is used to solve thermoacoustic scattering system by particles, in chapters 4 and 5, using methods of Gaunaurd *et al.* [46] and Greengard and Rokhlin [47]. From this we will calculate the scattering coefficients for two systems. In chapter 4 we consider the case of two spheres in-line with the incident plane wave, and in chapter 5 the case where the incident wave is at some arbitrary angle of the orientation of the particles.

The second aim of this thesis is to use the results of the two methods in chapters 4 and 5, to improve the prediction of scattering theory at higher concentrations by incorporating multiple scattering effects from thermal overlap. This is explored in chapter 6.

Another objective of this thesis is to obtain experimental data on mono- and bi-disperse colloidal systems in order to test the theoretical predictions. In the next chapter, the details of the experimental systems studied for this thesis are presented. Scattering results are shown in chapter 3 and show that current acoustic scattering theory does not adequately capture the behaviour of two different sized dispersions in a single continuous phase. This data will then be compared, in chapter 6 with the new multiple scattering theory which can model the behaviour of different size particles.

The final objective is to develop an apparatus for in-line detection of sedimentation in pipes. This is investigated in chapter 7, where we develop a system of a pair of rotating ultrasound transducers to monitor the attenuation and sound through the pipe at different angles.

Chapter 2

Materials and Methods

2.1 Introduction

In this chapter we look at three different experimental studies and the techniques and materials used in these. The main purpose of the experiments to follow is to demonstrate the need for an improved acoustic multiple scattering model. The first study involves the varying of concentration of a mono-disperse colloidal system. To measure it we use a Malvern Ultrasizer, which measures attenuation from 2 to 120 MHz, and the TF Intrustments ResoScan, which measures velocity and attenuation at a single frequency of around 8 MHz. The purpose of this study is to investigate how the velocity and attenuation measurements change with concentration of the dispersed phase from the dilute, in which single scattering dominates, to concentrated where multi-scattering dominates.

The second study looks at a bi-disperse system, at different concentration levels. This has the dual purpose of validating single scattering theory for mixtures of different particles and challenging the bi-spherical theory developed in this thesis. This study will be conducted using the Malvern Ultrasizer.

The third study, based again on bi-disperse systems, looks at how these systems cream over time. Using the Acoustiscan we can monitor the attenuation and velocity across the height of a sample at a single frequency. This allows us to see how two particle sizes affect how the sample behaves.

2.2 Studied systems

All the following materials have their relevant properties provided in table 2.1.

2.2.1 Water

For each of the systems described in this thesis we will be using *Millipore Water*. This is purified water provided through a *Milli-Q* water purifying system, supplied by *Millipore Corporation*, Massachusetts, USA. Milli-Q using a de-ionisation system, with an added microfiltation process that removes particulate impurities that de-ionisation may not remove. In particular, the filtration removes small surfactant molecules which can have the unfortunate effect of stabilising small bubbles which interfere with ultrasound propagation. For the purposes of this thesis, we will now exclusively refer to Millipore water, when we use the word "water".

2.2.2 Bromohexadecane in water

This system is made up of: *1-Bromohexadecane* 97% supplied by *Sigma-Aldrich Company Ltd.*, Dorset, UK; *Caflon* GL0700 Alcohol Ethoxylate, supplied by *Univar*, Illinois, USA. Note this material is hazardous, use appropriate safety precautions, and water. Bromohexadecane is used as it is density matched with water, however, its other properties provide a good thermal difference to produce large thermal acoustic effects. It is also known to create stable emulsions. Caflon is used as a surfactant, to lower the surface tension between bromohexadecane and water. The caflon creates a single molecule layer around a sphere of bromohexadecane. The amount of caflon added determines the size of the spheres created in the homogenisation process described in section 2.3.

2.2.3 Hexadecane in water

This system is made up of: *n-Hexadecane* 99% supplied by *Alfa Aesar*, Keysham, UK; Caflon, and water. This system is used, like bromohexadecane as it provides good thermal contract to produce large thermo-acoustic effects and creates a stable emulsions. However, unlike bromohexadecane it is not density matched with water. Caflon is again used as a surfactant.

2.2.4 Silica in water

This system is made up of: *Silica* Ballotini solid soda glass balls, *SiLibeads*® supplied by *Jencons-PLS*, Pennsylvania, USA; and water. This system is used as the Silica beads sediment quickly so can be used for sedimentation measurements in chapter 7.

2.2.5 Polystyrene-PEGMA

This system is made up of: styrene, PEGMA 2000 stabiliser and water. The PEGMA 2000 is used as surfactant. Three samples of this system were provided of size 100nm, 400nm and 900nm. These samples were kindly provided by Dr. H. N. Yow, University of Leeds, as part of a project looking at the acoustic properties of these materials in relation to ink jet printing methods. Details of samples can be found in table 2.3.

2.2.6 Silicone Oil

Dow Corning® 200/50cS fluid, silicone oil, supplied by *VWR International Ltd*, Poole, England, is used as it has a higher viscosity than water, so the effects of stirring speeds can be observed.

2.3 Sample preparation

One litre of hexadecane or bromohexadecane in water emulsion was prepared by first calculating the required amount of surfactant (Caflon) by using the following,

$$V_{\text{caflon}} = 4\pi R r^2 \times \frac{\phi m 10^{-6}}{\rho \frac{4}{3}\pi r^3}, \tag{2.1}$$

where ρ is the density, R is the radius of the surfactant molecule, r is the desired particle radius, ϕ is the weight percentage of the disperse phase, and m is the

Media	Sound velocity $v\ (m\,s^{-1})$	Density $\rho\ (kg\,m^{-3})$	Shear viscosity $\mu\ (Pa\,s)$	Shear modulus (solids) $\nu\ (Pa)$	Thermal conductivity $\sigma\ (W\,m^{-1}K^{1})$	Specific heat $C_p\ (J\,kg^{-1}\,K^{-1})$	Attenuation exponent p	Attenuation factor $\alpha\ (Np\,m^{-1}\,MHz^{-p})$	Thermal expansion coefficient $\beta\ (K^{-1})$
Water [48]	1497	997	0.00089	-	0.595	4179	2	0.0215	0.00021
Bromohexadecane [49]	1299.4	1000	0.00663	-	0.141	2090.8	2	0.145	0.000775
Hexadecane [48]	1357.9	773.0	0.00334	-	0.14	2093	2	0.101	0.00091
Silicone Oil [27, 49]	1004	975	0.3395	-	0.15	1460	2	2.5	0.00094
Polystyrene [19]	2365	1053.5	-	$1.27 \cdot 10^{9}$	0.115	1194.8	1.77	0.10016	0.000268
Silica [50, 51]	5960	2200	-	$3.13 \cdot 10^{10}$	1.37	742	1	0.00017	$1.22 \cdot 10^{-6}$

Table 2.1

Properties for materials used in this thesis at 25°C.

total mass. Stir the sample with a magnetic flea for ten minutes to ensure it has been thoroughly mixed. Place the sample in a water bath at 5°C to remove any excess gas within the sample for 60 minutes. The sample is then passed through a high pressure homogeniser. Often multiple passes are required to create an emulsion with the desired particle size. After each pass use a Mastersizer 3000 (Malvern Instruments) to take a light scattering measurement of the average particle size and spread. When creating particle sizes of less than around 800nm, it is recommend to first make a emulsion with a particle size larger than that is required, then adding additional surfactant to create smaller particles. Once the emulsion has been created it can be stored at room temperature, provided it is covered, to prevent evaporation. Details of the particular samples can be found in tables 2.2 and 2.3

2.4 Ultrasound experiments

Three different acoustic measurement devices were used to analyse these fluid systems. While all three instruments measure the attenuation of ultrasound through a material, they operate at different frequencies and require different sample volumes, as summarised in table 2.4.

2.4.1 Ultrasizer

The *Ultrasizer MSV* from Malvern Ltd [52] (see figure 2.1) is an acoustic spectroscopy device for measuring acoustic attenuation. It functions by using the "pitch and catch" transmission method (see figure 2.2). A voltage generates an acoustic signal in a transducer that is received in a second transducer. The voltage is measured in the second transducer and the attenuation is calculated by comparing the signal amplitude and the distance between transducers. A key feature of this instrument is that it provides a broad range of frequencies. There are two pairs of broadband transducers to cover the frequency range. The low frequency pair covers frequencies from 2MHz to 20MHz and the high frequency pair measures from 18MHz up to 120MHz. The distance between these pairs of transducers is varied to optimise the signal to noise ratio and is calculated

Continuous phase mass (g)	Disperse phase mass (g)	Surfactant mass (g)	Concentration v/v%	Measured size distribution (nm)	Size distribution used in model (nm)
420	139.14	0.85	30	901.2	900
420	139.14	7.68	30	104.8	100
480	92.76	0.57	20	897.2	900
480	92.76	5.12	20	98.5	100
510	69.57	0.43	15	903.1	900
510	69.57	3.84	15	105.3	100
540	46.38	0.28	10	896.8	900
540	46.38	2.56	10	101.9	100
570	23.19	0.14	5	904.2	900
570	23.19	1.28	5	101.1	100

Table 2.2

Details of composition of Hexadecane-in-water experimental systems. Each makes 600ml.

Mean particle size (nm)	Size used in model (nm)
393.0	400
898.1	900

Table 2.3

Details of Polystyrene PEGMA particles in experimental systems kindly provided by Dr. H.N. Yow.

Instrument	Frequency (MHz)	Sample Volume (ml)	Pulse or continuous	Attenuation	Velocity
Acoustiscan	2-5	20 to 300	Pulse	✓	✓
ResoScan	7.3-8.4	0.2	Pulse	✓	✓
Ultrasizer	2-120	500	Quasi-Continuous	✓	✘

Table 2.4

Comparison of experimental methods.

automatically by the device software. The device compares the measurements at two distances to factor out errors. It also automatically calibrates the effects of diffraction to reduce errors. One drawback of this device is that it requires large amount of sample, 500ml, to be used. The chamber is heated using a *Huber MiniStat* heater. The temperature is also recorded when a measurement takes place.

The chamber also contains a stirrer, this can be set to have an angular speed from 0 to 3000 RPM. The manufactures guidelines suggest a minimum stirring speed of 200 RPM with 500 RPM being a generally appropriate setting. Stirring reduces flocculation and creaming effects, as well as keeping the temperature even throughout the sample. However, over stirring can lead to air being drawn into the sample, or vibrate the apparatus too vigorously. Following the manufacturer's instructions for the software, multiple automated measurements can be made.

Control data was obtained with water at $25°C$ at different stirring speeds. In figure 2.3 we present the attenuation spectrum of water, with stirrer at 100 RPM and 1000 RPM. It can be seen that both stirring speeds are able to recover the attenuation coefficient for Millipore water. From this we can set the stirrer at 500RPM as a mean value. Further analysis on how to calibrate the system based on bulk viscosity has been carried out by Holmes *et al.* [53].

There are a number of problems that can arise under certain situations. One peculiar phenomenon can occur when using high concentration samples when varying the stirrer speed. In figure 2.4 there is an artefact at 40MHz which is more prominent at lower stirring speeds. It has been speculated that the

Figure 2.1

The Malvern Ultrasizer MSV [52].

system will want to set the distance between the transducers to be very small. This reduces the amount the stirrer effects the fluid in the chamber between the transducers, providing erroneous readings. A study, using *COMSOL Multiphysics* was carried out to monitor the flow in this section of the chamber. The minimum distance between the transducers is 5.08mm. In figure 2.5 we see a diagram of the ultrasizer fluid chamber, which shows how the transducers can move together or apart to create different distances between the transducers. In figure 2.6, we have the Comsol model of the Ultrasizer measurement chamber with the transducer distance set to 5.08mm. Also seen in the model is the stirring mechanism. Using the rotating machinery, laminar flow module in Comsol, the flow in between can be monitored. In figure 2.7, we see a fluid velocity magnitude profile of the plane equidistant between the transducers for stirring at 100RPM. The flow between the transducers and above is reduced to around 1mm s^{-1}, whereas the section below the transducers has a high velocity, indicating mixing is occurring in this region.

To investigate this effect further, Dow Corning 200 50cS silicone oil was put into the Ultrasizer and stirred at different angular velocities, as this has an increased viscosity. In figure 2.8, the sample had been stirred at different angular velocities from 100 to 1500RPM. This is compared to the attenuation coefficient of silicone oil. It can be seen that stirring speed has little effect on the attenuation of the sample.

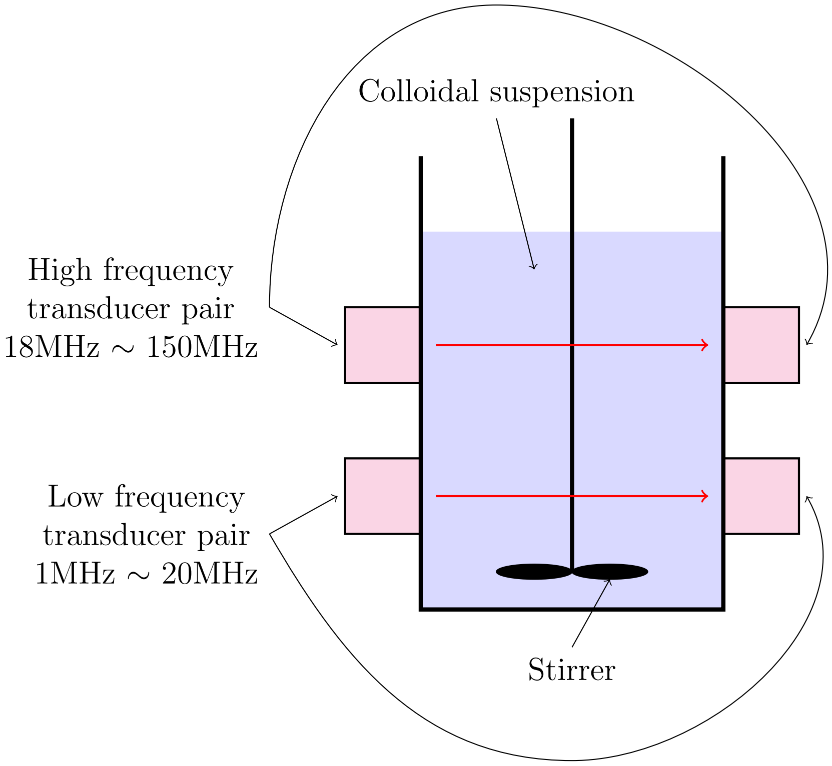

Figure 2.2

A schematic diagram of Malvern Ultrasizer. Two pairs of transducers, one low frequency (2MHZ to 20MHZ) and one high frequency (18MHz to 120MHZ) transmit acoustic signals across the sample whilst the sample is stirred.

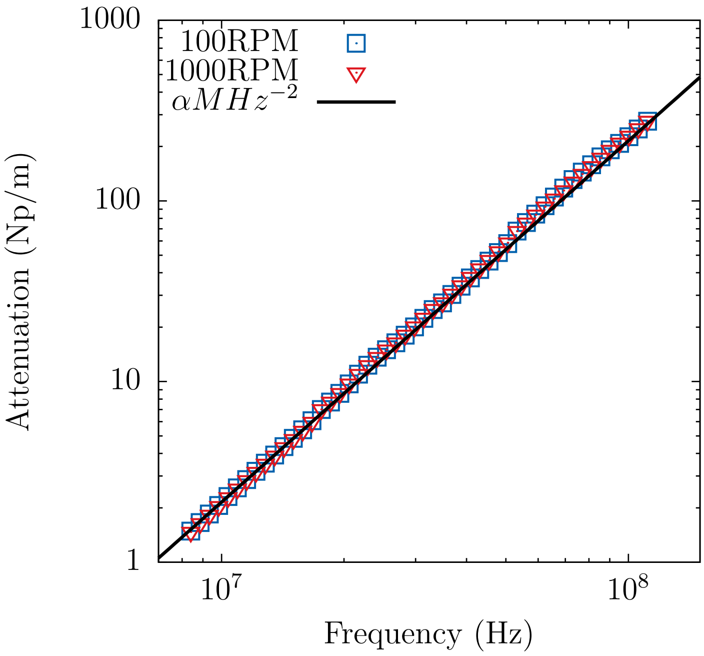

Figure 2.3

Attenuation-frequency calibration data for water, for different stirrer speeds at 25°C *using the Malvern Ultrasizer. The theory line is provided by the attenuation factor of water in table 2.1. Notice from equation* (1.14) *that attenuation increases as frequency squared increases. It can be seen that both stirring speeds are able to recover the attenuation coefficient for water.*

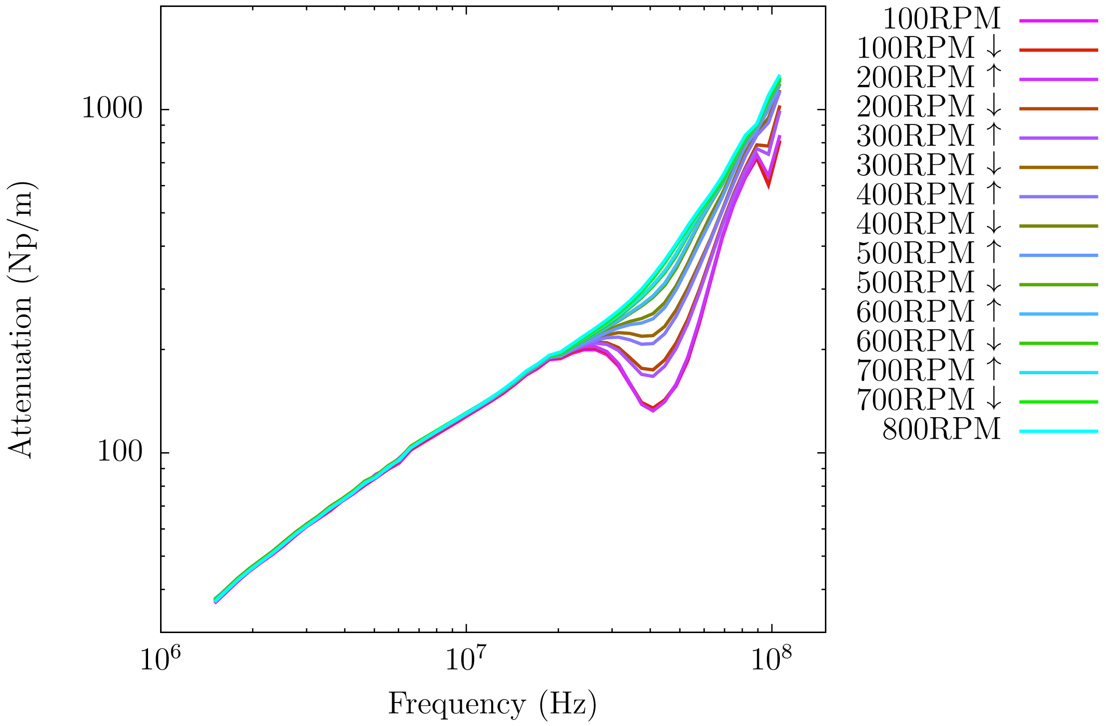

Figure 2.4

Attenuation-frequency data for 800nm 30% *hexadecane-in-water emulsion, for different stirrer speeds first rising and then decreasing in speed at* 25°*C using the Malvern Ultrasizer. The* ↓ *and* ↑ *represent whether the stirrer was decreased or increased to the angular speed. At around 40MHz a measurement artefact occurs with slower stirring speeds.*

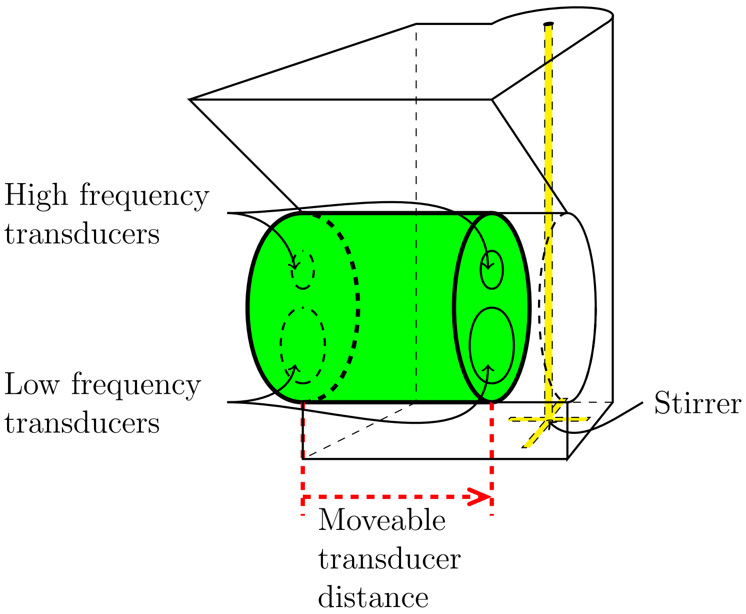

Figure 2.5

Diagram of Ultrasizer sample chamber. Green area can be reduced or expanded depending on required transducer separation.

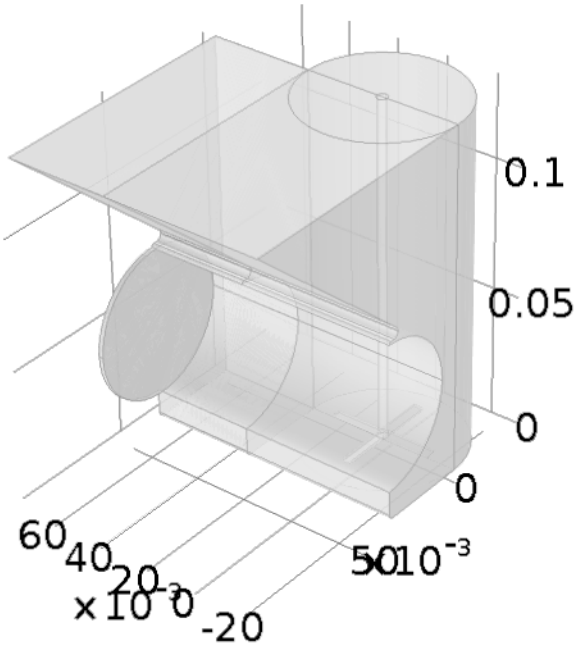

Figure 2.6

COMSOL Multiphysics model of the geometry of the Ultrasizer chamber. The distance between the transducers is set to the minimum 5.06mm (0.2 inch) to determine fluid flow between the transducers.

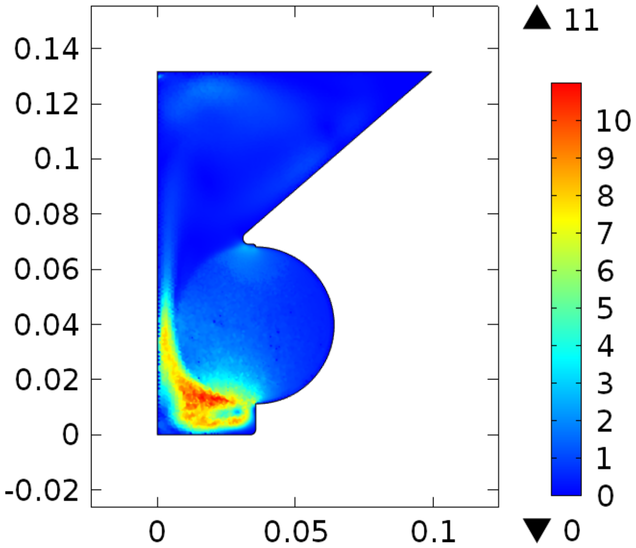

Figure 2.7

COMSOL Multiphysics model showing the flow in mm/s in the Ultrasizer chamber equidistant between the transducers for 100RPM when they are at the minimum distance, 5.06mm, apart.

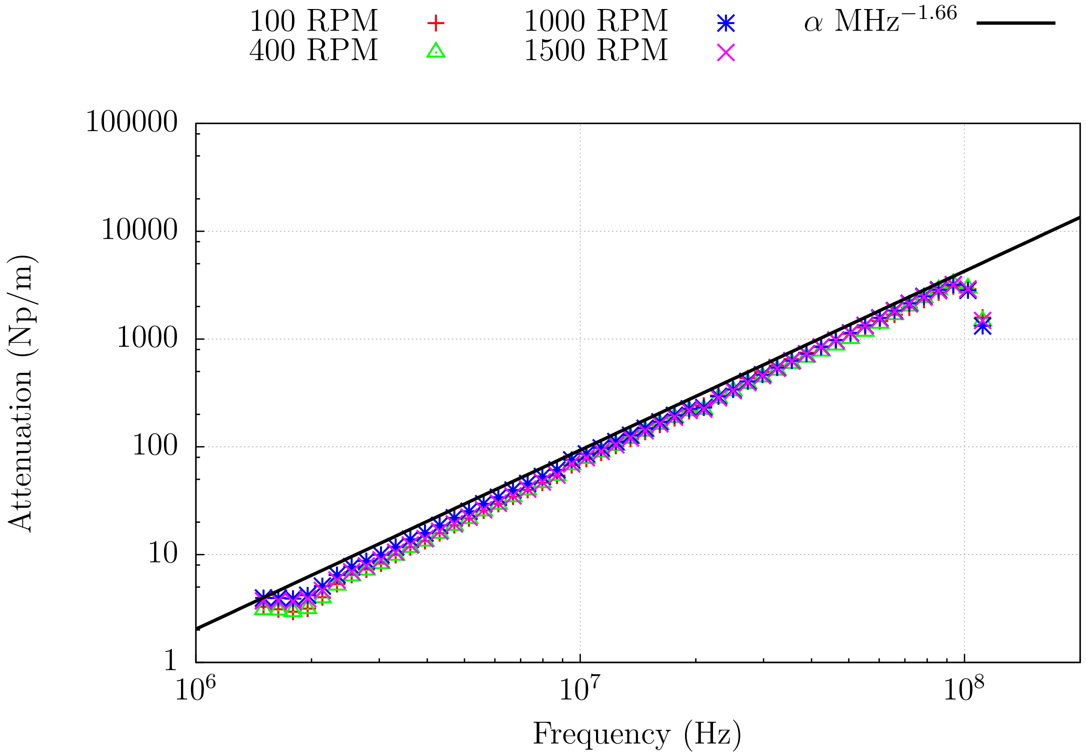

Figure 2.8

Pure Dow Corning 200 50cS silicone oil stirred at different angular velocities. The increase in stirring speed has little effect on the attenuation of the sample.

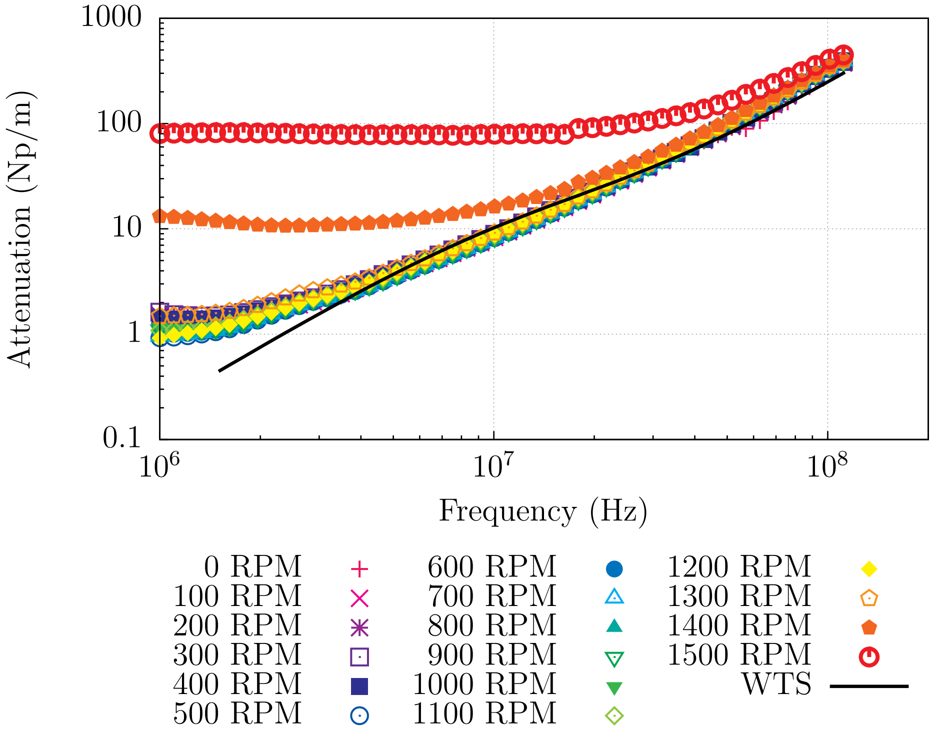

Figure 2.9

Polystyrene PEGMA 5% 100nm and 5% 900nm, stirred at different angular velocities, compared with weak thermal scattering model.

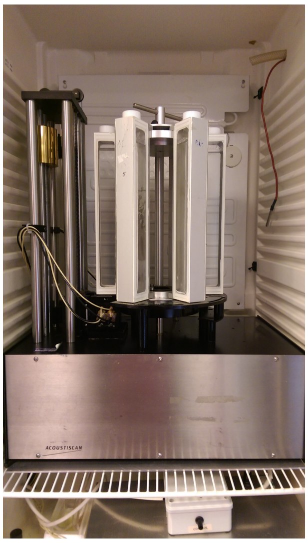

Figure 2.10

Acoustiscan ultrasound profiler.

This test was carried out again, with more intermittent steps, with Polystyrene PEGMA 5% 100nm and 5% 900nm, shown in figure 2.9. At low stirring speeds the attenuation is not affected. As the stirring increases to high speeds, above 1300RPM, we see a large increase in the attenuation at low frequencies. However, this could be attributed to the high stirring speeds introducing air into the system. Further analysis of the Ultrasizer system can be found from Povey [54].

2.4.2 Acoustiscan

The *Acoustiscan* ultrasound profiler (as seen in figure 2.10) was designed by Phillip Nelson and Malcolm Povey for the purpose of providing information about the destabilisation of emulsions, dispersions and colloidal systems by measuring the velocity of sound and the attenuation of a sample multiple times along a vertical cross-section of the sample [55].

The velocity and attenuation of a sample are measured by two pairs of ultrasonic transducers, with centre frequencies of 2MHz and 5MHz, although they have a frequency scanning range of 0.6MHz to 10HMz. The transducers have a pulse generated for them by a *NDT solutions* pulse receiver unit. The received pulse is measured, as are the echoes to provide greater accuracy. These transducers are placed against two $300 \times 35 \times 1\text{mm}^3$ glass panels, in which the sample sits between, as seen in figure 2.11. To couple the transducers with the glass windows, Dow Corning silicone oil is used. This also acts as a lubricant for the movement of the transducers. The amount of lubricant is carefully controlled to keep measurements consistent and repeatable. The transducer aperture can be moved up and down the sample container in steps as small as 1mm, which is around 10% of the transducer size. Taking measurement of step size of 5mm for a 250mm sample can take 7 minutes to complete. Once a measurement is complete the transducer aperture is moved off the end of the sample holder and a carousel is rotated to bring the next sample on to the measurement platform. The carousel can contain up to six samples. The whole apparatus is contained in an insulating cabinet so that temperate can be regulated. The temperature is controlled by an inflow of compressed air cooled and dried in a vortex cooler, together with three lamps working in tandem.

To calibrate, one must use distilled water. The calibration data can be seen in figure 2.12. To calibrate correctly, we need to calculate the speed of sound in water using Marczak's equation [56]

$$\begin{aligned} v_{\text{water}} &= 1.402385 \times 10^3 + 5.038813T - 5.799136 \times 10^{-2}T^2 \\ &+3.287156 \times 10^{-4}T^3 - 1.398845 \times 10^{-6}T^4 + 2.787860 \times 10^{-9}T^5, \end{aligned} \tag{2.2}$$

where T is temperature in degrees Celsius, as shown in figure 2.13. Calibrating also accounts for the signal delay due to the walls of the sample container. Diffraction is also accounted for by assuming the speed of sound between water and samples does not vary greatly, such that diffraction does not significantly change compared to water. Data 5mm near the top and the bottom of the sample has to be discarded due to diffraction effects around the edge of the samples. Further information about the Acoustiscan can be found from Nelson *et al.* [55] and Povey [54].

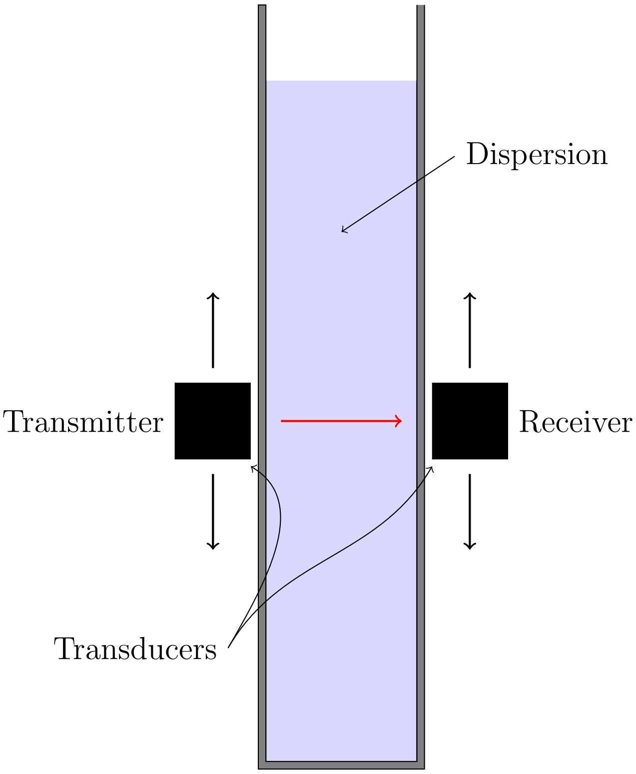

Figure 2.11

Schematic diagram of an Acoustiscan ultrasound profiler.

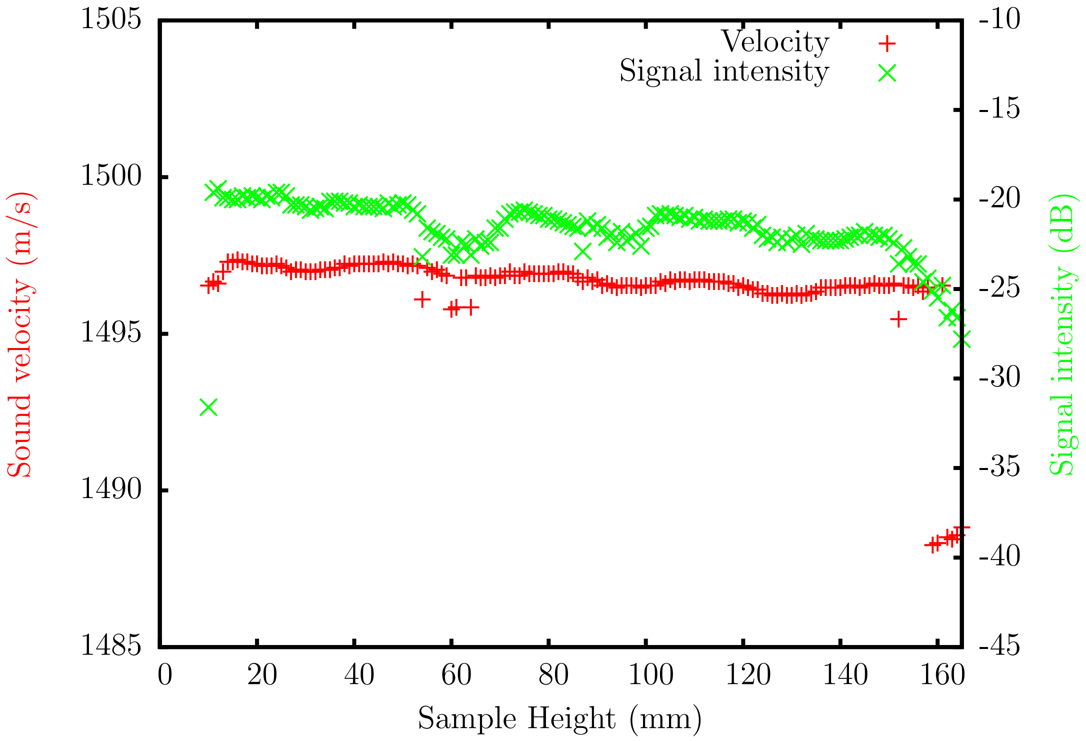

Figure 2.12

Typical calibration data for distilled water in an Acoustiscan ultrasound profiler. Edge effects can be seen at the top of the sample, which are more gradual for the intensity reading than for the velocity reading.

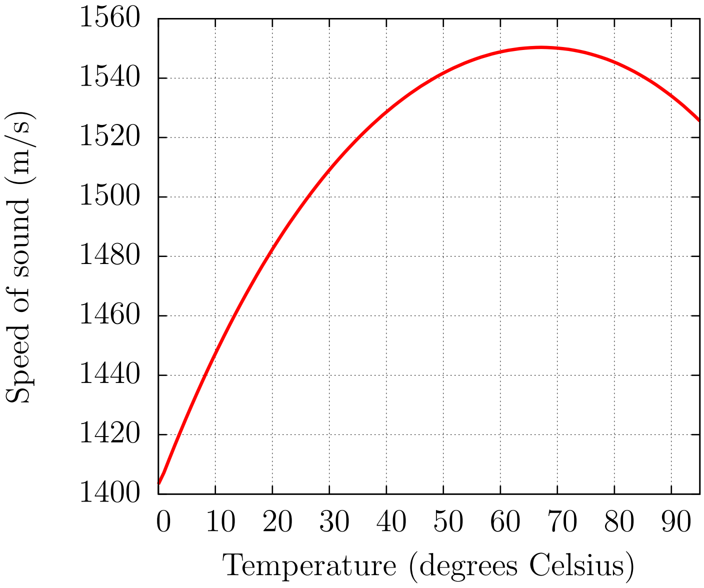

Figure 2.13

The speed of sound in pure water as a function of temperature as described by Marczak's equation (2.2).

2.4.3 Resoscan

The *Resoscan*, TF Instruments Inc. (as seen in figure 2.14), is a ultrasonic high precision relative measurement device. It contains two 200μl cells which measure sound velocity and attenuation simultaneously. The transducers have a working frequency of 7.3-8.4MHz. The temperature of the cells can be very precisely set from 5 to 70°C by a Peltier thermostat. The instrument can be set to automatically measure samples with a varying temperature range.

Following the method of Holmes *et al.* [57], the device can be calibrated by putting Millipore water in the sample chambers and comparing with literature sources [56], shown in figure 2.13. Further analysis of the Resoscan system can be found in [54].

Figure 2.14

Resoscan, TF instruments Inc. [58].

Chapter 3

Experiment and comparison with existing theories

Two main studies were carried out as part of this research. Firstly, a number of experiments were carried out investigating the effect of different concentrations of monodisperse colloidal dispersions on the attenuation spectrum measured by the Malvern Ultrasizer (see section 2.4.1). This data is also compared with data from Herrmann [5]. This was then compared with readings of velocity and attenuation taken from the ResoScan (section 2.4.3) at varying concentration levels. The ResoScan study was then expanded over a temperature range, again measurements of velocity and attenuation were taken over this region.

The second study was looking at how attenuation is effected by the mixing two different sized dispersions. The Ultrasizer was used to carry out a frequency sweep of the samples to acquire attenuation spectra. These samples were then measured using the AcoustiScan (section 2.4.2) over time to monitor how these samples behave.

These experiments are compared with the current theories described in chapter 1 to show the area where improvements in the acoustic theories need to be made.

3.1 Mono-disperse experiments

3.1.1 Concentration

This first series of experiments are designed to test how measurements of samples are effected by increasing concentrations of the disperse phase in mono-disperse emulsions, as the theories presented in chapter 1 have been shown to be inaccurate at higher concentrations due to overlaps in the thermal dissipation fields.

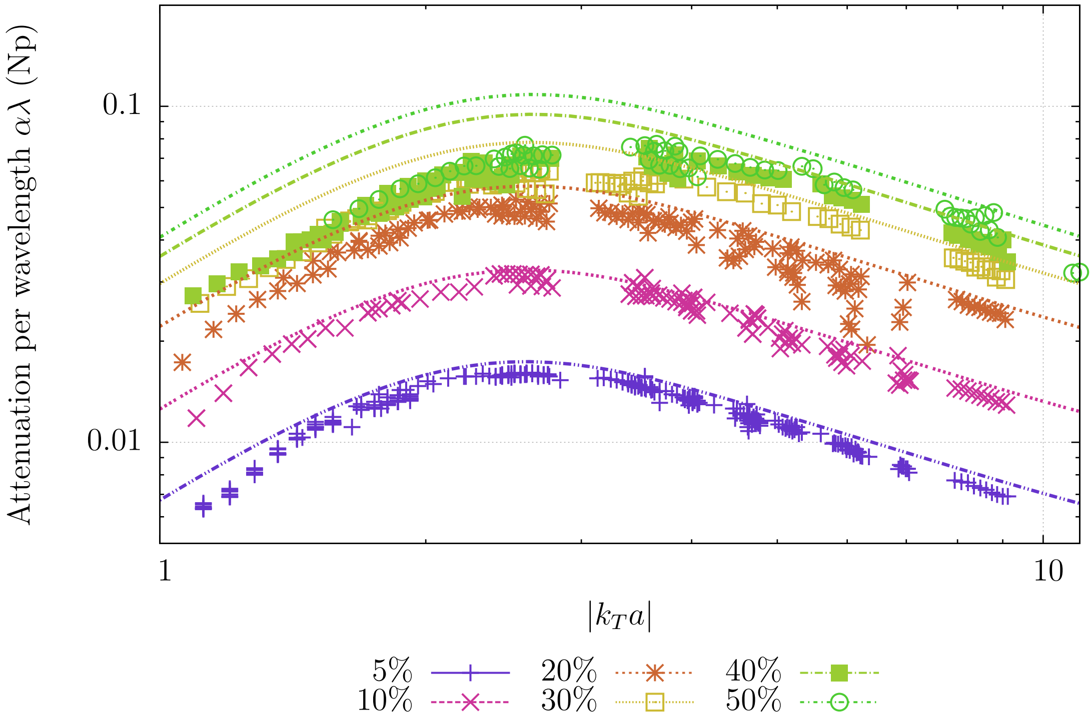

Figure 3.1

Silicone-in-water dispersion data for particle radii 230-760nm, from Herrmann [5], compared with single weak thermal scattering theory. The lines represent the theoretical prediction and the symbols represent the data.

Herrmann *et al.* [5] carried out silicone-oil-in-water experiments using a fixed-path ultrasonic interferometer, described by Herrmann [59] and Eggers [60]. Using a frequency range of 0.5 and 10 MHz, they measured emulsions with particle radii of 230-760nm, with concentrations increasing from 5% to 50%. Each of the concentrations is compared to single weak thermal scattering theory (see section 1.3.7.3) and plotted for thermal wave number $|k_T a|$ against attenuation per wave length (Np), as seen in figure 3.1. It can be seen for low concentrations, 5% and 10% that the prediction is quite accurate, however as the concentration increases the prediction becomes more inaccurate, especially for lower values of $|k_T a|$. with the experimental data providing a lower attenuation than the prediction. Also notice how the peak of the experimental data is shifted positively along the $|k_T a|$ axis.

Two of the Polystyrene PEGMA samples provided were ∼400nm and ∼900nm in radius. These were both measured in the ResoScan, measuring the velocity and the attenuation of the sample. The attenuation in the ResoScan is measured in Nps^2m^{-1} so it is necessary to multiply it by f^2 to provide an attenuation measurement compatible to the other experiments. We can see in figures 3.2 and 3.3 that, while the prediction is accurate at lower concentrations, at around 11% the experiments provide results with a lower velocity and attenuation than expected.

3.1.2 Discussion

In figure 3.1 we see the attenuation prediction for hexadecane in water become more inaccurate as the concentration increases. When the concentration reaches above 10% we see deviation from the prediction, especially for lower values of $|k_T a|$. As the concentration increases, the experimental data deviates even more the prediction, with the peak of the data moving in a positive direction along the $|k_T a|$ axis. This indicates that multiple scattering effects are occurring which single scatting theory does not account for. This is reaffirmed in the polystyrene PEGMA in water experiments, as seen in figure 3.3, where the two attenuation experiments deviate from the prediction of weak thermal scattering, which needs to be accounted for.

In addition to the attenuation measurements, in figure 3.2 we see a similar phenomenon occurring with the velocity of the sample. While for low concen-

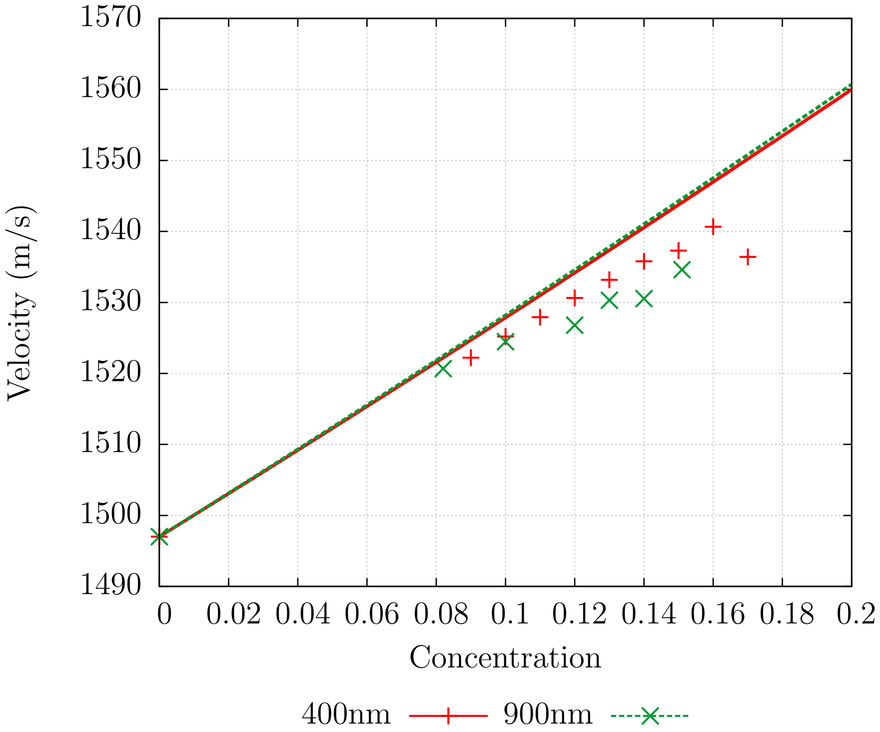

Figure 3.2

∼400 nm and ∼900 nm Polystyrene PEGMA in water velocity for concentrations measurements from ResoScan at ∼8MHz, compared to single weak thermal scattering theory. The points represent the experimental data, and the lines are the prediction.

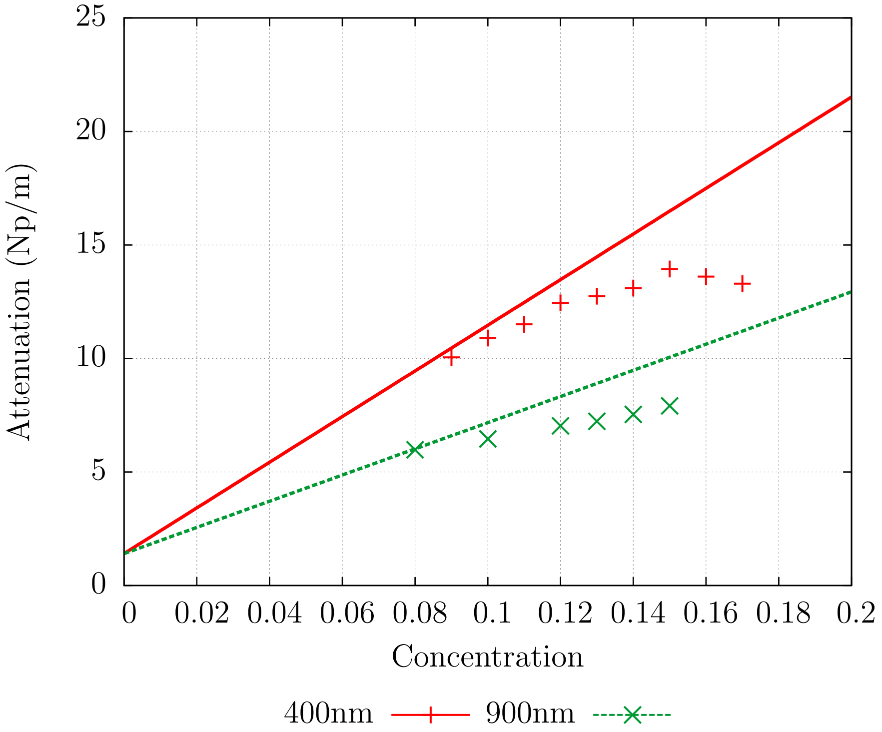

Figure 3.3

∼400 nm and ∼900 nm Polystyrene PEGMA in water attenuation for concentrations measurements from ResoScan at ∼8MHz, compared to single weak thermal scattering theory. The points represent the experimental data, and the lines are the prediction.

trations, the particle size has little effect on the velocity, the experimental data does suggest that for larger particles we see a larger contribution to changes in velocity at higher concentrations.

3.1.3 Temperature

Continuing with the ResoScan, we monitored the change in velocity and attenuation due to temperature changes. In figure 3.4, 17% ∼400nm Polystyrene PEGMA was heated from 25°C to 40°C and back to 25°C. It can be seen that for both attenuation and velocity this provided stable results. However, performing a similar test on 8.2% 900nm Polystyrene PEGMA, in figure 3.5, did not provide so consistent results. This time the sample was heated from 25°C to 60°C, down to 15°C, back to 60°C, and then returned to 25°C. While the sound velocity remains repeatable over the temperature scan, the attenuation does not. It can be seen as the temperature is reduced for the first time that it does not follow the profile as it did when heating up, and does not return to the initial attenuation for 25°C. Between 15 and 25°C the attenuation reading is repeatable, but as it increases over 25°C is increases from the previous readings. This suggests that the heating of the same is transforming it somehow.

The experiment was repeated on 8.8% ∼400nm Polystyrene PEGMA in figure 3.6. However, this time the temperature began at 15°C, was heating to 25°C and reduced to 15°C. This was repeated with increasing maximum temperature by 5°C each repetition until 60°C, then the maximum temperature was decreased 5°C until 25°C. Again the velocity reading is highly repeatable, but the attenuation reading increases every repetition. However, the attenuation increases with every pass of the temperature, although it does plateau further into the experiment, suggesting there is a transformation in the sample but it reaches some equilibrium.

3.1.4 Discussion

While the velocity of the samples in figures 3.4–3.6 across the temperature range remains consistent and repeatable, we find that the attenuation of the samples increases as the heat and cooling cycles progress. It is concluded that the sam-

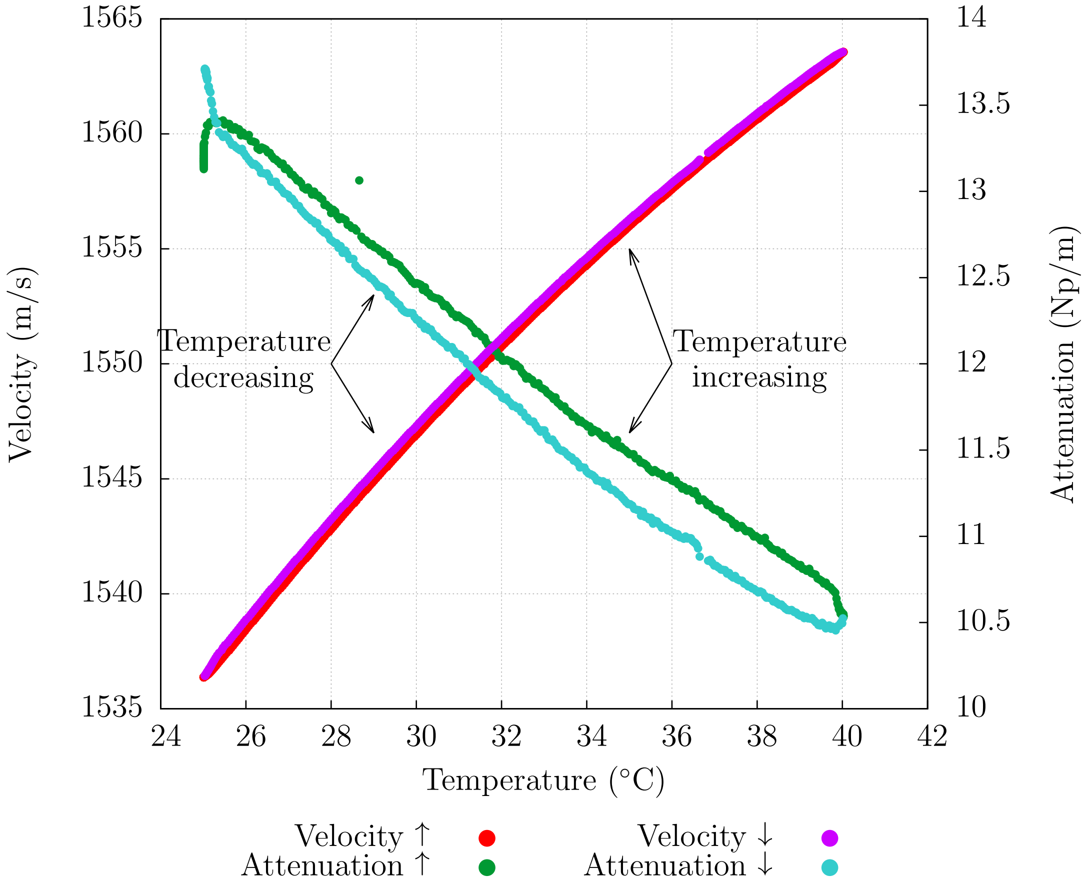

Figure 3.4

17.0% 400nm Polystyrene PEGMA in water ResoScan, at ∼8MHz, of velocity and attenuation compared to change in temperature. The sample was heated from 25° C to 40° C , and then let to cool down to 25° C . ↑ represent the sample heating up and ↓ represent the sample cooling down.

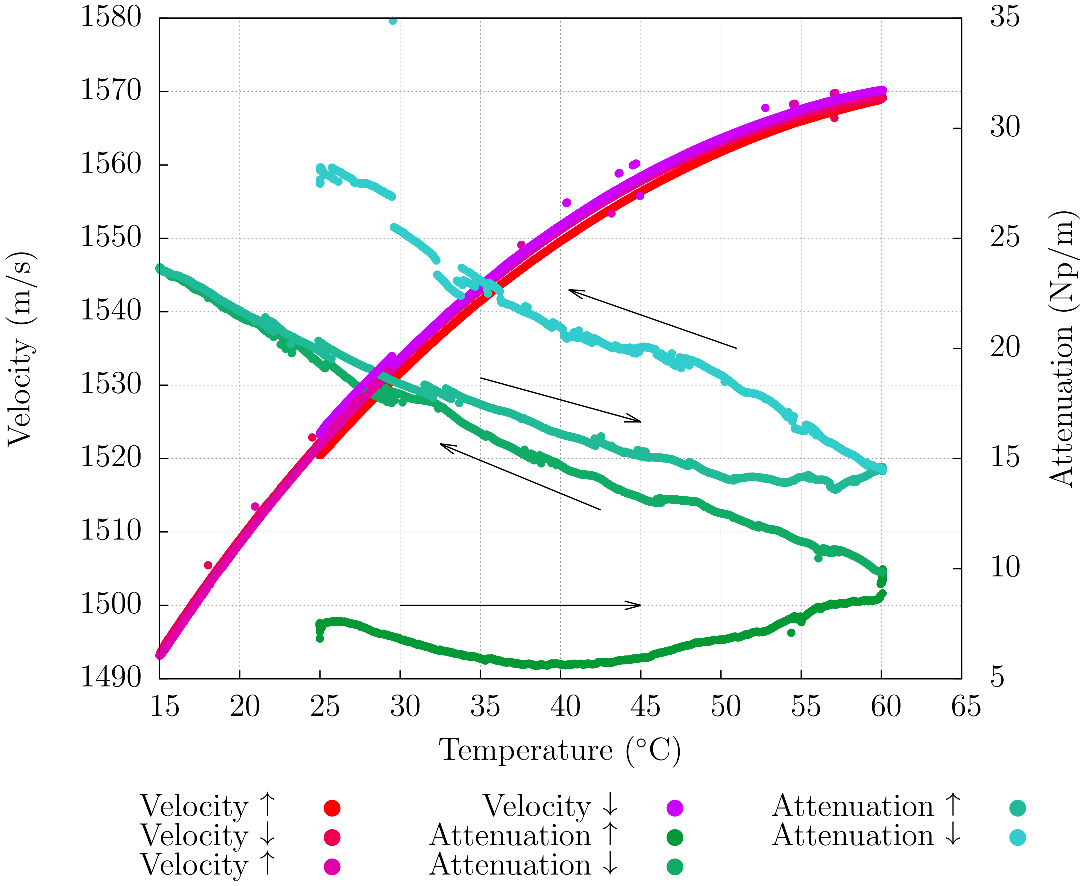

Figure 3.5

8.2% 900nm Polystyrene PEGMA in water ResoScan, at ∼8MHz, of velocity and attenuation compared to change in temperature. The sample was heated and cooled from 25°C → 60°C → 15°C → 60°C → 15°C starting from the red and green points respectively. ↑ *represent the sample heating up and* ↓ *represent the sample cooling down.*

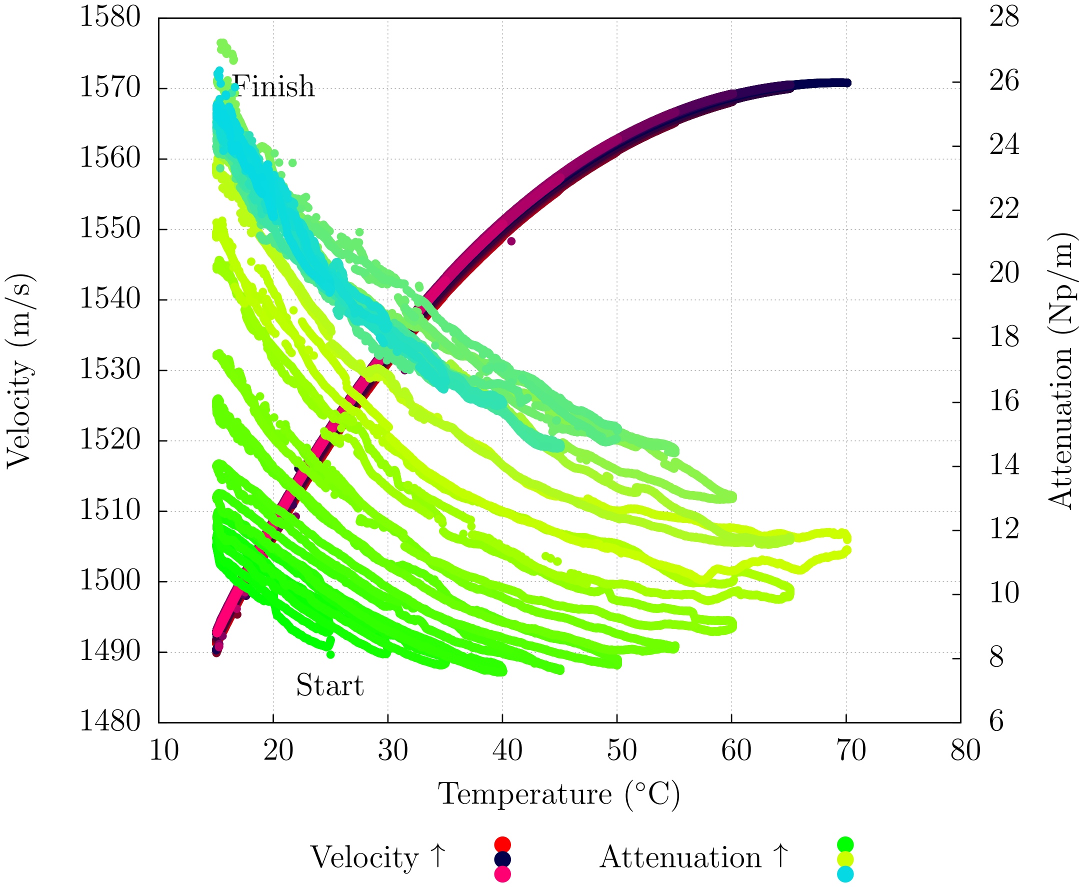

Figure 3.6

8.8% 400nm Polystyrene PEGMA in water ResoScan, at ∼8MHz, of velocity and attenuation compared to change in temperature. The sample was heated and cooled from 15° C to 25° C and cooled back down to 15° C, this process was repeated but the maximum temperature was increased by 5° C each time until 60° C, then down at intervals of 5 ° C until 25° C, starting from the red and green points respectively.

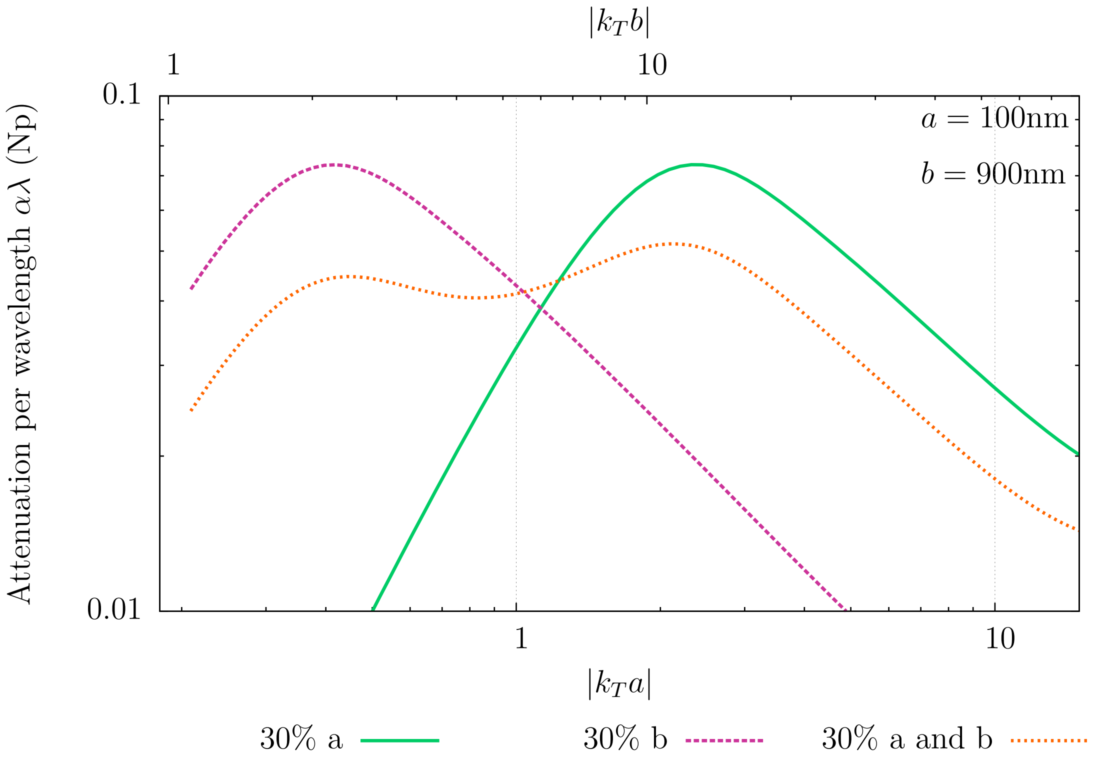

Figure 3.7

Weak thermal scattering predictions of three hexadecane in water emulsions. 1. 30% 100nm, 2. 30% 900nm, 3. 15% 100nm and 15% 900nm, 30% total volume.

ples are destabilised by increasing temperature and that probably an aggregation process is occurring which affects the attenuation more than the velocity.

3.2 Polydisperse

The next set of experiments revolved around mixing two different sized mono-disperse emulsions together. This is to test to see how accurate the theories in chapter 1 are when applied to bi-disperse systems. In each of these experiments the attenuation was calculated by adding together the volume averaged attenuation from the individual attenuation predictions for two mono-disperse emulsions.

First we look at the weak thermal scattering prediction of two mono-disperse

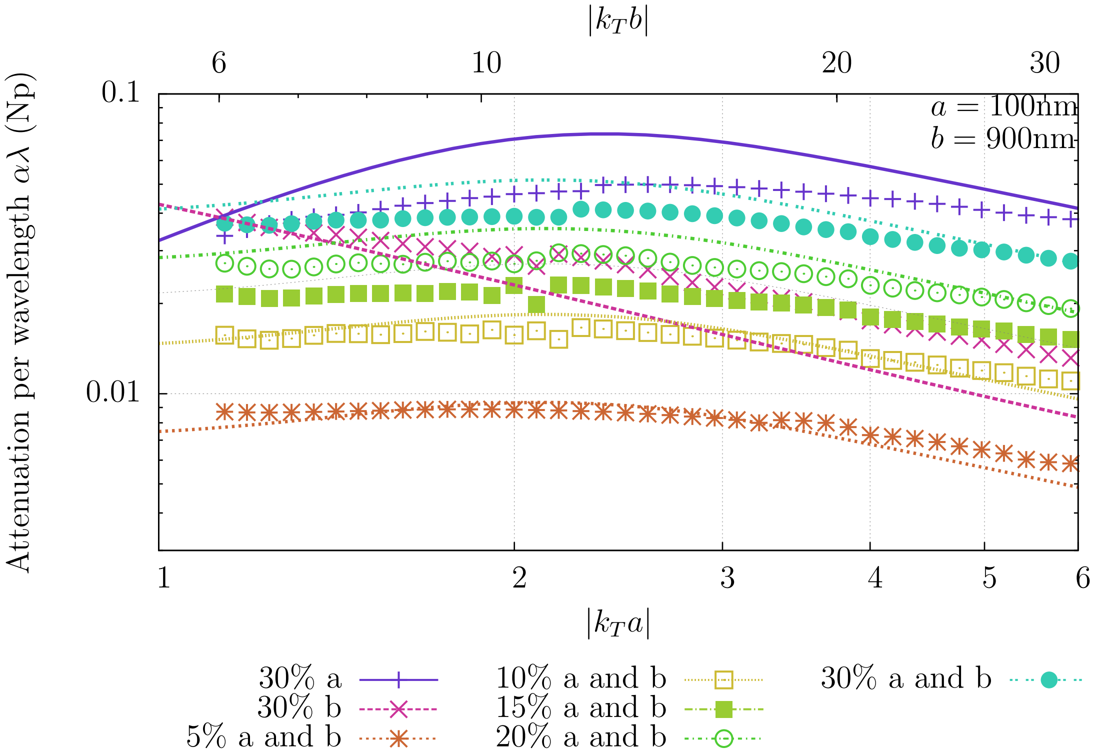

Figure 3.8

Attenuation spectrum of two hexadecane in water emulsions, of size 100nm and 900nm, separately and mixed (shown by points) compared with single weak thermal scattering theory (shown by lines). The mixed samples are mixed 50% v/v each for 100nm and 900nm. The mixed weak thermal scattering solutions were obtained by combining the attenuation from both 100nm and 900nm spectrum.

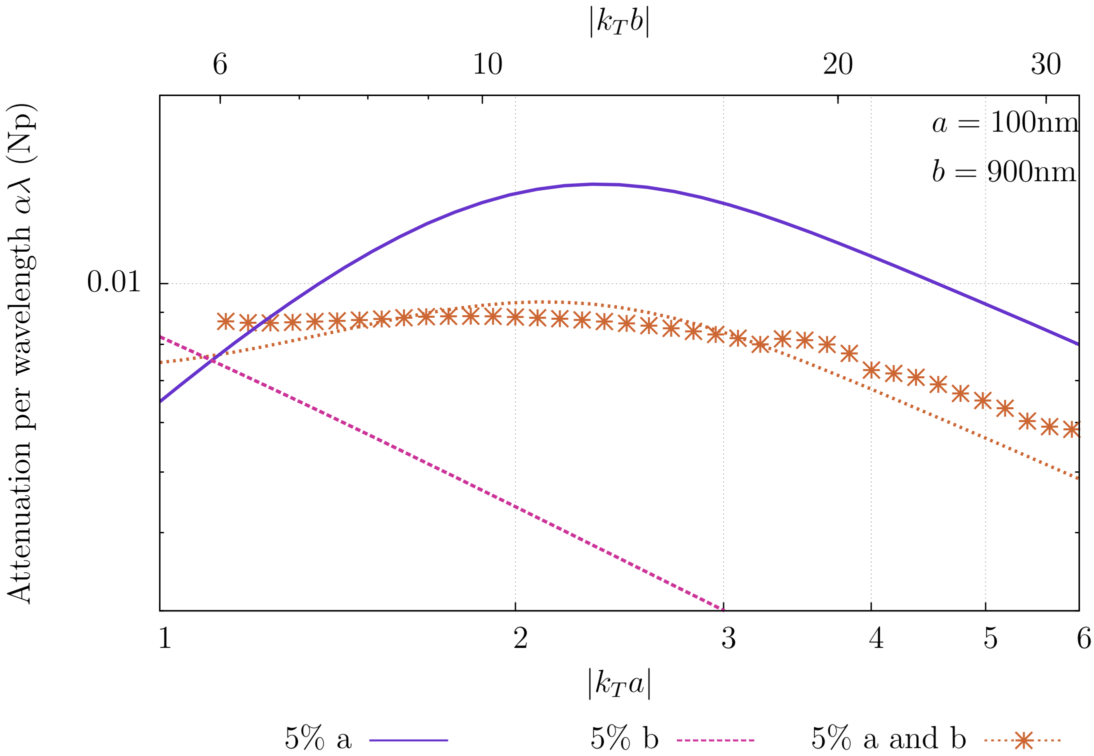

Figure 3.9

A closer look at weak thermal scattering predictions of three hexadecane in water emulsions compared with experimental data for the third data set. 1. 5% 100nm, 2. 5% 900nm, 3. 2.5% 100nm and 2.5% 900nm, 5% total volume.

and the subsequent mixture of these two emulsions behave. See in figure 3.7 how a 30% 100nm and a 30% 900nm weak thermal scattering theories combines. The first experiment considered were two mono-disperse 30% hexadecane-in-water emulsions, one ∼100nm, the other ∼900nm, as seen by the dark blue and the pink points respectively in figure 3.8, which now just considers points over the range of measurements from the instrument. Similar to the results in figure 3.1 we see at 30% the single weak scattering theory prediction (solid lines) over-estimates the prediction of the attenuation. The peak of the curve for the experimental data has also shifted slightly in the positive $|k_T a|$ direction also. For 900nm, we see the we under-estimate the prediction, this may be due to $|k_T b| > 1$ at this point. The subsequent experimental data is for the two samples mixed together, 50% v/v for each of the samples. As the concentration decreases, the experimental data fits the prediction better, although around $|k_T a|$ the experimental data increases in attenuation more than the prediction expects. In figure 3.9, we take a closer look at the 5% sample, and note that we obtain a fairly accurate prediction just using single weak thermal scattering theory.

The next series of experiments involved putting the same samples each into their own cell in the Acoustiscan (see section 2.4.2). These are kept at 25°C and left over time. The cells are measured every seven hours for time of flight and intensity of a pulse. These can be, with calibration, used to calculated the velocity and attenuation of a sample.

The first sample of 30% 900nm hexadecane in water can be seen in figures 3.10–3.13, where the time is represented by the change in colour from blue at the start of the experiment to red at the end of the experiment. It can be seen that the sample has a fairly even velocity across the whole height at around 1442ms^{-1}, as with the attenuation levels at approximately 60 Np/m. However, at the end of the sample we can see that the velocity has spilt into two regions, one which has the velocity of water and one which almost has the velocity of hexadecane. Similarly, the attenuation has spilt into two regions. This suggests the emulsion has separated into two regions, one of water and one of hexadecane. We can interpret the velocity data to a concentration by using the ultrasound

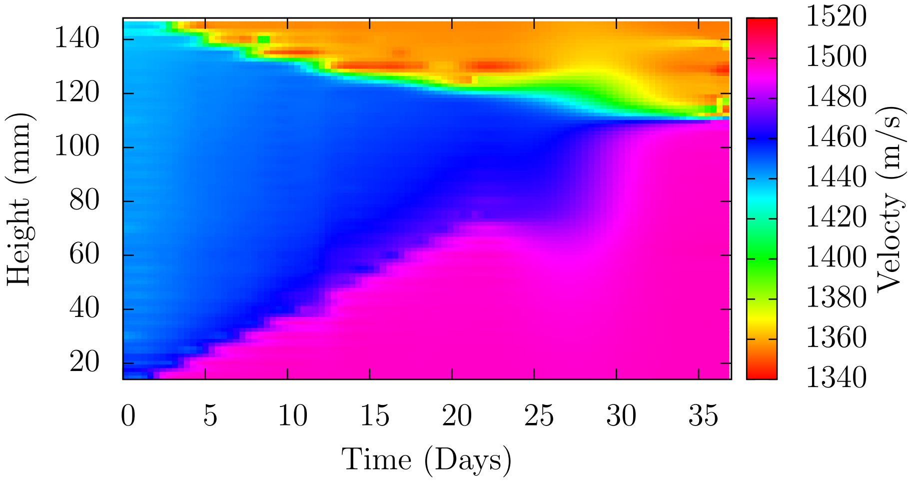

Figure 3.10

Acoustiscan velocity measurement of 30% 900 nm hexadecane in water over 37 days.

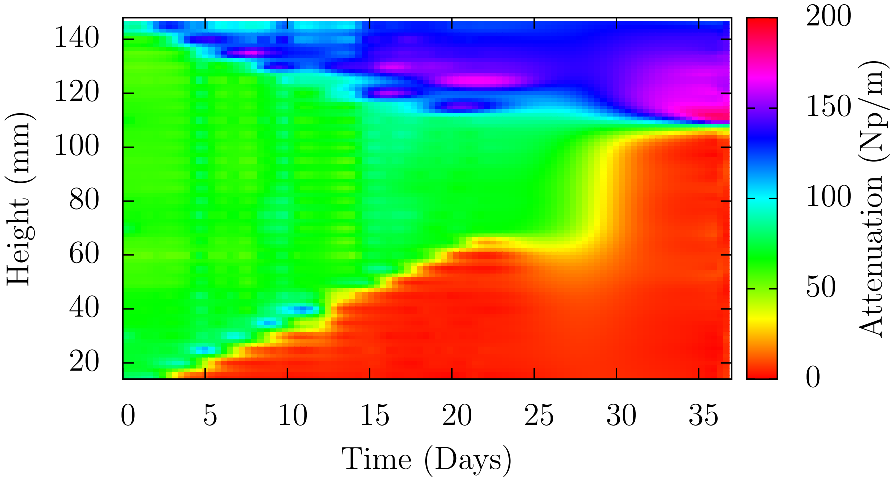

Figure 3.11

Acoustiscan attenuation measurement of 30% 900 nm hexadecane in water over 37 days.

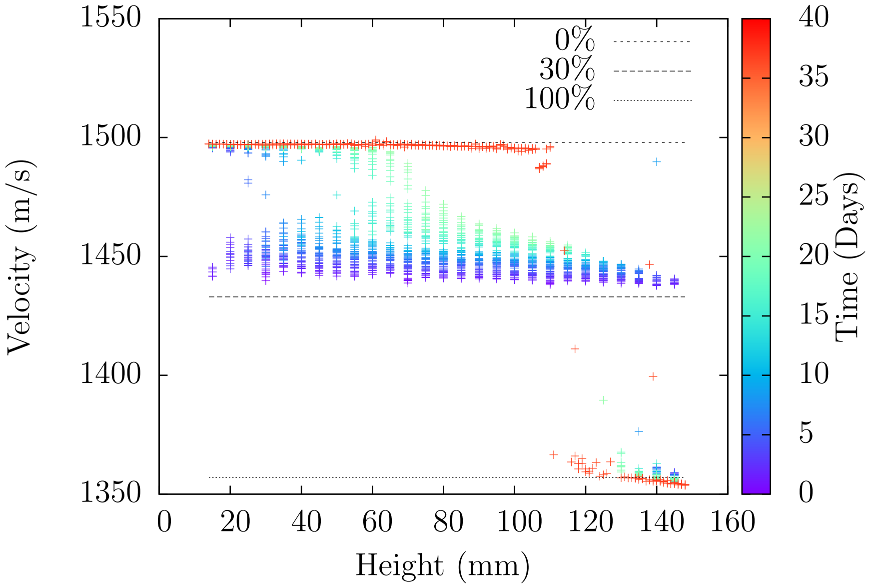

Figure 3.12

Acoustiscan velocity profile measurement of 30% 900 nm hexadecane in water over 37 days, where the dashed lines represent the predicted velocity at 0%, 30% and 100%.

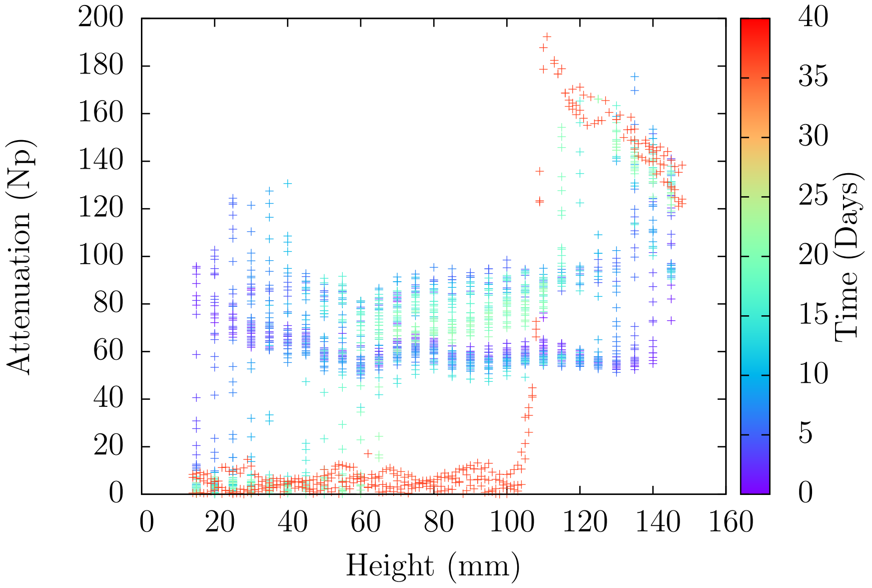

Figure 3.13

Acoustiscan attenuation profile measurement of 30% 900 nm hexadecane in water over 37 days.

normalisation profiling technique described by Pinfield *et al.* [61] as,

$$\phi = \delta\left(\Delta\frac{1}{v_m^2}\right) + \epsilon\left(\Delta\frac{1}{v_m^2}\right)^2, \tag{3.1}$$

where

$$\Delta\frac{1}{v_m^2} = \frac{1}{v_m^2} - \frac{1}{v^2}, \tag{3.2}$$

$$\delta = \frac{\phi_0}{\langle\Delta\frac{1}{v_m^2}\rangle_{h,0}}, \tag{3.3}$$

and

$$\epsilon = \frac{\phi_0}{\langle\left(\Delta\frac{1}{v_m^2}\right)^2\rangle_{h,t}}\left(1 - \frac{\langle\Delta\frac{1}{v_m^2}\rangle_{h,t}}{\langle\Delta\frac{1}{v_m^2}\rangle_{h,0}}\right), \tag{3.4}$$

where ϕ is the concentration, ϕ_0 is the initial concentration, v_m is the measured velocity, v is the continuous phase velocity and $\langle f\rangle_{h,t}$ represents the average of the scalar quantity f over the height of the sample at time t.

The advantage of this technique is that only information about the continuous phase velocity and the initial concentration are required. Also it can be applied regardless of the knowledge of the full scattering parameters, or even if Urick's equation applied. However, this method has some drawbacks, as it neglects the contribution of attenuation relative to the real part of the wave number. Also it assumes that ultrasound velocity is independent of the size of the scattering particle. For poly-disperse emulsions, this can cause departures of the solution from what is actually happening. Further discussion of this restriction can be found in Pinfield *et al.* [62]

Using this technique produces the concentration profile found in figure 3.14. The calculated concentration can then be used with the weak thermal scattering theory to generate predicted attenuation. In figure 3.15 we compared the logarithm of the measured attenuation with that predicted. A perfect prediction would give the results of zero, however we can see that the majority of the values at the start of the experiment are around -1 but as the experiment progresses they move towards zero as the concentration in the lower part of the suspension is decreasing. These calculations are carried out with the remaining samples as

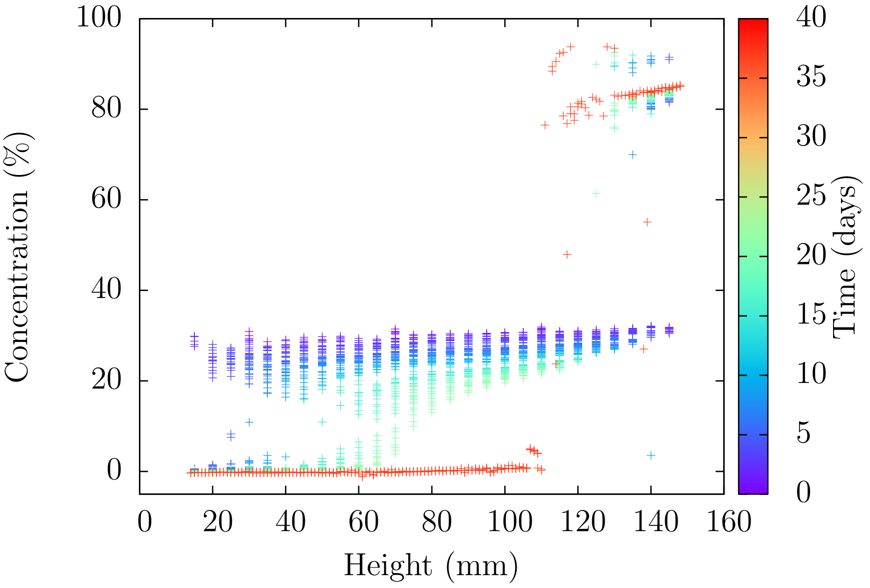

Figure 3.14

Acoustiscan concentration profile measurement of 30% 900 nm hexadecane in water over 37 days.

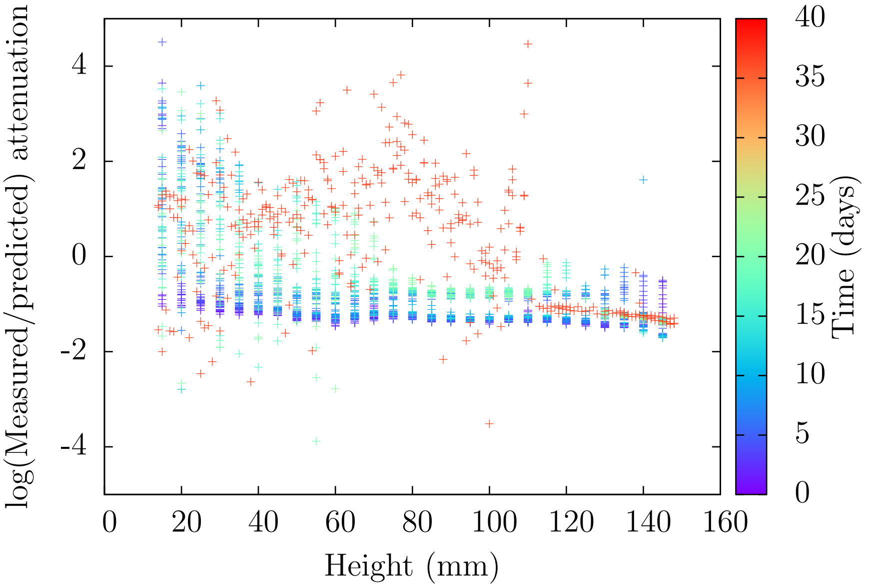

Figure 3.15

Acoustiscan comparison of the weak thermal scattering attenuation prediction and measurement of 30% 900 nm hexadecane in water over 37 days.

seen in the following figures.

In figures 3.16 and 3.17 for 100nm 30% hexadecane in water, we see little change across the whole height of the sample for the attenuation and velocity. However, at the end of the experiment we do see a region of low velocity at the top of the sample and a region of high velocity at the bottom of the sample. Similarly, we see a region of high attenuation at the top of the sample, suggesting that creaming has occurred. In figure 3.18 the concentration profile shows that the concentration does not vary much over time compared with the 30% 900nm sample, however by the end of the experiment we see that there is a slight gradient across the sample. In figure 3.19 we see the logarithm of measured over predicted attenuation is close to zero for most of the points. The prediction being more accurate for the smaller particle radius is consistent with equation (1.149) as the critical volume is less. However, the accuracy here maybe due to over prediction, as weak thermal scattering is not optimal as $|k_T a| \approx 11.3$, which is constant with figure 3.8.

In figures 3.20–3.23 for 15% 900nm and 15% 100nm hexadecane in water, we see similar patterns as previous samples. The concentration profile starts uniformly at 30% and over time decreases near the bottom of the sample, and increases to around 60% at the top. The measured attenuation compared to the predicted attenuation shows that the accuracy of the prediction increases over time in the lower concentration regions as the concentration is decreasing.

In figures 3.24–3.27 for 10% 900nm and 10% 100nm hexadecane in water, we see similar patterns as previous samples. The concentration profile starts uniformly at 20% and over time decreases near the bottom of the sample, and increases to around 60% at the top, similar to the figure 3.26.

In figures 3.28–3.31 for 7.5% 900nm and 7.5% 100nm hexadecane in water, we see similar patterns as previous samples. The concentration profile starts uniformly at 15% and over time decreases near the bottom of the sample, and increases to around 60% at the top, similar to the figure 3.26. The comparison between the predicted data and measured data shows that the accuracy of the prediction increases as the concentration is lower at the end of the experiment.

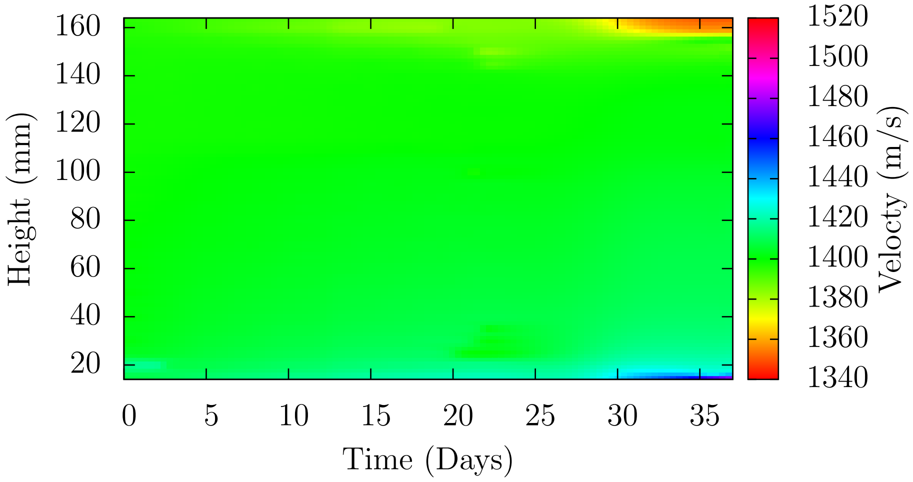

Figure 3.16

Acoustiscan velocity measurement of 30% 100 nm hexadecane in water over 37 days.

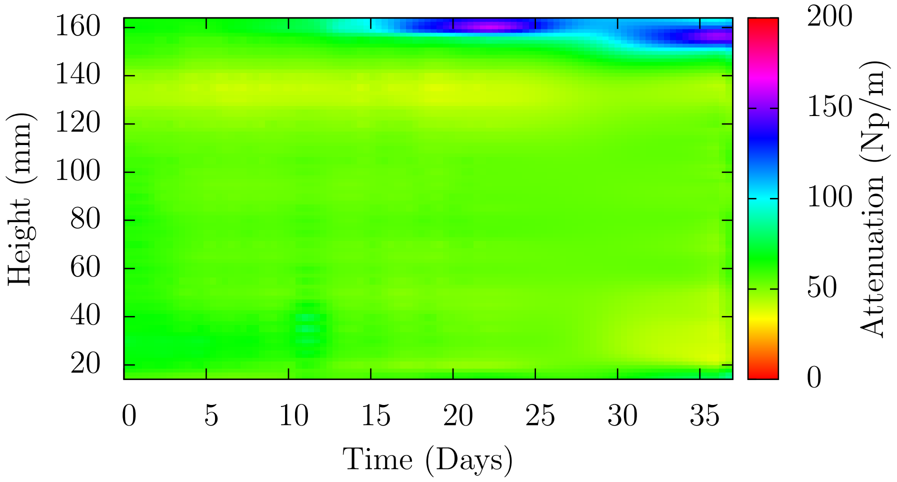

Figure 3.17

Acoustiscan attenuation measurement of 30% 100 nm hexadecane in water over 37 days.

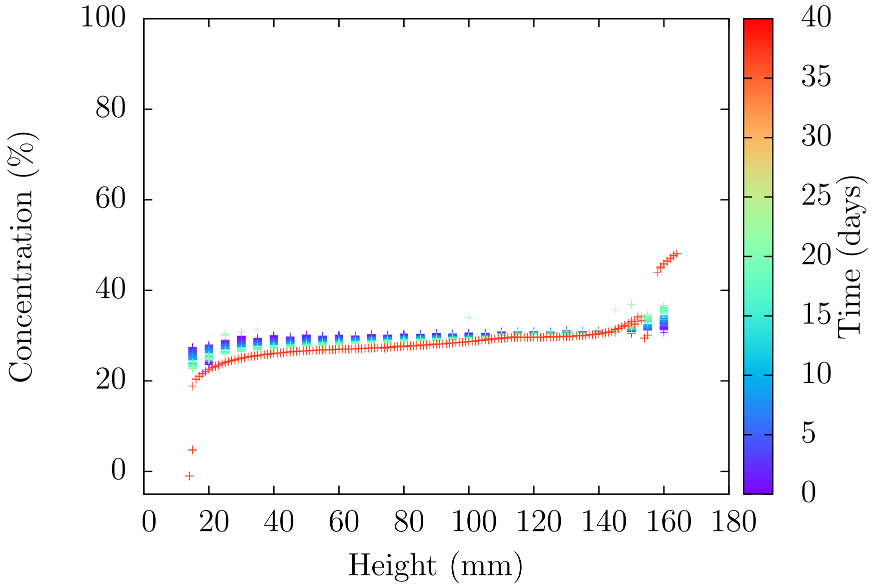

Figure 3.18

Acoustiscan concentration profile measurement of 30% 100 nm hexadecane in water over 37 days.

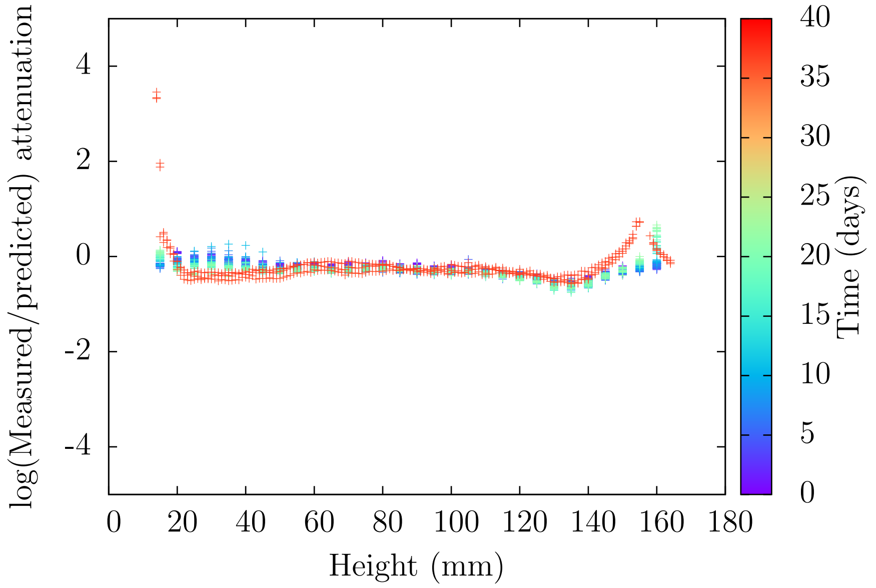

Figure 3.19

Acoustiscan comparison of the weak thermal scattering attenuation prediction and measurement of 30% 100 nm hexadecane in water over 37 days.

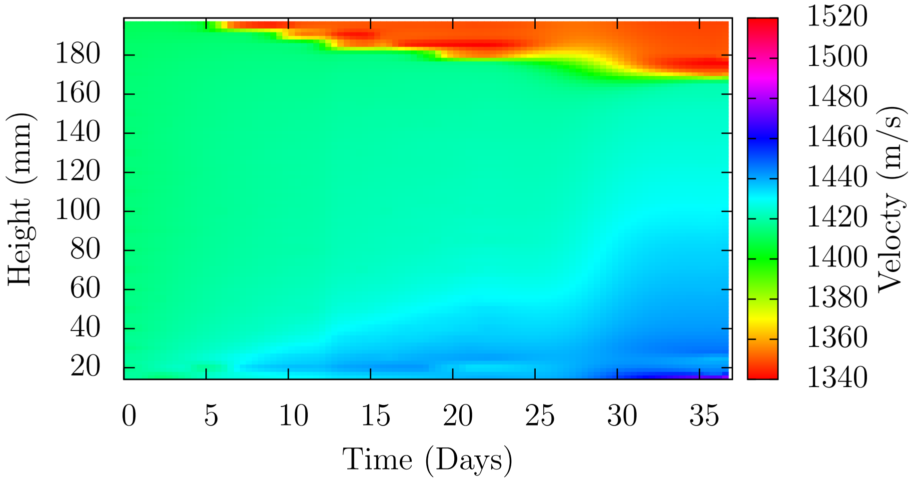

Figure 3.20

Acoustiscan velocity measurement of 15% 900nm and 15% 100nm hexadecane in water over 37 days.

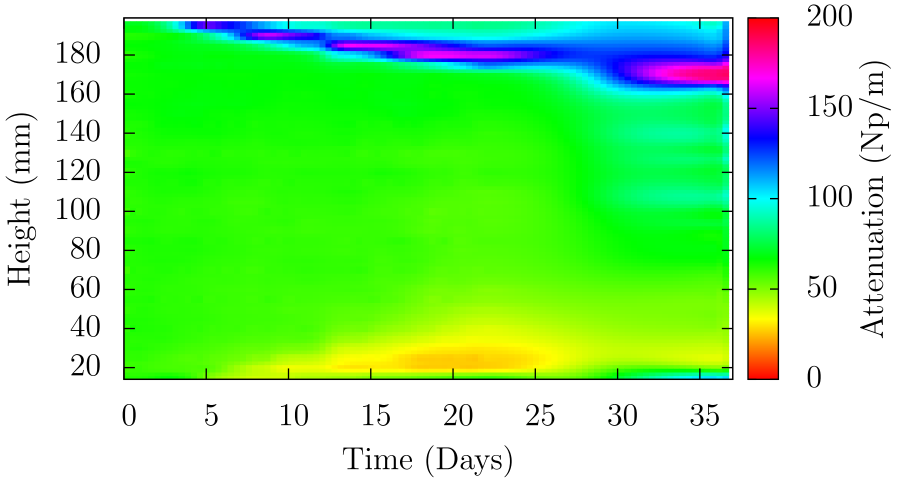

Figure 3.21

Acoustiscan attenuation measurement of 15% 900nm and 15% 100nm hexadecane in water over 37 days.

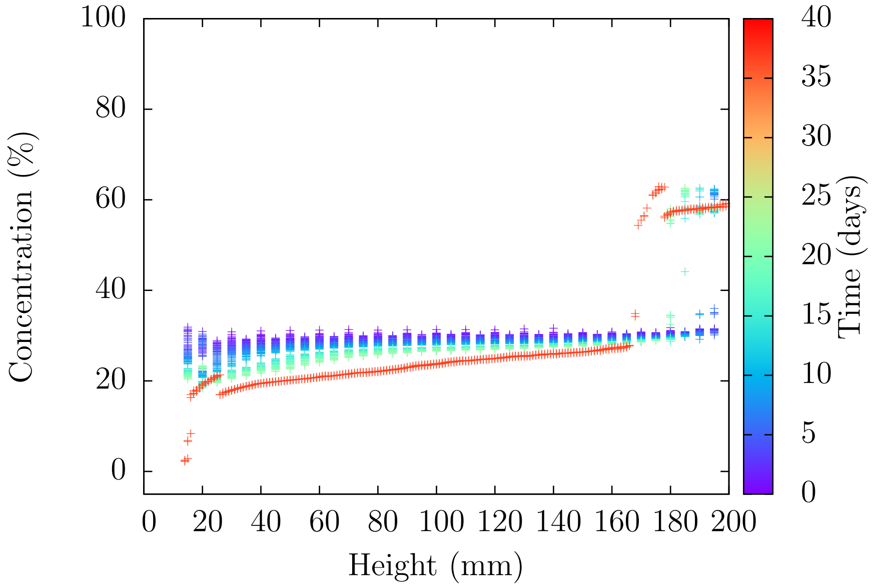

Figure 3.22

Acoustiscan concentration profile measurement of 15% 900nm and 15% 100nm hexadecane in water over 37 days.

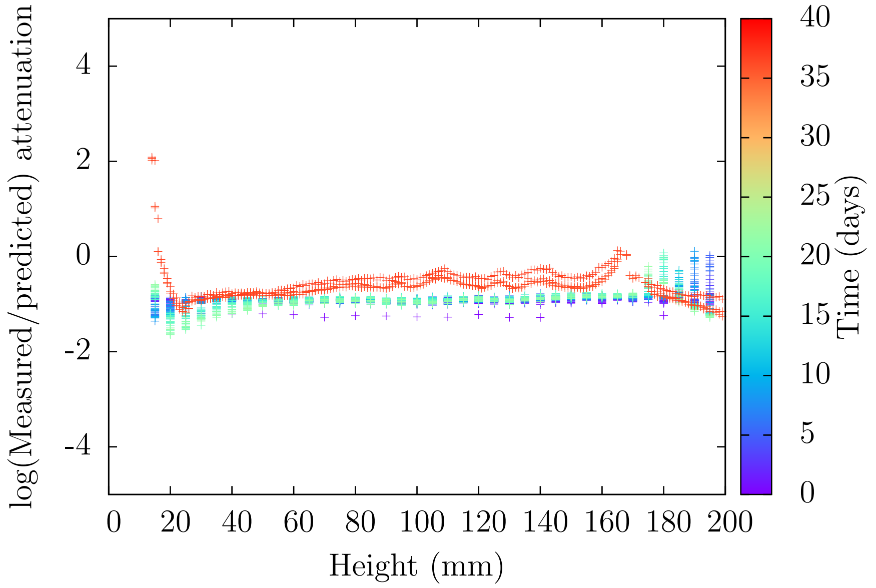

Figure 3.23

Acoustiscan comparison of the weak thermal scattering attenuation prediction and measurement of 15% 900nm and 15% 100nm hexadecane in water over 37 days.

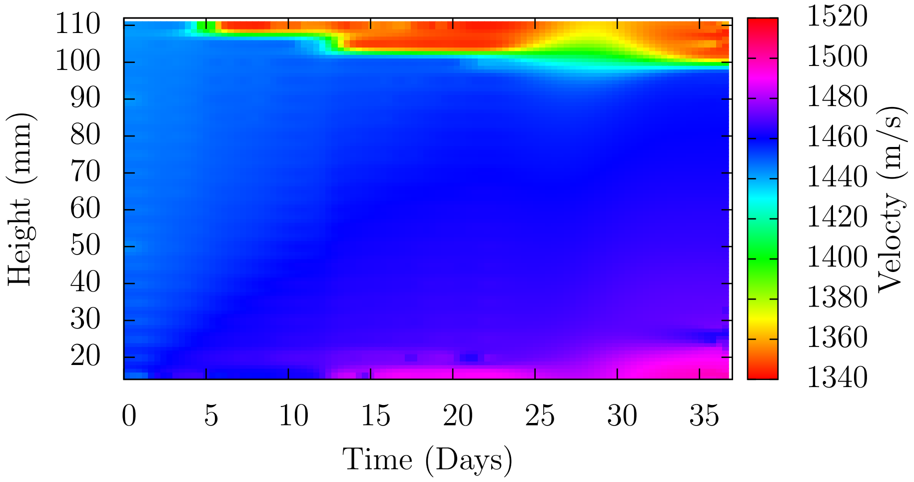

Figure 3.24

Acoustiscan velocity measurement of 10% 900nm and 10% 100nm hexadecane in water over 37 days.

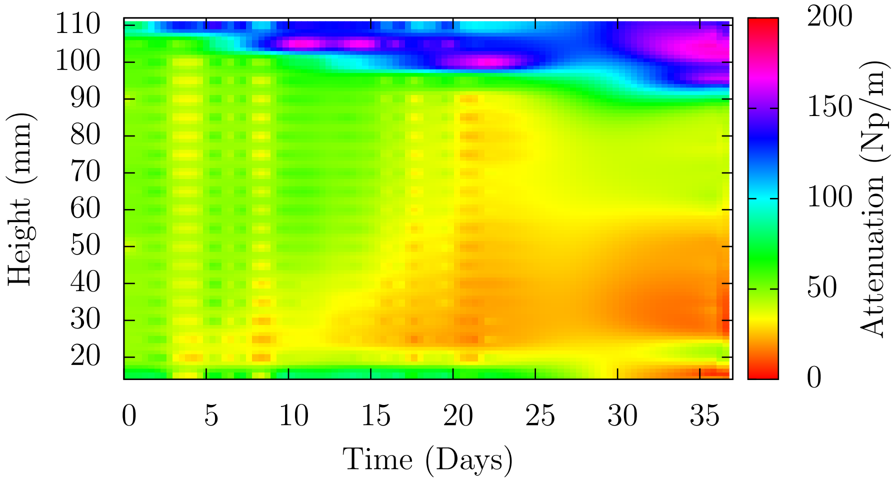

Figure 3.25

Acoustiscan attenuation measurement of 10% 900nm and 10% 100nm hexadecane in water over 37 days.

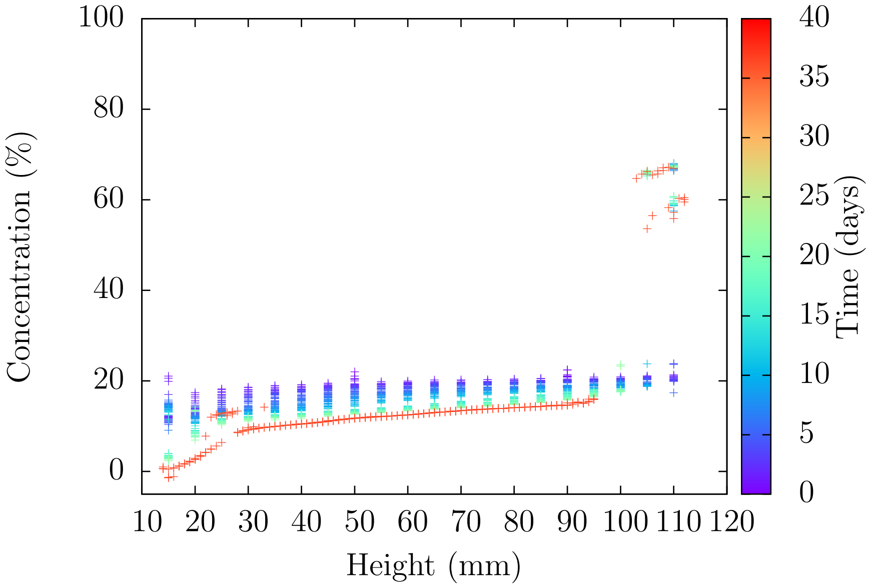

Figure 3.26

Acoustiscan concentration profile measurement of 10% 900nm and 10% 100nm hexadecane in water over 37 days.

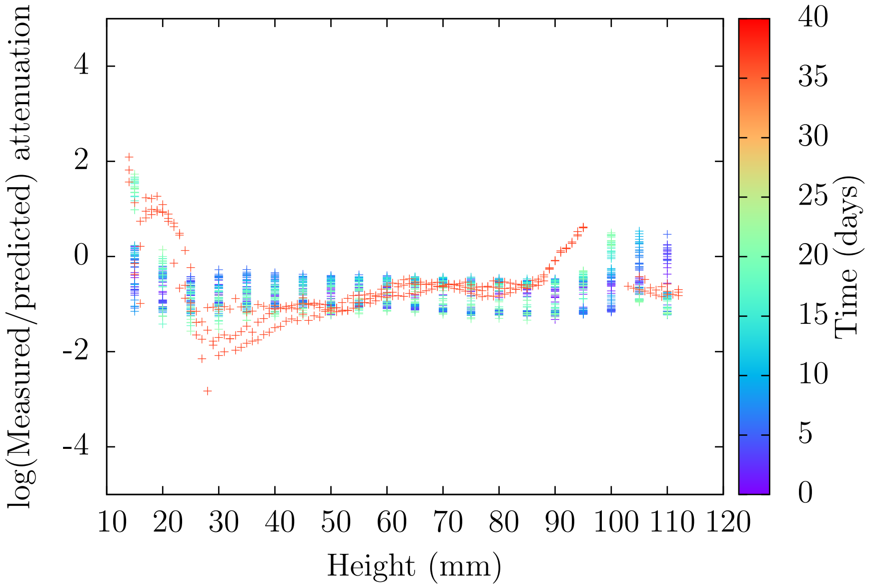

Figure 3.27

Acoustiscan comparison of the weak thermal scattering attenuation prediction and measurement of 10% 900nm and 10% 100nm hexadecane in water over 37 days.

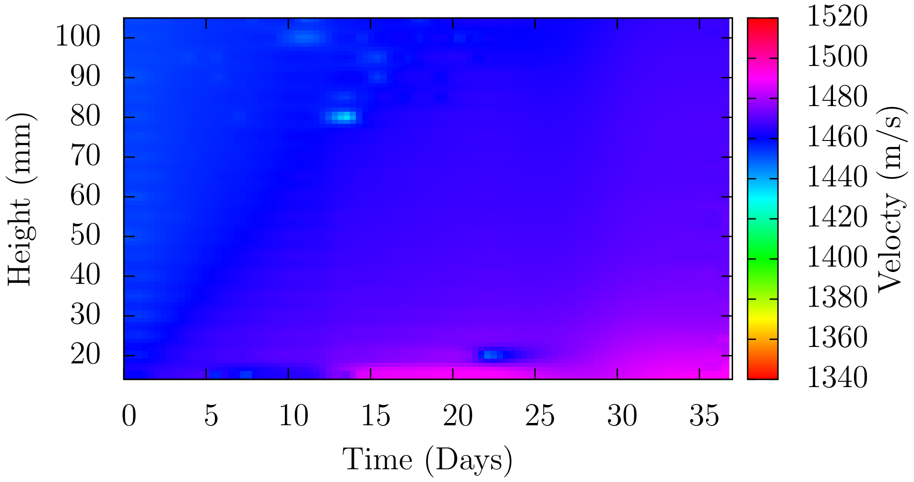

Figure 3.28

Acoustiscan velocity measurement of 7.5% 900nm and 7.5% 100nm hexadecane in water over 37 days.

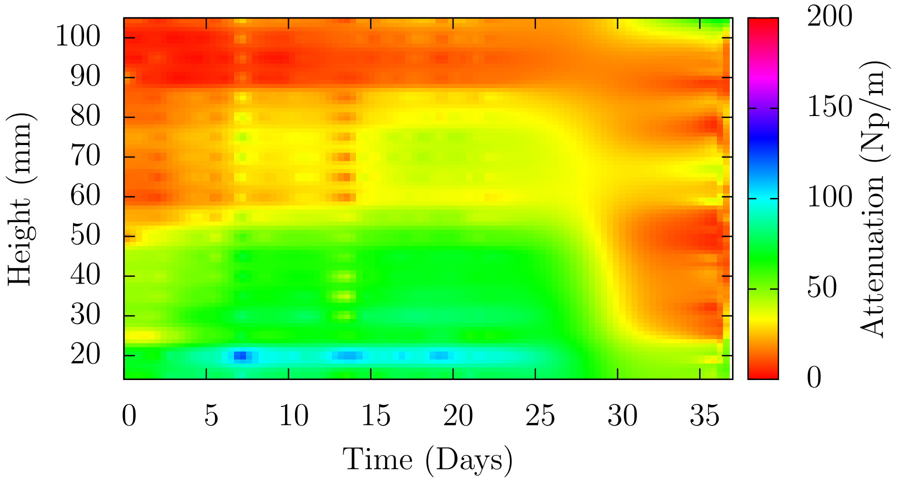

Figure 3.29

Acoustiscan attenuation measurement of 7.5% 900nm and 7.5% 100nm hexadecane in water over 37 days.

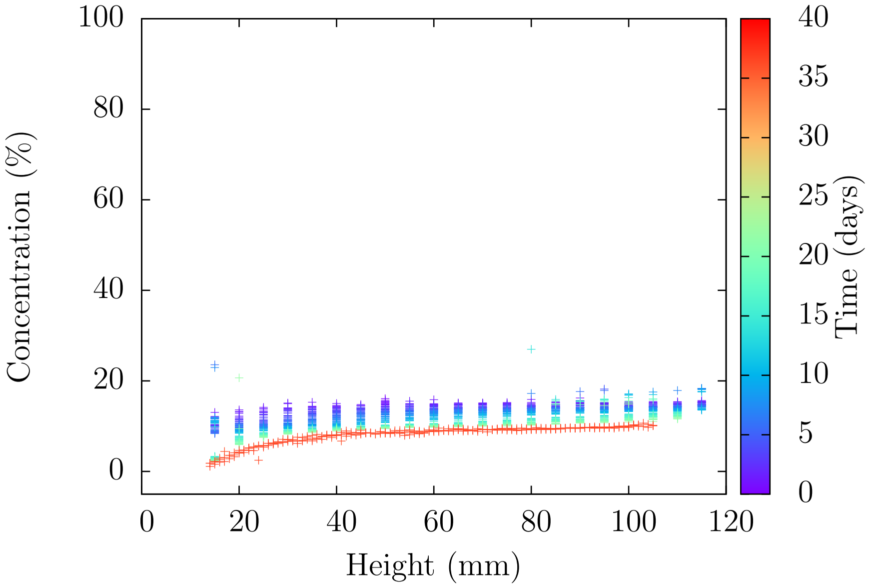

Figure 3.30

Acoustiscan concentration profile measurement of 7.5% 900nm and 7.5% 100nm hexadecane in water over 37 days.

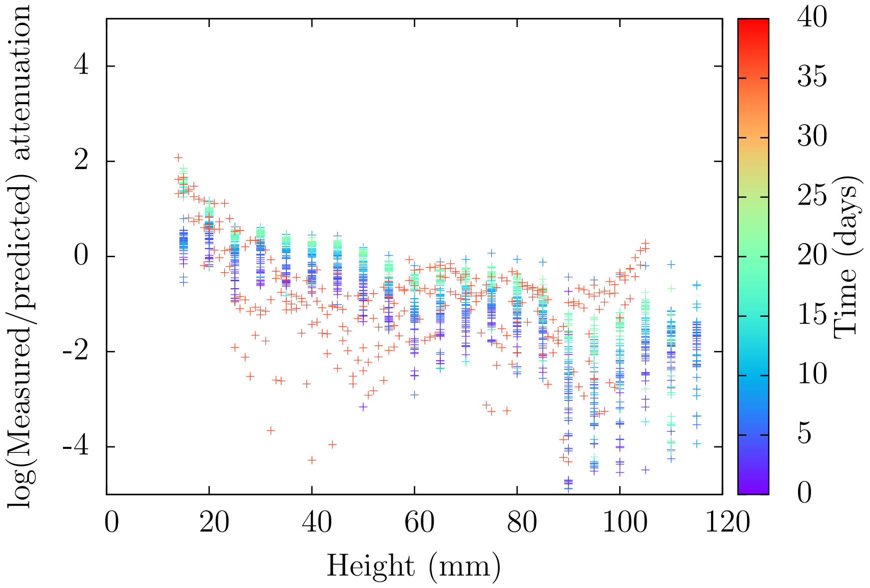

Figure 3.31

Acoustiscan comparison of the weak thermal scattering attenuation prediction and measurement of 7.5% 900nm and 7.5% 100nm hexadecane in water over 37 days.

3.2.1 Discussion

Throughout these experiments, we find that that there is a theme of higher concentrations of emulsions having their attenuation being over predicted. In figure 3.8, we see that that the higher concentration samples follow this trend. We also see variation from the predicted attenuation due to the mixing of two different particles sizes, which is more predominant at lower frequencies. This suggests that thermo-acoustic effects are stronger at lower frequencies, which is consistent with current theory (equation (1.147)).

From the experimental data for 30% 900nm hexadecane in water and 30% 100nm hexadecane, we have shown that the 100nm emulsion remain fairly stable over the course of the experiment, as seen in figure 3.18. The 900nm emulsion, on the other hand, has some drastic creaming occurring, however it can be seen for at least the first five days that the sample was stable. However, it is worth noting while the emulsion is in its creaming state that the ultrasonic measurement is likely to have some inaccuracies as it is difficult to say how exactly the emulsion is creaming, which scattering theory does not account for.

For the data for the 100nm and 900nm samples mixed together, we find similar behaviour as with the samples separated. However, now we find that the finer emulsion is no longer stable as it is being destabilised by the larger particles. This can be seen in each of the experiments. While the predicted concentration for the samples seems to agree with the idea that larger particles are destabilising more rapidly, we see that the whole sample is destabilised soon after the initial destabilisation, leaving the sample segregated between two regions of hexadecane and water. The comparison between the attenuation predicted from the calculated concentration and the experimental data, however, does not provide as accurate of a comparison. We find that at the start of each sample the measured attenuation is lower than the predicted attenuation, which is consistent with the other experiments carried out in this chapter. However, the mixtures do not always get more accurate as the concentration is lowered. This could be due to the scattering of different size particles interacting which has not been accounted for with current scattering theories.

Chapter 4

Two particle perturbation solution (in-line)

4.1 Introduction

In chapter 1, I discussed that current models for predicting ultrasonic scattering fail to be accurate at higher concentrations compared to experimental data, such as that presented in chapter 3. This is because these models do not fully account for the effects of multiple scattering, in particular the overlap of the thermal and visco-inertial boundary layers surrounding each particle. It was also shown in chapter 1, that taking asymptotic solutions for $k_c a \ll 1$ the original ECAH single particle solution can be accurately approximated and the numerical solutions are no longer ill-conditioned. In this chapter we explore thermoacoustic scattering by a pair of spheres to study how the overlap of the fields affects ultrasound scattering.

In this chapter, we expand the method of treating $|k_c a| \ll 1$, in particular the weak thermal scattering method (see section 1.3.7.3,) from Harlen *et al.* [27], where $|k_T a| \sim 1$. This method is combined with the method from Gaunaurd *et al.* [46], who describe a translation addition theorem for solutions to Helmholtz equations, and Greengard and Roklin [47], who descibe a translation addition theorem for solutions to Laplace's equation. While this method is briefly described in the paper by Hazlehurst *et al.* [63], here we will go into more detail.

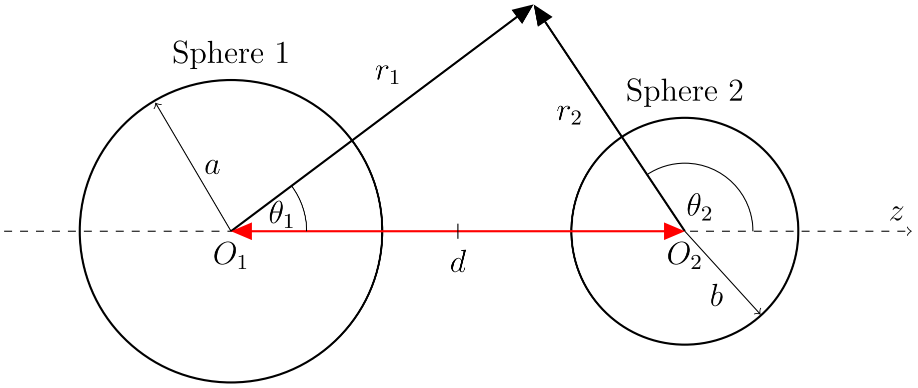

Figure 4.1

Figure of two sphere problem.

Let us consider two particles, 1 and 2, with radii of a and b respectively, where a and b are of the same order. These two particles are placed at a distance d between their centres, on an axis, z, say, such that $d > a + b$. A plane wave traverses parallel to the direction of the z axis. We define an origin at the centre of each particle, O_1 and O_2, say. From each origin there is a set of spherical polar coordinates, which due to the axisymmetry of this geometry can be reduced to just (r_1, θ_1) and (r_2, θ_2). This coordinate system is illustrated in figure 4.1.

The surfaces of the spheres are defined by

$$r_1 = a = \sqrt{x^2 + y^2 + \left(z + \frac{d}{2}\right)^2} \tag{4.1}$$

and

$$r_2 = b = \sqrt{x^2 + y^2 + \left(z - \frac{d}{2}\right)^2}. \tag{4.2}$$

As in the case of the single particle the acoustic and thermal waves must satisfy Helmholtz equations, in the continuous and discrete phases, so that

$$(\nabla^2 + k_c^2)\varphi = 0, \quad (\nabla^2 + k_T^2)\psi = 0, \quad \text{in the continuous phase} \tag{4.3}$$

and

$$(\nabla^2 + k_c'^2)\varphi' = 0, \quad (\nabla^2 + k_T'^2)\psi' = 0, \quad \text{in the discrete phase.} \tag{4.4}$$

The incident acoustic wave is a plane wave travelling in the positive z direction

$$\varphi_{\text{inc}} = e^{ik_c z} = e^{ik_c r \cos\theta}. \tag{4.5}$$

where r is the distance from the midpoint between the sphere centres. However, in order to apply the boundary conditions at each particle surface we shall instead write this field in terms of the local coordinates centred on O_1 and O_2 as

$$\varphi_{\text{inc}}^{(1)} = e^{ik_c z} = e^{ik_c(r_1 \cos\theta_1)} e^{-k_c \frac{d}{2}}, \tag{4.6}$$

$$\varphi_{\text{inc}}^{(2)} = e^{ik_c z} = e^{ik_c(r_2 \cos\theta_2)} e^{ik_c \frac{d}{2}}, \tag{4.7}$$

for particle 1 and 2, respectively.

4.1.1 Boundary conditions

For the two particle system, the same boundary conditions from the single particle case are used (equation (1.64)), however, now they have to be applied on both particles. On each particle boundary, $r_1 = a$ and $r_2 = b$, there are pressure, normal velocity, temperature and heat flux conditions:

$$\varphi_{\text{inc}} + \varphi + \psi = \hat{\rho}\left(\varphi' + \psi'\right), \tag{4.8}$$

$$\frac{\partial}{\partial n}\left(\varphi_{\text{inc}} + \varphi + \psi\right) = \frac{\partial}{\partial n}\left(\varphi' + \psi'\right), \tag{4.9}$$

$$\Gamma_c\left(\varphi_{\text{inc}} + \varphi\right) + \Gamma_T \psi = \Gamma'_c \varphi' + \Gamma'_T \psi', \tag{4.10}$$

$$\Gamma_c \frac{\partial}{\partial n}\left(\varphi_{\text{inc}} + \varphi\right) + \Gamma_T \frac{\partial}{\partial n}\psi = \hat{\tau}\left(\Gamma'_c \frac{\partial}{\partial n}\varphi' + \Gamma'_T \frac{\partial}{\partial n}\psi'\right), \tag{4.11}$$

where $\hat{\rho} = \frac{\rho'}{\rho}$ and $\hat{\tau} = \frac{\tau'}{\tau}$.

4.2 Weak thermal scattering approximation

We now use the method of Harlen *et al.* [27] to find an approximate solution that is valid in the limit $|k_c a| \ll 1$ and $|k_c b| \ll 1$, when $|k_T a| \sim 1$ and $|k_T b| \sim 1$. Using the small acoustic wave number limit, the problem is transformed to a regular problem by introducing

$$\tilde{\varphi}^{(1)} = e^{-ik_c(r_1-a)}\varphi^{(1)}, \tag{4.12}$$

for solutions around sphere 1, and

$$\tilde{\varphi}^{(2)} = e^{-ik_c(r_2-b)}\varphi^{(2)}, \tag{4.13}$$

for solutions around sphere 2 from equation (1.87). Since $|r_2 - r_1| < d$ the radiation boundary condition

$$\lim_{r_1\to\infty} r_1 \left(\frac{\partial \varphi^{(1)}}{\partial r_1} - ik_c \varphi^{(1)} \right) = 0 \tag{4.14}$$

still holds provided that $\tilde{\varphi}^{(1)}$ is regular at infinity.

Following the approach of Harlen *et al.* [27] we seek an asymptotic solution by expanding the potentials as Poincaré series. For ease of notation it is convenient to choose k_c as the small parameter where we understand this to be in units based on the average particle size $\frac{a+b}{2}$. The appropriate scaling of the thermal terms is given by defining

$$\frac{\Gamma_c}{\Gamma_T} = -(k_c)^2 G_c, \tag{4.15}$$

and

$$\frac{\Gamma_c'}{\Gamma_T'} = -(k_c)^2 G_c', \tag{4.16}$$

from which the boundary conditions for sphere 1 can now be written as,

$$\varphi_{\text{inc}}^{(1)} + \tilde{\varphi}^{(1)} + \psi^{(1)} = \hat{\rho}\left(\varphi'^{(1)} + \psi'^{(1)}\right), \tag{4.17}$$

$$\frac{\partial \varphi_{\text{inc}}^{(1)}}{\partial r_1} + \left(ik_c \tilde{\varphi}^{(1)} + \frac{\partial \tilde{\varphi}^{(1)}}{\partial r_1} \right) + \frac{\partial \psi^{(1)}}{\partial r_1} = \frac{\partial}{\partial r_1}\left(\varphi'^{(1)} + \psi'^{(1)}\right), \tag{4.18}$$

$$-(k_c)^2 G_c \left(\varphi_{\text{inc}}^{(1)} + \tilde{\varphi}^{(1)} \right) + \psi^{(1)} = \hat{\Gamma}\left(-(k_c)^2 G_c' \varphi'^{(1)} + \psi'^{(1)} \right), \tag{4.19}$$

$$-(k_c)^2 G_c \left(\frac{\partial \varphi_{\text{inc}}^{(1)}}{\partial r_1} + ik\tilde{\varphi}^{(1)} + \frac{\partial \tilde{\varphi}^{(1)}}{\partial r_1} \right) + \frac{\partial \psi^{(1)}}{\partial r_1} = \hat{\Gamma}\hat{\tau}\left(-(k_c)^2 G_c' \frac{\partial \varphi'^{(1)}}{\partial r_1} + \frac{\partial \psi'^{(1)}}{\partial r_1} \right), \tag{4.20}$$

where $\hat{\Gamma} = \frac{\Gamma_T'}{\Gamma_T}$. Similar boundary conditions for sphere 2 can be obtained in the same manner. The transformations in equation (4.12) allow for a regular perturbation expansions in (ik_c),

$$(\varphi_{\text{inc}}^{(1)}, \tilde{\varphi}^{(1)}, \varphi'^{(1)}, \psi^{(1)}, \psi'^{(1)}) = \sum_{n=0}^{\infty} (ik_c)^n (\varphi_{\text{inc}n}^{(1)}, \tilde{\varphi}_n^{(1)}, \varphi_n'^{(1)}, \psi_n^{(1)}, \psi_n'^{(1)}), \tag{4.21}$$

where the superscript (1) represents solutions in the frame of the first sphere in the frame (r_1, θ_1). Similarly, the transformation in equation (4.13) allow perturbation expansions around (ik_c) for solutions in the frame (r_2, θ_2),

$$(\varphi_{\text{inc}}^{(2)}, \tilde{\varphi}^{(2)}, \varphi'^{(2)}, \psi^{(2)}, \psi'^{(2)}) = \sum_{n=0}^{\infty} (ik_c)^n (\varphi_{\text{inc}n}^{(2)}, \tilde{\varphi}_n^{(2)}, \varphi_n'^{(2)}, \psi_n^{(2)}, \psi_n'^{(2)}). \tag{4.22}$$

These two expansions can be used to transform our acoustic Helmholtz equations (4.3) and (4.4) into the following inhomogeneous equations,

$$\nabla^2 \tilde{\varphi}_n^{(1)} = -\frac{2}{r_1} \frac{\partial}{\partial r_1} \left(r_1 \tilde{\varphi}_{n-1}^{(1)} \right) \quad \text{for } r_1 > a, r_2 > b, \tag{4.23}$$

$$\nabla^2 \varphi_n'^{(1)} = -\frac{k_c'^2}{k_c^2} \frac{1}{a^2} \varphi_{n-2}' \quad \text{for } r_1 < a, \tag{4.24}$$

and,

$$\nabla^2 \varphi_n'^{(2)} = -\frac{k_c'^2}{k_c^2} \frac{1}{b^2} \varphi_{n-2}' \quad \text{for } r_2 < b. \tag{4.25}$$

Note that equation (4.23) can also be expressed as

$$\nabla^2 \tilde{\varphi}_n^{(2)} = -\frac{2}{r_2} \frac{\partial}{\partial r_2} \left(r_2 \tilde{\varphi}_{n-1}^{(2)} \right) \quad \text{for } r_2 > b, r_1 > a, \tag{4.26}$$

where $\tilde{\varphi}_n = \varphi_n' = 0$ for $n < 0$. The thermal Helmholtz equations (4.3) and (4.4) are transformed simply as

$$\left(\nabla^2 + k_T^2 \right) \psi_n = 0 \quad \text{for } r_1 > a, r_2 > b, \tag{4.27}$$

and

$$\left(\nabla^2 + k_T'^2\right)\psi_n' = 0 \quad \text{for } r_1 < a \text{ or } r_2 < b. \tag{4.28}$$

Using these perturbations, the boundary conditions from equations (4.17)–(4.20) can again now be rewritten at order $(ik_c)^n$ as,

$$\varphi^{(1)}_{\text{inc}_n} + \tilde{\varphi}^{(1)}_n + \psi^{(1)}_n = \hat{\rho}\left(\varphi'^{(1)}_n + \psi'^{(1)}_n\right), \tag{4.29}$$

$$\frac{\partial \varphi^{(1)}_{\text{inc}_n}}{\partial r_1} + \left(\frac{1}{a}\tilde{\varphi}^{(1)}_{n-1} + \frac{\partial \tilde{\varphi}^{(1)}_n}{\partial r_1}\right) + \frac{\partial \psi^{(1)}_n}{\partial r_1} = \frac{\partial}{\partial r_1}\left(\varphi'^{(1)}_n + \psi'^{(1)_n}\right), \tag{4.30}$$

$$G_c\left(\varphi^{(1)}_{\text{inc}_{n-2}} + \tilde{\varphi}^{(1)}_{n-2}\right) + \psi^{(1)}_n = \hat{\Gamma}\left(G_c'\varphi'^{(1)}_{n-2} + \psi'^{(1)}_n\right), \tag{4.31}$$

$$G_c\left(\frac{\partial \varphi^{(1)}_{\text{inc}_{n-2}}}{\partial r_1} + \frac{1}{a}\tilde{\varphi}^{(1)}_{n-3} + \frac{\partial \tilde{\varphi}^{(1)}_{n-2}}{\partial r_1}\right) + \frac{\partial \psi^{(1)}_n}{\partial r_1} = \hat{\Gamma}\hat{\tau}\left(G_c'\frac{\partial \varphi'^{(1)}_{n-2}}{\partial r_1} + \frac{\partial \psi'^{(1)}_n}{\partial r_1}\right), \tag{4.32}$$

and similarly for sphere 2 at order $(ik_c)^n$,

$$\varphi^{(2)}_{\text{inc}_n} + \tilde{\varphi}^{(2)}_n + \psi^{(2)}_n = \hat{\rho}\left(\varphi'^{(2)}_n + \psi'^{(2)_n}\right), \tag{4.33}$$

$$\frac{\partial \varphi^{(2)}_{\text{inc}_n}}{\partial r_2} + \left(\frac{1}{b}\tilde{\varphi}^{(2)}_{n-1} + \frac{\partial \tilde{\varphi}^{(2)}}{\partial r_2}\right) + \frac{\partial \psi^{(2)}_n}{\partial r_2} = \frac{\partial}{\partial r_2}\left(\varphi'^{(2)}_n + \psi'^{(2)}_n\right), \tag{4.34}$$

$$G_c\left(\varphi^{(2)}_{\text{inc}_{n-2}} + \tilde{\varphi}^{(2)}_{n-2}\right) + \psi^{(2)}_n = \hat{\Gamma}\left(G_c'\varphi'^{(2)}_{n-2} + \psi'^{(2)}_n\right), \tag{4.35}$$

$$G_c\left(\frac{\partial \varphi^{(2)}_{\text{inc}_{n-2}}}{\partial r_2} + \frac{1}{b}\tilde{\varphi}^{(2)}_{n-3} + \frac{\partial \tilde{\varphi}^{(2)}_{n-2}}{\partial r_2}\right) + \frac{\partial \psi^{(2)}_n}{\partial r_2} = \hat{\Gamma}\hat{\tau}\left(G_c'\frac{\partial \varphi'^{(2)}_{n-2}}{\partial r_2} + \frac{\partial \psi'^{(2)}_n}{\partial r_2}\right). \tag{4.36}$$

These eight boundary conditions can be split up into four pairs. Equations (4.31) and (4.32) provide the solutions to the thermal field for $n \geq 2$ at $r_1 = a$. Similarly, equations (4.35) and (4.36) provide the solutions for the thermal field for $n \geq 2$ at $r_2 = b$. The other two pairs provide a solution to the acoustic field at order n. The two pairs of boundary conditions for each sphere decouple at each order allowing the calculations of the acoustic and thermal waves to be done sequentially in the order $\tilde{\varphi}^{(1)}_0, \tilde{\varphi}^{(2)}_0, \tilde{\varphi}^{(1)}_1, \tilde{\varphi}^{(2)}_1, \psi^{(1)}_2, \psi^{(2)}_2, \tilde{\varphi}^{(1)}_2, \tilde{\varphi}^{(2)}_2, \psi^{(1)}_3, \ldots$.

Now the outgoing waves can be decomposed into spherical harmonics [64],

$$\tilde{\varphi}_n^{(1)} = \sum_{m=0}^{\infty} \left[A_{nm} \frac{a^{m+1}}{r_1^{m+1}} P_m(\cos\theta_1) + B_{nm} \frac{b^{m+1}}{r_2^{m+1}} P_m(\cos\theta_2) \right] + I_n^{(1)}(r_1, \theta_1), \quad (4.37)$$

$$\varphi_n'^{(1)} = \sum_{m=0}^{\infty} a_{nm} \frac{r_1^m}{a^m} P_m(\cos\theta) + I_n'^{(1)}(r_1, \theta_1), \quad (4.38)$$

$$\psi_n^{(1)} = \sum_{m=0}^{\infty} C_{nm} h_m(k_T r_1) P_m(\cos\theta_1) + D_{nm} h_m(k_T r_2) P_m(\cos\theta_2), \quad (4.39)$$

$$\psi_n'^{(1)} = \sum_{m=0}^{\infty} c_{nm} j_m(k_T' r_1) P_m(\cos\theta_1), \quad (4.40)$$

$$\tilde{\varphi}_n^{(2)} = \sum_{m=0}^{\infty} \left[B_{nm} \frac{b^{m+1}}{r_2^{m+1}} P_m(\cos\theta_2) + A_{nm} \frac{a^{m+1}}{r_1^{m+1}} P_m(\cos\theta_1) \right] + I_n^{(2)}(r_2, \theta_2), \quad (4.41)$$

$$\varphi_n'^{(2)} = \sum_{m=0}^{\infty} b_{nm} \frac{r_2^m}{b^m} P_m(\cos\theta) + I_n'^{(2)}(r_2, \theta_2), \quad (4.42)$$

$$\psi_n^{(2)} = \sum_{m=0}^{\infty} D_{nm} h_m(k_T r_2) P_m(\cos\theta_2) + C_{nm} h_m(k_T r_1) P_m(\cos\theta_1), \quad (4.43)$$

$$\psi_n'^{(2)} = \sum_{m=0}^{\infty} d_{nm} j_m(k_T' r_2) P_m(\cos\theta_2), \quad (4.44)$$

where $I_n^{(1)}, I_n'^{(1)}, I_n^{(2)}$ and $I_n'^{(2)}$ are the particular solutions of the inhomogeneous equations equations (4.23)–(4.26) respectively. However, in the current form, these equations are posed in different coordinate systems, hence these need to be transformed into equations with a single coordinate system.

4.2.1 Decomposition of incoming plane wave

The incoming plane wave also needs transforming into the appropriate system. Taking a Taylor expansion of the exponential function provides,

$$\varphi_{\text{inc}}^{(1)} = e^{ik_c r_1 \cos\theta_1 - \frac{d}{2}} = 1 + ik_c \left(r_1 \cos\theta_1 - \frac{d}{2} \right) - \frac{k_c^2 \left(r_1 \cos\theta_1 - \frac{d}{2} \right)^2}{2} + ... \quad (4.45)$$

so that,

$$\varphi^{(1)}_{\mathrm{inc}_0} = 1, \tag{4.46}$$

$$\varphi^{(1)}_{\mathrm{inc}_1} = r_1 \cos\theta_1 - \frac{d}{2}, \tag{4.47}$$

$$\varphi^{(1)}_{\mathrm{inc}_2} = \frac{r_1^2}{3}\left(2P_2(\cos\theta_1) + 1\right) - dr_1\cos\theta_1 + \frac{d^2}{4}, \tag{4.48}$$

about sphere 1, and,

$$\varphi^{(2)}_{\mathrm{inc}_0} = 1, \tag{4.49}$$

$$\varphi^{(2)}_{\mathrm{inc}_1} = r_2 \cos\theta_2 + \frac{d}{2}, \tag{4.50}$$

$$\varphi^{(2)}_{\mathrm{inc}_2} = \frac{r_2^2}{3}\left(2P_2(\cos\theta_2) + 1\right) + dr_2\cos\theta_2 + \frac{d^2}{4}, \tag{4.51}$$

about sphere 2. Note that the terms in d arise from translation of the origin from midpoint between spheres to the centre of spheres 1 and 2.

4.2.2 Translation addition theorem for Helmholtz solutions.

In section 1.3.6 we noted that the general radiating solution of Helmholtz equation can be written as

$$\psi = \sum_{n=0}^{\infty} C_n h_n(k_T r) P_n(\cos\theta). \tag{4.52}$$

Hence from linear superposition we may construct the radiating solutions from two different spheres as,

$$\psi = \sum_{n=0}^{\infty} \left[C_n h_n(k_T r_1) P_n(\cos\theta_1) + D_n h_n(k_T r_2) P_n(\cos\theta_2)\right]. \tag{4.53}$$

While this is the general solution for the two particle problem, this form is not convenient for applying the boundary conditions on the surface of the two spheres. The solution of the radiating wave from the other sphere needs to be translated and added to the solution of the sphere where the boundary conditions are being applied. To do this we can use the translation addition theorem set out by Gaunaurd *et al.* [46], and applying it to translation along the z axis. The following translates a solution from the (r_1, θ_1) frame to the (r_2, θ_2) frame,

$$h_n(k_T r_1) P_n(\cos\theta_1) = \sum_{q=0}^{\infty} Q_{(0n0q)} j_q(k_T r_2) P_q(\cos\theta_2). \tag{4.54}$$

Similarly, the backwards translation from the frame of (r_2, θ_2) to the frame of (r_1, θ_1) is provided by

$$h_n(k_T r_2) P_n(\cos\theta_2) = \sum_{q=0}^{\infty} (-1)^{n+q} Q_{(0n0q)} j_q(k_T r_1) P_q(\cos\theta_1), \tag{4.55}$$

where

$$Q_{(0n0q)} = i^{q-n}(2n+1) \sum_{\sigma=|n-q|}^{n+q} i^{\sigma}(-1)^{\sigma} b_{\sigma}^{(n0q0)} \begin{cases} j_{\sigma}(k_T d), & \text{for } r > d, \\ h_{\sigma}(k_T d), & \text{for } r < d, \end{cases} \tag{4.56}$$

and

$$b_{\sigma}^{(n0q0)} = (2\sigma+1) \left(\begin{array}{cc:c} n & q & \sigma \\ 0 & 0 & 0 \end{array} \right)^2, \tag{4.57}$$

where the Wigner $3-j$ symbol is defined in appendix A.

Using this translation, equation (4.53) can be written in two forms, one in the frame of (r_1, θ_1) and a second in the frame of (r_2, θ_2):

$$\psi^{(1)} = \sum_{n=0}^{\infty} \left[C_n h_n(k_T r_1) P_n(\cos\theta_1) + D_n \sum_{q=0}^{\infty} (-1)^{n+q} Q_{(0n0q)} j_q(k_T r_1) P_q(\cos\theta_1) \right], \tag{4.58}$$

$$\psi^{(2)} = \sum_{n=0}^{\infty} \left[D_n h_n(k_T r_2) P_n(\cos\theta_2) + C_n \sum_{q=0}^{\infty} Q_{(0n0q)} j_q(k_T r_2) P_q(\cos\theta_2) \right], \tag{4.59}$$

which now allow the boundary conditions in equations (4.8)–(4.11) to be evaluated on each of the spheres.

4.2.3 Translation addition theorem for Laplace's equation solutions

A similar procedure is applied to the solutions to Laplace's equation in the expansion of the acoustic spherical harmonics. The general exterior solution of Laplace's equation is given by,

$$\varphi = \sum_{n=0}^{\infty} A_n \frac{1}{r^{n+1}} P_n(\cos\theta). \tag{4.60}$$

and so the solution outside two spheres maybe written as,

$$\varphi = \sum_{n=0}^{\infty} \left[A_n \frac{1}{r_1^{n+1}} P_n(\cos\theta_1) + B_n \frac{1}{r_2^{n+1}} P_n(\cos\theta_2) \right]. \tag{4.61}$$

As with the Helmholtz solution, to be able to impose the boundary condition, the solution from the frame of one particle need to be translated into the frame of the second. The translation along the z axis, from frame (r_2, θ_2) to (r_1, θ_1) is given by Greengard and Rokhlin [47] as,

$$\frac{P_n(\cos\theta_2)}{r_2^{n+1}} = \frac{1}{d^{n+1}} \sum_{q=0}^{\infty} \left(\frac{r_1}{d}\right)^q \frac{(n+q)!}{n!q!} P_n(\cos\theta_1). \tag{4.62}$$

Similarly, the translation from frame (r_2, θ_2) to (r_1, θ_1) is given by,

$$\frac{P_n(\cos\theta_1)}{r_1^{n+1}} = \left(\frac{-1}{d}\right)^{n+1} \sum_{q=0}^{\infty} \left(\frac{r_2}{d}\right)^q \frac{(n+q)!}{n!q!} P_n(\cos\theta_2). \tag{4.63}$$

This now allows equation (4.61) to be written in both the (r_1, θ_1) and (r_2, θ_2) frames,

$$\varphi^{(1)} = \sum_{n=0}^{\infty} \left[A_n \frac{1}{r_1^{n+1}} P_n(\cos\theta_1) + B_n \frac{1}{d^{n+1}} \sum_{q=0}^{\infty} \left\{ \left(\frac{r_1}{d}\right)^q \frac{(n+q)!}{n!q!} P_q(\cos\theta_1) \right\} \right], \tag{4.64}$$

and

$$\varphi^{(2)} = \sum_{n=0}^{\infty} \left[B_n \frac{1}{r_2^{n+1}} P_n(\cos\theta_2) + A_n \left(\frac{-1}{d}\right)^{n+1} \sum_{q=0}^{\infty} \left\{ \left(\frac{r_2}{d}\right)^q \frac{(n+q)!}{n!q!} P_q(\cos\theta_2) \right\} \right], \tag{4.65}$$

which now allow the boundary conditions in equations (4.8)–(4.11) to be solved on each of the spheres.

4.3 Thermoacoustic scattering by two spheres

Using these transformations the external field equations equations (4.37), (4.39), (4.41) and (4.43) may be written as

$$\begin{aligned}\tilde{\varphi}_n^{(1)} &= \sum_{m=0}^{\infty} \left[A_{nm} \frac{a^{m+1}}{r_1^{m+1}} P_m(\cos\theta_1) \right. \\ &\left. + B_{nm} \left(\frac{b}{d}\right)^{m+1} \sum_{q=0}^{\infty} \left\{ \left(\frac{r_1}{d}\right)^q \frac{(m+q)!}{m!q!} P_q(\cos\theta_1) \right\} \right] + I_n^{(1)}(r_1,\theta_1),\end{aligned} \tag{4.66}$$

$$\begin{aligned}\tilde{\varphi}_n^{(2)} &= \sum_{m=0}^{\infty} \left[B_{nm} \frac{b^{m+1}}{r_2^{m+1}} P_m(\cos\theta_2) \right. \\ &\left. + A_{nm} \left(\frac{-a}{d}\right)^{m+1} \sum_{q=0}^{\infty} \left\{ \left(\frac{r_2}{d}\right)^q \frac{(m+q)!}{m!q!} P_q(\cos\theta_2) \right\} \right] + I_n^{(2)}(r_2,\theta_2),\end{aligned} \tag{4.67}$$

$$\psi_n^{(1)} = \sum_{m=0}^{\infty} \left[C_{nm} h_m(k_T r_1) P_m(\cos\theta_1) + D_{nm} \sum_{q=0}^{\infty} (-1)^{m+q} Q_{(0m0q)} j_q(k_T r_1) P_q(\cos\theta_1) \right], \tag{4.68}$$

and

$$\psi_n^{(2)} = \sum_{m=0}^{\infty} \left[D_{nm} h_m(k_T r_2) P_m(\cos\theta_2) + C_{nm} \sum_{q=0}^{\infty} Q_{(0m0q)} j_q(k_T r_2) P_q(\cos\theta_2) \right]. \tag{4.69}$$

We can now proceed to find the solutions following the method of Harlen *et al.* [27].

4.3.1 Order one solution

At order one in the ik_c expansion the incident field is constant while the leading order acoustic fields satisfy

$$\nabla^2 \tilde{\varphi}_0^{(1)} = 0, \tag{4.70}$$

$$\nabla^2 \varphi_0'^{(1)} = 0, \tag{4.71}$$

$$\nabla^2 \tilde{\varphi}_0^{(2)} = 0, \tag{4.72}$$

$$\nabla^2 \varphi_0'^{(2)} = 0, \tag{4.73}$$

as $\tilde{\varphi}_{-1}^{(1)} = \tilde{\varphi}_{-1}^{(2)} = \varphi_{-2}'^{(1)} = \varphi_{-2}'^{(2)} = 0$. From the boundary conditions (4.31), (4.32), (4.35) and (4.36) we deduce that $\psi_0^{(1)} = \psi_0^{(2)} = \psi_0'^{(1)} = \psi_0'^{(2)} = 0$. Thus only boundary conditions (4.29), (4.30), (4.33) and (4.34) need to be considered.

As in the case of the single sphere the solution consists of a constant field $\frac{1}{\hat{\rho}}$ inside each particle so that

$$a_{00} = b_{00} = \frac{1}{\hat{\rho}}, \tag{4.74}$$

with all other coefficients being zero.

4.3.2 Order ik_c solutions

At order ik_c the incident field, expressed with respect to sphere one, is of the form $r_1 P_1(\cos\theta_1) - \frac{d}{2}$. Since, the constant does not produce any external field we can use the solution from order one and simply add this to the solution for $r_1 P_1(\cos\theta_1)$ and $r_2 P_2(\cos\theta_2)$.

At this order the acoustic fields satisfy

$$\nabla^2 \tilde{\varphi}_1^{(1)} = 0, \tag{4.75}$$

$$\nabla^2 \varphi_1'^{(1)} = 0, \tag{4.76}$$

$$\nabla^2 \tilde{\varphi}_1^{(2)} = 0, \tag{4.77}$$

$$\nabla^2 \varphi_1'^{(2)} = 0. \tag{4.78}$$

and from the boundary conditions boundary conditions (4.31), (4.32), (4.35) and (4.36), $\psi_1^{(1)} = \psi_1^{(2)} = \psi_1'^{(1)} = \psi_1'^{(2)} = 0$. Applying the boundary conditions (4.29), (4.30), (4.33) and (4.34), we obtain

$$\sum_{m=0}^{\infty} \left[\left(A_{1m} - \hat{\rho} a_{1m}\right) \delta_{mq} + B_{1m} \left(\frac{b}{d}\right)^{m+1} \left(\frac{a}{d}\right)^{q} \frac{(m+q)!}{m!q!} \right] = a\delta_{1q}, \tag{4.79}$$

$$\sum_{m=0}^{\infty} \left[\left(B_{1m} - \hat{\rho} b_{1m}\right) \delta_{mq} + A_{1m} \left(\frac{-a}{d}\right)^{m+1} \left(\frac{b}{d}\right)^{q} \frac{(m+q)!}{m!q!} \right] = b\delta_{1q}, \tag{4.80}$$

$$\sum_{m=0}^{\infty} \left[\left(-(m+1)A_{1m} - m a_{1m}\right) \delta_{mq} + B_{1m} q \left(\frac{b}{d}\right)^{m+1} \left(\frac{a}{d}\right)^{q} \frac{(m+q)!}{m!q!} \right] = a\delta_{1q}, \tag{4.81}$$

and

$$\sum_{m=0}^{\infty} \left[\left(-(m+1)B_{1m} - m b_{1m}\right) \delta_{mq} + A_{1m} q \left(\frac{-a}{d}\right)^{m+1} \left(\frac{b}{d}\right)^{q} \frac{(m+q)!}{m!q!} \right] = b\delta_{1q}, \tag{4.82}$$

where δ_{mq} is Kronecker's delta, defined as

$$\delta_{mq} = \begin{cases} 1 & \text{if } m = q, \\ 0 & \text{if } m \neq q. \end{cases} \tag{4.83}$$

This is an infinite system of linear equations. However, the higher order terms decay rapidly as shown in figure 4.4, so we truncate the system at order $q_{\max}$ leaving a $4q_{\max} \times 4q_{\max}$ matrix problem. Note that in the limit $d \to \infty$, the coupling tends to zero and we recover

$$A_{11\infty} = \left(\frac{\hat{\rho} - 1}{2\hat{\rho} + 1}\right) a, \tag{4.84}$$

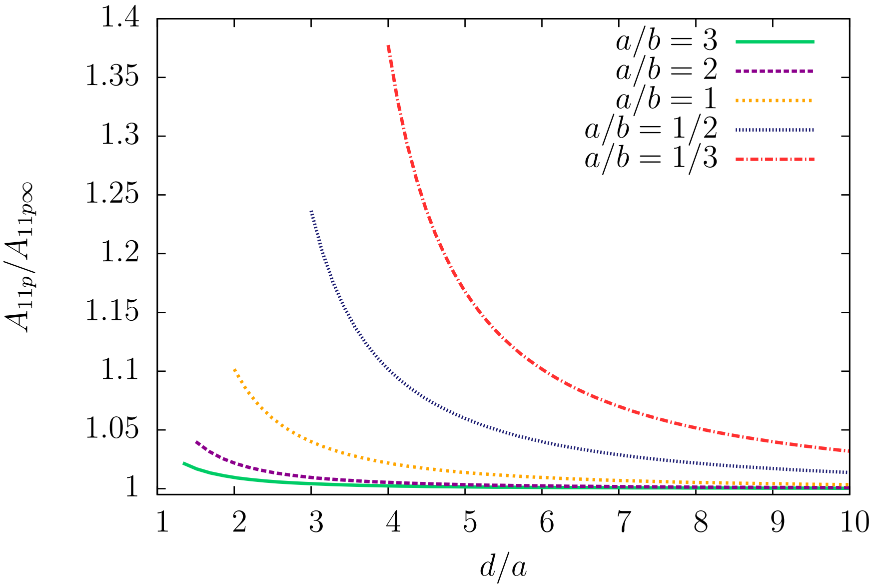

Figure 4.2

The behaviour of $A_{11}/A_{11\infty}$ *with increasing separation for* $a/b = 1/3, 1/2, 1, 2, 3$ *for silica in water.*

$$B_{11\infty} = \left(\frac{\hat{\rho} - 1}{2\hat{\rho} + 1}\right) b, \tag{4.85}$$

$$a_{11\infty} = \frac{3a}{2\hat{\rho} + 1}, \tag{4.86}$$

and

$$b_{11\infty} = \frac{3b}{2\hat{\rho} + 1}, \tag{4.87}$$

the single sphere solutions of Harlen *et al.* [27]. In figures 4.2 and 4.3 we show how A_{11} and a_{11} behave as a function of d for different values of a, b. As $d/a \to \infty$ the solutions for the two sphere problem converge to the sum of single sphere solutions. However, even when the spheres are touching the changes to A_{11} and a_{11} compared with the single sphere solutions are small.

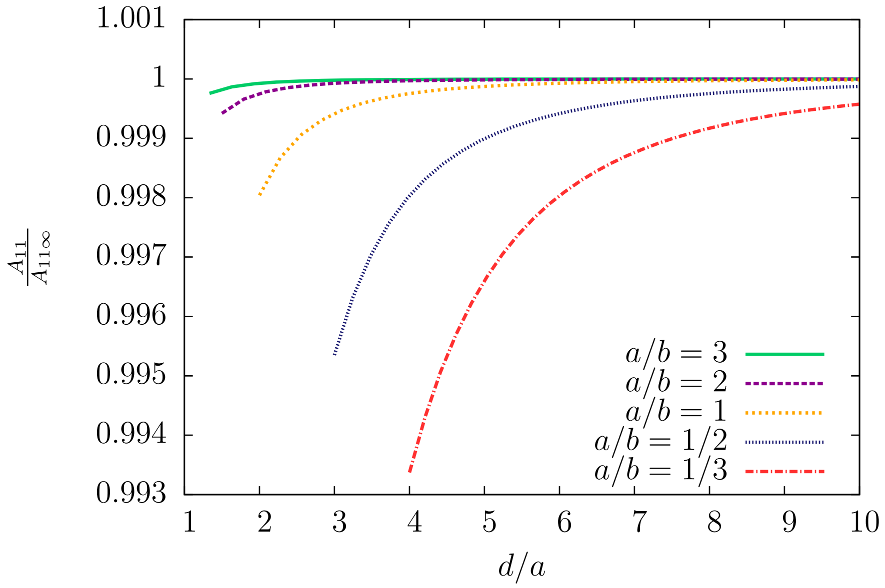

Figure 4.3

The behaviour of $a_{11}/a_{11\infty}$ *with increasing separation for* $a/b = 1/3, 1/2, 1, 2, 3$ *for silica in water.*

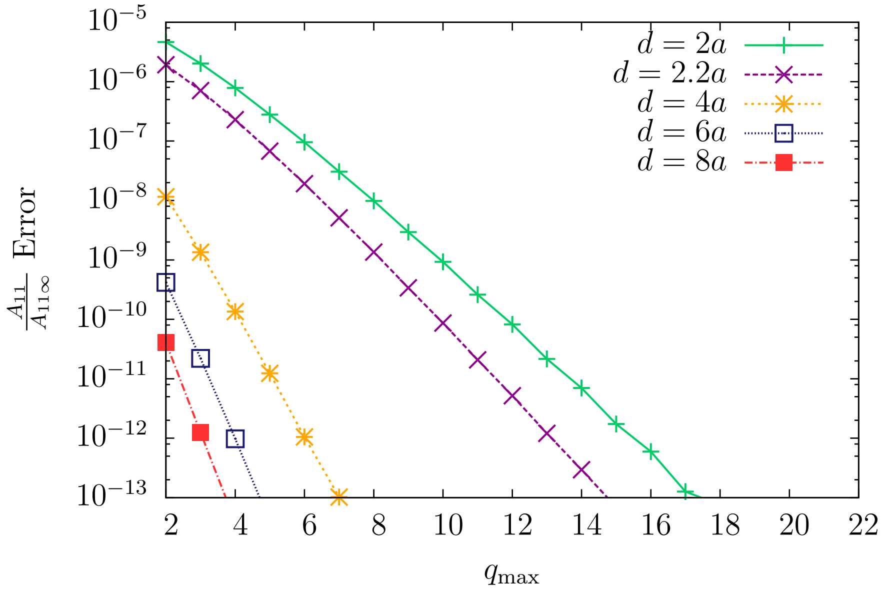

Figure 4.4

Error of A_{11} *for different values of* q_{max}*. It can be seen after a couple of terms that the solution converges rapidly. As d is increased the solution converges even more rapidly.*

4.3.3 Order $(ik_c)^2$ solutions

At order $(ik_c)^2$ the thermal terms come into effect, so that boundary conditions (4.31), (4.32), (4.35) and (4.36) now have to be considered. Hence the thermal boundary conditions lead to the equations

$$\begin{aligned} \sum_{m=0}^{\infty} \Big[\Big(C_{2m} h_m(k_T a) - \hat{\Gamma} c_{2m} j_q(k'_T a) \Big) \delta_{qm} + D_{2m} (-1)^{m+q} Q_{(0m0q)} j_q(k_T a) \Big] \\ = \left[\frac{\hat{\Gamma} G'_c}{\hat{\rho}} - G_c \right] \delta_{q0}, \end{aligned} \tag{4.88}$$

$$\begin{aligned} \sum_{m=0}^{\infty} \Big[\Big(D_{2m} h_m(k_T b) - \hat{\Gamma} d_{2m} j_q(k'_T b) \Big) \delta_{qm} + C_{2m} Q_{(0m0q)} j_q(k_T b) \Big] \\ = \left[\frac{\hat{\Gamma} G'_c}{\hat{\rho}} - G_c \right] \delta_{q0}, \end{aligned} \tag{4.89}$$

$$\begin{aligned} \sum_{m=0}^{\infty} \Big[\Big(C_{2m} k_T a h'_m(k_T a) - c_{2m} \hat{\Gamma} \hat{\tau} k'_T a j'_m(k'_T a) \Big) \delta_{qm} \\ + D_{2m} (-1)^{m+q} Q_{(0m0q)} k_T a j'_q(k_T a) \Big] = 0, \end{aligned} \tag{4.90}$$

and

$$\begin{aligned} \sum_{m=0}^{\infty} \Big[\Big(D_{2m} k_T b h'_m(k_T b) - d_{2m} \hat{\Gamma} \hat{\tau} k'_T b j'_m(k'_T b) \Big) \delta_{qm} \\ + C_{2m} Q_{(0m0q)} k_T b j'_q(k_T a) \Big] = 0, \end{aligned} \tag{4.91}$$

for the thermal coefficients. Again this system can be truncated at order $q_{\max}$.

While this can be solved as a separate matrix problem, it is convenient to see this as part of a larger linear system involving the acoustic boundary conditions at this order.

At this order the acoustic field equations are inhomogeneous,

$$
\begin{aligned}
\nabla^2 \tilde{\varphi}_2^{(1)} &= \frac{-2}{r_1}\frac{\partial}{\partial r_1}\left(r_1 \varphi_1^{(1)}\right), & (4.92)\\
\nabla^2 \varphi_2'^{(1)} &= -\frac{k_c'^2}{k_c^2}\frac{1}{a}\varphi_0'^{(1)}, & (4.93)\\
\nabla^2 \tilde{\varphi}_2^{(2)} &= \frac{-2}{r_1}\frac{\partial}{\partial r_2}\left(r_2 \varphi_1^{(2)}\right), & (4.94)\\
\nabla^2 \varphi_2'^{(2)} &= -\frac{k_c'^2}{k_c^2}\frac{1}{a}\varphi_0'^{(2)}. & (4.95)
\end{aligned}
$$

and applying the boundary conditions (4.29), (4.30) and (4.33), (4.34) leads to the equations,

$$
\begin{aligned}
&\sum_{m=0}^{\infty}\Bigg[\left(A_{2m} + C_{2m} h_m(k_T a) - \hat{\rho} a_{2m} - \hat{\Gamma} c_{2m} j_m(k_T' a)\right)\delta_{qm}\\
&+B_{2m}\left(\frac{b}{d}\right)^{m+1}\left(\frac{a}{d}\right)^{q}\frac{(m+q)!}{m!q!} + D_{2m}(-1)^{m+q} Q_{(0m0q)} j_q(k_T a)\Bigg]\\
&= \Bigg[-\frac{2}{3}\delta_{q2} + \left(\hat{c} - \frac{1}{3}\right)\delta_{q0}\\
&+\sum_{m=0}^{\infty}\left\{\frac{2}{m+1}A_{1m}\delta_{qm} - \frac{2}{q+2}B_{1m}\left(\frac{a}{d}\right)^{q}\left(\frac{b}{d}\right)^{m+1}\frac{(m+q)!}{m!q!}(q+1)\right\}\Bigg], \qquad (4.96)
\end{aligned}
$$

$$
\begin{aligned}
&\sum_{m=0}^{\infty}\Bigg[\left(B_{2m} + D_{2m} h_m(k_T b) - \hat{\rho} b_{2m} - \hat{\Gamma} d_{2m} j_m(k_T' b)\right)\delta_{qm}\\
&+A_{2m}\left(\frac{-a}{d}\right)^{m+1}\left(\frac{b}{d}\right)^{q}\frac{(m+q)!}{m!q!} + C_{2m} Q_{(0m0q)} j_q(k_T a)\Bigg]\\
&= \Bigg[-\frac{2}{3}\delta_{q2} + \left(\hat{c} - \frac{1}{3}\right)\delta_{q0}\\
&+\sum_{m=0}^{\infty}\left\{\frac{2}{m+1}B_{1m}\delta_{qm} - \frac{2}{q+2}A_{1m}\left(\frac{b}{d}\right)^{q}\left(\frac{-a}{d}\right)^{m+1}\frac{(m+q)!}{m!q!}(q+1)\right\}\Bigg], \qquad (4.97)
\end{aligned}
$$

$$\sum_{m=0}^{\infty}\Bigg[\left(-(m+1)A_{2m}+C_{2m}k_Tah'_m(k_Ta)-ma_{2m}-c_{2m}k'_Taj'_m(k'_Ta)\right)\delta_{qm}$$
$$+B_{2m}q\left(\frac{b}{d}\right)^{m+1}\left(\frac{a}{d}\right)^{q}\frac{(m+q)!}{m!q!}+D_{2m}(-1)^{m+q}Q_{(0m0q)}k_Taj'_q(k_Ta)\Bigg]$$
$$=\left[-\frac{4}{3}\delta_{q2}-\frac{2}{3}\delta_{q0}+\sum_{m=0}^{\infty}\left\{-A_{1m}\delta_{qm}-B_{1m}\left(\frac{a}{d}\right)^{q}\left(\frac{b}{d}\right)^{m+1}\frac{(m+q)!}{m!q!}\right\}\right], \quad (4.98)$$

and

$$\sum_{m=0}^{\infty}\Bigg[\left(-(m+1)B_{2m}+D_{2m}k_Tbh'_m(k_Tb)-mb_{2m}-d_{2m}k'_Tbj'_m(k'_Tb)\right)\delta_{qm}$$
$$+A_{2m}q\left(\frac{-a}{d}\right)^{m+1}\left(\frac{b}{d}\right)^{q}\frac{(m+q)!}{m!q!}+C_{2m}Q_{(0m0q)}k_Tbj'_q(k_Tb)\Bigg]$$
$$=\left[-\frac{4}{3}\delta_{q2}-\frac{2}{3}\delta_{q0}+\sum_{m=0}^{\infty}\left\{-B_{1m}\delta_{qm}-A_{1m}\left(\frac{b}{d}\right)^{q}\left(\frac{-a}{d}\right)^{m+1}\frac{(m+q)!}{m!q!}\right\}\right], \quad (4.99)$$

where $\hat{c}=\frac{k_c'^2}{k_c^2}$. Here again we have excluded the contribution from the incident field that arise from shifting the origin to the centre of each sphere. As before the constant term does not contribute to the external field, while the linear term does not produce a contribution to A_{20} or B_{20}, which are the only terms needed to determine the far field scattering.

We can use Rayleigh's formulae to determine the values of the spherical Bessel function [24],

$$j_n(z)=z^n\left(-\frac{1}{z}\frac{d}{dz}\right)^n\frac{\sin z}{z} \quad (4.100)$$

and

$$h_n(z)=z^n\left(-\frac{1}{z}\frac{d}{dz}\right)^n\frac{e^{iz}}{z}. \quad (4.101)$$

This matrix system of size $8q_{\max}\times 8q_{\max}$ can be solved to provide the results as seen in figure 4.5.

Again in the limit $d \to \infty$ we recover the single particle solution given by Harlen *et al* [27] in which the only non-zero components are C_{20}, D_{20}, c_{20} and d_{20}.

$$C_{20} = \frac{ik_T a\hat{\tau}(G_c\hat{\rho} - \hat{\Gamma}G_c')(k_T' a\cos k_T' a - \sin k_T' a)}{e^{ik_T a}\hat{\rho}\,(\hat{\tau}k_T' a\cos k_T' a + (1 - \hat{\tau} - ik_T a)\sin k_T' a)}, \tag{4.102}$$

$$D_{20} = \frac{ik_T b\hat{\tau}(G_c\hat{\rho} - \hat{\Gamma}G_c')(k_T' b\cos k_T' b - \sin k_T' b)}{e^{ik_T b}\hat{\rho}\,(\hat{\tau}k_T' b\cos k_T' b + (1 - \hat{\tau} - ik_T b)\sin k_T' b)}, \tag{4.103}$$

$$c_{20} = \frac{(G_c\hat{\rho} - \hat{\Gamma}G_c')(ik_T a - 1)}{\hat{\Gamma}\hat{\rho}\,(\hat{\tau}k_T' a\cos k_T' a + (1 - \hat{\tau} - ik_T a)\sin k_T' a)}, \tag{4.104}$$

and

$$d_{20} = \frac{(G_c\hat{\rho} - \hat{\Gamma}G_c')(ik_T b - 1)}{\hat{\Gamma}\hat{\rho}\,(\hat{\tau}k_T' b\cos k_T' b + (1 - \hat{\tau} - ik_T b)\sin k_T' b)}. \tag{4.105}$$

In figure 4.5, we show how coefficients behave as as a function of d, for different values of a and b with $|k_T a| = 1$. At large d/a, the results converge towards the single particle solution, however the approach is not monotonic. This is due to the oscillating behaviour of $\sin(k_T' a)$, $\cos(k_T' a)$, $\sin(k_T' b)$ and $\cos(k_T' b)$. In figure 4.6 we see how C_{20} differs from the single particle solution when $a = b$. When the particles are touching we see the biggest difference at around $|k_T a| = 2$. As the particles move further apart, the peak difference reduces, and decreases with $k_T a$. A negative difference is also observed at around $|k_T a| = 3$. As d is increased, the peak and the trough are translated in the negative $|k_T a|$ direction, as well as reducing in size. This is due to the solution converging to the single particle solution.

For the acoustic coefficients, we can show in a similar way that as $d \to \infty$, we

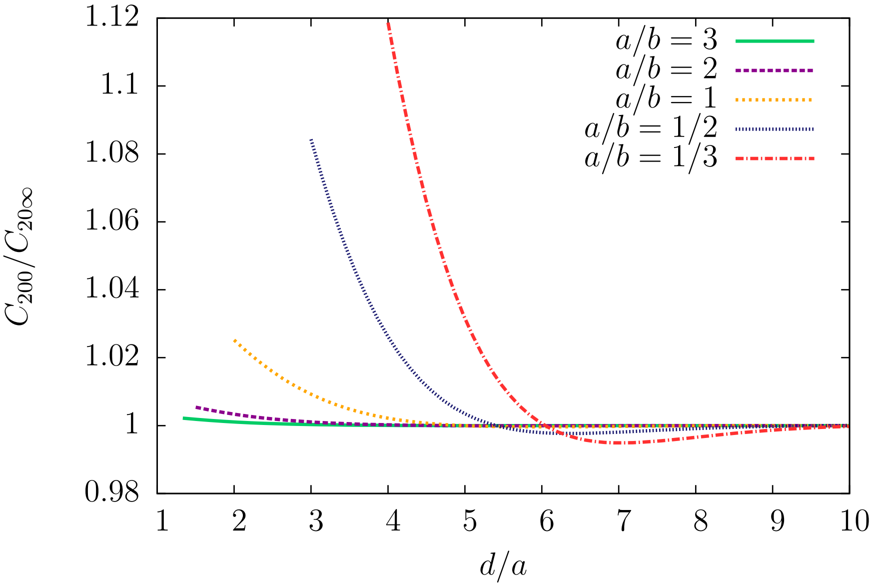

Figure 4.5

The behaviour of $|C_{20}/C_{20\infty}|$ *with increasing separation for* $a/b = 1/3, 1/2, 1, 2, 3$ *for silicone in water and* $|k_T a| = 1$.

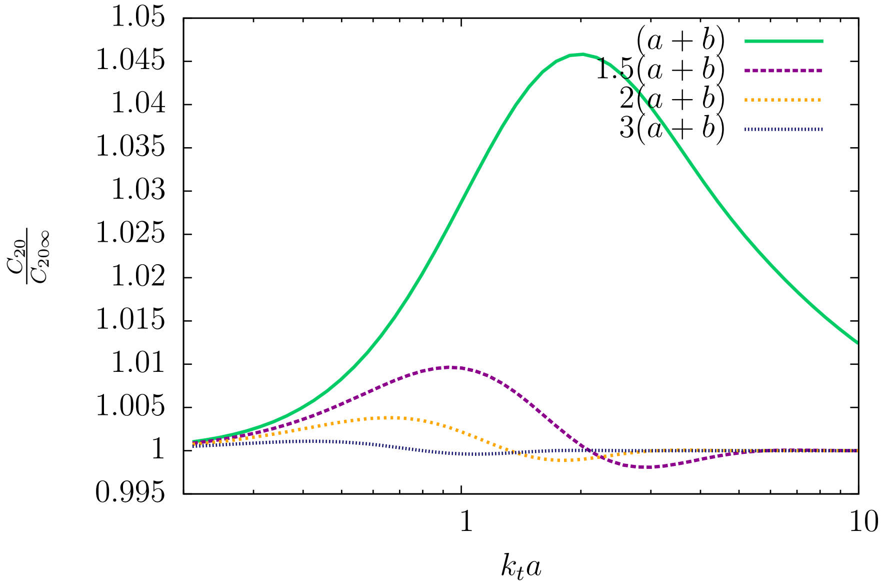

Figure 4.6

A comparison of the behaviour of $|C_{20}|/C_{20\infty}$ *over* $k_T a$ *for different values of* d *and* $a = b$.

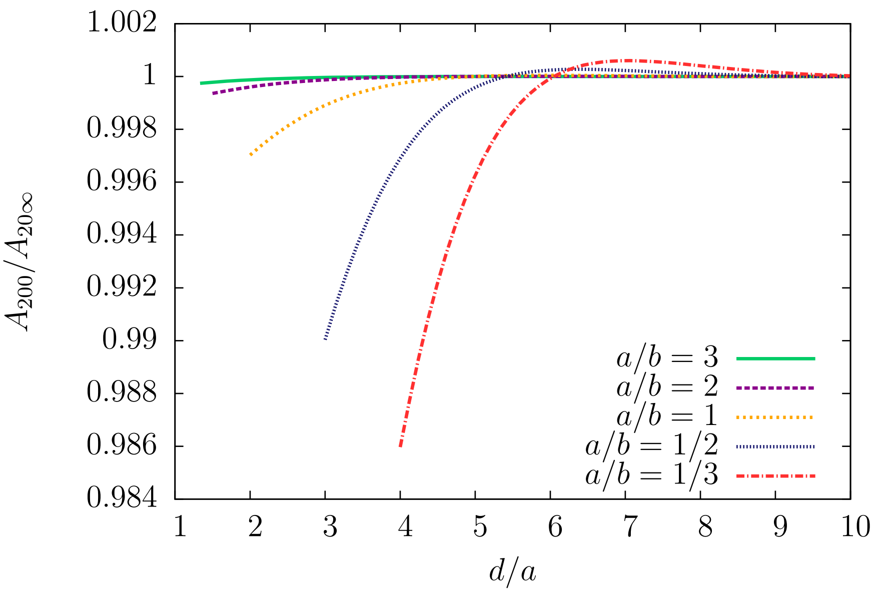

Figure 4.7

The behaviour of $|A_{20}/A_{20\infty}|$ *with increasing separation for* $a/b = 1/3, 1/2, 1, 2, 3$ *for silicone in water.*

obtain the single particle solutions for A_{20} and B_{20}

$$A_{20} = \frac{\hat{\rho} - \hat{c}}{3\hat{\rho}} + \frac{(\hat{\Gamma}\hat{\tau} - 1)(\hat{\Gamma}G'_c - \hat{\rho}G_c)\,(k'_T a - \tan k'_T a)\,(ik_T a - 1)}{\hat{\Gamma}\hat{\rho}\,(\hat{\tau}k'_T a + (1 - \hat{\tau} - ik_T a)\tan k'_T a)}, \qquad (4.106)$$

$$B_{20} = \frac{\hat{\rho} - \hat{c}}{3\hat{\rho}} + \frac{(\hat{\Gamma}\hat{\tau} - 1)(\hat{\Gamma}G'_c - \hat{\rho}G_c)\,(k'_T n - \tan k'_T b)\,(ik_T b - 1)}{\hat{\Gamma}\hat{\rho}\,(\hat{\tau}k'_T b + (1 - \hat{\tau} - ik_T b)\tan k'_T b)}. \qquad (4.107)$$

In figure 4.7, we can see how these coefficients behave as $d \to \infty$, for different values of a and b, converge towards the single particle solution.

For the coefficient A_{20}, it is also possible to see how fast this term converges, so we are able to limit the number of terms needed to be calculated, figure 4.8.

It is also possible to observe how these coefficients behave across a range of $k_T a$ values to see where these effects are most prominent, as in figure 4.9. As with C_{20}, in figure 4.6 we see the largest difference when the particles are touching,

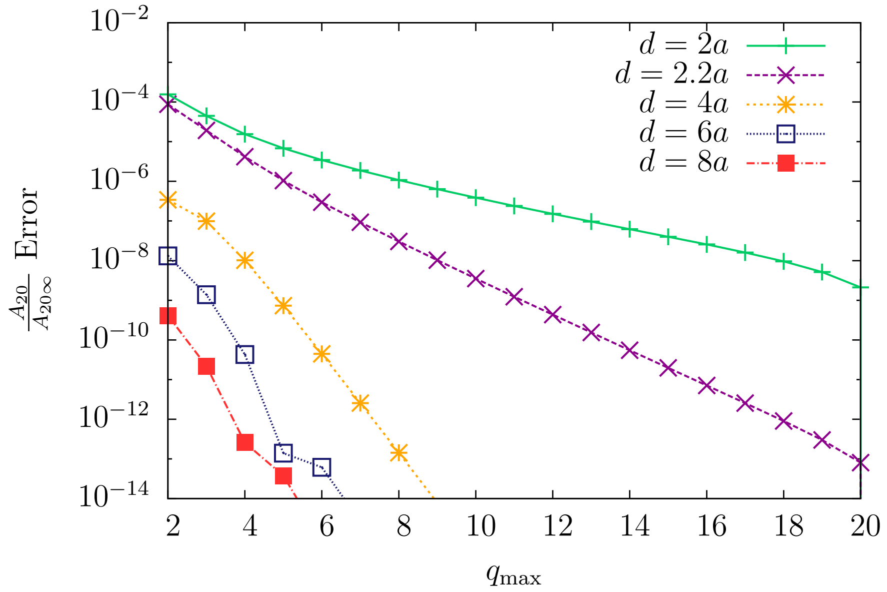

Figure 4.8

Error of $A_{20}/A_{20\infty}$ *for different values of* q_{max}*. It can be seen after a couple of terms that the solution converges rapidly. As d is increased the solution converges even more rapidly.*

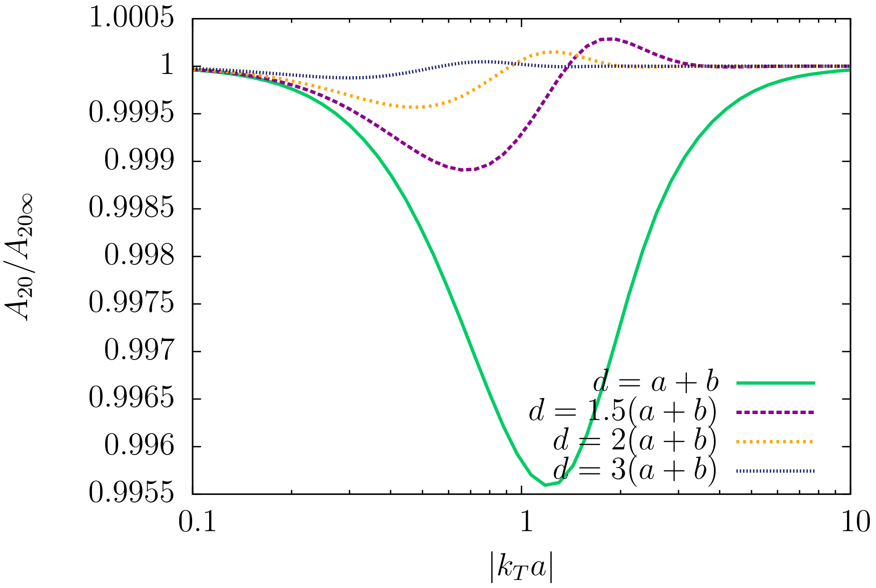

Figure 4.9

A comparison of the behaviour of $|A_{20}|/A_{20\infty}$ *over* $k_T a$ *for different values of* d*.*

however, A_{20} is less than the single particle solution.

4.4 Far field

Using the coefficients that were generated in section 4.3, we can calculate the far field contribution. For a single sphere far from the particle the reflected acoustic wave has the form [27],

$$\varphi \sim \frac{e^{ik_c r}}{r} f^{\text{single}}(\theta), \tag{4.108}$$

which, for small $k_T a$ gives the far field pattern

$$f^{\text{single}}(\theta) = k_c^2 a^3 \left(A_{11} \cos\theta - A_{20}\right) + O(|k_c a|^3) \text{ as } r \to \infty. \tag{4.109}$$

Note this only contains the acoustic terms as the thermal wave is non-propagation and thus does not appear in the far field. For two particles, the far field can be expressed by

$$\varphi^{(1)+(2)} \sim \frac{e^{ik_c r}}{r} \left(f^{(1)}(\theta) + f^{(2)}(\theta) e^{ik_c d} \right) \tag{4.110}$$

by taking a (ik_c) expansion of the two particle far field solution from Gaunaurd *et al.* [46]. Which gives,

$$f^{(1)}(\theta) = k_c^2 a^3 \left(A_{11} \cos\theta - A_{20} \right) + O(|k_c a|^3) \text{ as } r \to \infty, \tag{4.111}$$

and

$$f^{(2)}(\theta) = k_c^2 b^3 \left(B_{11} \cos\theta - B_{20} \right) + O(|k_c b|^3) \text{ as } r \to \infty. \tag{4.112}$$

However, what we are most interested in is the change to the far field due to multiple scattering,

$$f^{\text{excess}}(\theta) = \frac{f^{(1)}(\theta)}{f^{\text{single}}(\theta)}, \tag{4.113}$$

which tells us the contribution the thermoacoustic multiple scattering has on the far field.

In figures 4.10–4.13 we see the effect multiple thermoacoustic scattering has on the far field. For $d = (a + b)$, in figure 4.10, we see that when b is greater than a that the difference between the single far field scatter and the multiple far field scatter is larger in magnitude. For $a/b = 3$ the lowest point is around $|k_T a| = 0.9$ ($|k_T b| = 2.7$). As a/b increases, the lowest point moves in the positive $|k_T a|$ direction, however decreases in size. This suggests that larger particles have a greater influence on smaller particles but smaller particles have a lesser effect on larger ones. This also suggests that the attenuation spectrum would have its peak reduced suggesting a lower concentration of colloid.

In figure 4.11 we have $d = 1.5(a + b)$. Notice now that the amount of change from the single far field solution is now less than for $d = (a + b)$. However, the lowest point has now moved in the negative $|k_T a|$ direction. While the pattern of the lowest point being shifted in the positive $|k_T a|$ direction remains, we now have peak which is greater than the single far field. This suggests now that the

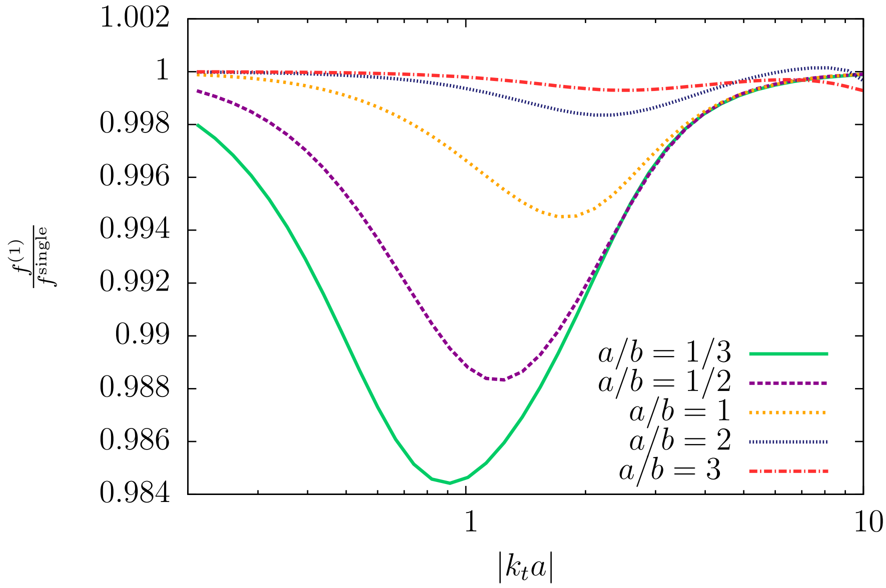

Figure 4.10

Excess far field as a result of in-line multiple thermoacoustic scattering for $d = (a + b)$.

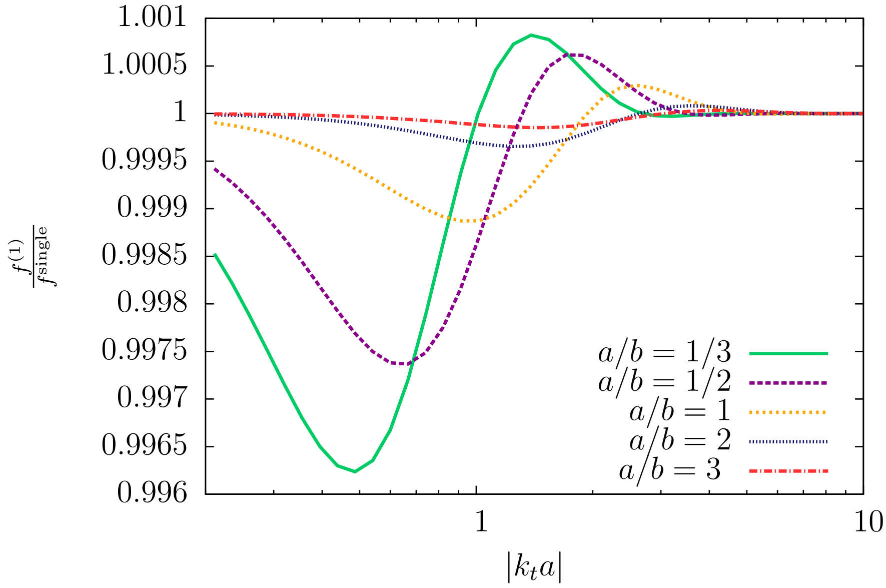

Figure 4.11

Excess far field as a result of in-line multiple thermoacoustic scattering for $d = 1.5(a + b)$.

attenuation peak would now be shifted in the positive $|k_T a|$ suggesting that the two particles are behaving like a single larger particle size.

In figures 4.12 and 4.13, we see similar behaviour with $d = 2(a + b)$ and $d = 3(a + b)$ as with $1.5(a + b)$, but even more so with the curves being shifted in the negative $|k_T a|$ direction, but with even less magnitude, suggesting that the further the particles are apart the less multiple scattering has an effect.

4.5 Close field

We can use the solutions in the previous sections to provide an insight to how the acoustic and thermal fields behave when two particles are close together for particles of the same size, and those of different sizes. These plots are the maximum pressure and temperature excursion arising from the sinusoidal exciting pressure field for the second order terms.

In figure 4.14, when the particles are touching they behave as a single particle larger than a particle of that size on its own, which is in agreement with figure 4.10, as the drop in the far field at $|k_T a| = 1$ suggests that the attenuation prediction will provide a curve one would expect from a larger particle size. This behaviour is reflected in figure 4.19, as it too is showing behaviour of a single larger particle.

As the particles are moved further apart as in figure 4.15, we see now that even though there is distance between the two particles, that the pressure around both spheres still behaves as if it were one larger sphere. As they are further apart and behaving as a single sphere, it suggests that it is behaving as an even larger sphere as in figure 4.14. This behaviour is reflected also in figure 4.20. This suggests even though they are further apart, multiple scatter still has a large effect.

If we increase the size of one of the particles as in figures 4.16 and 4.17 and their temperature counterparts figures 4.21 and 4.22, we see the bigger particle has more effect on the close field than the smaller particle. This is mirrored in figures 4.11–4.13, where when one particle much larger then it has more influence over the other. Figures 4.17 and 4.22 emphasise this even more as d is increased the influence the larger particle has on the pair is still observed.

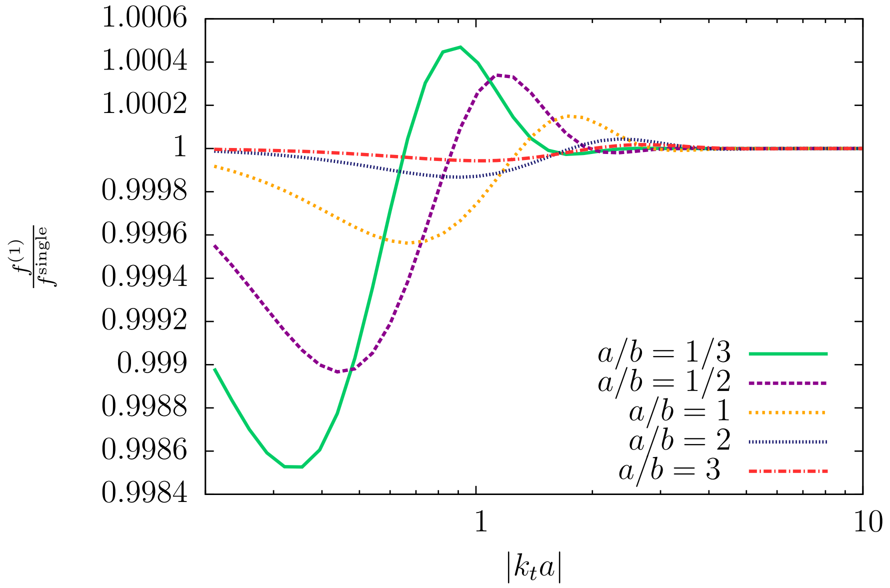

Figure 4.12

Excess far field as a result of in-line multiple thermoacoustic scattering for $d = 2(a + b)$.

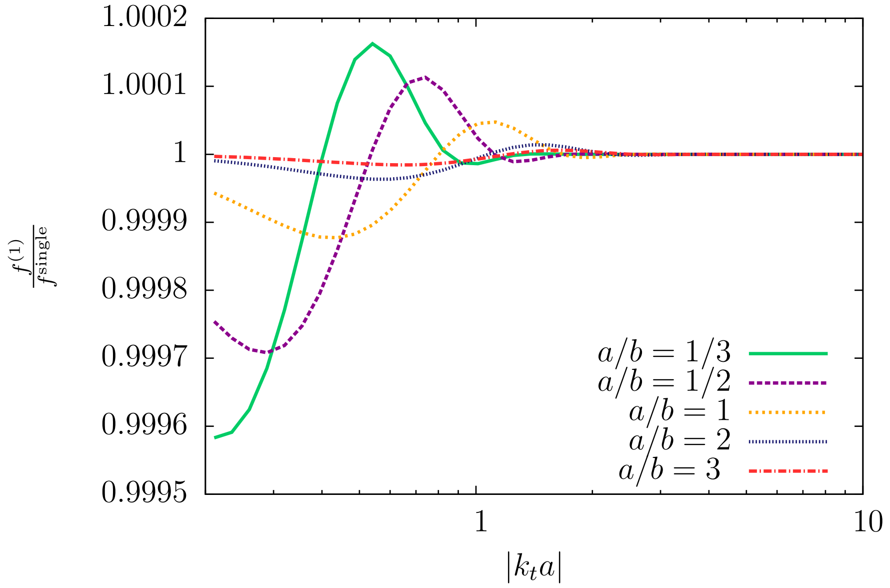

Figure 4.13

Excess far field as a result of in-line multiple thermoacoustic scattering for $d = 3(a + b)$.

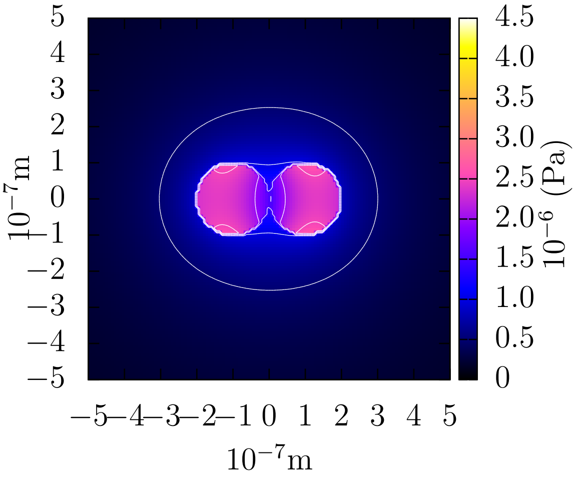

Figure 4.14

Close field plot of pressure for

$a/b = 1$ *and* $d = a + b$ *and* $|k_T a| = 1$.

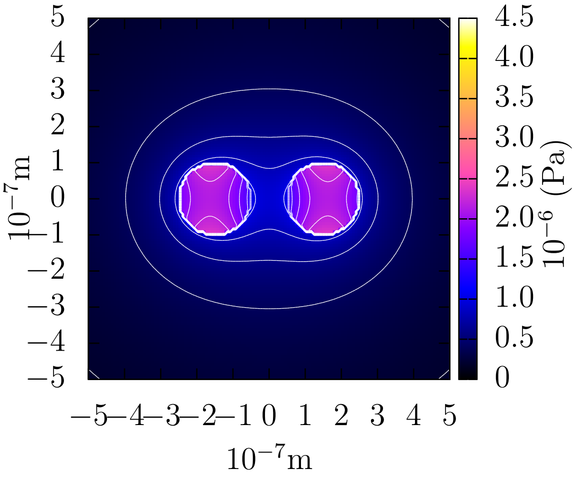

Figure 4.15

Close field plot of pressure for

$a/b = 1$ *and* $d = 2a + b$ *and*

$|k_T a| = 1$.

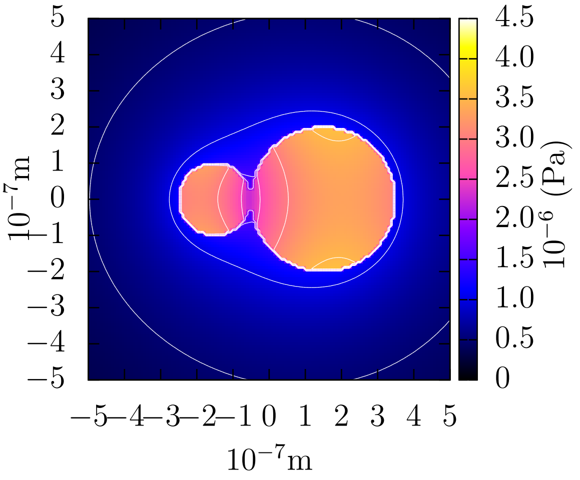

Figure 4.16

Close field plot of pressure for

$a/b = 1/2$ *and* $d = a + b$ *and*

$|k_T a| = 1$.

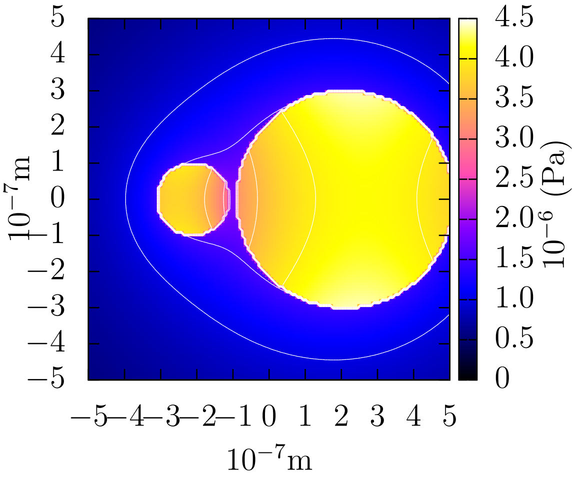

Figure 4.17

Close field plot of pressure for

$a/b = 1/3$ *and* $d = 1.2a + b$ *and*

$|k_T a| = 1$.

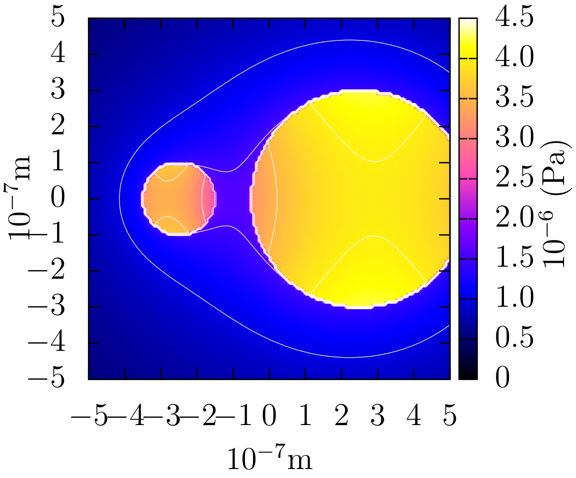

Figure 4.18

Close field plot of pressure for $a/b = 1/3$ and $d = 2a + b$ and $|k_T a| = 1$.

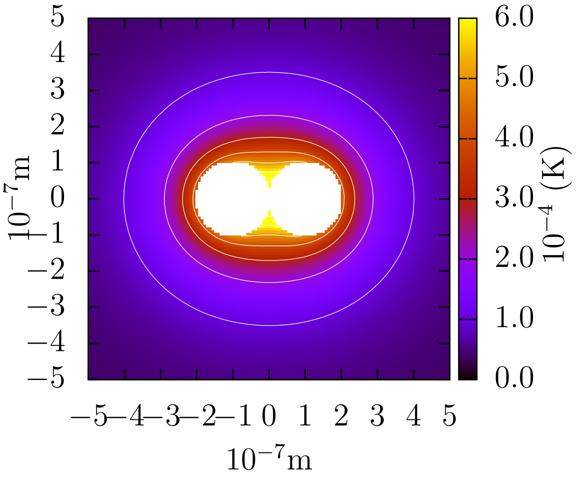

Figure 4.19

Close field plot of temperature for $a/b = 1$ and $d = a + b$ and $|k_T a| = 1$.

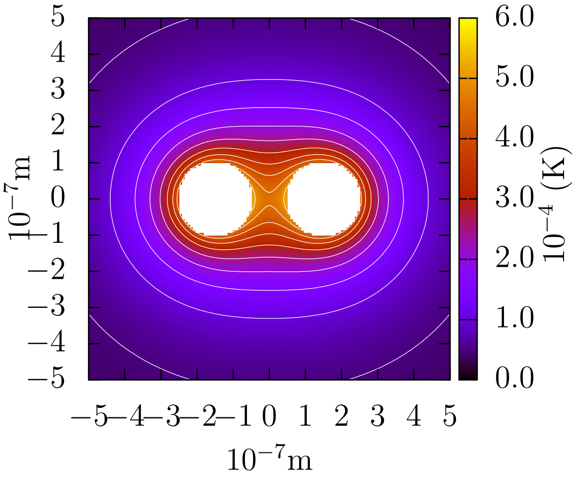

Figure 4.20

Close field plot of temperature for $a/b = 1$ and $d = 2a + b$ and $|k_T a| = 1$.

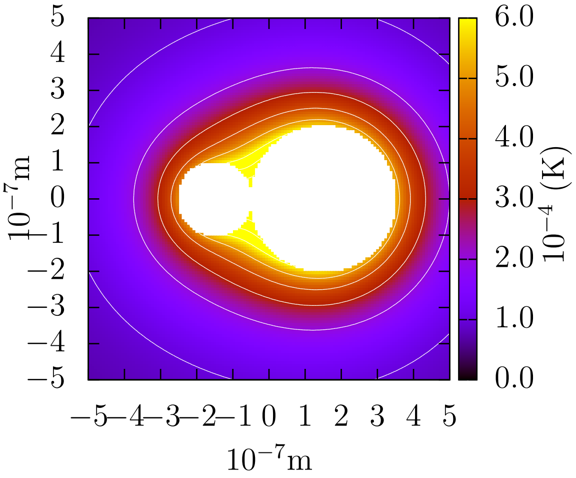

Figure 4.21

Close field plot of temperature for $a/b = 1/2$ and $d = a + b$ and $|k_T a| = 1$.

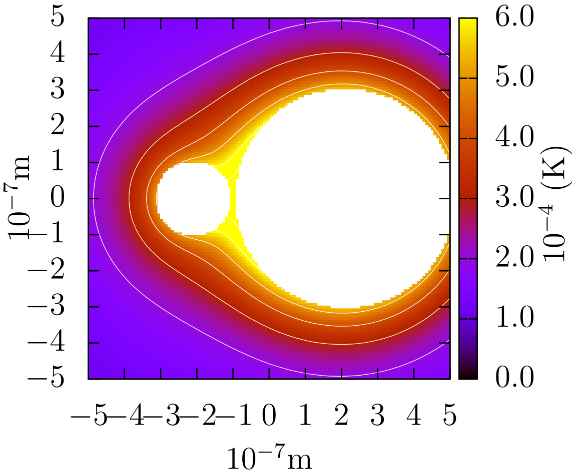

Figure 4.22

Close field plot of temperature for $a/b = 1/3$ *and* $d = 1.2a + b$ *and* $|k_T a| = 1$.

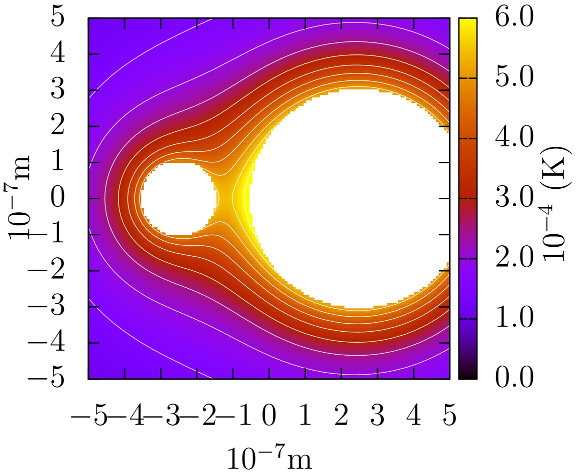

Figure 4.23

Close field plot of temperature for $a/b = 1/3$ *and* $d = 2a + b$ *and* $|k_T a| = 1$.

Chapter 5

Two particle perturbation solution (general angle)

5.1 Introduction

In chapter 4, we looked at weak thermal scattering of two particles which are aligned perpendicular to the direction of the plane wave. However, in reality, this will not be the case, and thus we must consider the general case when there are two particles not aligned with the incoming wave.

Although the problem is no longer axisymmetric we can use the same methods as in chapter 4; the weak thermal scattering approach of $|k_c a| \ll 1$ and $|k_T a| \sim 1$ from Harlen *et al.* [27], with translation addition theorems for Helmholtz and Laplace's equations from Gaunaurd *et al.* [46], and Greengard and Rokhlin [47] respectively.

Let us consider two particles, as seen in figure 5.1, 1 and 2, with radii a and b respectively, where a and b are of the same order. These two particles are placed at a distance d between their centres, on an axis, z say, such that $d > a + b$. Now consider a plane wave propagating at an angle α from the z axis. We define an orgin at the centre of each particle, O_1 and O_2. From each origin we define a set of spherical polar coordinate, (r_1, θ_1, ϕ_1) and (r_2, θ_2, ϕ_2), with respect to the centre of each particle and the z-axis.

The surfaces of the spheres are defined by equations (4.1) and (4.2). As with

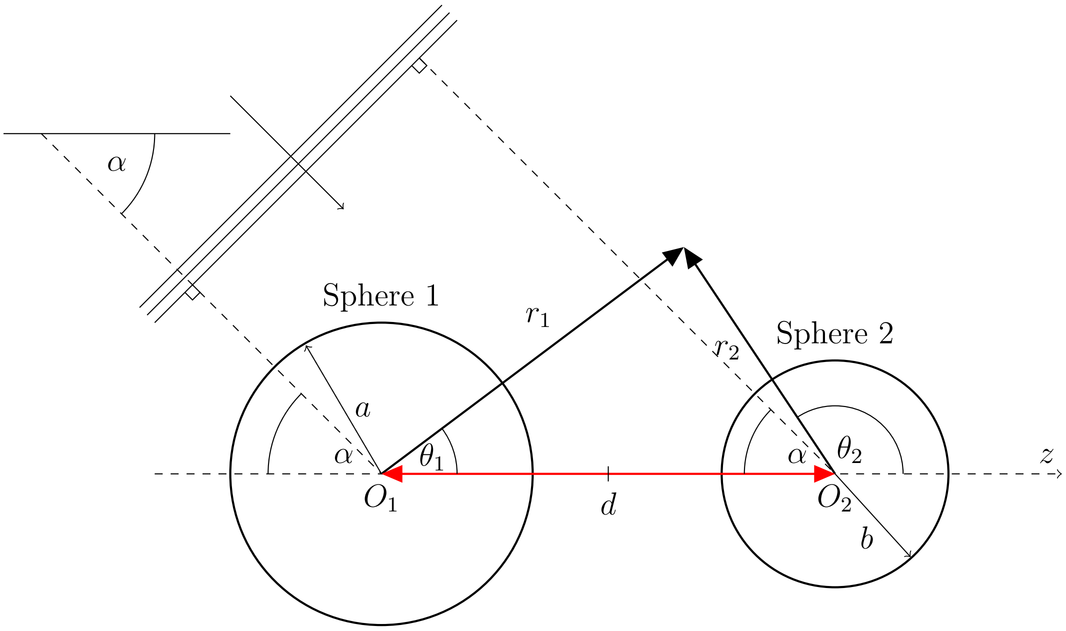

Figure 5.1

Figure of two sphere problem with general direction incoming plane wave at angle α from the z axis.

the case of the single particle and the two particles in-line case, the acoustic and thermal waves must satisfy, in the continuous and discrete phases, the Helmholtz equations (4.3) and (4.4). The incident acoustic wave is travelling perpendicular to angle α from the z axis, defined as,

$$\varphi_{\text{inc}} = e^{i\mathbf{k}\cdot\mathbf{x}} = e^{ik_c r\cos(\theta-\alpha)}, \tag{5.1}$$

where r is the distance from the midpoint of the spheres and the wave vector lies in the plane $\phi = 0$. In each sphere's frame about origins O_1 and O_2, this equation becomes

$$\varphi_{\text{inc}}^{(1)} = e^{ik_c r\cos(\theta-\alpha)} = e^{ik_c r_1\cos(\theta_1-\alpha)}e^{-ik_c\frac{d}{2}} \tag{5.2}$$

and

$$\varphi_{\text{inc}}^{(2)} = e^{ik_c r\cos(\theta-\alpha)} = e^{ik_c r_2\cos(\theta_2-\alpha)}e^{ik_c\frac{d}{2}} \tag{5.3}$$

for sphere 1 and 2, respectively.

5.1.1 Boundary conditions and weak thermal scattering

The boundary conditions and the method of transforming the problem into a weak thermal scattering problem for the general angle are dealt with in the same manner as in sections 4.1.1 and 4.2, so to avoid repetition the reader is referred to the previous chapter for these expressions.

5.1.2 Decomposition of incoming plane wave

As with the case of the previous chapter, in the limit $k_c a \ll 1$ and $k_c b \ll 1$, the incoming wave can be expanded by taking a Taylor expansion of equations (5.2) and (5.3),

$$\varphi_{\text{inc}}^{(1)} = e^{ik_c\left(r_1\cos(\theta_1-\alpha)-\frac{d}{2}\right)} = 1+ik_c\left(r_1\cos(\theta_1-\alpha)-\frac{d}{2}\right)-\frac{k_c^2\left(r_1\cos(\theta_1-\alpha)-\frac{d}{2}\right)^2}{2}+\cdots \tag{5.4}$$

and

$$\varphi_{\text{inc}}^{(2)} = e^{ik_c\left(r_2\cos(\theta_2-\alpha)+\frac{d}{2}\right)} = 1+ik_c\left(r_2\cos(\theta_2-\alpha)+\frac{d}{2}\right)-\frac{k_c^2\left(r_2\cos(\theta_2-\alpha)+\frac{d}{2}\right)^2}{2}+\cdots \tag{5.5}$$

so that equation (4.21) can be written as a power series in ik_c,

$$\varphi_{\text{inc}}^{(1)} = \sum_{n=0}^{\infty}(ik_c)^n\varphi_{\text{inc}_n}^{(1)}, \tag{5.6}$$

where,

$$\begin{aligned}
\varphi_{\text{inc}_0}^{(1)} &= 1, && (5.7)\\
\varphi_{\text{inc}_1}^{(1)} &= r_1\cos\left(\theta_1-\alpha\right)-\frac{d}{2}\\
&= r_1\left(P_1^0(\cos\theta_1)\cos\alpha+P_1^1(\cos\theta_1)\sin\alpha\right)-\frac{d}{2}, && (5.8)\\
\varphi_{\text{inc}_2}^{(1)} &= \frac{r_1^2}{3}\left(2P_2(\cos\left(\theta_1-\alpha\right))+1\right),\\
&= r_1^2\left[\frac{\cos^2\alpha}{3}\left(2P_2^0(\cos\theta_1)+1\right)-\frac{1}{3}\sin(2\alpha)P_2^1(\cos\theta_1)+\frac{\sin^2\alpha}{3}P_2^2(\cos\theta_1)\right]\\
&\quad - r_1 d\left[P_1^0(\cos\theta_1)\cos\alpha+P_1^1(\cos\theta_1)\sin\alpha\right]+\frac{d^2}{4}, && (5.9)
\end{aligned}$$

for sphere 1 and, similarly,

$$\varphi_{\text{inc}}^{(2)} = \sum_{n=0}^{\infty}(ik_c)^n\varphi_{\text{inc}_n}^{(2)}, \tag{5.10}$$

where,

$$
\begin{aligned}
\varphi^{(2)}_{\text{inc}_0} &= 1, && (5.11)\\
\varphi^{(2)}_{\text{inc}_1} &= r_2 \cos(\theta_2 - \alpha)\\
&= r_2 \left(P_1^0(\cos\theta_2)\cos\alpha + P_1^1(\cos\theta_2)\sin\alpha \right), && (5.12)\\
\varphi^{(2)}_{\text{inc}_2} &= \frac{r_2^2}{3}\left(2P_2(\cos(\theta_2-\alpha))+1\right),\\
&= r_2^2\left[\frac{\cos^2\alpha}{3}\left(2P_2^0(\cos\theta_2)+1\right) - \frac{1}{3}\sin(2\alpha)P_2^1(\cos\theta_2) + \frac{\sin^2\alpha}{3}P_2^2(\cos\theta_2)\right]\\
&\quad - r_2 d\left[P_1^0(\cos\theta_2)\cos\alpha + P_1^1(\cos\theta_2)\sin\alpha\right] + \frac{d^2}{4}, && (5.13)
\end{aligned}
$$

for sphere 2. Here $P_n^m(\cos\theta)$ are the associated Legendre polynomials [24].

5.1.3 Translation addition theorem for Helmholtz solutions in a non-axis-symmetric geometry

As with section 4.2.2 we consider a general radiation solution to the Helmholtz equation, however, we drop the condition of axisymmetry so that ψ has the general form,

$$\psi = \sum_{n=0}^{\infty}\sum_{m=-n}^{n} C_{nm} h_n(k_T r) P_n^{|m|}(\cos\theta) e^{im\phi}. \qquad (5.14)$$

Thus for two spheres the solution can be written as

$$
\begin{aligned}
\psi = \sum_{n=0}^{\infty}\sum_{m=-n}^{n} &\left[C_{nm} h_n(k_T r_1) P_n^{|m|}(\cos\theta_1) e^{im\phi_1}\right.\\
&\left. + D_{nm} h_n(k_T r_2) P_n^{|m|}(\cos\theta_2) e^{im\phi_2}\right]. \qquad (5.15)
\end{aligned}
$$

As with the axis-symmetric case, we can apply the translation addition theorem

[46] to translate a solution form the (r_1, θ_1, ϕ_1) frame to the (r_2, θ_2, ϕ_2) frame,

$$h_n(k_T r_1) P_n^{|m|}(\cos\theta_1) e^{im\phi_1} = \sum_{q=|m|}^{\infty} Q_{(mnmq)} j_q(k_T r_2) P_q^{|m|}(\cos\theta_2) e^{im\phi_2}, \tag{5.16}$$

and similarly the converse relationship,

$$h_n(k_T r_2) P_n^{|m|}(\cos\theta_2) e^{im\phi_2} = \sum_{q=|m|}^{\infty} (-1)^{n+q} Q_{(mnmq)} j_q(k_T r_1) P_q^{|m|}(\cos\theta_1) e^{im\phi_1}, \tag{5.17}$$

where

$$Q_{(mnmq)} = i^{q-n}(2n+1)\frac{(n-m)!}{(n+m)!} \sum_{\sigma=|n-q|}^{n+q} i^{\sigma}(-1)^{\sigma} b_{\sigma}^{(nmqm)} \begin{cases} j_\sigma(k_T d), & \text{for } r > d, \\ h_\sigma(k_T d), & \text{for } r < d \end{cases} \tag{5.18}$$

and

$$b_{\sigma}^{(nmqm)} = (-1)^{-m}(2\sigma+1)\sqrt{\frac{(n+|m|)!(q+|m|)!}{(n-|m|)!(q-|m|)!}} \left(\begin{array}{cc:c} n & q & \sigma \\ 0 & 0 & 0 \end{array}\right) \left(\begin{array}{cc:c} n & q & \sigma \\ m & -m & 0 \end{array}\right), \tag{5.19}$$

where the Wigner $3-j$ symbols are defined in appendix A. This now allows equation (5.15) to be expressed in either, the (r_1, θ_1, ϕ_1) frame or the (r_2, θ_2, ϕ_2) frame, as

$$\psi^{(1)} = \sum_{n=0}^{\infty} \sum_{m=-n}^{n} \Bigg[C_{nm} h_n(k_T r_1) P_n^{|m|}(\cos\theta_1) + D_{nm} \sum_{q=|m|}^{\infty} (-1)^{n+q} Q_{(mnmq)} j_q(k_T r_1) P_q^{|m|}(\cos\theta_1) \Bigg] e^{im\phi_1}, \tag{5.20}$$

or as,

$$\psi^{(2)} = \sum_{n=0}^{\infty}\sum_{m=-n}^{n}\Bigg[D_{nm}h_n(k_T r_2)P_n^{|m|}(\cos\theta_2)$$

$$+C_{nm}\sum_{q=|m|}^{\infty}Q_{(mnmq)}j_q(k_T r_2)P_q^{|m|}(\cos\theta_2)\Bigg]e^{im\phi_2}, \tag{5.21}$$

which can now be applied to the boundaries around each particle.

5.1.4 Translation addition theorem for Laplace's equation solutions in a non axis-symmetric geometry

In the long wave asymptotic approximation the external acoustic wave at each order is obtained from the solution of a Poisson equation of the form

$$\nabla^2\varphi = g, \tag{5.22}$$

where the function g is known from lower-order solutions. Thus, as with the in line case, there is a similar problem of translating the general external solution of Laplace's equation in spherical polar coordinates,

$$\varphi = \sum_{n=0}^{\infty}\sum_{m=-n}^{n}A_{nm}\frac{1}{r^{n+1}}P_n^{|m|}(\cos\theta)e^{im\phi}, \tag{5.23}$$

to a solution for two radiating points in the same field, of the form

$$\varphi = \sum_{n=0}^{\infty}\sum_{m=-n}^{n}\left[A_{nm}\frac{1}{r_1^{n+1}}P_n^{|m|}(\cos\theta_1)e^{im\phi_1} + B_{nm}\frac{1}{r_2^{n+1}}P_n^{|m|}(\cos\theta_2)e^{im\phi_2}\right]. \tag{5.24}$$

As with the Helmholtz solution this equation needs to be transformed into two equations, one in the frame of (r_1, θ_1, ϕ_1) and one in the frame of (r_2, θ_2, ϕ_2). This can be done by following the method of Greengard and Rokhlin [47], with rearrangement from Rico *et al.* [65], using the following translations:

$$\frac{P_n^{|m|}(\cos\theta_2)e^{im\phi_2}}{r_2^{n+1}} = \frac{1}{d^{n+1}} \sum_{q=|m|}^{\infty} W_{(mnmq)} \left(\frac{r_1}{d}\right)^q P_q^{|m|}(\cos\theta_1)e^{im\phi_1}, \tag{5.25}$$

and

$$\frac{P_n^{|m|}(\cos\theta_1)e^{im\phi_1}}{r_1^{n+1}} = \left(\frac{(-1)}{d}\right)^{n+1} \sum_{q=|m|}^{\infty} W_{(mnmq)} \left(\frac{r_2}{d}\right)^q P_q^{|m|}(\cos\theta_2)e^{im\phi_2}, \tag{5.26}$$

where the Wigner coefficients $W_{(mnmq)}$ are given by

$$W_{(mnmq)} = (-1)^{n+m}\frac{(n+q)!}{(n-|m|)!(q+|m|)!}. \tag{5.27}$$

This allows equation (5.24) to be expressed in either the frame of (r_1, θ_1, ϕ_1) or the frame of (r_2, θ_2, ϕ_2),

$$\begin{aligned}\varphi_1 = \sum_{n=0}^{\infty}\sum_{m=-n}^{n} &\left[\frac{A_{nm}}{r_1^{n+1}}P_n^{|m|}(\cos\theta_1)\right.\\ &\left.+\frac{B_{nm}}{d^{n+1}}\sum_{q=|m|}^{\infty} W_{(mnmq)}\left(\frac{r_1}{d}\right)^q P_q^{|m|}(\cos\theta_1)\right]e^{im\phi_1},\end{aligned} \tag{5.28}$$

and

$$\begin{aligned}\varphi_2 = \sum_{n=0}^{\infty}\sum_{m=-n}^{n} &\left[\frac{B_{nm}}{r_2^{n+1}}P_n^{|m|}(\cos\theta_2)\right.\\ &\left.+\frac{A_{nm}(-1)^{n+1}}{d^{n+1}}\sum_{q=|m|}^{\infty} W_{(mnmq)}\left(\frac{r_2}{d}\right)^q P_q^{|m|}(\cos\theta_2)\right]e^{im\phi_2},\end{aligned} \tag{5.29}$$

from which we can now apply the boundary conditions on both spheres.

5.2 Thermoacoustic scattering by two spheres

We can use the weak thermal scattering approximation from section 4.2 to construct the solution for the acoustic and thermal fields as Poincaré expansions of the form

$$\varphi^{(1)} = e^{ik(r_1-a)} \sum_{n=0}^{\infty} (ik_c)^n \tilde{\varphi}_n^{(1)}, \tag{5.30}$$

and

$$\psi^{(1)} = \sum_{n=0}^{\infty} (ik_c)^n \psi_n^{(1)}, \tag{5.31}$$

where $\tilde{\varphi}_n^{(1)}$ and $\psi_n^{(1)}$ are solutions of the exterior Poisson and Helmholtz equations together with corresponding expansions for the interior fields. The general form for the solutions at each order are obtained from equations (5.20), (5.21) and (5.23)–(5.29) as

$$\begin{aligned}\tilde{\varphi}_n^{(1)} = &\sum_{q=0}^{\infty} \sum_{p=-q}^{q} \Bigg[A_{nqp} \left(\frac{a}{r_1}\right)^{q+1} P_q^{|p|}(\cos\theta_1) \\ &+B_{nqp} \left(\frac{b}{d}\right)^{q+1} \sum_{s=|p|}^{\infty} W_{(pqps)} \left(\frac{r_1}{d}\right)^{s} P_s^{|p|}(\cos\theta_1) \Bigg] e^{ip\phi} + I_n^{(1)}(r_1,\theta_1,\phi),\end{aligned} \tag{5.32}$$

$$\begin{aligned}\tilde{\varphi}_n^{(2)} = &\sum_{q=0}^{\infty} \sum_{p=-q}^{q} \Bigg[B_{nqp} \left(\frac{b}{r_2}\right)^{q+1} P_q^{|p|}(\cos\theta_2) \\ &+A_{nqp}(-1)^{q+1} \left(\frac{a}{d}\right)^{q+1} \sum_{s=|p|}^{\infty} W_{(pqps)} \left(\frac{r_2}{d}\right)^{s} P_s^{|p|}(\cos\theta_2) \Bigg] e^{ip\phi} + I_n^{(2)}(r_2,\theta_2,\phi),\end{aligned} \tag{5.33}$$

$$\varphi_n^{\prime(1)} = \sum_{q=0}^{\infty} \sum_{p=-q}^{q} a_{nqp} \left(\frac{r_1}{a}\right)^{q} P_q^{|p|}(\cos\theta_1) e^{ip\phi} + I_n^{\prime(1)}(r_1,\theta_1,\phi), \tag{5.34}$$

$$\varphi_n^{\prime(2)} = \sum_{q=0}^{\infty} \sum_{p=-q}^{q} b_{nqp} \left(\frac{r_2}{b}\right)^{q} P_q^{|p|}(\cos\theta_2) e^{ip\phi} + I_n^{\prime(2)}(r_2,\theta_2,\phi), \tag{5.35}$$

$$\psi_n^{(1)} = \sum_{q=0}^{\infty}\sum_{p=-q}^{q}\Bigg[C_{nqp}h_q(k_Tr_1)P_q^{|p|}(\cos\theta_1)$$

$$+D_{nqp}\sum_{s=|p|}^{\infty}(-1)^{q+s}Q_{(pqps)}j_s(k_Tr_1)P_s^{|p|}(\cos\theta_1)\Bigg]e^{im\phi}, \tag{5.36}$$

$$\psi_n^{(2)} = \sum_{q=0}^{\infty}\sum_{p=-q}^{q}\Bigg[D_{nqp}h_q(k_Tr_2)P_q^{|p|}(\cos\theta_2)$$

$$+C_{nqp}\sum_{s=|p|}^{\infty}Q_{(pqps)}j_s(k_Tr_2)P_s^{|p|}(\cos\theta_2)\Bigg]e^{im\phi}, \tag{5.37}$$

$$\psi_n'^{(1)} = \sum_{q=0}^{\infty}\sum_{p=-q}^{q}c_{nqp}j_q(k_T'r_1)P_q^{|p|}(\cos\theta_1)e^{ip\phi}, \tag{5.38}$$

$$\psi_n'^{(2)} = \sum_{q=0}^{\infty}\sum_{p=-q}^{q}d_{nqp}j_q(k_T'r_2)P_q^{|p|}(\cos\theta_2)e^{ip\phi}, \tag{5.39}$$

where I_n are the particular solutions of the inhomogeneous terms in the Poisson equations. The unknown coefficients $A_{nqp}, B_{nqp}, C_{nqp}, D_{nqp}, a_{nqp}, b_{nqp}, c_{nqp}$ and d_{nqp} are determined by applying the four pairs of boundary conditions equations (4.29)–(4.36).

5.2.1 Order one solutions

As with the single particle case, and the axis-symmetric solution case the solution at order one is simply,

$$a_{000} = b_{000} = \frac{1}{\hat{\rho}}. \tag{5.40}$$

with all other coefficients being equal to zero.

5.2.2 Order ik_c solutions

At order ik_c, as with the axis-symmetric case, the incident field has a constant term $-\frac{d}{2}$, that does not produce any external field, thus the solution can be calculated without the constant and the contribution simply added to the interior solution. The thermal field is zero at this order, while the acoustic field terms are solutions of the Laplace equations (4.75)–(4.78) together with boundary conditions (4.29), (4.30), (4.33) and (4.34). Substituting the solutions in the form of equations (5.32)–(5.35) for $n = 1$ we obtain the system of equations,

$$\sum_{s=|p|}^{\infty} \left[\left(A_{1sp} - \hat{\rho} a_{1sp}\right) \delta_{qs} + B_{1sp} \left(\frac{b}{d}\right)^{s+1} \left(\frac{a}{d}\right)^{q} W_{(pspq)} \right] = a \left(\delta_{q1}\delta_{|p|0} \cos\alpha - \delta_{q1}\delta_{|p|1} \sin\alpha\right), \tag{5.41}$$

$$\sum_{s=|p|}^{\infty} \left[\left(B_{1sp} - \hat{\rho} b_{1sp}\right) \delta_{qs} + A_{1sp}(-1)^{s+1} \left(\frac{a}{d}\right)^{s+1} \left(\frac{b}{d}\right)^{q} W_{(pspq)} \right] = b \left(\delta_{q1}\delta_{|p|0} \cos\alpha - \delta_{q1}\delta_{|p|1} \sin\alpha\right), \tag{5.42}$$

$$\sum_{s=|p|}^{\infty} \left[\left(-(s+1)A_{1sp} - s a_{1sp}\right) \delta_{qs} + B_{1sp} q \left(\frac{b}{d}\right)^{s+1} \left(\frac{a}{d}\right)^{q} W_{(pspq)} \right] = a \left(\delta_{q1}\delta_{|p|0} \cos\alpha - \delta_{q1}\delta_{|p|1} \sin\alpha\right), \tag{5.43}$$

and

$$\sum_{s=|p|}^{\infty} \left[\left(-(s+1)B_{1sp} - s b_{1sp}\right) \delta_{qs} + A_{1sp}(-1)^{s+1} q \left(\frac{a}{d}\right)^{s+1} \left(\frac{b}{d}\right)^{q} W_{(pspq)} \right] = b \left(\delta_{q1}\delta_{|p|0} \cos\alpha - \delta_{q1}\delta_{|p|1} \sin\alpha\right). \tag{5.44}$$

Note that since the only inhomogeneous terms are for $p = 0$ and $p = \pm 1$ only the $p = 0$ and $p = \pm 1$ coefficients are non-zero and in particular, when $\alpha = 0$, we recover equations (4.79)–(4.82).

While in principle this is an infinite system, higher order terms decay rapidly, as shown in figure 5.2, so the system can be truncated at order $q_{\max}$, resulting in two independent sets of $4q_{\max}^2$ matrix problems.

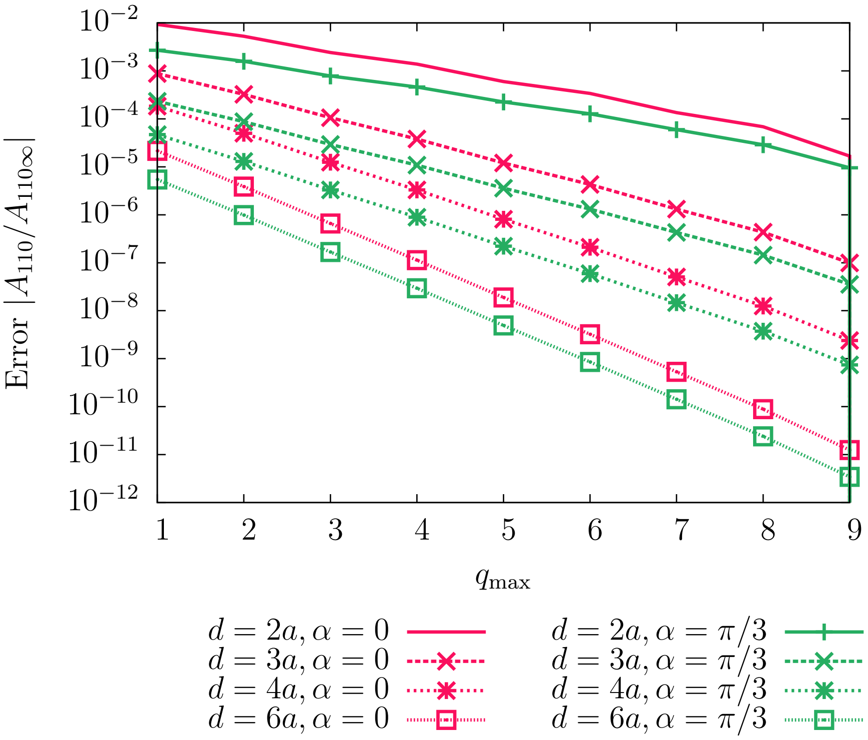

Figure 5.2

Error of $A_{110}/A_{11\infty}$ *for the case* $a = b$ *for different values of* q_{max} *and* α*. It can be seen that the coefficients error reduces exponentially with* q_{max}*. As d is increased, the rate of convergence increases. However, the value of* α *has little impact on the rate of convergence.*

As with the axis-symmetric case, it can be shown that in the limit $d \to \infty$ the coupling tends to zero and we recover,

$$A_{110} = \left(\frac{\hat{\rho}-1}{2\hat{\rho}+1}\right) a\cos\alpha, \tag{5.45}$$

$$A_{111} = \left(\frac{\hat{\rho}-1}{2\hat{\rho}+1}\right) a\sin\alpha, \tag{5.46}$$

$$B_{110} = \left(\frac{\hat{\rho}-1}{2\hat{\rho}+1}\right) b\cos\alpha, \tag{5.47}$$

$$B_{111} = \left(\frac{\hat{\rho}-1}{2\hat{\rho}+1}\right) b\sin\alpha, \tag{5.48}$$

$$a_{110} = \frac{3a}{2\hat{\rho}+1} a\cos\alpha, \tag{5.49}$$

$$a_{111} = \frac{3a}{2\hat{\rho}+1} a\sin\alpha, \tag{5.50}$$

$$b_{110} = \frac{3a}{2\hat{\rho}+1} b\cos\alpha, \tag{5.51}$$

and

$$b_{111} = \frac{3a}{2\hat{\rho}+1} b\sin\alpha. \tag{5.52}$$

These are the same as the single sphere solutions presented by Harlen *et al.* [27].

As with the axis-symmetric case, the solution converges towards the single particle solution as $d \to \infty$ for any α. However, we also need to consider the rotation of the incident wave, in figure 5.3 we see how the behaviour of A_{11p}, defined as $\sqrt{A_{110}^2 + 2A_{111}^2}$, changes as the incident angle changes for different values of d. It is clear to see that the most difference from the single particle solution occurs when $\alpha = 0$ or $\pm\pi$, the in-line case, while there is no effect of the interaction where the direction of the wave is perpendicular. At this order the interaction is driven by the gradient in pressure, so that when the particles are aligned perpendicular to the field they experience the same pressure and so do not interact.

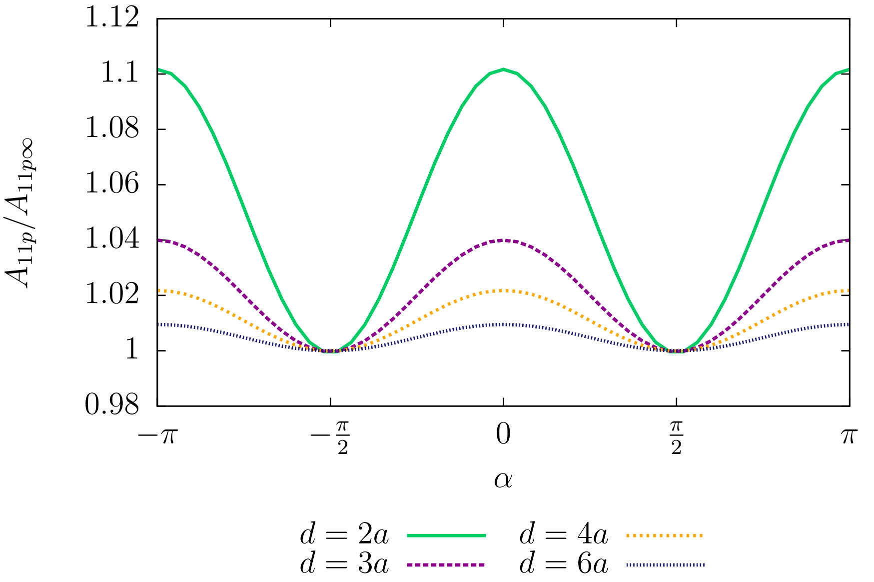

Figure 5.3

The behaviour of A_{11p} as the incident angle changes for different values of d.

We can see how A_{111} behaves in figure 5.4 as $d/a \to \infty$ for different α, as the solution converges to the single particle solution.

5.2.3 Order $(ik_c)^2$ solutions

Order $(ik_c)^2$ is the leading order at which the thermal terms come into effect, so boundary conditions from equations (4.31), (4.32), (4.35) and (4.36) are also considered. The thermal boundary conditions lead to the equations

$$\sum_{s=|p|}^{\infty} \left[\left(C_{2sp} h_s(k_T a) - \hat{\Gamma} c_{2sp} j_s(k_T' a) \right) \delta_{qs} + D_{2sp} (-1)^{q+s} Q_{(pspq)} j_q(k_T a) \right] P_q^{|p|}(\cos\theta_1)$$
$$= \left[\frac{\hat{\Gamma} G_c'}{\hat{\rho}} - G_c \right] \delta_{q0} \delta_{p0}, \tag{5.53}$$

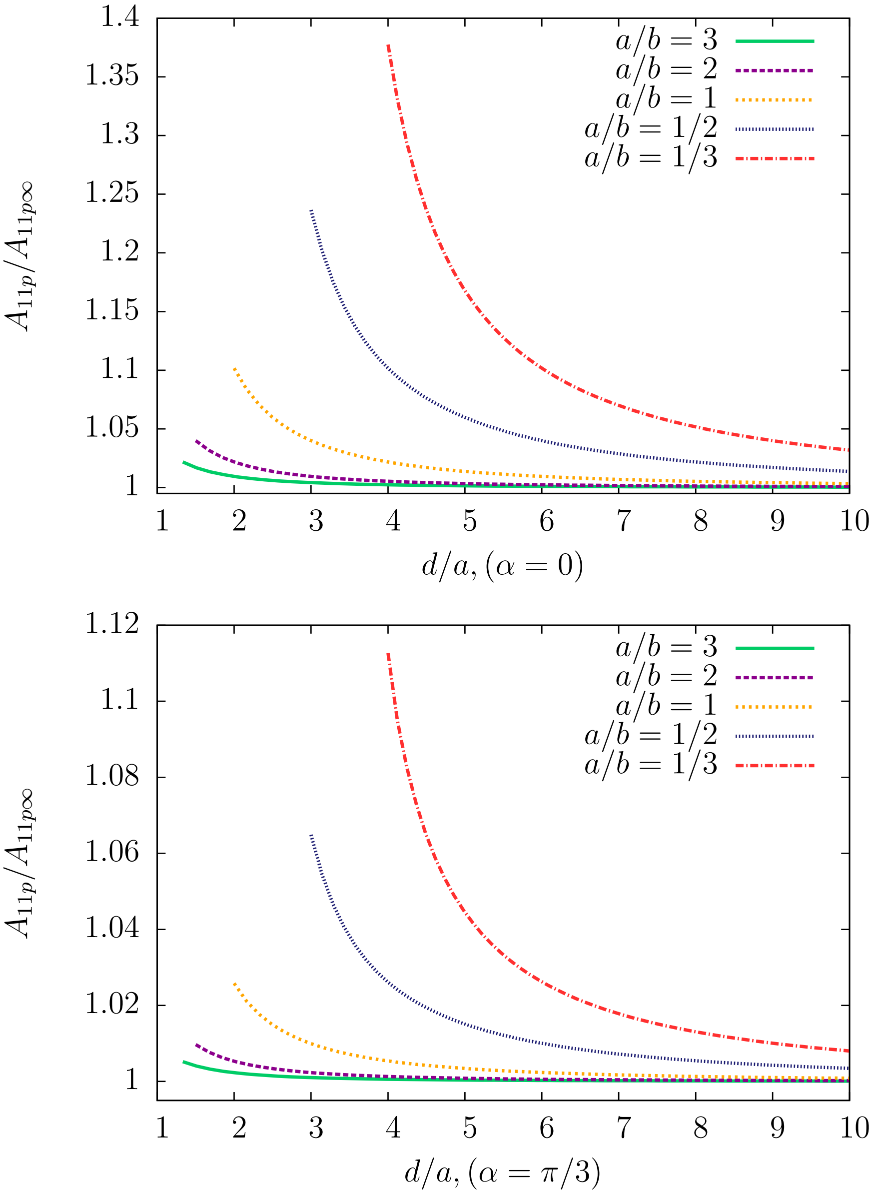

Figure 5.4

Behaviour of A_{11p} for the single sphere solution compared to the two sphere arbitrary angle solution for varying d and α.

$$\sum_{s=|p|}^{\infty}\left[\Big(D_{2sp}h_s(k_Tb)-\hat{\Gamma}d_{2sp}j_s(k_T'b)\Big)\,\delta_{qs}+C_{2sp}Q_{(pspq)}j_q(k_Tb)\right]P_q^{|p|}(\cos\theta_1)$$
$$=\left[\frac{\hat{\Gamma}G_c'}{\hat{\rho}}-G_c\right]\delta_{q0}\delta_{p0}, \tag{5.54}$$

$$\sum_{s=|p|}^{\infty}\Big[\Big(C_{2sp}k_Tah_q'(k_Ta)-c_{2sp}\hat{\Gamma}\hat{\tau}k_T'aj_s'(k_T'a)\Big)\,\delta_{qs}$$
$$+D_{2sp}(-1)^{q+s}Q_{(pspq)}k_Taj_q'(k_Ta)\Big]=0, \tag{5.55}$$

and

$$\sum_{s=|p|}^{\infty}\Big[\Big(D_{2sp}k_Tbh_s'(k_Tb)-d_{2sp}\hat{\Gamma}\hat{\tau}k_T'bj_s'(k_T'b)\Big)\,\delta_{qs}$$
$$+C_{2sp}Q_{(pspq)}k_Tbj_q'(k_Tb)\Big]=0 \tag{5.56}$$

for the thermal coefficients. Again this system can be truncated at order $q_{\max}$.

An immediate observation is that the $p=0$ equations are the same as equations (4.88)–(4.91). Furthermore, since the equations for different p are uncoupled it also follows that the coefficients for $p\neq 0$ are all zero. Thus at this order the $C_{2q0}, D_{2q0}, c_{2q0}$ and d_{2q0} coefficients are identical to the coefficients of the in-line case and so there is no α dependence of the solution and we can use the calculation from chapter 4. In figure 5.5 we see how the solution tends to the single particle solution as $d\to\infty$ for any arbitrary angle.

The physics behind this is that the leading order contribution to the thermal field arises purely from the differential heating of the two phases under a homogeneous compression and so does not depend on the direction of the incident wave.

As with the in-line case, this can be solved as a separate matrix problem, but it is more convenient for this to be part of a larger linear system involving the acoustic boundary conditions at this order also.

At this order the acoustic field equations are inhomogeneous, as given by equations (4.92)–(4.95) and applying the boundary conditions (4.29), (4.30) and (4.33), (4.34) leads to the equations,

$$\begin{aligned}
&\sum_{s=|p|}^{\infty}\Bigg[(A_{2sp}-\hat{\rho}a_{2sp})\delta_{qs}+(C_{2s0}h_s(k_Ta)-\hat{\Gamma}c_{2s0}j_s(k_T'a))\delta_{qs}\delta_{0p}\\
&\quad+B_{2sp}\left(\frac{b}{d}\right)^{s+1}\left(\frac{a}{d}\right)^{q}W_{(pspq)}+D_{2s0}(-1)^{s+q}Q_{(0s0q)}j_q(k_Ta)\delta_{0p}\Bigg]\\
&=-\frac{\cos^2\alpha}{3}\left(2\delta_{q2}\delta_{p0}+\delta_{q0}\delta_{p0}\right)+\frac{1}{3}\sin 2\alpha\delta_{q2}\delta_{p1}-\frac{\sin^2\alpha}{3}\delta_{q2}\delta_{p2}+\hat{c}\delta_{q0}\delta_{p0}\\
&\quad+\sum_{s=|p|}^{\infty}\left[\frac{2}{s+1}A_{1sp}\delta_{qs}-\frac{2}{q+2}B_{1sp}\left(\frac{a}{d}\right)^{q}\left(\frac{b}{d}\right)^{s+1}W_{(pspq)}\right],
\end{aligned}\tag{5.57}$$

$$\begin{aligned}
&\sum_{s=|p|}^{\infty}\Bigg[(B_{2sp}-\hat{\rho}b_{2sp})\delta_{qs}+(D_{2s0}h_s(k_Tb)-\hat{\Gamma}d_{2s0}j_s(k_T'b))\delta_{qs}\delta_{0p}\\
&\quad+(-1)^{s+1}A_{2sp}\left(\frac{a}{d}\right)^{s+1}\left(\frac{b}{d}\right)^{q}W_{(pspq)}+C_{2s0}(-1)^{s+q}Q_{(0s0q)}j_q(k_Tb)\delta_{0p}\Bigg]\\
&=-\frac{\cos^2\alpha}{3}\left(2\delta_{q2}\delta_{p0}+\delta_{q0}\delta_{p0}\right)+\frac{1}{3}\sin 2\alpha\delta_{q2}\delta_{p1}-\frac{\sin^2\alpha}{3}\delta_{q2}\delta_{p2}+\hat{c}\delta_{q0}\delta_{p0}\\
&\quad+\sum_{s=|p|}^{\infty}\left[\frac{2}{s+1}B_{1sp}\delta_{qs}-\frac{2}{q+2}(-1)^{s+1}A_{1sp}\left(\frac{b}{d}\right)^{q}\left(\frac{a}{d}\right)^{s+1}W_{(pspq)}\right],
\end{aligned}\tag{5.58}$$

$$\begin{aligned}
&\sum_{s=|p|}^{\infty}\Bigg[(-(s+1)A_{2sp}-\hat{\rho}sa_{2sp})\delta_{qs}+(C_{2s0}k_Tah_s'(k_Ta)-\hat{\Gamma}c_{2s0}k_T'aj_s'(k_T'a))\delta_{qs}\delta_{0p}\\
&\quad+qB_{2sp}\left(\frac{b}{d}\right)^{s+1}\left(\frac{a}{d}\right)^{q}W_{(pspq)}+D_{2s0}(-1)^{s+q}Q_{(0s0q)}k_Taj_q'(k_Ta)\delta_{0p}\Bigg]\\
&=-\frac{2\cos^2\alpha}{3}\left(2\delta_{q2}\delta_{p0}+\delta_{q0}\delta_{p0}\right)+\frac{2}{3}\sin 2\alpha\delta_{q2}\delta_{p1}-\frac{2\sin^2\alpha}{3}\delta_{q2}\delta_{p2}\\
&\quad+\sum_{s=|p|}^{\infty}\left[-A_{1sp}\delta_{qs}-B_{1sp}\left(\frac{a}{d}\right)^{q}\left(\frac{b}{d}\right)^{s+1}W_{(pspq)}\right],
\end{aligned}\tag{5.59}$$

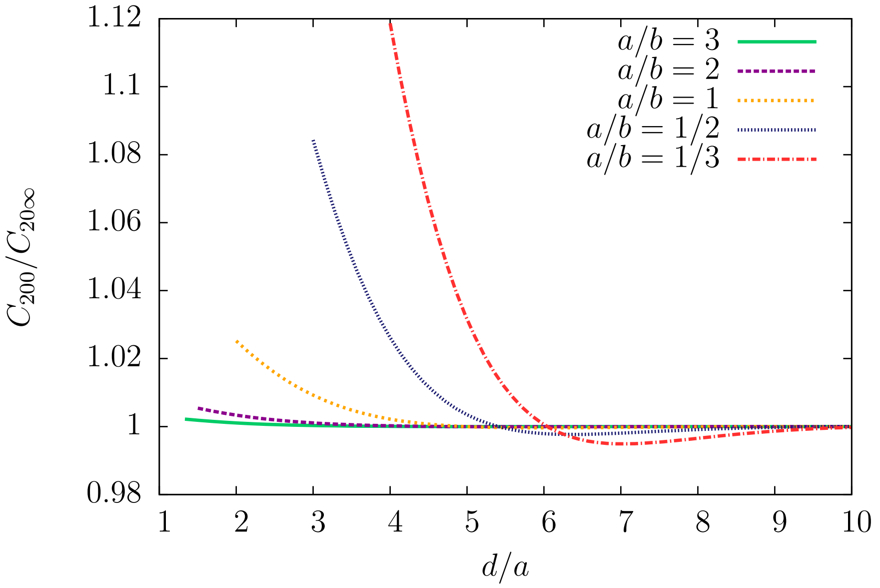

Figure 5.5

The behaviour of $|C_{200}/C_{20\infty}|$ *with increasing separation for* $a/b = 1/3, 1/2, 1, 2, 3$ *for silicone in water and* $|k_T a|$ *= 1.*

$$\sum_{s=|p|}^{\infty}\Bigg[(-(s+1)B_{2sp}-\hat{\rho}sb_{2sp})\delta_{qs}+(D_{2s0}k_Tbh'_s(k_Tb)-\hat{\Gamma}d_{2s0}k'_Tbj'_s(k'_Tb))\delta_{qs}\delta_{0p}$$
$$+(-1)^{s+1}qA_{2sp}\left(\frac{a}{d}\right)^{s+1}\left(\frac{b}{d}\right)^{q}W_{(pspq)}+C_{2s0}(-1)^{s+q}Q_{(0s0q)}k_Tbj'_q(k_Tb)\delta_{0p}\Bigg]$$
$$=-\frac{2\cos^2\alpha}{3}(2\delta_{q2}\delta_{p0}+\delta_{q0}\delta_{p0})+\frac{2}{3}\sin 2\alpha\delta_{q2}\delta_{p1}-\frac{2\sin^2\alpha}{3}\delta_{q2}\delta_{p2}$$
$$+\sum_{s=|p|}^{\infty}\left[-B_{1sp}\delta_{qs}-(-1)^{s+1}A_{1sp}\left(\frac{b}{d}\right)^{q}\left(\frac{a}{d}\right)^{s+1}W_{(pspq)}\right]. \qquad (5.60)$$

Note, only the $p = 0$ terms for the thermal coefficients $C_{2sp}, D_{2sp}, c_{2sp}$ and d_{2sp}, are considered and so the $p \neq 0$ terms are zero. Again, the contribution in the incident field brought about by the shift in the origin has been excluded. Solving these terms, as with the in-line gives us solutions that reduce to the single particle solution as $d \to \infty$.

The acoustic coefficients, however, do depend on the angle of the incident wave, however the systems of equations for each of p are uncoupled and we have non-zero solutions for $|p| \leq 2$. The solutions for A_{200} are shown in figures 5.6 and 5.7. The largest difference between the single particle solution and the two particle solution coefficients is when the particles are in-line, with the least difference when the particles are perpendicular to the incident wave.

In figure 5.8 we show how many terms of $q_{\max}$ are required to generate a solution with an acceptable amount of error. When the particles are touching we see that the solution required 8 terms to reduce the error to $10^{-6}\%$, where at larger distances the convergence is more rapid.

It is also possible to see where these effects are most prominent by observing how these coefficients behave across a range of $k_T a$, as seen in figure 5.9.

5.3 Far field

Using the coefficients generated in section 5.2, the far field can be calculated. As with the in-line case, provided $k_c a \ll 1$, we can express the far field radiation from both spheres as in equation (4.110) However, what we are most interested in is the change in the far field due to additional scattering due to the second sphere, thus we calculate in equation (4.113) $f^{\text{excess}}(\theta)$, which shows us the contribution that the multiple thermoacoustic scattering has on the far field. It can be seen in figure 5.10 that as expected the closer the particles are to each other the larger the change to the far field scatter, however, it can also be seen that the change in incident angle only appears to change the magnitude of the far field scatter and not frequency dependence. The frequency dependence arises from the thermal interactions which at this order do not depend on the angle of the incident wave. The effect the distance of the particles from each other has on the far field is the same as for the two particles in line case. This suggests when the particles are touching that the far field behaves like a single particle in the region of $|k_T a| \sim 1$. However, as the particles move further apart, the thermal overlap still occurs, creating an increase in the far field around $|k_T a| \sim 2$. This peak reduces as the particles are moved further apart.

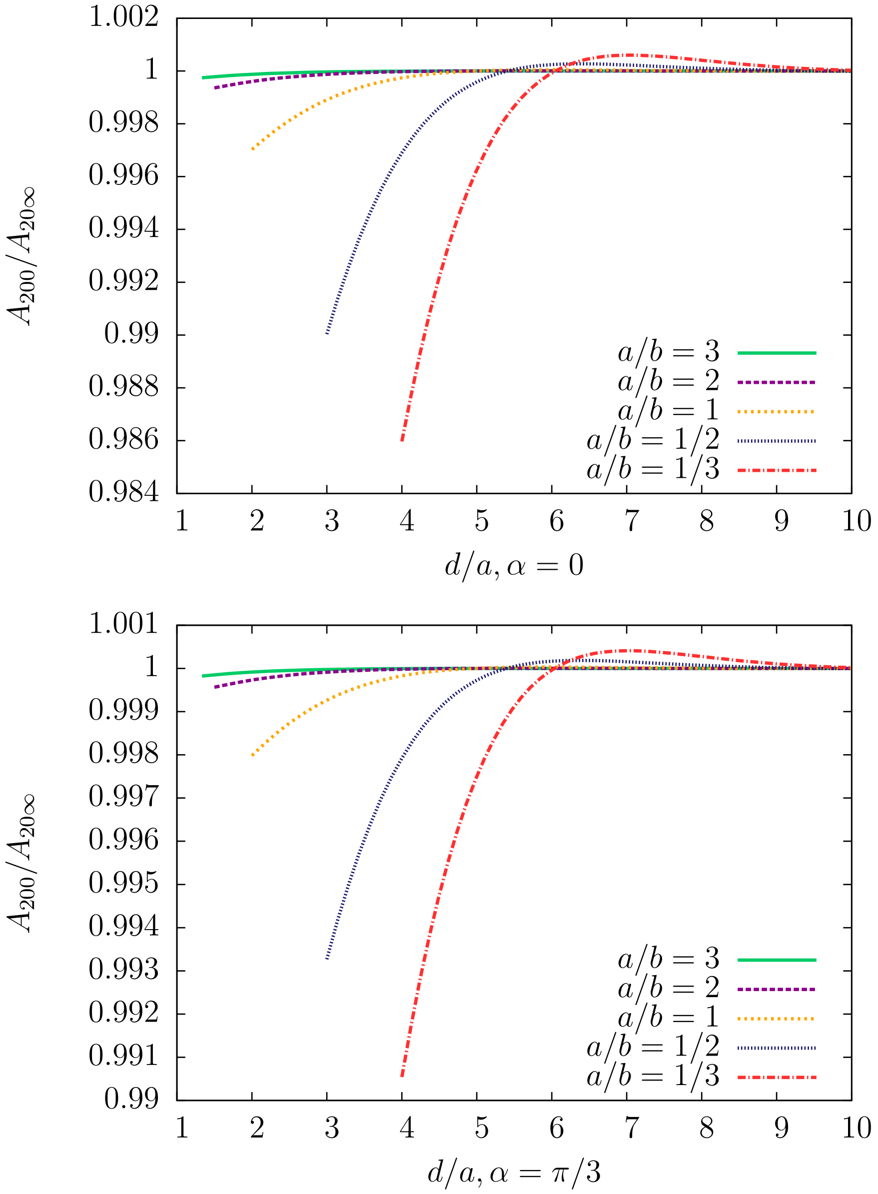

Figure 5.6

The behaviour of $A_{200}/A_{20\infty}$ for different incident wave angles for different values of d for silicone in water and $|k_T a|$ = 1

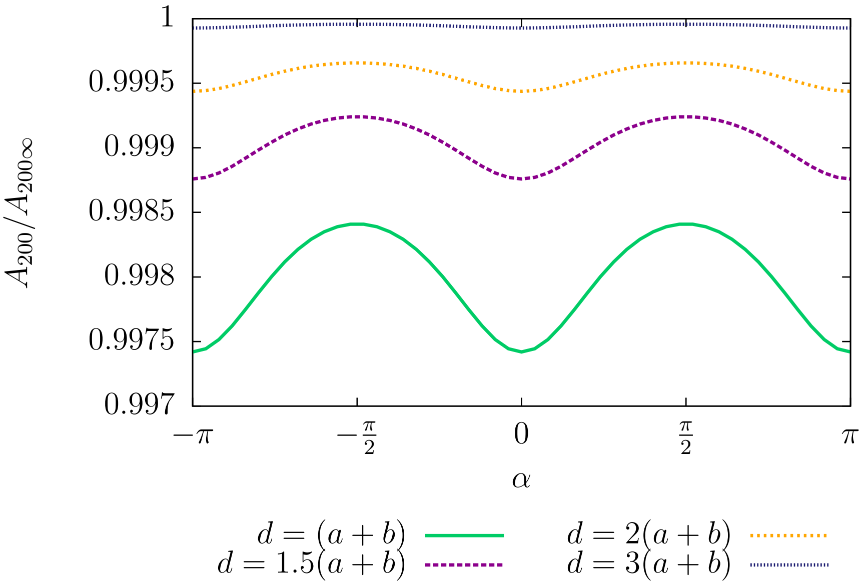

Figure 5.7

The behaviour of $A_{200}/A_{20\infty}$ *for different* d *as the incident angle* α *is rotated for silicone in water.*

5.4 Close field

We can also use the solutions in the previous sections to provide an insight as to how the acoustic and thermal fields behave when two particles are close together for particles of the same size, and when they have different sizes. These plots are the maximum pressure and temperature excursion arising from the sinusoidal pressure field at the second order. Each of figures 5.11–5.20 has been rotated so that the incident wave travels along the horizontal axis.

In figure 5.11, the particles are touching, so they behave as a single particle larger than a particle of that size on its own. This agrees with, figure 5.10, as the drop in the far field at $|k_T a| = 1$ suggests that the attenuation prediction will provide a curve one would expect from a larger particle size. The change of incident wave angle is noticed most internally. This behaviour is again seen in figure 5.16, as the thermal field is almost spherical just a particle distance away.

In figure 5.12 the particles are further apart, the pressure around both spheres still behaves as if it were one larger sphere. Being further part and still having

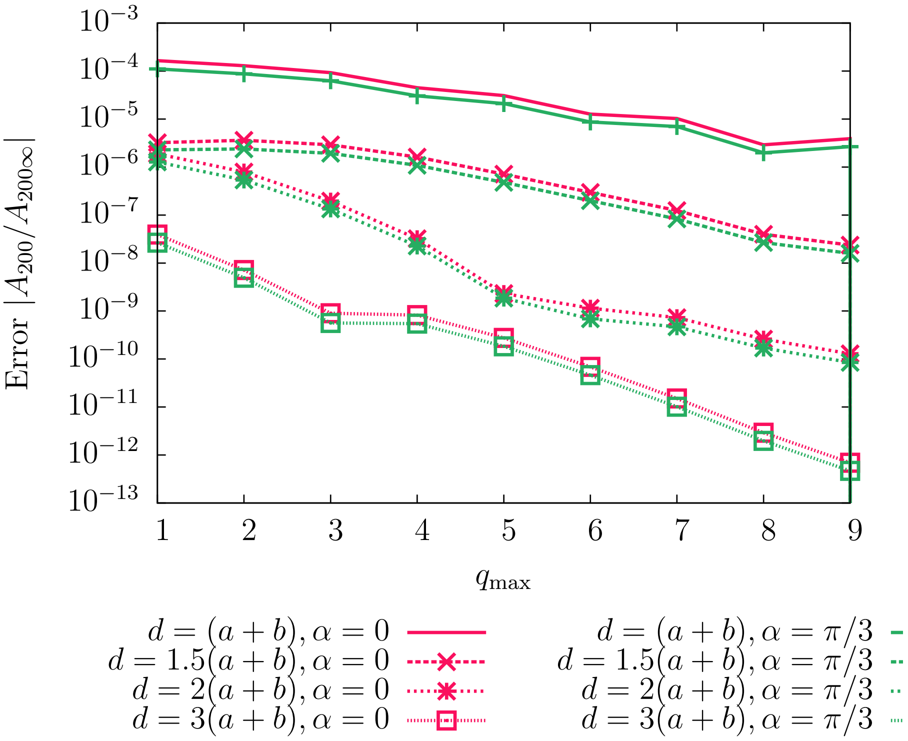

Figure 5.8

Error of $A_{200}/A_{200\infty}$ for different values of q_{max} and α with $a = b$. It can be seen after a couple of terms that the solution converges rapidly. As d is increased the solution converges even more rapidly. When the incident wave angle changes there is a slight increase in convergence, but it is not significant.

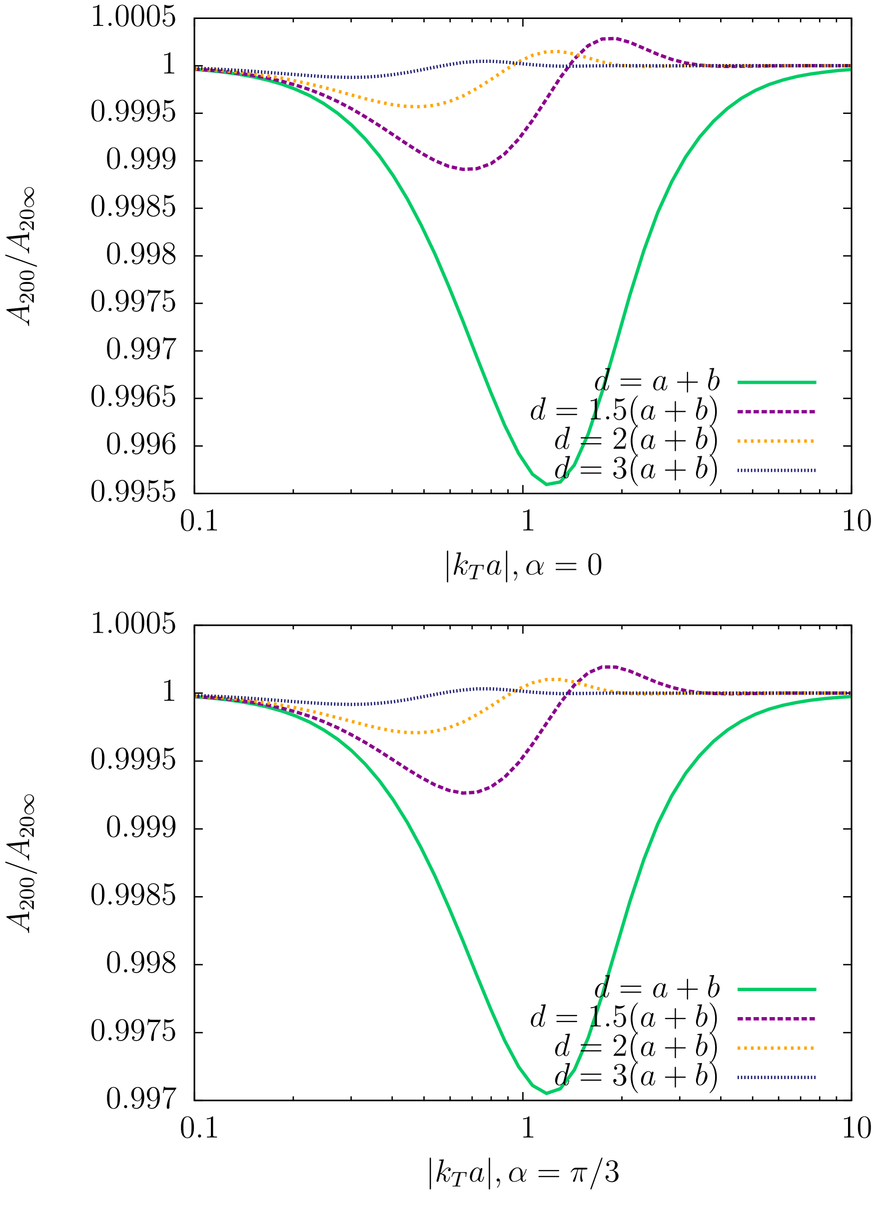

Figure 5.9

A comparison of the behaviour of $|A_{200}/A_{200\infty}|$ *over* $k_T a$ *for different values of* d *and* $\alpha = 0, \pi/3$ *for* $a = b$.

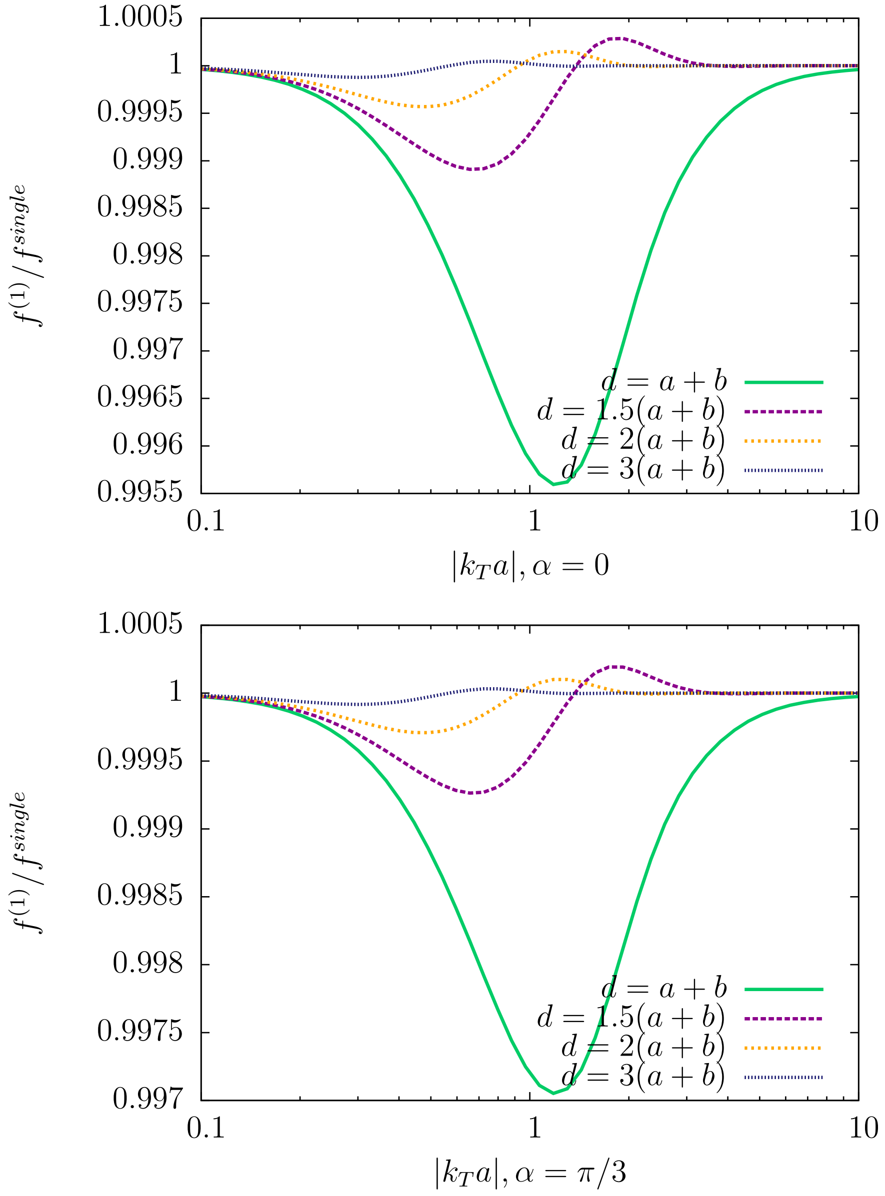

Figure 5.10

Excess far fields as a result of multiple thermoacoustic scattering for different d *and* $\alpha = 0, \pi/3$.

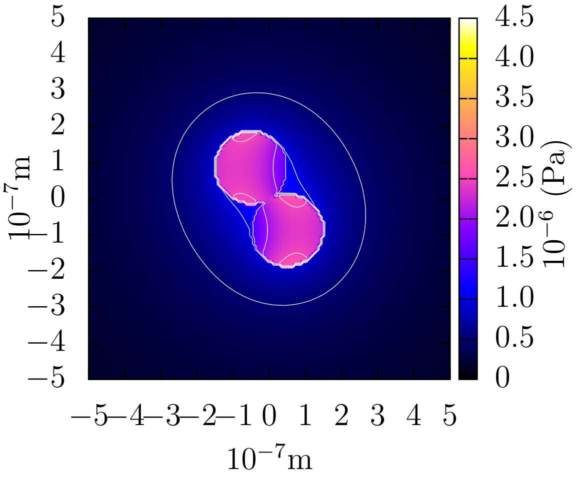

Figure 5.11

Close field plot of pressure for $a/b = 1$ and $d = a + b$, $|k_T a| = 1$ and $\alpha = \pi/3$. The plot has been rotated so the incident wave travels along the horizontal direction.

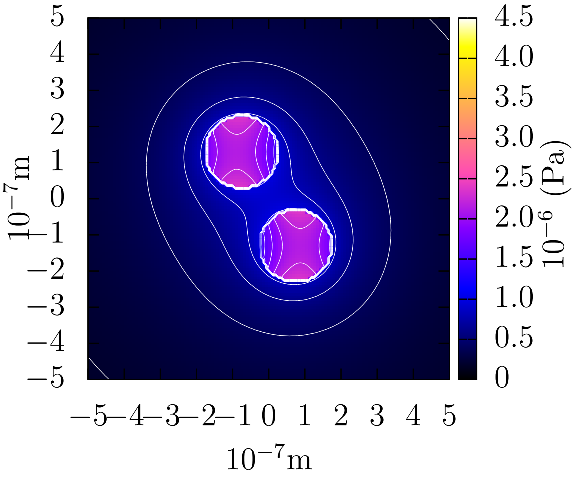

Figure 5.12

Close field plot of pressure for $a/b = 1$ and $d = 2a + b$, $|k_T a| = 1$ and $\alpha = \pi/3$. The plot has been rotated so the incident wave travels along the horizontal direction.

their thermal field over lapping creates the impression of an even larger sphere than in figure 5.11. This behaviour is reflected also in figure 5.12, suggesting even though they are further apart, multiple scattering still has a large effect.

When increasing the size of one of the particles figures 5.13 and 5.14 and their temperature counterparts figures 5.13 and 5.14, the effects of the smaller particle are lost within the effect of the bigger particles. However, when the distance is increased between the smaller particle and the bigger particle, as in figures 5.15 and 5.20, the thermal field of the smaller particle has an influence on the bigger particle, as smaller particle have larger thermal fields.

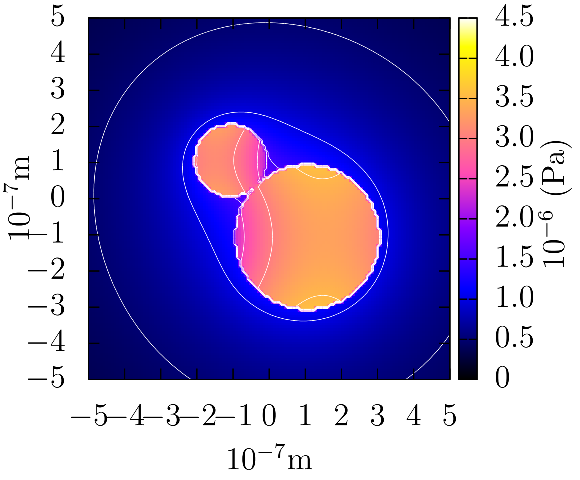

Figure 5.13

Close field plot of pressure for $a/b = 1/2$ *and* $d = a + b$, $|k_T a| = 1$ *and* $\alpha = \pi/4$. *The plot has been rotated so the incident wave travels along the horizontal direction.*

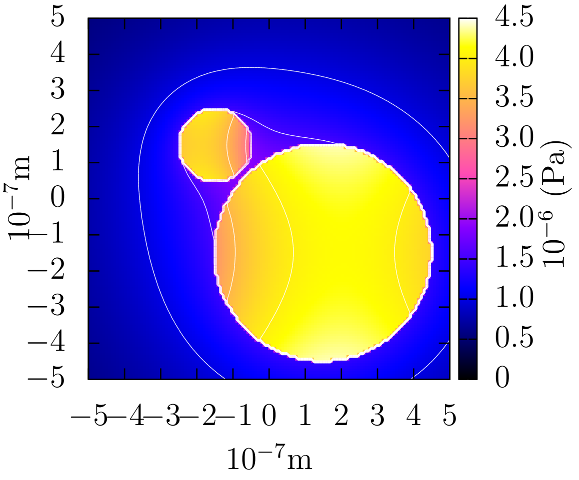

Figure 5.14

Close field plot of pressure for $a/b = 1/3$ *and* $d = 1.2a + b$, $|k_T a| = 1$ *and* $\alpha = \pi/4$. *The plot has been rotated so the incident wave travels along the horizontal direction.*

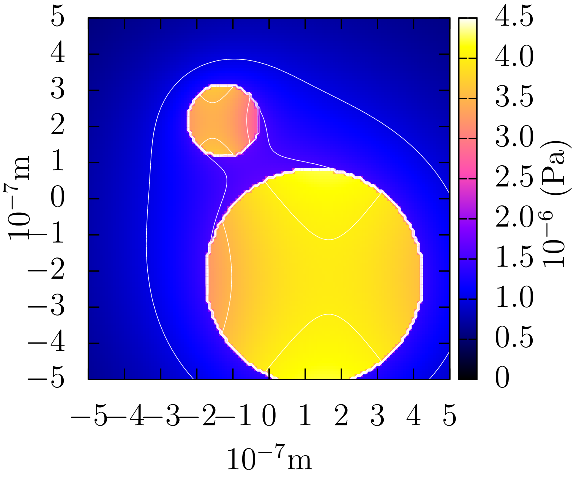

Figure 5.15

Close field plot of pressure for $a/b = 1/3$ and $d = 2a + b$, $|k_T a| = 1$ and $\alpha = \pi/3$. The plot has been rotated so the incident wave travels along the horizontal direction.

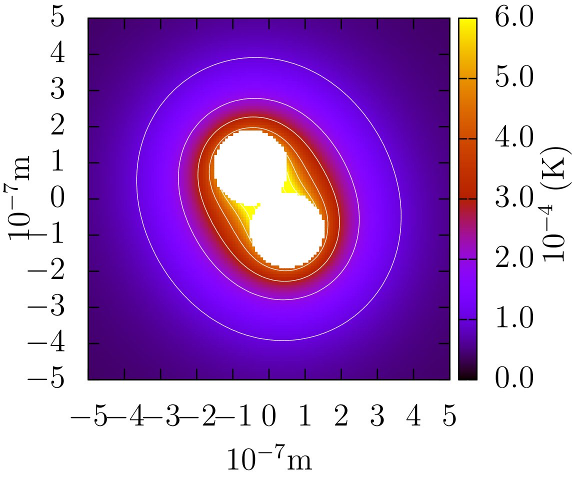

Figure 5.16

Close field plot of temperature for $a/b = 1$ and $d = a + b$, $|k_T a| = 1$ and $\alpha = \pi/3$. The plot has been rotated so the incident wave travels along the horizontal direction.

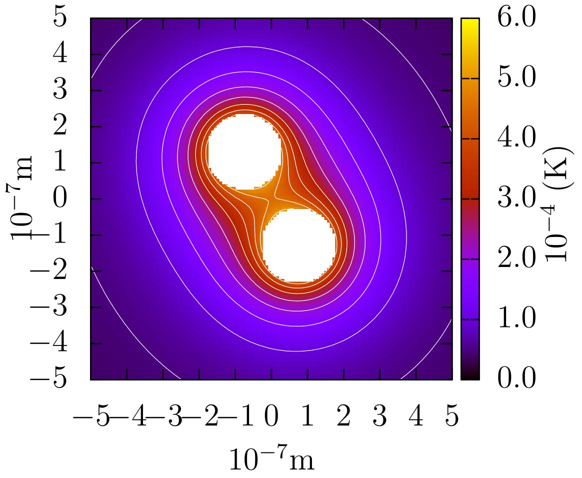

Figure 5.17

Close field plot of temperature for $a/b = 1$ and $d = 2a + b$, $|k_T a| = 1$ and $\alpha = \pi/3$. The plot has been rotated so the incident wave travels along the horizontal direction.

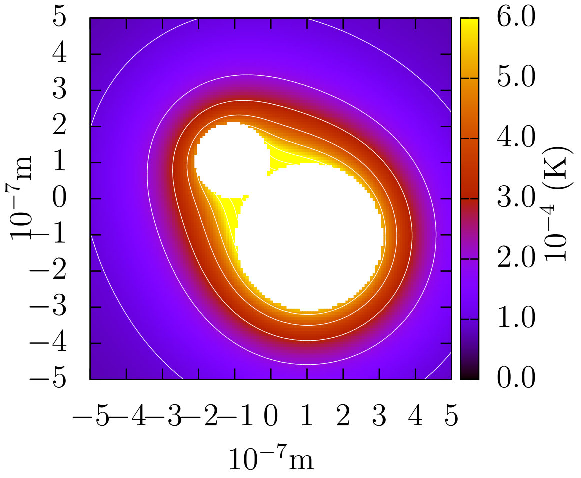

Figure 5.18

Close field plot of temperature for $a/b = 1/2$ and $d = a + b$, $|k_T a| = 1$ and $\alpha = \pi/4$. The plot has been rotated so the incident wave travels along the horizontal direction.

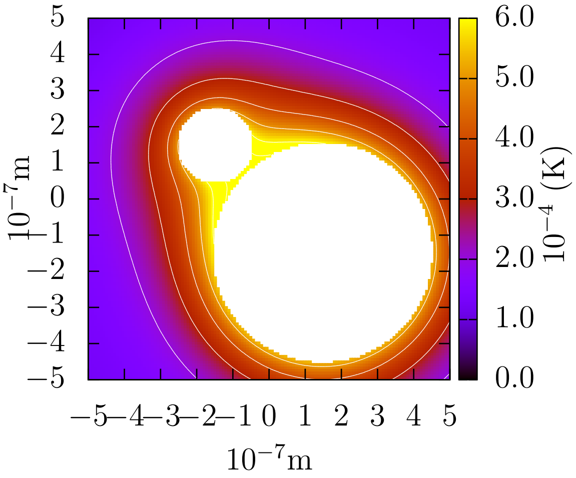

Figure 5.19

Close field plot of temperature for $a/b = 1/3$ *and* $d = 1.2a + b$, $|k_T a| = 1$ *and* $\alpha = \pi/4$. *The plot has been rotated so the incident wave travels along the horizontal direction.*

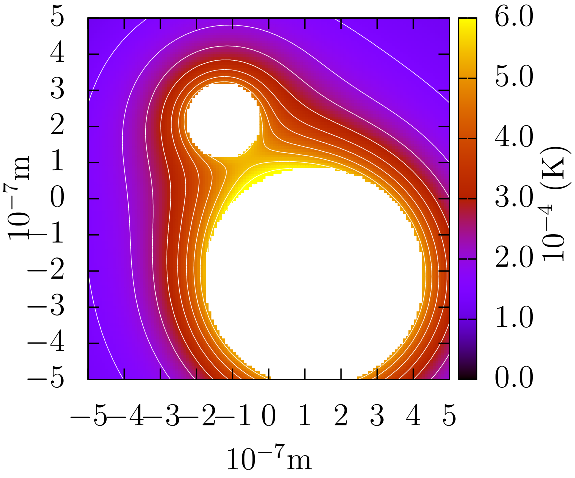

Figure 5.20

Close field plot of temperature for $a/b = 1/3$ *and* $d = 2a + b$, $|k_T a| = 1$ *and* $\alpha = \pi/3$. *The plot has been rotated so the incident wave travels along the horizontal direction.*

Chapter 6

Multiple Scattering Theory

6.1 Introduction

In this chapter, we look at how the results in chapters 4 and 5 can be applied to scattering in an emulsion. These calculations show that the far field thermo-acoustic radiation pattern from a pair of closely separated spheres differs from the superposition of two isolated spheres due to the overlap in the thermal field. This effect is not taken into account in the Lloyd and Berry [35] approximation to multiple scattering, that only includes the long-range interactions of the acoustic field and assumes that scatters can be approximated as points. Here we use the formulation of Linton and Martin [39] to include the effect of interactions between neighbouring particles by averaging the results obtained in the previous chapters over orientation and radial distribution the results prediction for the attenuation are compared to the previous theories and experimental data shown in chapter 3.

6.2 Approach to multiple scattering

Current Lloyd and Berry theory [35] has several limitations, which limits its use for accurately predicting multiple scattering behaviour in concentrated emulsions. Firstly, it treats each particle as a point isotropic scatter. This assumption fails for our model as we have shown in chapter 5 that there is a strong angular dependence on the incident wave angle to a pair of scattering particles. The

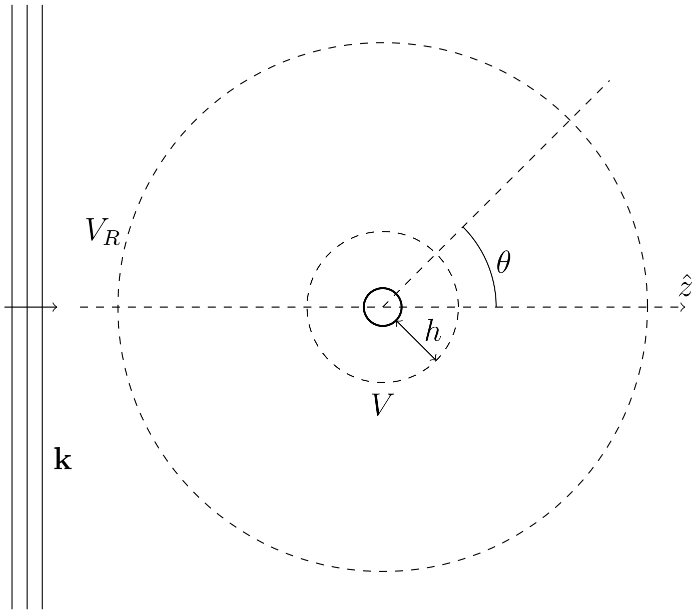

Figure 6.1

Large volume V_R, with radius R, around a sphere, with a second smaller volume V, with radius h.

Lloyd and Berry method also assumes a uniform pair probability distribution, outside of the excluded volume. However multiple studies, including those by McClements and Dickinson [66], and Choudhury and Ghosh [67] have shown that is not valid for concentrated emulsions.

We begin by considering the formulation of the multiple scattering problem given by Linton and Martin [39]. Let us a consider a large volume V_R, with radius R centred around a particle, with an incident sound wave $\mathbf{k} = k_c\hat{\mathbf{z}}$, as shown in figure 6.1.

For a single particles we can consider the scattered acoustic wave to be of the form (equation (1.140))

$$\varphi_{scat} = \sum_{n=0}^{\infty} A_n^{\text{iso}} h_n(k_c R) P_n \cos\theta \sim \frac{e^{ik_c R}}{ik_c R} f(\theta), \tag{6.1}$$

where

$$f(\theta) = \sum_{n=0}^{\infty} A_n^{\text{iso}} P_n \cos\theta \tag{6.2}$$

is the far field pattern and A_n^{iso} is the scattering coefficient from a single isolated sphere. Now consider replacing the single particle with two particles a displacement $\mathbf{D}$ apart, using two coordinate systems, one based around each particle, such that,

$$\varphi_{scat} = \sum_{n=0}^{\infty} A_n^{\text{non-iso}} h_n(k_c R_1) P_n(\cos\theta_1) + \sum_{n=0}^{\infty} B_n^{\text{non-iso}} h_n(k_c R_2) P_n(\cos\theta_2), \tag{6.3}$$

where $A_n^{\text{non-iso}}$ and $B_n^{\text{non-iso}}$ are the two-sphere system scattering coefficients. However provided $R_1 \gg \mathbf{D}$ we can approximate

$$R_1 \approx R_2 = R, \tag{6.4}$$

$$\theta_1 \approx \theta_2 = \theta. \tag{6.5}$$

Therefore, we can now write

$$\begin{aligned}\varphi_{scat} &= \sum_{n=0}^{\infty} \left(A_n^{\text{non-iso}} + B_n^{\text{non-iso}}\right) h_n(k_c R) P_n(\cos\theta), \\ &\sim \frac{e^{ik_c R}}{ik_c R} \left(A_n^{\text{non-iso}} + B_n^{\text{non-iso}}\right) P_n(\cos\theta). \end{aligned}\tag{6.6}$$

However, $A_n^{\text{non-iso}}$ and $B_n^{\text{non-iso}}$, can be defined as a combination of the single sphere scattering coefficient and the additional associated with the presence of the neighbouring sphere, so that

$$A_n^{\text{non-iso}} = A_n^{\text{iso}} + A_n^{\text{pair}}(\mathbf{D}), \tag{6.7}$$

and

$$B_n^{\text{non-iso}} = B_n^{\text{iso}} + B_n^{\text{pair}}(-\mathbf{D}), \tag{6.8}$$

where $\mathbf{D} = (D, \alpha)$ is the distance and orientation of the pair of particles compared to the incident wave, as shown in figure 6.2. Now equation (6.6) becomes,

$$\varphi_{scat} \sim \frac{e^{ik_c R}}{ik_c R} \left(A_n^{\text{iso}} + A_n^{\text{pair}}(\mathbf{D}) + B_n^{\text{iso}} + B_n^{\text{pair}}(-\mathbf{D})\right) h_n(k_c R) P_n(\cos\theta). \tag{6.9}$$

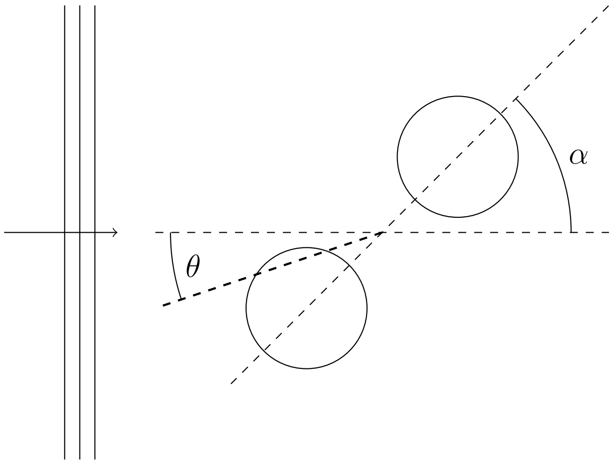

Figure 6.2

Two sphere in orientation of incident wave

If spheres are identical ($A = B$) this can be simplified,

$$\varphi_{scat} \sim \frac{e^{ik_cR}}{ik_cR}\left(2A_n^{\text{iso}} + A_n^{\text{pair}}(\mathbf{D}) + A_n^{\text{pair}}(-\mathbf{D})\right) h_n(k_cR)P_n\left(\cos\theta\right). \tag{6.10}$$

Now that the arms A_n^{pair} decay to zero rapidly as $D \to \infty$. Let us now extend this to N particles in a volume V, where $V^{\frac{1}{3}} = R$, then,

$$\varphi_{scat} \sim \frac{e^{ik_cR}}{ik_cR}\sum_{n=0}^{\infty}\underbrace{\left(A_n^{(N)} + B_n^{(N)} + \cdots\right)}_{N\text{ terms}} P_n(\cos\theta), \tag{6.11}$$

where $A_n^{(N)}$ is the scattering coefficient of a particle in an N particle system. Again, we define each scattering coefficient as the single isolated sphere scattering coefficient combined with the additional scattering generated the presence of each of the other spheres in the volume. However, since our calculations for pairs of particle show that this is short-range, we shall approximate this as the superposition of all possible pair interactions, so that,

$$A_n^{(N)} \approx A_n^{\text{iso}} + \sum_{j=2}^{N} A_n^{\text{pair}}(\mathbf{D}_j). \tag{6.12}$$

Now we need to take an average of equation (6.11) over V,

$$\langle \varphi_{scat} \rangle \sim \int \cdots \int \varphi_{scat}(\mathbf{r}_1, \mathbf{r}_2, \mathbf{r}_3, \cdots, \mathbf{r}_N) p(\mathbf{r}_1, \mathbf{r}_2, \mathbf{r}_3, \cdots, \mathbf{r}_N) dV_1 \cdots dV_N, \quad (6.13)$$

where $p(\mathbf{r}_1, \mathbf{r}_2, \mathbf{r}_3, \cdots, \mathbf{r}_N)$ is the probability density function for the configuration where the particles are located at $\mathbf{r}_1, \mathbf{r}_2, \mathbf{r}_3, \cdots, \mathbf{r}_N$. However, since we are only including the single and pair contributions we only require the single particle $p(\mathbf{r})$ and pair particle probability densities.

Since the suspension is assumed to be homogeneous, the single density probability density is given by,

$$p(\mathbf{r}) = \frac{n_0}{N}, \quad (6.14)$$

where n_0 is the number density of spheres. The pair-correlation function is given by

$$p(\mathbf{r}_1, \mathbf{r}_2) = \frac{n_0^2}{N^2} g(\mathbf{D}), \quad (6.15)$$

where $\mathbf{D} = \mathbf{r}_2 - \mathbf{r}_1$ and $g(\mathbf{D})$ is the radial distribution function.

6.2.1 Radial distribution function

The Lloyd and Berry [35] method assumes that the particles are distributed evenly throughout the fluid by the Heaviside function,

$$g(D) = H(D - 2a), \quad (6.16)$$

where

$$H(x) = \begin{cases} 1 \text{ for } x > 0, \\ 0 \text{ for } x \leq 0. \end{cases} \quad (6.17)$$

However, it has been shown in multiple studies of colloidal particle distribution, including those by McClements and Dickinson [66], and Choudhury and Ghosh [67], that this is only accurate for very low concentrations of colloids. These studies have shown that short-range inter-particle forces (such as Van der Waals forces) are important factors in determining the radial distribution function.

By assuming that colloidal particles are spherical and isotropic, the distribution of colloidal particles can be derived using the same statistical mechanics methods used for atomic distributions. Despite that colloidal particle dynamics are based on friction dominated, diffusive dynamics, the micro-structure of both colloids and atomic particles are very similar, only with different orders of magnitude and time scales. For colloids the inter-particle forces consist of a short-range repulsion modelled using the Lennard-Jones potential equation [68, 69],

$$u_{LJ}(r) = 4\epsilon\left[\left(\frac{a}{2r}\right)^{12} - \left(\frac{a}{2r}\right)^{6}\right], \tag{6.18}$$

where $u(r)$ is the potential energy, and ϵ is an amplitude parameter, which is an attractive force for $2r > a$ and a repulsive force for $2r < a$, and the Van der Waals pair potential [70, 71], which is a longer range attractive potential,

$$u_{vdW} = -\frac{A_{eff}}{6}\left[\frac{2a^2}{r^2-4a^2} + \frac{2a^2}{r^2} + \ln\left(1 - \frac{4a^2}{r^2}\right)\right], \tag{6.19}$$

where a is the particle radius, and A_{eff} is the effective Hamaker constant. Assuming that the system is in thermodynamic equilibrium, the pair probability distribution is given formally by integrating over the distribution of the remaining $N-2$ particles

$$g^{(2)}(\mathbf{D}) = \frac{V^2 N!}{N^2(N-2)!} \cdot \int \cdots \int e^{-\beta U_N} d\mathbf{r}_3 \cdots d\mathbf{r}_N, \tag{6.20}$$

here $\beta = 1/k_B T$ and U_N is the potential energy, where k_B is the Boltzmann constant and T is the temperature. In this form the integral is not particularly useful, but Ornstein-Zernike integration methods can be applied [72]. Combining this with the Percus-Yevick approximation [73], a solution for $g(\mathbf{r}_2)$ can be obtained [74, 75].

In figure 6.3, the particle distribution for different concentrations has been plotted, compared to the distance between each of the spheres, using a *MATLAB* code provided by Sandler [76]. Note that as ϕ increases that $g(D)$ becomes increasing non-uniform with maxima at interger numbers of diameters, representing shells of particles, as seen in figure 6.4.

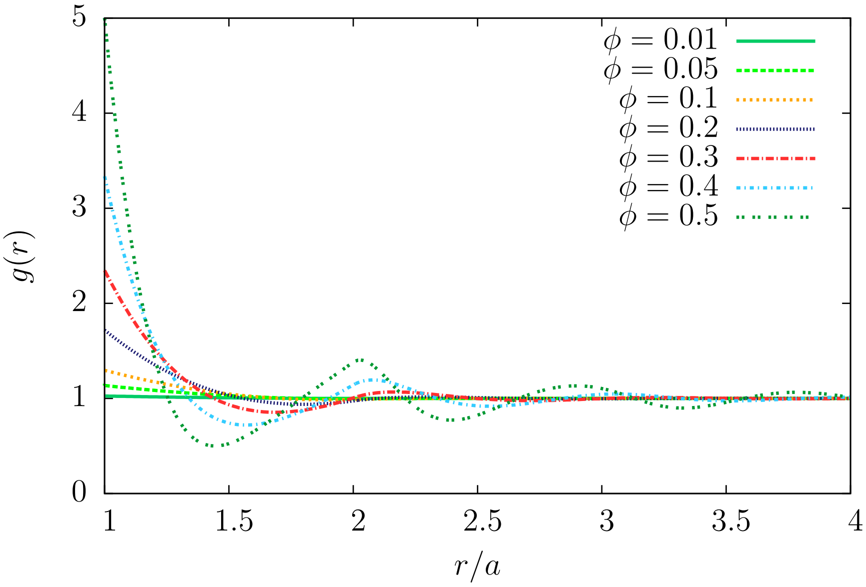

Figure 6.3

Radial distribution function for different ϕ

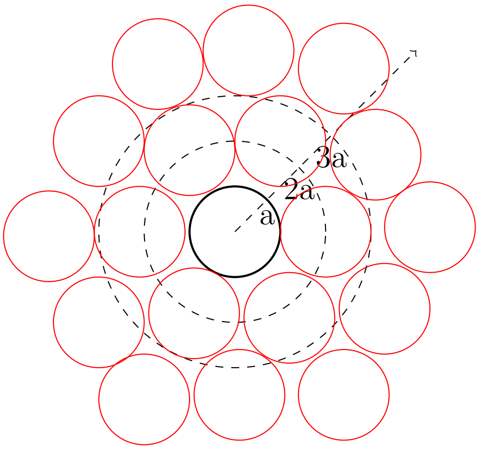

Figure 6.4

Particle packing for closely packed particles.

Returning to equation (6.13), this now allows us to write the total scattering,

$$\varphi_{scat} = NA_n^{\text{iso}} + N(N-1)\iiint A_n^{\text{pair}}(\mathbf{D})g(\mathbf{D})d^3\mathbf{D}, \tag{6.21}$$

where

$$g(\mathbf{D}) = \frac{1}{4\pi}g(D). \tag{6.22}$$

This integral, over the volume V gives,

$$\iiint A_n^{\text{pair}}(\mathbf{D})g(\mathbf{D})d^3\mathbf{D} = \frac{1}{2}\int_0^\pi \sin(\alpha)\left(\int_0^h g(D)A_n^{\text{pair}}(D,\alpha)dD\right)d\alpha, \tag{6.23}$$

where h is the radius of V.

6.3 Far field scatter

To be able to utilise this theory more effectively, it is useful to consider the far field scatter, rather than the individual scattering coefficients. Averaging over all possible pair configurations the far field pattern is given by,

$$f(\theta) = f^{\text{iso}} + 2\pi n_0 \int_0^\pi \int_0^\infty g(D)\sin(\alpha)f^{\text{pair}}(D,\alpha)dDd\alpha, \tag{6.24}$$

where the integral now expands to infinity as the far field scattering effects due to the close proximity of pairs reduces rapidly as D increases. Here we can include the volume fraction, $\phi = 4\pi a^3 n_0/3$. This can then be used in the Lloyd and Berry [35] approximation up to $n = 1$ to the derive the effective wave number,

$$\left(\frac{\tilde{k_c}}{k_c}\right)^2 = 1 + \frac{3\phi}{k_c^2 a^3}f(0) + \frac{9\phi^2}{4k_c^4 a^6}\left(f^2(\pi) - f^2(0) - \int_0^\pi d\theta \frac{1}{\sin(\theta/2)}\left(\frac{d}{d\theta}f^2(\theta)\right)\right). \tag{6.25}$$

We can now use this, combined with equation (6.24) to calculate a new effective wave number $\tilde{k_c}$. This can be separated into the velocity and attenuation parts, by

$$\tilde{k}_c = \frac{\omega}{\tilde{v}} + i\tilde{\alpha}, \tag{6.26}$$

where $\tilde{v}$ is the effective sound velocity in the dispersion and the imaginary part $\tilde{\alpha}$ is the total attenuation from the continuous and suspended phases of the dispersion as well as the contribution from scattering. To determine the attenuation additional due to scattering alone α_{scat}, the contributions from the phases must be subtracted,

$$\alpha_{scat} = \tilde{\alpha} - \alpha_c(1 - \phi) - \alpha_s\phi, \tag{6.27}$$

where α_c and α_d are the attenuation coefficients of the continuous and suspended phases respectively, and ϕ is the volume concentration of the suspended phase.

6.4 Results

In this section we look at the experimental data from chapter 3 and compare it to our new two particle weak thermal scattering solution.

6.4.1 Monodisperse

In figure 6.5 we compare the silicone oil-in-water data from Herrmann [5], described in section 3.1.1, with the previous scattering theory (represented by the dashed lines) and the new two sphere scattering theory solution (represented by the solid lines). At low concentrations, the difference between the two sphere and single sphere weak thermal scattering solutions is negligible. At lower concentrations the particles are further apart and thus multiple scattering has little effect on the scattering as a whole. However, both solutions match the experimental data curve, which suggests that the existing theory captures the scattering mechanisms at this concentrations.

As the concentration of the emulsion increases, we start to see slight variation between the single and the two sphere weak thermal scattering solutions. This is almost exclusively in the lower frequency range, where $|k_T a| < 2$. At lower

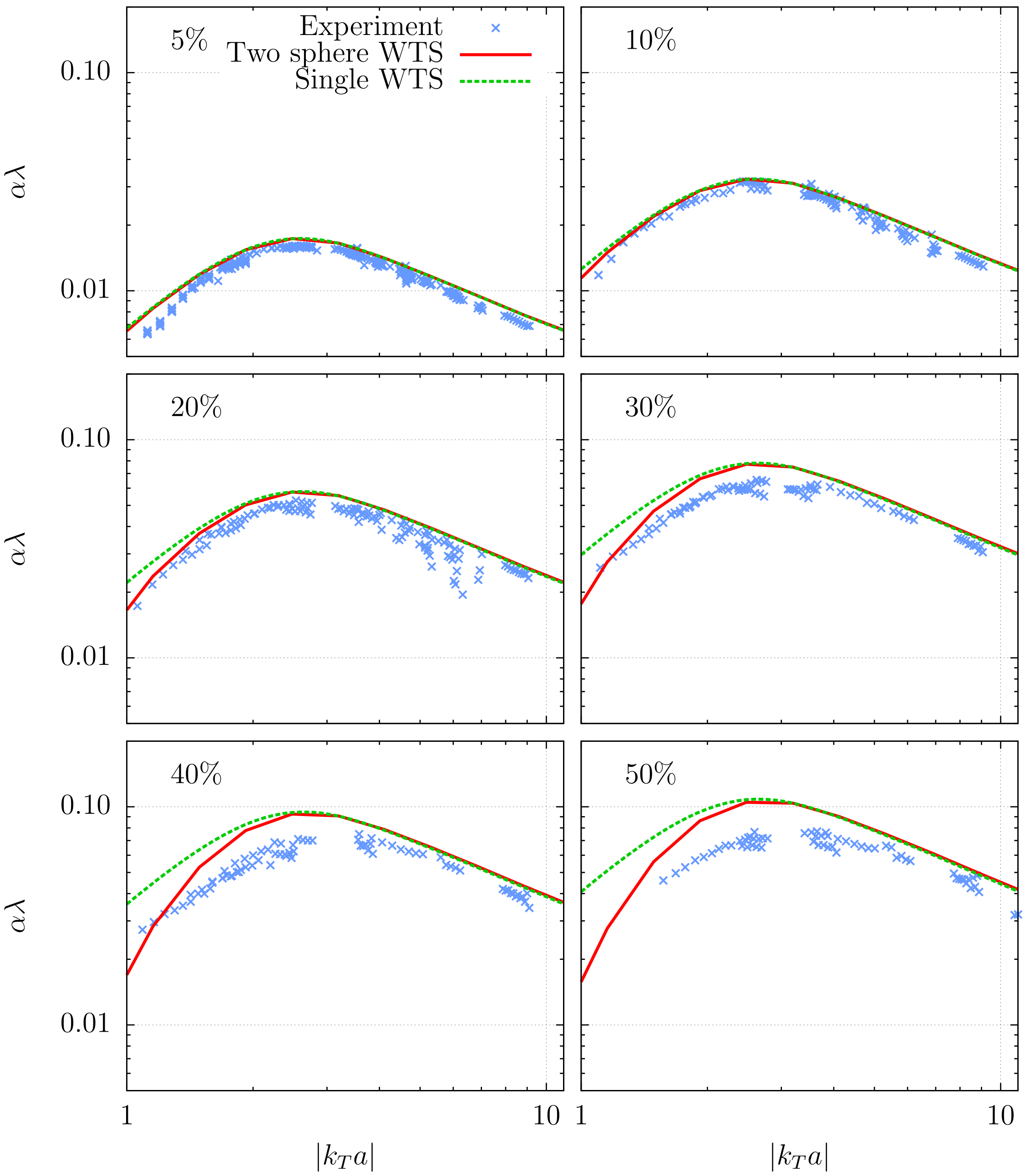

Figure 6.5

Silicone oil-in-water dispersion data for particle radii 230-760nm, from Herrmann [5], compared with single weak thermal scattering theory (WTS) (dashed), and two sphere multiple scattering weak thermal scattering theory (WTS) (solid). The lines represent the theoretical prediction and the symbols represent the data.

frequencies the thermal field around each particle has a larger radius, of $\sqrt{\sigma/\omega}$, as described in equation (1.147), so that the proximity of other particles has a greater thermal boundary effect on the thermal fields, whereas for $|k_T a| > 2$ the thermal boundary layer is sufficiently thin that there is little overlap.

As the concentration of the disperse phase is increased to 20%, we see the discrepancy between the two solution increase at lower $|k_T a|$. The single weak thermal scattering theory prediction over estimates the level of attenuation in this region, while the two particle weak thermal scattering prediction reduces the predicted level of attenuation in-line with the experimental data, providing a good correlation. However, while the peak in the experimental data, matches that of the prediction, we find that overall the prediction still overestimates the whole attenuation.

At 30% we see an increased discrepancy between the two solutions, particularly for lower values of $|k_T a|$. However, the two particle weak thermal scattering solution now under predicts the levels of attenuation at the lowest values of $|k_T a|$. This maybe because the superposition of pair corrections over estimating the effect of multiple scattering in groups of particles. Note, in section 5.3 we found the largest difference in the far field between the single and the two sphere solutions was when $|k_T a| \sim 1$, which seems to be the case here. On the other hand, we do find the peak in the attenuation curve has shifted slightly to a larger $|k_T a|$ value, which is also seen in the experimental data, where there is a slight shift in the peak compared to lower concentration data. Again we find the overall prediction still over-estimates the attenuation level.

For the 40% and 50% predictions, again there is a divergence between the two predictions at values $|k_T a|$ closer to 1. We find both of the two particle weak thermal scattering solutions both greatly over estimate the attenuation levels below $|k_T a| = 6$. There is a shift in the attenuation peaks consistent with the experimental data, however the experimental data shift is much greater in magnitude. As $|k_T a|$ approaches 1 we see the two particle weak thermal scattering prediction approach the attenuation levels seen in the experimental data.

Overall, we see that at lower concentrations the two particle weak thermal scattering method provides a prediction consistent with the experimental data. As the concentration increases to a point where the single weak thermal scattering solution is no longer accurate in predicting attenuation levels, the two particle solution provides more accurate predictions. However, as the concentration increases to even higher levels, while providing a closer prediction than previous methods, the prediction fails to quantitatively predict the behaviour of the experimental system. This is most likely because the two particle weak thermal scattering system excludes the combined scattering from more than two particles, which is reasonable in emulsions at around 20%, but is no longer valid as the concentration increases and the particles are packed even closer. However the results are sensitive to the two particle distribution function, which is another possible source of error.

The second series of experiments described in section 3.1.1 were two Polystyrene PEGMA samples, of sizes $\sim$ 400nm and $\sim$ 900nm, which had their velocity and attenuation measured in the ResoScan at different concentration levels. We can now compare this experimental data with the new two particle weak thermal scattering theory. In figure 6.6 we see a comparison of the dispersion velocity in two samples, compared to the single weak thermal scattering theory, shown by dashed lines, and two particle weak thermal scattering, shown by solid lines. It can be seen that for the 400nm prediction there is a good consistency between the experimental data and the two particle weak thermal scattering theory. It successfully predicts the velocity up to a concentration of 16%, unlike the single weak thermal scattering theory which is only consistent until 8%. However, we find that the 900nm two particle weak thermal scattering prediction over estimates the experimental data. While it provides a suitable prediction until 10%, which is greater than the single weak thermal scattering theory by 2%, it over predicts the velocity for concentrations higher than this. This discrepancy is probably caused by visco-inertial effects, as the contrast in density between the continuous and disperse phase is high, and the thermal contrast is smaller than for other emulsion systems.

This discrepancy is more prominent in figure 6.7, as the attenuation predicted by the two particle weak thermal scattering theory does not provide a significant improvement over single weak thermal scattering theory. Figure 6.7 follows the same convention as with figure 6.6, except considering attenuation as opposed to velocity of the emulsion. We find for both the 400nm and the 900nm that the two

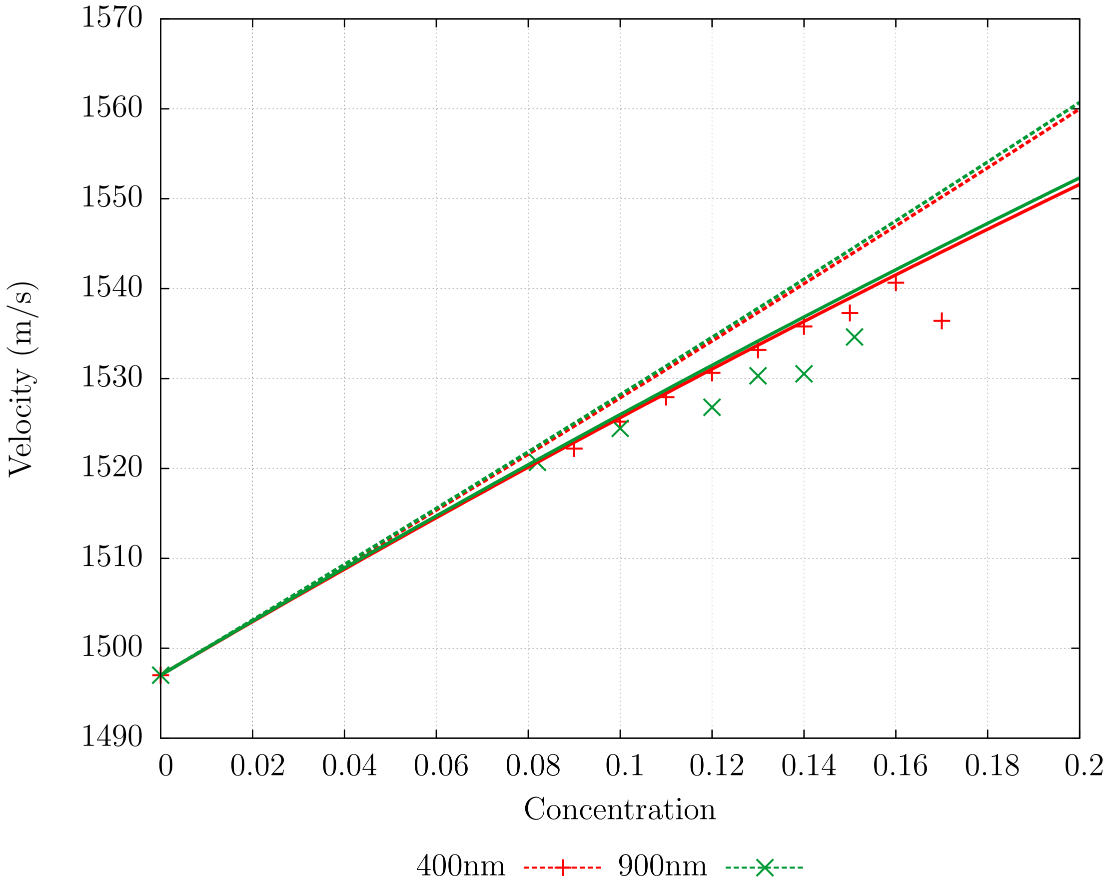

Figure 6.6

∼400 nm and ∼900 nm Polystyrene PEGMA in water velocity for concentrations measurements from ResoScan at ∼8MHz, compared to single weak thermal scattering theory (dashed) and compared to two particle weak thermal scattering (solid). The points represent the experimental data, and the lines are the prediction.

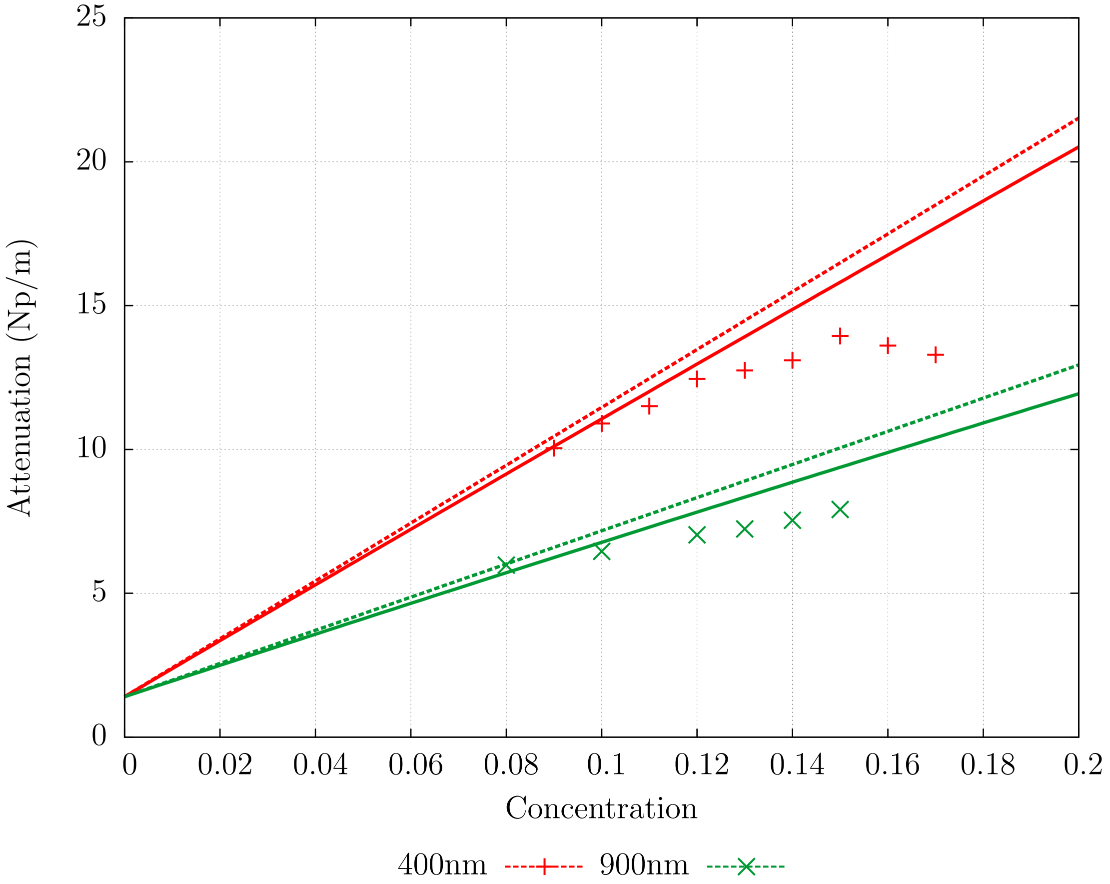

Figure 6.7

∼400 nm and ∼900 nm Polystyrene PEGMA in water attenuation for concentrations measurements from ResoScan at ∼8MHz, compared to single weak thermal scattering theory (dashed) and compared to two particle weak thermal scattering (solid). The points represent the experimental data, and the lines are the prediction.

particle weak thermal scattering theory is only consistent with the experimental data under 10%, which is only a minor improvement over the single weak thermal scattering method. As previously stated, this is likely due to visco-inertial effects being more prominent than the thermal effects studied in this thesis.

6.4.2 Polydisperse

The second set of experiments aimed to see whether bi-disperse emulsions could be predicted using scattering theory. Further details of the experimental set up of the experimental process can be found in section 3.2. In figure 6.8 we can see the experimental data for hexadecane-in-water, for mono-disperse, 100nm and 900nm emulsions at 30%, and a bi-disperse emulsion consisting of equal parts of 100nm and 900nm radii particles at different concentrations.

Here we define a to be the smaller particle, so that a frequency with $|k_T a| \sim 1$ corresponds to a thermal layer around each particle that is the depth equal to the radius of the smaller particles. This is however small compared to the radius of the large particles, so that corresponding values of $k_T b$ are larger. Unfortunately, the range of frequencies available are only able to probe $|k_T a|$ from 1 to 6, so that we do not have measurements in the range where $k_T b$ is of order one.

For each of the experiments two predictions have been calculated, one for single particle weak thermal scattering, shown by dashed lines, and one for two particle thermal scattering, shown by solid lines.

We first consider the two mono-disperse samples figure 6.8. As with the previous mono-disperse results for the silicone oil-in-water system, we see two main differences between the single particle and pair particle solution. First we have the peak shift in the attenuation curve, however, with the hexadecane system this shift is more predominant. This could be due to the greater density difference between the two phases compared with water and silicone oil, thus a greater peak shift. The second characteristic is the reduction in attenuation at lower $|k_T a|$ values. Again, we see an under prediction compared with the experimental data, this is again likely due to the two particle weak thermal scattering method only considering pairs of particles, and so overpredicting the effect of particle overlap. Overall, we see an over prediction in the attenuation levels with both

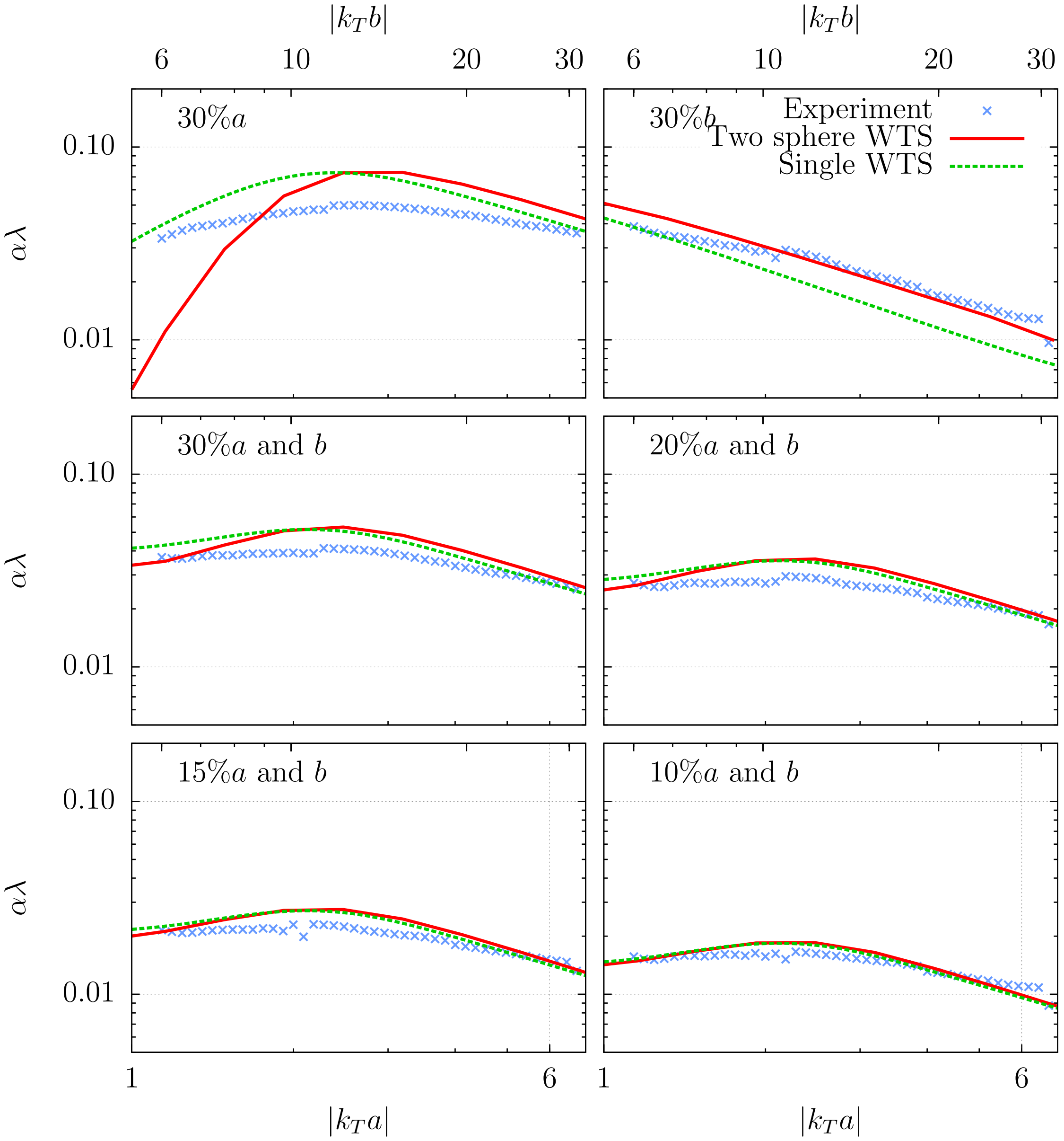

Figure 6.8

Attenuation spectrum of two hexadecane in water emulsions, of size 100nm and 900nm, separately and mixed (shown by points) compared with single weak thermal scattering theory (shown by dashed lines) and two particle weak thermal scattering (shown by solid lines). The mixed samples are mixed 50% v/v each for 100nm and 900nm. The mixed weak thermal scattering solutions were obtained by combining the attenuation from both 100nm and 900nm spectrum.

mono-disperse samples, which is consistent with previous samples in section 6.4.1. While the two particle weak thermal scattering solution does not give a complete solution to the problem, it does provide a better prediction than the single weak thermal scattering model.

Moving on to the bi-disperse emulsions, at the lowest concentration, we do not see much difference between the single and two particle weak thermal scattering solutions. The only discrepancy between the two solutions can be seen at $|k_T a| > 4$ above the attenuation peak, where the pair solution is more consistent with the experimental data. As the concentration increases to 10% we see that this increase in attenuation in the two particle weak thermal scattering solution compared to the single particle solution has increased, again in line with the experimental data. Also we see that the attenuation level is slightly lower at $|k_T a| > 4$ above the attenuation peak. These trends are found in increasing amount as the concentration increases, as well as increasing peak shift. However, two discrepancies remain. The overall level of the predicted attenuation is greater than the experimental data, particularly at higher concentration predictions. The second inconsistency is at $|k_T a| \sim 1$ where the experimental data in each of the bi-disperse emulsions starts to increase again as $|k_T a|$ is reduced. There is a second attenuation peak at $|k_T a| = 0.2$ caused by the larger particles. This is not shown in figure 6.8 as it is outside the range of the instrumentation. However, the experimental system is not purely bi-disperse and there will be a spread of particle sizes around 900nm and 100nm, which will cause a spreading of the attenuation peaks. So the increase in attenuation at lower $|k_T a|$ may be caused by particles between 100nm and 900nm.

Using the two particle weak thermal scattering solution for bi-disperse emulsions does provide an improvement over the single particle weak thermal scattering theory, however it suffers from the same problems as the mono-disperse solution. Again we can speculate that this is due to considering only pair thermo-acoustic interactions between particles, where as for higher concentrations, a particle is likely to be close to more than one other particle, thus creating different scattering behaviour. Another consideration is that for bi-disperse colloidal dispersions, the particles maybe not be simply being mixed uniformly. Instead, it is possible that the smaller particles are drawn preferentially towards the larger particles.

The final set of experiments looked at concentration variations in samples over a period of time due to creaming, described in section 3.2. Each of the figures 6.9–6.13, uses the velocity profile measurement to calculate a predicted concentration. This is then used with the two particle weak thermal scattering theory to produce an attenuation, which is compared with the experimentally measured attenuation. For reference the results with the single weak thermal scattering method approach from figures 3.15, 3.19, 3.23, 3.27 and 3.31 are reproduced here.

We find in figure 6.9 that the new prediction provides a closer match compared to the experiential data. This is consistent with figure 6.8 as at $|k_T b| \approx 11.3$ we see the two particle weak thermal scattering theory gives a better prediction. However, in each of the other samples, we find little change compared to the single weak thermal scattering theory. This is because $|k_T a| \approx 2.1$, we can see in region in figure 6.8 where the peak of the attenuation curve that there in negligible difference between the single and the two particle weak thermal scattering theories. Therefore, it can be seen that two particle weak thermal scattering theory does not significantly improve the attenuation prediction for 100nm particles.

6.5 Discussion

Overall, we can see that using a two particle weak thermal scattering provides some improvements over using single scattering theory, however, this method does not provide a definitive solution to the problem. While it does have some limitations, it has provided a good step in addressing some of the previous problem.

Using a two particle approach does change the attenuation curves shown in figures 6.5 and 6.8, in qualitative agreement with trends seen in the experimental data, such as the decrease in attenuation levels at lower frequencies. By accounting for the thermal field interactions between close pairs of particles, we are able to explan the reduction in attenuation at lower frequencies. This approximation works best at intermediate concentrations where the interactions are pairwise, while at higher concentrations it starts to under predict the levels of attenuation, due to the neglect of three and four particle interactions.

This method also provides some of the peak shift in the attenuation curve

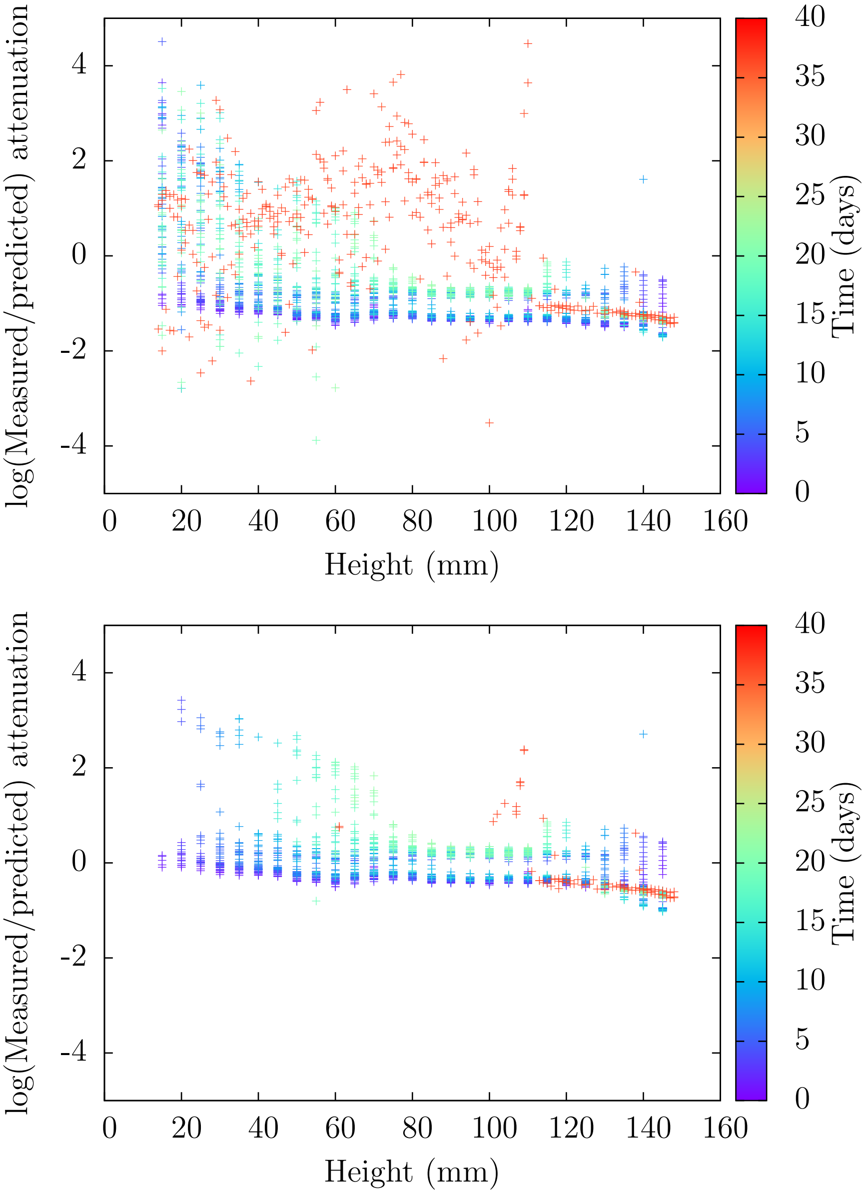

Figure 6.9

Acoustiscan comparison of the single sphere (top) and two sphere (bottom) weak thermal scattering attenuation prediction and measurement of 30% 900 nm hexadecane in water over 37 days.

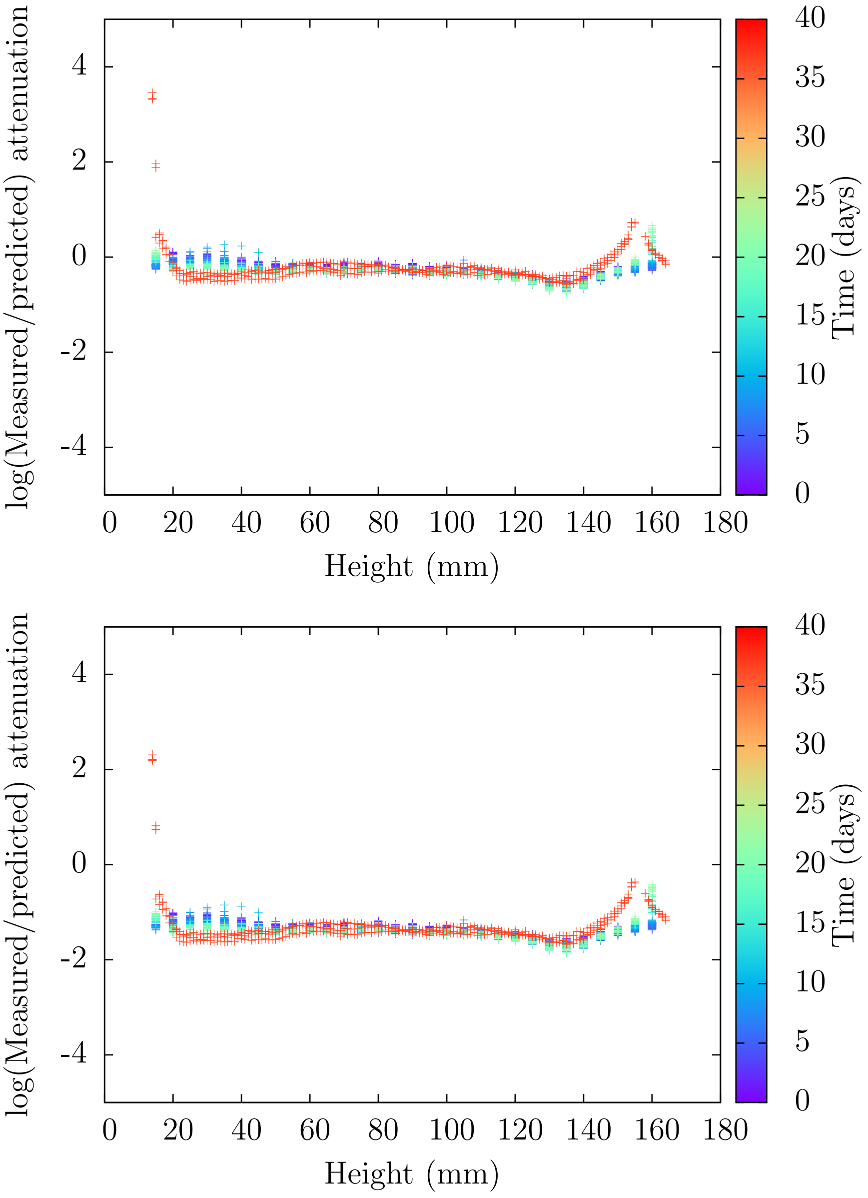

Figure 6.10

Acoustiscan comparison of the single sphere (top) and two sphere (bottom) weak thermal scattering attenuation predictions and measurement of 30% 100 nm hexadecane in water over 37 days.

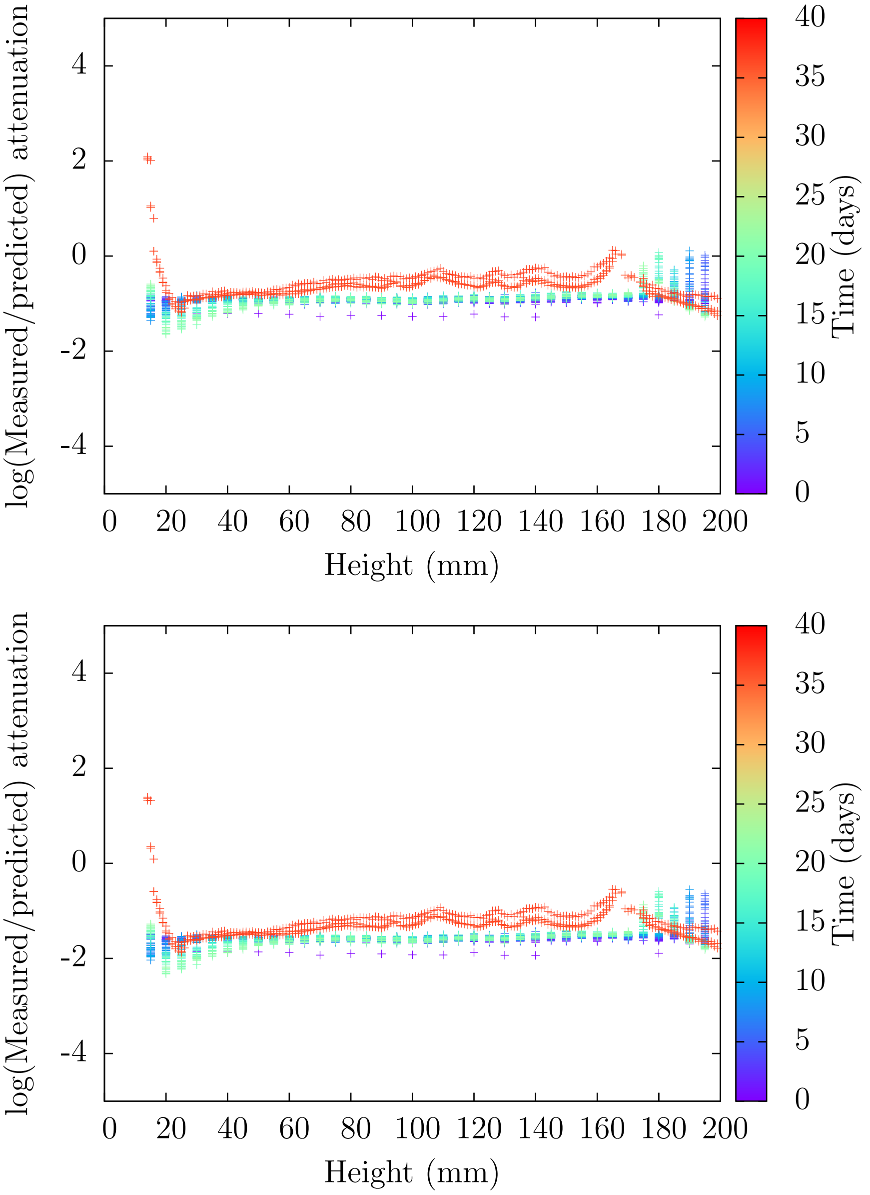

Figure 6.11

Acoustiscan comparison of the single sphere (top) and two sphere (bottom) weak thermal scattering attenuation prediction and measurement of 15% 900nm and 15% 100nm hexadecane in water over 37 days.

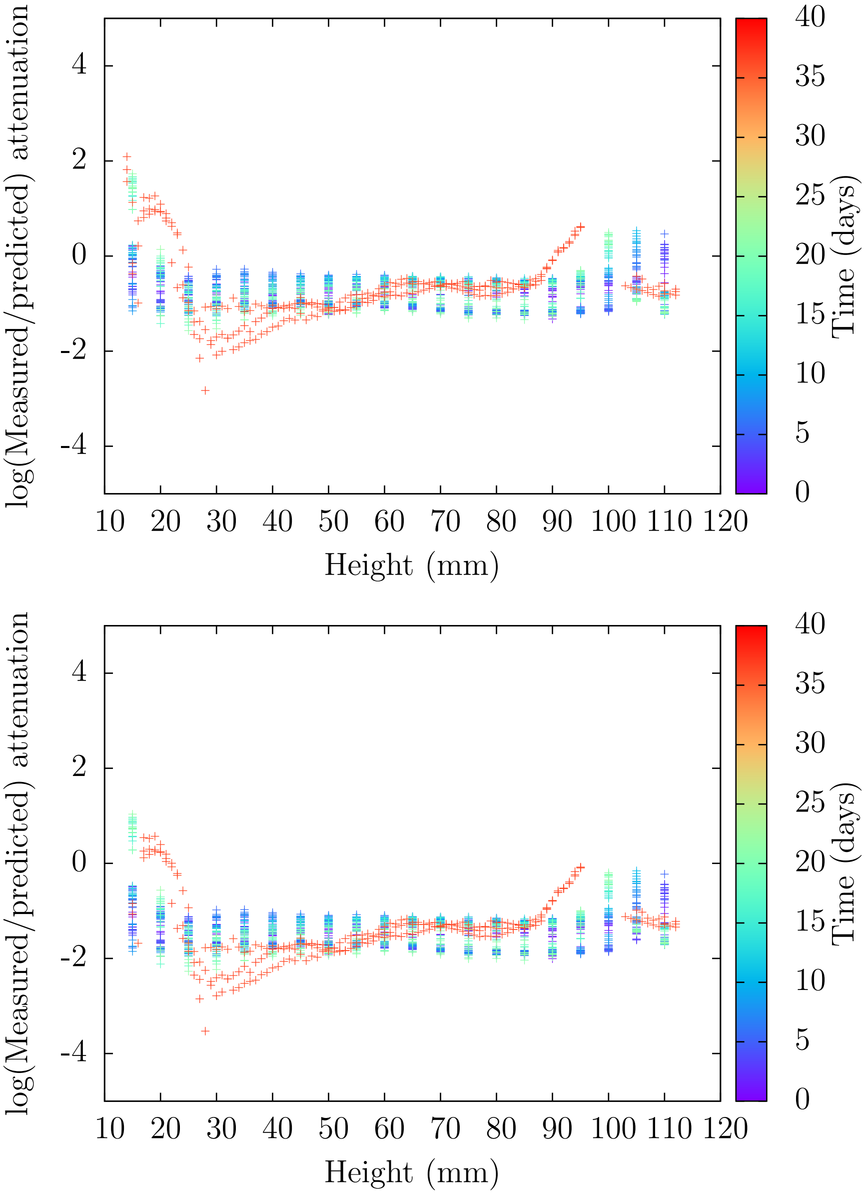

Figure 6.12

Acoustiscan comparison of the single sphere (top) and two sphere (bottom) weak thermal scattering attenuation prediction and measurement of 10% 900nm and 10% 100nm hexadecane in water over 37 days.

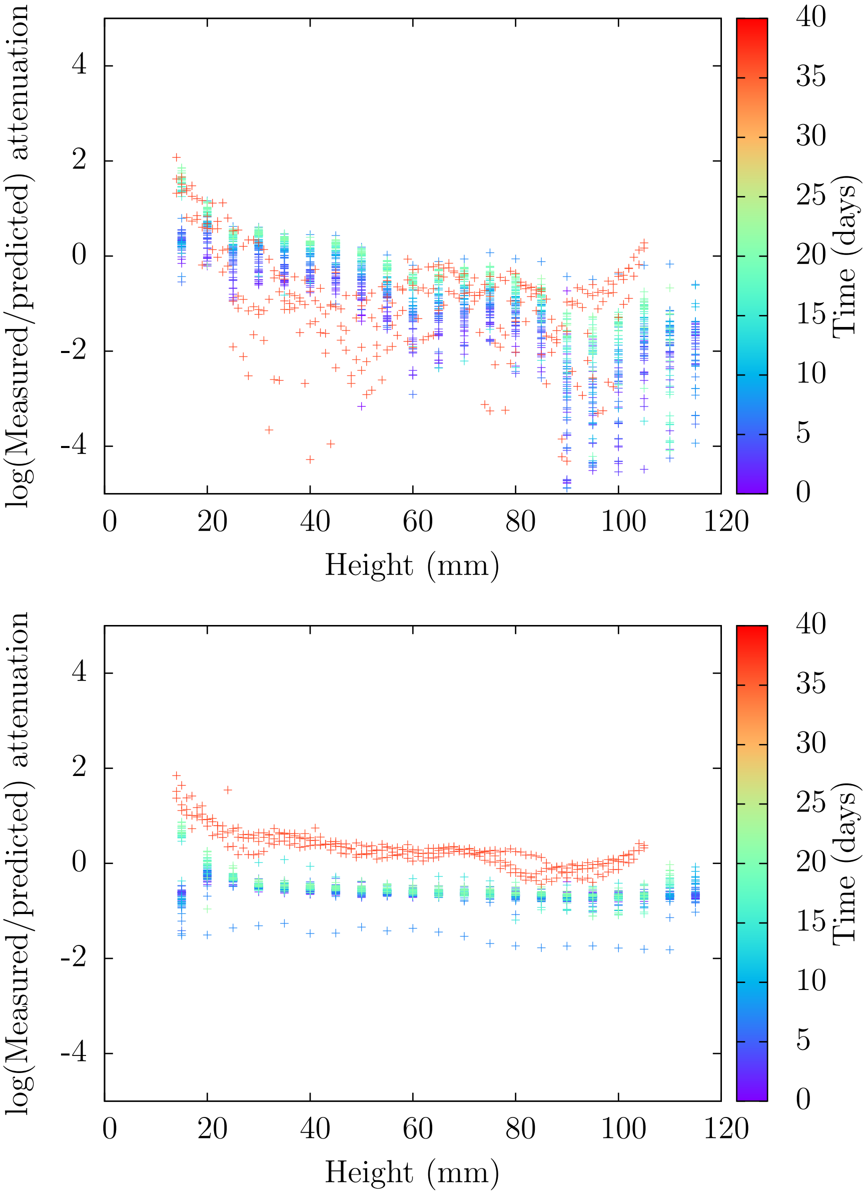

Figure 6.13

Acoustiscan comparison of the single sphere (top) and two sphere (bottom) weak thermal scattering attenuation prediction and measurement of 7.5% 900nm and 7.5% 100nm hexadecane in water over 37 days.

seen in the experimental data in figures 6.5 and 6.8. This again is due to the modelling of two particle close together, allowing the coupling between the fields to act like a single larger particle rather than two smaller particles.

However, the model is limited in a number of ways which could have been the cause of the inconsistencies between the model and the measured data. One consideration is that there are other effects occurring apart from thermo-acoustic effects, notably visco-inertial effects. While care was take in choosing materials where this effect was not prominent, it can not be completely removed from a system.

Another problem is that only pair interactions between particles are considered. While this is reasonable for lower concentrations as the particles are far apart, as the concentration increases the number of particles close to a single particle will increase, there is an increased likelihood of three or more particle clusters giving rise to a different scattering coefficient than just considering the summation of the different pair combinations within that three particle group.

This may also explain why the two particle weak thermal scattering method on bi-disperse colloids does not fully capture the scattering seen in experiments. As well as multiple particle clusters, the difference in size of the particle may have caused structural changes, such as the bigger particles attracting the smaller particles to it, creating a thermal effect of a single larger particle, or the smaller particles “cloaking” the bigger particle. Again this could be scope for further research, in particular into particle structuring in colloidal suspensions.

Chapter 7

Sedimentation detection in a pipe

7.1 Introduction

In the modern industrial world, pipes play an important role in the transport of fluids. They are vital in numerous industries from fluid and gas distribution [77–79], sewage drainage [80], manufacturing and mixing. When pipes are used to transport multiphase fluids, there are a number of processes, interactions and reactions that can happen inside a pipe; sedimentation at the bottom of the pipe, scale forming on the inner pipe wall, the material in the pipe completing a chemical reaction, the materials in the pipe forming a colloid, bubbles in the flow, demixing, or even blockages. While some of these situations are desirable, others can lead to productivity loss, from inefficient flow within the pipe, or even having to stop production altogether.

It is necessary to be able to determine what the current fluid and flow conditions within pipe are. However, current methods to determine this are less than desirable, as they may require physical removal of sections of pipe to inspect the interior. This technique also does not tell you any information about the flow when any process is taking place. Light scattering techniques could be used to determine information about the inside of the pipe, however, this would require the manufacture of specialist pipe sections with the apparatus built in to the pipe wall and cannot be used for bulk property determination in opaque materials. Generally this method is impractical due to cost, and retrofitting to an existing plant would require the halting of any process during installation. Furthermore, this system would only allow measurement on this particular section of pipe. Using ultrasound for this problem has many advantages, as ultrasound can penetrate most pipe walls, so transducers can be mounted on the outside of any pipe in use. As no specialist section of pipe is required, costs can be reduced and the system can be used on any section of pipe, allowing for greater flexibility. Ultrasonic techniques are currently widely used in the inspection of pipe walls, for the detection of flaws on the surface or subsurface [81], so ultrasonic detection of behaviour inside the pipe could be developed from these systems.

In this chapter, we develop an ultrasonic technique for determining the state of the fluid inside of a pipe. We expand on the work of Soe *et al.* [82] and Lee [83] by introducing a pair of transducers and that can be rotated around the pipe to give a detialed picture of the fluid structure within the pipe. We first look at the theoretical background for the problem, bringing together the ideas from chapter 6. This will be compared to modelling work completed using *COMSOL Multiphysics*. Lastly, we compare both models with experimental data on a 25.4mm diameter stainless steel pipe, with a silica in water suspension provided by Luis Martin de Juan from Procter and Gamble Newcastle Innovation Centre.

7.2 Experimental methods

The measurement system used was a commercial ultrasonic transmitter, receiver and pre-amplifier system, known as a *US-Key*, manufactured by *Lecoeur Electronique*, France. The system can be seen in figure 7.1. This system is mounted on a section steel of pipe, 25.4mm in diameter with a 1.6mm thickness. This has been capped on one end and has a cap leading to rubber tubing on the other end to prevent any build up of pressure. One pair of transducers (*Olympus M1057*, manufactured by *Olympus NDT Inc.*, Massachusetts, USA) with a central frequency of 5MHz were used. These transducers were placed in a bespoke holder which applies a constant pressure to each transducer through the use of springs and allows the transducer pair to be freely rotated around the pipe. Between the transducer and the pipe wall, an acoustic coupling gel, *Sonotech Soundsafe* ®, manufactured by *Magnaflux*, Illinois, USA, was applied. The gel is also used as a lubricant, which allows the smooth rotation of the holder. The transducers are connected to the *US-Key*, which in turn was connected via USB to a computer running *MATLAB* that both controls the pulse transmission and processes the signal received from the transducers. A pulse is sent from one, usually the lower of the two transducers, into the pipe. The signal is measured at both transducers, which allows for measurement of both the reflected and transmitted signal. This allows for more accurate measurement of time of flight and attenuation of the pulses. To measure the data, the time difference between each pulse received and the maximum amplitude of these pulses is measured, using the pitch and catch, pulse-echo techniques described in section 1.2.1. These values are calculated using the *US-Key's* supplied code. Using multiple reflections allows a more accurate calculation of the attenuation and time of flight.

The test fluids consisted of different concentrations of silica beads in water. The silica beads are approximately 400-600 microns in size, from *Jencons (Scientific) Ltd*, UK. Three different concentrations were used, $0\%, 5\%$ and 10%. The samples were poured into the pipe, shaken up and allowed to settle over a few minutes. The ultrasonic measurements were first obtained with the transducer pair located at zero degrees to vertical, vertically aligned ($\theta = 0°$ in figure 7.2). They were rotated in 5° steps, with measurements taken, until 90°, the horizontal alignment, where the angle measured is shown in figure 7.2.

7.3 Modelling of acoustic propagation in the pipe experiment

To model the propagating compressional wave through a pipe, we will be modelling in two ways. Firstly, one dimensional model based on the profile of the pipe. Secondly, *COMSOL Multiphysics* [84] is used to create a numerical finite element model. In each of the models we consider a steel pipe, with a solid layer of silica to simulate the silica bead sediment layer inside the pipe, and then the remainder of the interior of the pipe filled with water.

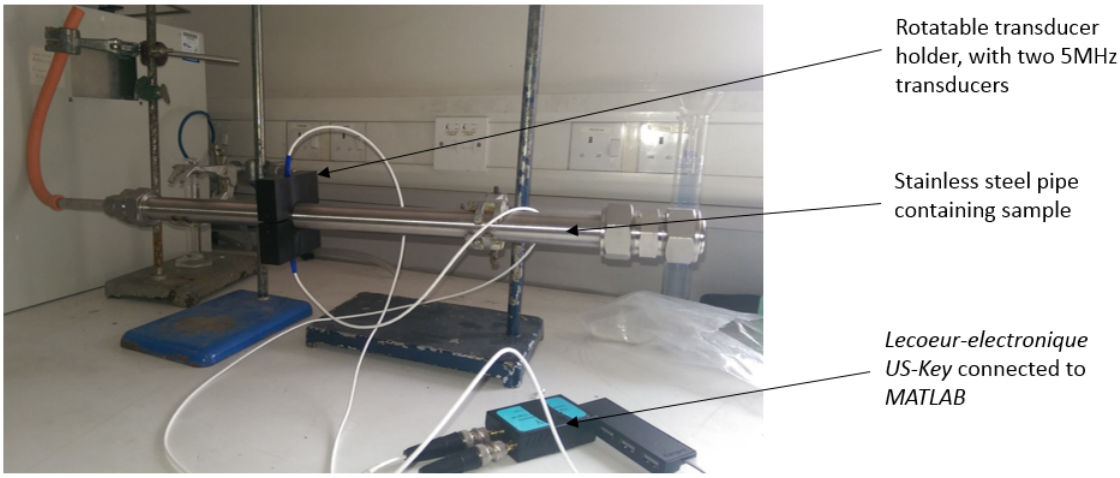

Figure 7.1

Picture of physical set up ultrasonic system for use in the experiment attached to a section of steel pipe.

7.3.1 Plane wave interaction at a surface boundary

When the ultrasonic pulse encounters a step change in acoustic properties, such as at the edge of the pipe wall or sedimentation layer, a portion of the compressional wave is reflected with some transmitted through the materials. The levels at which this occurs is dependent on the acoustic impedance of each media, and the angle of incidence. Acoustic impedance is defined as

$$Z = \rho v. \tag{7.1}$$

Let us consider a plane boundary at $x = 0$ separating two homogeneous materials with acoustic impedance Z_1 on the negative side and Z_2 on the positive side of the x axis. Now let us consider an incident wave, heading in a positive direction toward the boundary at an angle θ_i, as in figure 7.3, of the form

$$p_i = A_i e^{i(k_1 x \cos\theta_i + k_1 y \sin\theta_i - \omega t)}, \tag{7.2}$$

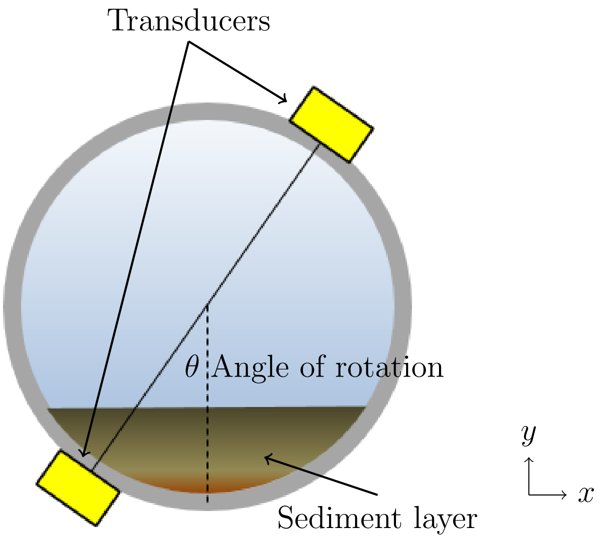

Figure 7.2

Cross section of the pipe experiment set up. The transducer pair are in yellow. The angle of rotation θ is measured from the vertical line through the centre.

which, from the solution of Helmholtz equations, in turn, generates a reflected wave,

$$p_r = A_r e^{-i(k_1 x \cos\theta_r - k_1 y \sin\theta_r + \omega t)}, \tag{7.3}$$

and a transmitted wave

$$p_t = A_t e^{i(k_2 x \cos\theta_t + k_2 y \sin\theta_t - \omega t)}, \tag{7.4}$$

where the subscripts i, r and t represent the incident, reflected and transmitted waves respectively; $k_1 = \frac{\omega}{v_1}$ and $k_2 = \frac{\omega}{v_2}$ are the wave numbers of materials 1 and 2; and A are the amplitudes of each wave.

We need to consider what happens to these waves at the boundary. For wave transmissions, there are two boundary conditions that need to be met. Firstly, the acoustic pressures need to be equal on both sides of the boundary, namely,

$$p_- = p_+ \text{ at } x = 0, \tag{7.5}$$

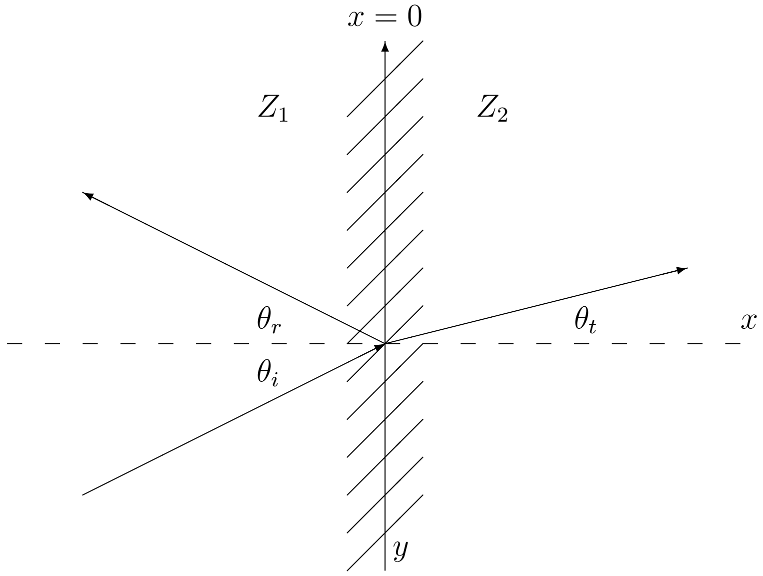

Figure 7.3

Diagram showing how an acoustic wave is reflected and transmitted when it incident on a boundary (at $x = 0$) between two materials.

where p_- and p_+ are the acoustic pressures on the negative and positive sides of the x-axis respectively. Secondly, the normal components of the particle velocity on both sides of the boundary must be equal,

$$\frac{1}{\rho_1}\mathbf{n}\cdot\nabla p_- = \frac{1}{\rho_2}\mathbf{n}\cdot\nabla p_+ \text{ at } x = 0, \tag{7.6}$$

where $\mathbf{n}$ is the normal unit vector to the boundary. Substituting the first of these gives

$$A_i e^{ik_1 y\sin\theta_i} + A_r e^{ik_1 y\sin\theta_r} = A_t e^{ik_2 y\sin\theta_t}, \tag{7.7}$$

for all y. For this to hold, the exponents must all be equal, giving

$$\sin\theta_i = \sin\theta_r, \tag{7.8}$$

and

$$\frac{\sin\theta_i}{v_1} = \frac{\sin\theta_t}{v_2}, \tag{7.9}$$

known as *Snell's Law* [85]. Thus equation (7.7) can be reduced to

$$1 + R = T, \tag{7.10}$$

where R and T are the *reflection and transmission coefficients* defined as

$$R = \frac{A_r}{A_i} \tag{7.11}$$

and

$$T = \frac{A_t}{A_i}. \tag{7.12}$$

Now applying the boundary condition from equation (7.6) we obtain

$$1 - R = \frac{Z_1}{Z_2}\frac{\cos\theta_t}{\cos\theta_i}T, \tag{7.13}$$

giving

$$R = \frac{Z_2\cos\theta_i - Z_1 cos\theta_t}{Z_2\cos\theta_i + Z_1 cos\theta_t}. \tag{7.14}$$

This is known as the *Rayleigh reflection coefficient* [85]. It is also possible to write $\cos\theta_t$ in terms of θ_i by Snell's Law (7.9),

$$\cos\theta_t = \left(1 - \sin^2\theta_t\right)^{\frac{1}{2}} = \left[1 - \left(\frac{v_2}{v_1}\right)^2 \sin^2\theta_i\right]^{\frac{1}{2}}. \tag{7.15}$$

Three distinct cased for the reflected and transmitted waves can be deduced from this equation.

1. If $v_1 > v_2$ then the angle of the transmitted wave is always less than that of the transmitted wave, $\theta_i > \theta_t$.

2. For the case $v_1 < v_2$ we define the *critical angle*, θ_c, as

$$\sin\theta_c = \frac{v_1}{v_2}. \tag{7.16}$$

When $v_1 < v_2$ and $\theta_i < \theta_c$ the transmitted wave is at a larger angle from the incident but still propagates into the medium.

3. When $v_1 < v_2$ and $\theta_i > \theta_c$ the the transmitted wave in equation (7.4), is of the form

$$p_t = A_t e^{\mu x} e^{i(k_1 \sin\theta_i - \omega t)}, \tag{7.17}$$

where

$$\mu = k_2 \left[\left(\frac{v_2}{v_1} \right)^2 \sin^2\theta_i - 1 \right]^{\frac{1}{2}}. \tag{7.18}$$

These waves travels in the y-direction, parallel to the boundary, but decays exponentially. This is called an evanescent wave and no energy is transmitted in to the material. Consequently, all the sound energy is reflected back but with a phase given by

$$R = e^{i\psi}, \tag{7.19}$$

where

$$\psi = 2\tan^{-1} \left[\left(\frac{\rho_1}{\rho_2} \right) \sqrt{\left(\frac{\cos\theta_c}{\cos\theta_i} \right)^2 - 1} \right]. \tag{7.20}$$

This is known as *total internal reflection.*

Provided that the acoustic wave length is short compared with the pipe and sediment layer thickness, we can approximate the propagation of sound as a plane wave though a series of parallel slabs.

7.3.2 COMSOL Model definition

A computational model was created using COMSOL Multiphysics 4.4 to simulate ultrasonic propagation through a pipe wall. One model was made that can be used to simulate the pipe with different transducer positions, and varying amounts of sediment. The model used the COMSOL transient pressure acoustics model and was created in two dimensions. While the experiment would be carried out in three dimensions, the small element size and simulation time step required to accurately model this system in three dimensions would increase the run time for the simulation to unacceptable levels with the current computational set-up. The model report, generated by COMSOL multiphysics, can be found in appendix B.

7.3.3 Geometry

The geometry of the COMSOL model can be found in figure 7.4. There is a circular cross section of a pipe with diameter of 25.4mm with a thickness of 1.6mm. These dimensions are the same as the experimental pipe. Running through the pipe there is a horizontal boundary. The distance, h, between the lowest point of the interior wall, shown in figure 7.5, and the boundary is determined from the concentration, ϕ, of the silica phase, using

$$h = r\left(1 - \cos(\theta)\right), \tag{7.21}$$

where r is the internal radius of the pipe, and θ is determined by the Taylor expansion of

$$\phi = \frac{1}{2\pi}\left(2\theta - \sin(2\theta)\right). \tag{7.22}$$

Attached on opposite sides of the pipe are two transducers. These are marked on figure 7.4 by red and blue lines. They have width of 6.35mm, as the transducers in the experiment have diameter of this amount. The red line transducer is the transmitter and the blue line is the receiver. This pair of transducers can be rotated freely, using the centre of the pipe as a point of rotation, at any angle that is desired.

7.3.4 Acoustic wave propagation

To model the propagating wave, we used the Transient Pressure Acoustics physics contained within the Acoustic module in COMSOL. A plane wave was emitted from the transmitter transducer, shown by the red line in figure 7.4. The pulse emitted at a frequency of 5MHz to match the experimental procedure. This pulse then travels through the pipe and is measured at the receiver transducer, shown by the blue line in figure 7.4. The pulse is also measured at the transmitter transducer, so reflections in the system can also be measured. The measurements are taken by using a probe along the boundary. The probe takes an integral across the boundary to make a measurement, as in the case of acoustic transducers. The acoustic properties of the materials, which include the longitudinal speed of sound and the material's density, can be found in table 2.1.

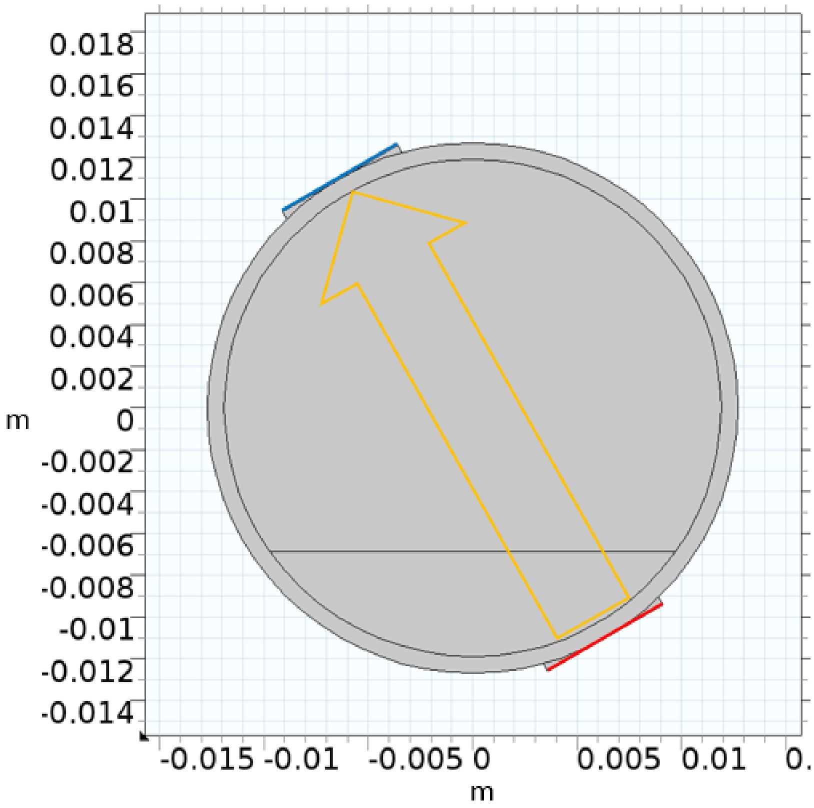

Figure 7.4

Geometry of COMSOL Multiphysics model. A 25.4mm diameter pipe with thickness of 1.6mm. A sedimentation layer is represented by the horizontal line within the pipe. The transducers are highlighted with the red and blue lines. The red line represents the transmitter and the blue line the receiver. The orange arrow shows the direction of the propagating ultrasound wave.

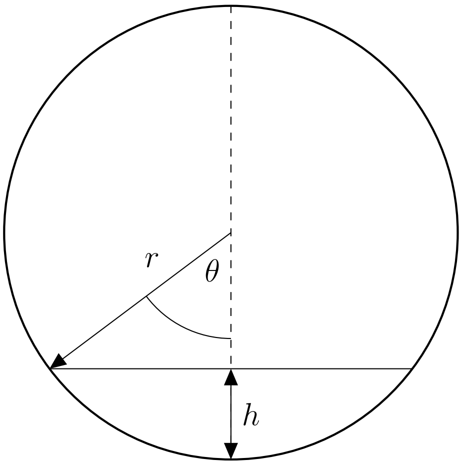

Figure 7.5

The relationship between h and θ as described in equation (7.21), where h is the shortest distance between the lowest point in the pipe and the sediment layer, theta is the angle between the intersect between the sediment layer and the pipe wall with the centre of the pipe, and r is the radius of the pipe.

7.3.5 Finite element mesh

A finite element mesh was used to discretise the configuration in figure 7.4. In this model a free triangular mesh was used. As with all computer modelling a trade off between accuracy and computation time is necessary, so we followed the work by Watson *et al.* [86] by selecting the maximum element size e_{max} to be

$$e_{max} = \frac{\lambda}{10}, \tag{7.23}$$

where λ is the wavelength. This allows for a wave to be sampled ten times in each wavelength, which allows for wave form to still be accurately represented.

7.3.6 Solver configurations

There is only one solver configured in the model, a time dependant solver. The time steps taken are important as they determine the duration and the accuracy of the simulation. Following the work of Mylavarapu and Boddapati [87], we set the time step, t_{step}, to be

$$t_{\text{step}} = \frac{1}{10f}, \tag{7.24}$$

where f is the frequency.

7.3.7 Data analysis

The data generated by COMSOL Multiphysics is measured in the same way as in the experiment in section 7.2, so direct comparisons can be made. The simulation was run over a range of different transducer angles from 0 to 90 degrees. The level of sedimentation was also varied between 0% and 10%.

The advantage of using a software package like COMSOL, is that it allows the visualisation of the wave inside of the pipe, that we would not have otherwise. As we can see in figure 7.6, a propagating wave after 10 microseconds has begun to traverse the pipe. Also seen is the wave reflecting inside the sediment layer.

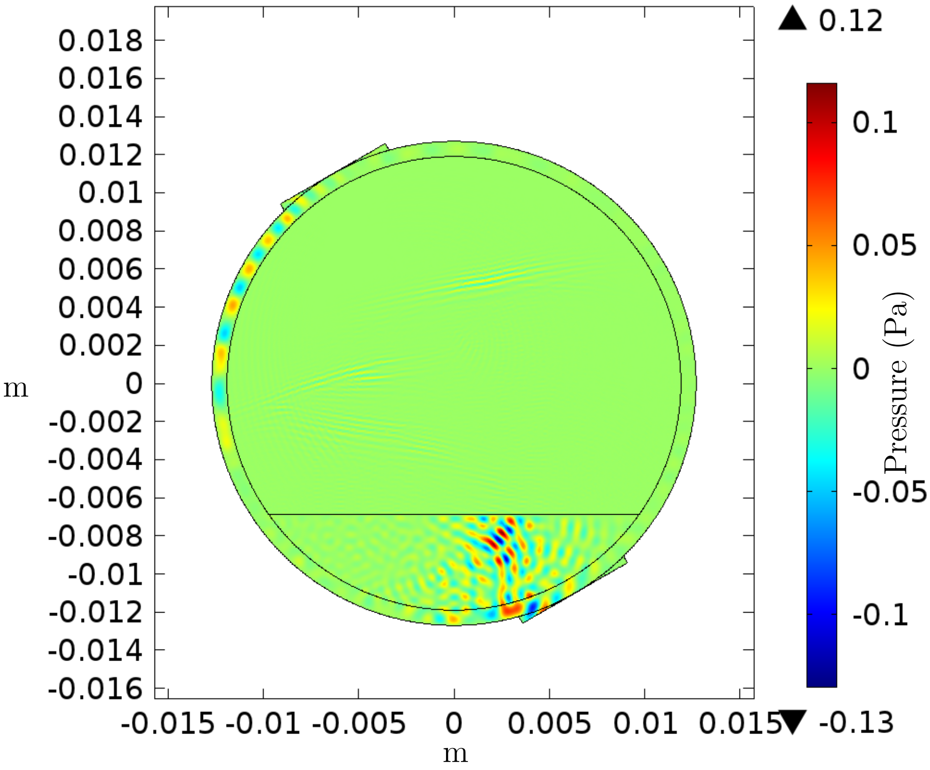

Figure 7.6

COMSOL Multiphysics model of a ultrasonic propagating wave though a pipe after 10 microseconds. This shows the total acoustic pressure field in Pascals. The wave propagating through the pipe can be seen, as well as the reflections in the sediment layer.

7.4 Results

Figures 7.7 and 7.8 show the time of flight and attenuation data for 5% and 10%v/v silica in water comparisons of one dimensional model, COMSOL Multiphysics model and experimental data.

Using a one dimensional model, the time of flight of the sections of the pipe, in figure 7.7, containing water is calculated to be $15.35\mu s$. The angle that the sediment begins is at 36.3° and 46.6° for 5% and 10%, respectively. Without sedimentation layer and only within the pipe, the cross sections of the pipe, both the one dimensional model and the COMSOL Multiphysics are in good agreement with the experimental data. However, as the transducers are rotated into the region where the sediment starts to have an effect we see that the COMSOL model deviates from the one dimensional model but providing a shorter time of flight with a difference of up to $3\mu s$. This could be due to the fact that a part of the plane wave transmitted through the transducer spends more time in the silica phase, in which the speed of sound is fast, before the wave is refracted into the water phase, which reduces the total time the wave takes to reach the receiving transducer. Both of these models deviate from the experimental data. For the 5% data we see that the time of flight remains fairly constant as the transducers are rotated with a steep drop at 10° to levels close to the COMSOL model. This maybe due to how the silica beads settled in the pipe. In both the models, we assumed that the silica layer was perfectly flat which may not be the case in reality. For the 10% we see that the experimental data stays constant until the transducer is rotated below 30° at this point the experimental data has reasonable agreement quite well with the COMSOL multiphysics data, bar a few exceptions. These may be caused by the fact that the silica beads in the pipe do not form a solid block of silica, as the models assume. These variations in the way that the beads are packed contribute towards the errors in the results.

The attenuation in figure 7.8 is calculated by comparing the measurements of the pipe when it only contains water to when there is silica in the pipe. Thus the attenuation in the sections of pipe which only contain water have a one dimensional predication of $0Np$ as no extra attenuation occurs. As the transducer is rotated below 36.3° and 46.6° for 5% and 10% respectively, the predicted attenua-

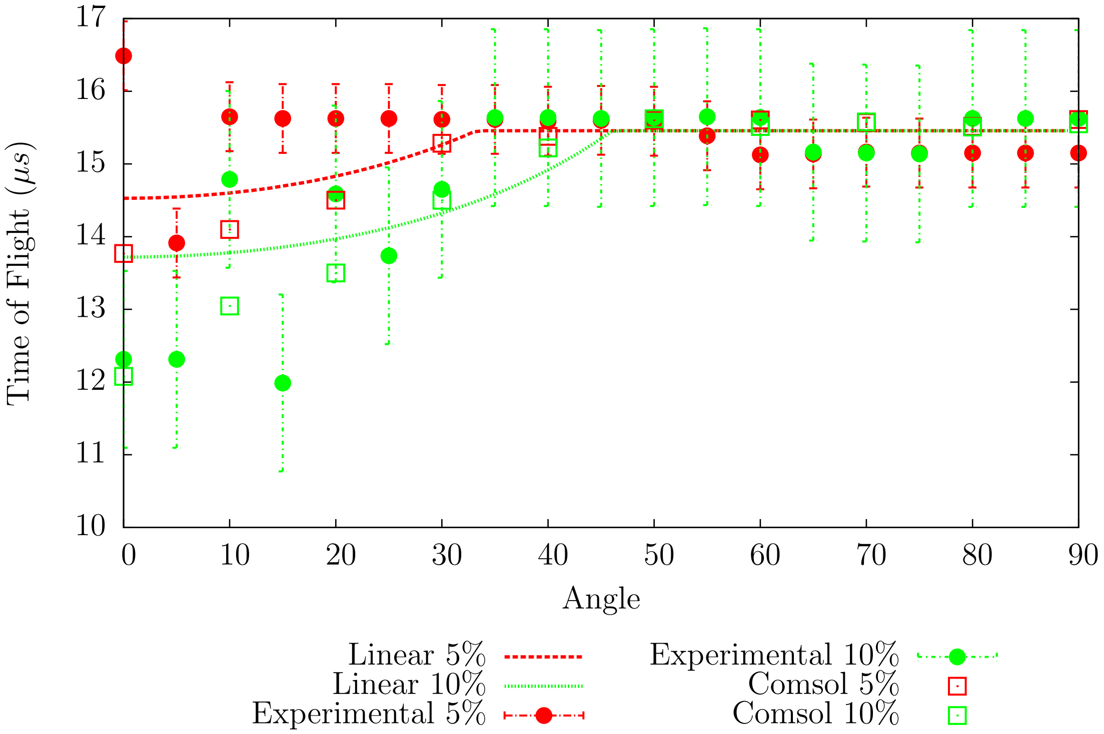

Figure 7.7

Time of flight of an acoustic wave through a pipe section for a one dimensional model (lines), COMSOL Multiphysics model (squares) and experimental data (circles), for 5% and 10% concentrations. It appears that the COMSOL model agrees with the experimental data, within experimental error.

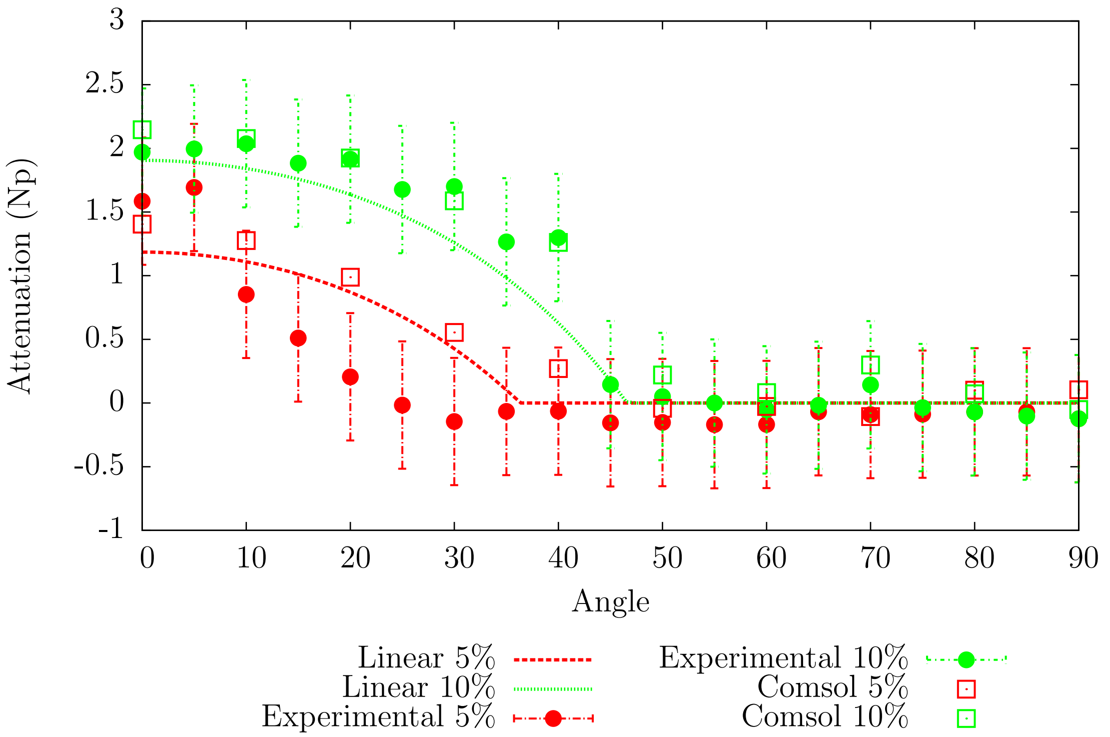

Figure 7.8

Relative attenuation of an acoustic wave through a pipe section for a one dimensional model (lines), COMSOL multiphysics model (squares) and experimental data (circles), for 5% and 10% concentrations. The COMSOL model agrees with the experimental data for the 10% and has reasonable agreement with the 5% data.

tion rises as it approaches 0° to $1.18Np$ and $1.91Np$. The COMSOL Multiphysics model follows the behaviour of the one dimensional models for high angles, but below 50° for 5% we see that the attenuation begins to rise. This is due to the fact that part of the transducer is starting to overlap with the region to the pipe where sediment occurs. As the transducers are rotated to 0° the COMSOL model behaves similarly to the one dimensional model, however with a slightly increased attenuation level. This effect again happens with the 10% sample, with the attenuation starting to rise below 60°, and remaining slightly above the one dimensional model as the angle decreases below 45°. The experimental data follows a similar trend as the time of flight data, the 5% experiment agrees quite well above the sediment layer, but as the transducers are rotated to lower angles we find the measured attenuation is lower than both models predict until 5° where the attenuation becomes slightly higher than one dimensional model, and agree with the COMSOL model. This again could be due to the assumption that the sediment layer is completely level, but in reality this may not be the case. The 10% data also agrees with the models in the region in which there is only water. As we move to lower angles the experimental data also agrees well with the COMSOL model, suggesting that the model indeed does provide a good prediction of the attenuation.

7.5 Conclusions

The purpose of this chapter was to determine whether the use of an in-line pair of rotating ultrasonic transducers can be used to increase its effectiveness in sedimentation measurement of solids in a fluid flow within a pipe. As part of this process we used a simple one dimensional mathematical model, which was improved upon by creating a computational two dimensional model of the monitoring system together with the sedimentation layer. This was used to evaluate whether a model of this type would provide reasonable predictions of the system. Experiments were carried out on a stainless steel pipe with a silica bead sediment layer. The effect of the sediment layer on the time of flight and the attenuation levels over different angles of the pipe were investigated.

The results of the two models show a decrease in the time of flight and an increase in the attenuation as the transducers were increasingly rotated into the sediment layer, with these effects even greater for the COMSOL Multiphysics model. The experimental results show a good quantitative comparison with the COMSOL model data, especially for the 10% silica sediment layer sample. However, some variations from the models occurred, this is due to the model representing the sediment as a continuous layer of silica rather than a packed layer of silica particles. Also, the assumption that the silica layer is perfectly flat may have caused some errors within the prediction as well, as the uneven surface may change the direction the compressional waves are refracted.

While the COMSOL model provided a good prediction of the experimental data, to increase its accuracy a full three dimensional model could be designed, as well as improvements to the properties of the silica sediment layer in regards to spherical packing. However, the long computational times of acoustic propagation models in COMSOL Multiphysics may prevent quick determination of the sediment layer within a pipe.

While the models may have had some variation compared to the experiment, we find that a pair of rotating transducers can be used as a tool in determining the extent of sedimentation occurring. Further testing of different concentration levels could be investigated to determine how small changes in the concentration effect the time of flight and attenuation data, as the current results provide encouraging results. To increase the functionality of the system it could be possible to include multiple transducers. To provide a faster measuring system, as well as provide opportunities for inverse methods for determining the contents of the pipe and distribution of the sedimentation layer.

Chapter 8

Discussion and conclusions

The aim of this thesis is to improve attenuation predictions of acoustic measurements of colloidal suspensions at higher concentrations by considering the thermoacoustic scattering overlap between neighbouring particles. This is motivated by the needs of industry to be able to size particles in ever increasingly concentrated systems that are optically opaque. Current theories provide good results at low concentrations, but over predict scattering at higher concentrations. Attempts to improve attenuation predictions have been made through incorporating the effects of multiple scattering, however, these do not fully capture the thermoacoustic behaviour between close pairs of particles. The main results of this thesis are:

- a new two particle scattering calculation for thermoacoustic scattering,
- incorporation of this new two-particle scattering calculations to improve multiple scattering predictions by considering pair interactions,
- providing new experimental data on mono-and bi-disperse colloidal systems in order to test theoretical predictions,
- developing an apparatus for in-line detection of sedimentation in pipes.

The purpose of this chapter is to briefly bring together the conclusions of the different parts of the study, and to present the conclusions as a whole. From this, suggestions for future research are considered.

Experiments were carried out to obtain new data for mono- and bi-disperse colloidal systems, in chapter 3. Comparing these to existing scattering theories, described in chapter 1 showed that these approaches fail for systems of concentrations above 10%, in particular at lower frequencies. In chapter 1, we saw that the thermal overlap between two particles, was most prominent at lower frequencies. This was the motivation for developing an improved multiple scattering calculation that resolves the thermal fields between particles. For this reason, it was decided to study how the thermal overlaps between two particles behave, and what implications these have on the acoustic measurements of a system as a whole.

In chapters 4 and 5 we determined the thermoacoustic interactions between pairs of particles. The method of solution followed the approach of Harlen *et al.* [27] in constructing asymptotic expansions for values of $|k_c a| \ll 1$ where the particle size is small compared with the acoustic wavelength but of the same order as the thermal decay length, $|k_T a| \sim 1$, since these are the conditions found in acoustic experiments. This is combined with the acoustic two particle scattering model of Greengard and Rokhlin [47]. This was the first step in answering the objective of this thesis.

The overlap of thermal fields when the particles are close together affected the scattering coefficients at orders k_c and $(k_c)^2$ significantly. Although the thermal terms do not come into effect until order k_c^2, at order k_c there is still a difference between the single scattering coefficient and the two particle scattering coefficient as the particles come close together due to interactions through the pressure. This is important as these coefficients contribute to the leading order far field scattering. More interesting is what happens to the second order terms, when the thermal contributions take effect. As with the first order scattering term, the difference between the single and two particle thermal coefficients, increased as the particles get closer. However the sign of the difference changes with frequency from being greater than to being less than the single particle case. The thermal field around the pair of particles produces a scattering response similar to that of a single larger particle even where the particles are not touching. As the second order thermal coefficients impact on the second order acoustic coefficients this suggests that thermoacoustic scattering has a large impact on the far field if the particles are close. We also noted how the different ratios in size between the two particles affected the scattering coefficients. It was seen that a larger particle has a greater impact on the scattering coefficients on a smaller particle, whereas a small particle has little impact on a larger one. This could be because the smaller particle is being "hidden" inside the larger particle's thermal field. We can speculate whether if we had many small particles surrounding a larger particle, as would be the case if there are attractive colloidal forces the small particles would "cloak" the larger particles, or would appear just one larger particle. However, this is beyond the scope of this work.

The dependence of the scattering solution on the angle of the incident wave compared to the axis of the line of centres of the two particles was considered in chapter 5. The two main conclusions from this chapter are: that the most additional scattering effects occurs when the particles are perpendicular to the incident wave, and that the thermal part of the scattering in unaffected by the angle of the incident wave. The case when the particles are orientated perpendicular to the incident wave provides the greatest multiparticle scattering effect as the first sphere shields the second sphere from the pressure field. However, when they are parallel to the incident wave, the acoustic scattering from each sphere can be accounted for from the single scattering result, and so at this order multiple scattering does not need to be accounted for. In contrast the thermal scattering is independent of orientation. The idea of the thermal scattering being independent of incident wave angle has been explored before by Pinfield [42]. In this paper she shows that the thermal incident wave generates an additional compressional scattering term based on the zero order thermal field, which is independent of the incident wave angle. This is consistent with the findings in this thesis.

In chapter 6, we consider how pair-wise interaction between particles can be included in multiple scattering theory, such as the Lloyd and Berry [35] theory. This method allows the inclusion of the modification to scattering due to all thermal overlaps between particles. The results from the previous two chapters are used to calculate a new effective wave number for a given system. Compared with calculations based on scattering by an isolated particle the new two-sphere weak thermal scattering provides lower predicted attenuation levels at the lower frequencies. This is in agreement with the mono- and bi-disperse experimental data gathered in chapter 3, and gives improved predictions at moderate concentrations, from 10% to 30%.

However, although it predicts qualitatively the peak shift that is found in the experimental data it is not quantitative. This may be due to visco-inertial effects which were not considered as part of this thesis. The more likely reason is that each of the pairs of particles were considered independently, i.e. clusters of greater than two spheres were not explicitly considered. It is not unreasonable to assume if two particle close together provide a thermal field of that of a larger single particle, then three particle close together could create a thermal field of an even larger particle, which would in turn, shift the peak in the attenuation prediction curve further.

Also, whilst the two particle weak thermal scattering solution improves the predictions for higher concentrations compared with what the single weak thermal scattering model provided, it is not particularly accurate at concentrations, greater than 30%. Again, we suspect that this is due to only considering two particle scattering, rather than clusters of larger numbers of particles.

Overall, each of the attenuation predictions at higher concentrations, while observing the peak shift and the lowering of attenuation at lower frequencies, still over predicted the levels of attenuation in a similar manner to the single weak thermal scattering theory. Thus, the next step would be to consider scattering from an ensemble of clusters of particles. The translation addition theorem approach could be used to develop a multiple particle scattering calculation, similar to the singularity method [88].

While there are some limitations to the theory presented in this work, it does provide a starting point for developing the theory of ultrasonic colloidal scattering at higher concentrations, that can be extended in a number of ways. These include the incorporation of visco-inertial effects into the system. While care was taken to choose samples in this thesis that minimised this effect, there are many other colloidal systems for which this must be considered. Other developments could include investigating whether considering multiple particle systems can provide a more effective prediction of a system. Multiple particle systems also could be used to investigate structures within colloidal systems, such as those with charged particles.

In chapter 7, it was demonstrated that the rotating pair of transducers on a pipe provided an effective way of detecting sedimentation inside a pipe. The two simulations provided an effective way to interpret the changes in the sound velocity and attenuation as the sedimentation levels change. The simple plane wave solution provides a rapid calculation that maybe of sufficient accuracy for many applications. The full two-dimensional solution provided by the COMSOL Multiphysics model provided better results, but took longer to compute. The model could be extended to a fully three dimensional system, however, computational restrictions would still be an issue.

8.1 Summary of Conclusions

Overall, it can be seen that one can improve acoustic solutions to the particle mixing problem in aqueous dispersions, by using thermoacoustics to look at the pair interactions between particles, and while it does not provide a complete solution to the problem, it does provide a good foundation and an increased understanding for expanding the solution further, to one day solve the problem completely. In summary the principal outputs of the thesis are:

- A full solution of thermoacoustic scattering between a pair of particles, both in-line and at a general angle to the incident wave.
- An improved multiple scattering prediction for concentrations between 10% and 30%.
    - By introducing two particle scattering with thermoacoustic effects
    - Improving multiple scattering theory by considering all pair thermoacoustic interactions
- Obtained new experimental data on bi-disperse emulsions.
- Effectively implemented an rotating pair of ultrasonic transducers on a pipe to detect sedimentation in-line for an opaque suspension.

Appendices

A Wigner $3-j$ Symbols

The Wigner $3-j$ symbols are defined by Edmonds [89] as

$$\left(\begin{array}{cc:c} j_1 & j_2 & j_3 \\ m_1 & m_2 & m_3 \end{array}\right). \tag{A.1}$$

The values j_1, j_2 and j_3, known as *angular momenta*, are all non-negative integers or one is a non-negative integer and the other two are half-odd positive integers. The three values represent three sides of a triangle, as shown in figure A.1, and thus must also satisfy the *triangle conditions*

$$|j_a - j_b| \leq j_c \leq j_a + j_b, \tag{A.2}$$

where a, b and c are any permutation of $1, 2$ and 3. The values m_1, m_2 and m_3 are known as *projective quantum numbers*, and shown in figure A.1, and are given by

$$m_a = -j_a, j_a + 1, \cdots, j_a - 1, j_a, \tag{A.3}$$

for $a = 1, 2, 3$, and must satisfy

$$m_1 + m_2 + m_3 = 0. \tag{A.4}$$

If either conditions from equations (A.2) and (A.4) are violated then

$$\left(\begin{array}{cc:c} j_1 & j_2 & j_3 \\ m_1 & m_2 & m_3 \end{array}\right) = 0. \tag{A.5}$$

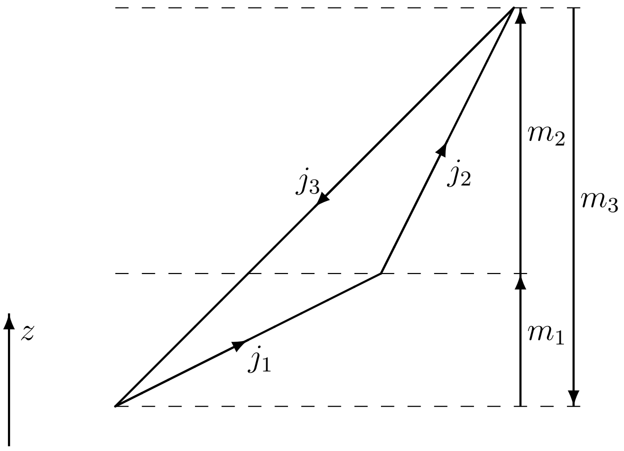

Figure A.1

Visual representation of j_a angular momenta *and* m_a projective quantum numbers *for* $a = 1, 2, 3$.

Otherwise,

$$\left(\begin{array}{cc|c} j_1 & j_2 & j_3 \\ m_1 & m_2 & m_3 \end{array}\right) = (-1)^{j_1-j_2-m_3}\sqrt{\frac{(j_1+j_2-j_3)!(j_1-j_2+j_3)!(-j_1+j_2+j_3)!}{j_1+j_2+j_3+1)!}}$$
$$\times\sqrt{(j_1+m_1)!(j_1-m_1)!(j_2+m_2)!(j_2-m_2)!(j_3+m_3)!(j_3-m_3)!}$$
$$\times\sum_s \frac{(-1)^s}{s!(j_1+j_2-j_3-s)!(j_1-m_1-s)!(j_2+m_2-s)!(j_3-j_2+m_1+s)!(j_3-j_1-m_2+s)!}, \tag{A.6}$$

where the summation value s is for all non-negative integers, such that none of the arguments contained in the factorials are negative.

B COMSOL Multiphysics Report

The following appendix is the report generated by COMSOL multiphysics.

`PipeUltrasoundParametricsweep.mph`

B.1 Global Definitions

B.1.1 Parameters 1

Name	Expression	Description
freq	5e6[Hz]	Frequency
v_steel	6100[m/s]	Speed of sound in steel
v_water	1497[m/s]	Speed of sound in water
v_silica	5960[m/s]	Speed of sound in silica
lambda_steel	v_steel/freq	Wavelength in steel
lambda_water	v_water/freq	Wavelength in water
lambda_silica	v_silica/freq	Wavelength in silica
meshsize_steel	lambda_steel/20	Mesh size in steel
meshsize_water	lambda_water/20	Mesh size in water
meshsize_silica	lambda_silica/20	Mesh size in silica
timestep	1/(freq/20)	Time step size
probeangle	20.0	Probe angle rotation
Sed	2.160241634627	Sedimentation height [mm]

Table B.1

Parameters.

B.1.2 Functions

B.1.2.1 Waveform 1

Function name	pulse
Function type	Wave

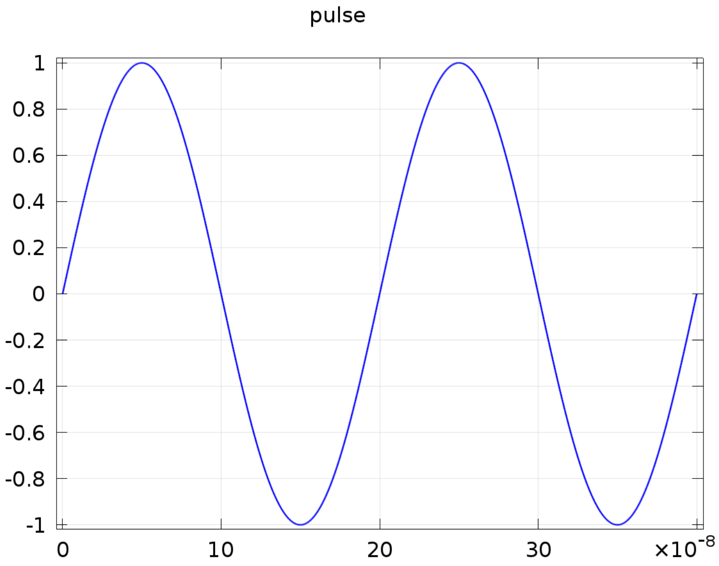

Figure B.1

Waveform 1.

Name	Value
Function name	pulse

Table B.2

Function name.

Name	**Value**
Angular frequency	2*pi*freq

Table B.3

Parameters.

B.1.2.2 Rectangle 1

Function name	rect
Function type	Rectangle

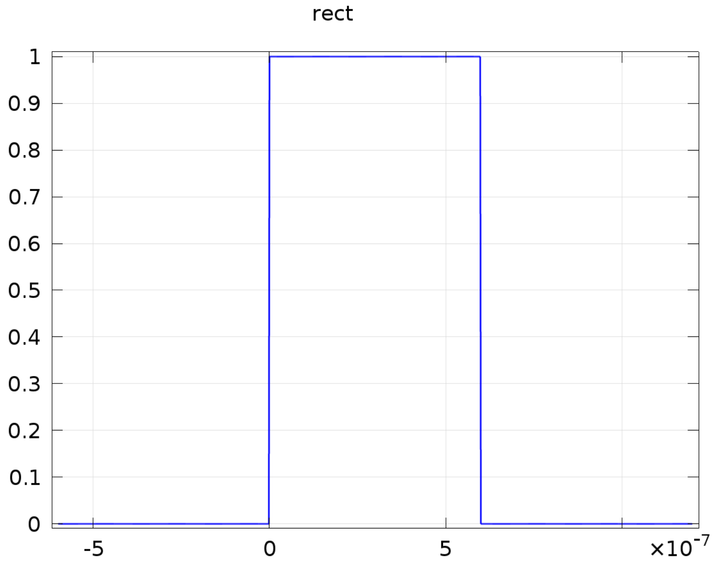

Figure B.2

Rectangle 1.

Name	**Value**
Function name	rect

Table B.4

Function name.

Name	**Value**
Lower limit	0
Upper limit	3/freq

Table B.5

Parameters.

Name	**Value**
Size of transition zone	Off

Table B.6

Smoothing.

B.1.2.3 Waveform 2

Function name	wv2
Function type	Wave

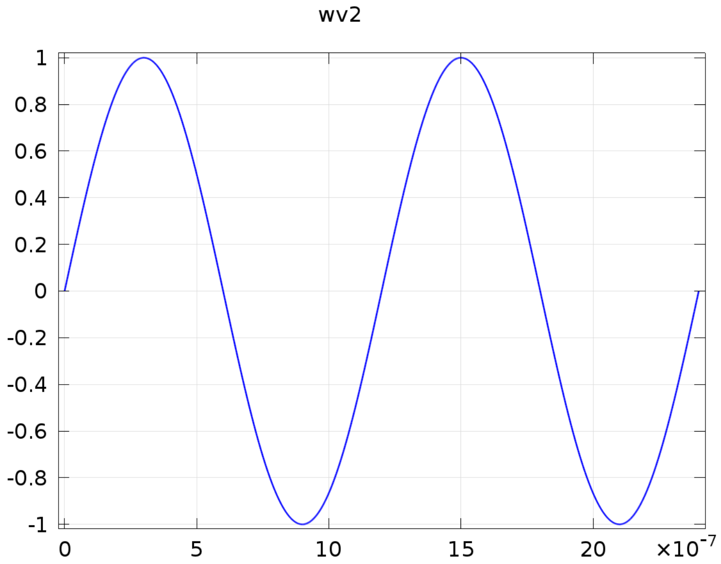

Figure B.3

Waveform 2.

Name	Value
Angular frequency	2*pi*freq/6

Table B.7

Parameters.

B.1.2.4 Analytic 1

Function name	an1
Function type	Analytic

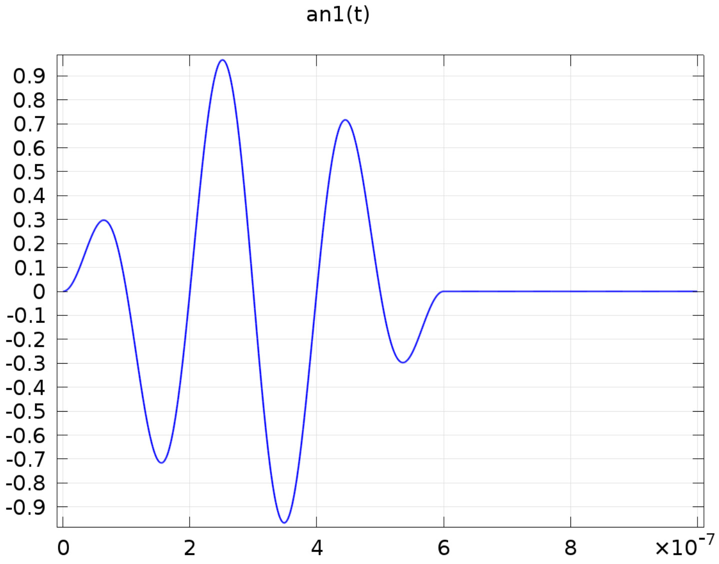

Figure B.4

Analytic 1.

Name	Value
Expression	rect(t)*wv2(t)*pulse(t)
Arguments	t

Table B.8

Definition.

B.1.2.5 Interpolation 1

Function name	sedheight
Function type	Interpolation

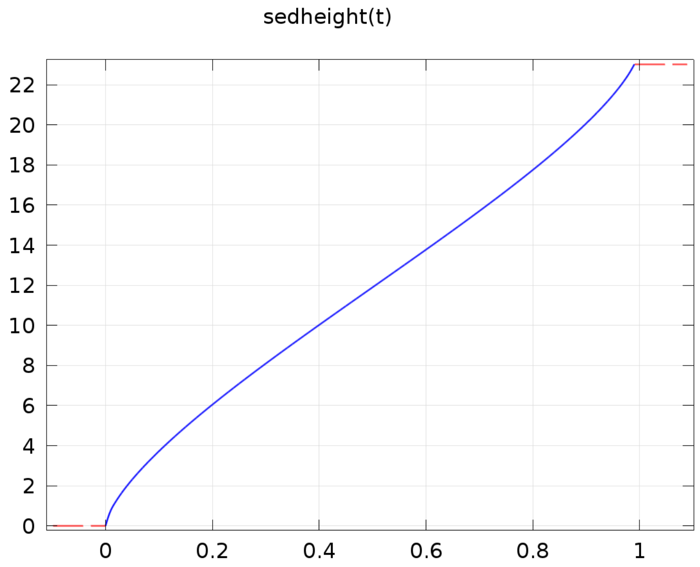

Figure B.5

Interpolation 1.

B.2 Component 1 (comp1)

B.2.1 Definitions

B.2.1.1 Probes

Top Probe

Probe type	Boundary probe

Geometric entity level	Boundary
Selection	Boundaries 2, 4

Table B.9

Selection.

Name	**Value**
Probe variable	top

Table B.10

Probe settings.

Name	**Value**
Expression	actd.p_t
Table and plot unit	Pa
Description	Total acoustic pressure field

Table B.11

Expression.

Name	**Value**
Output table	Probe Table 1
Plot window	Probe Plot 1

Table B.12

Table and window settings.

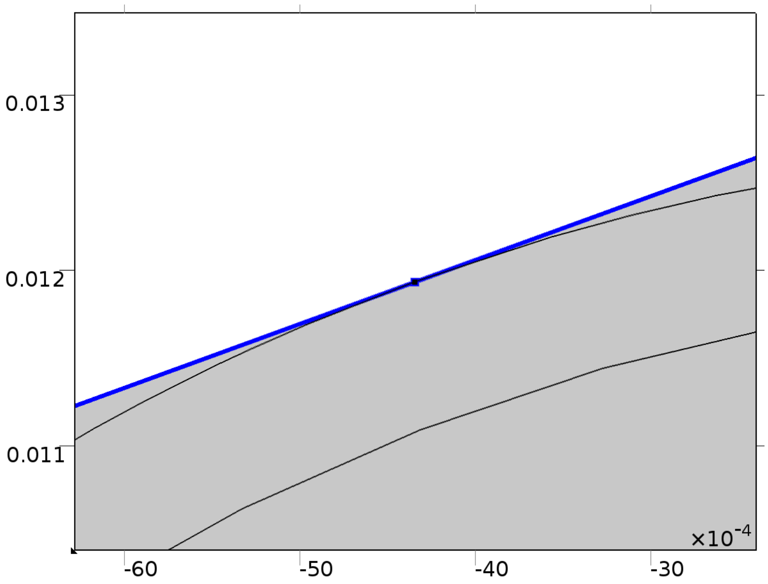

Figure B.6

Selection.

Bottom Probe

Probe type	Boundary probe

Geometric entity level	Boundary
Selection	Boundaries 7-8

Table B.13

Selection.

Name	**Value**
Probe variable	bottom

Table B.14

Probe settings.

Name	**Value**
Expression	actd.p_t
Table and plot unit	Pa
Description	Total acoustic pressure field

Table B.15

Expression.

Name	**Value**
Output table	Probe Table 1
Plot window	Probe Plot 1

Table B.16

Table and window settings.

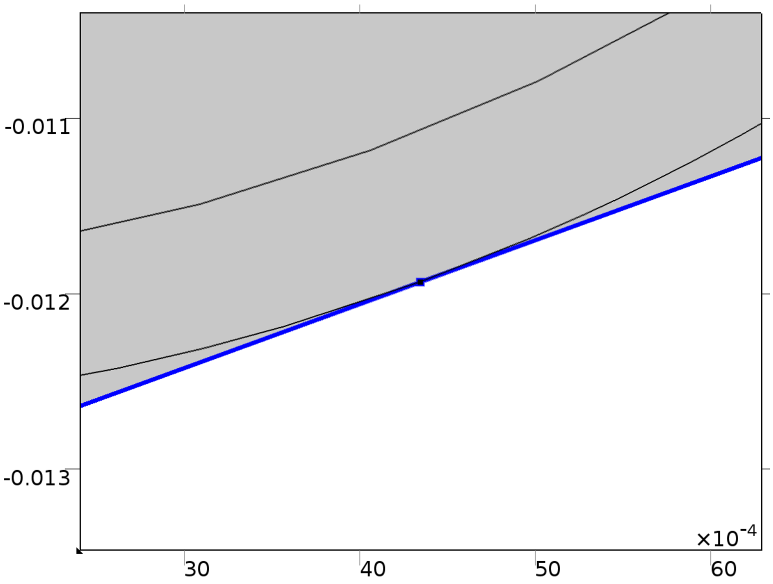

Figure B.7

Selection.

B.2.1.2 Coordinate Systems

Boundary System 1

Coordinate system type	Boundary system
Identifier	sys1

Name	**Value**
Coordinate names	{t1, n, to}
Create first tangent direction from	Global Cartesian

Table B.17

Settings.

B.2.2 Geometry 1

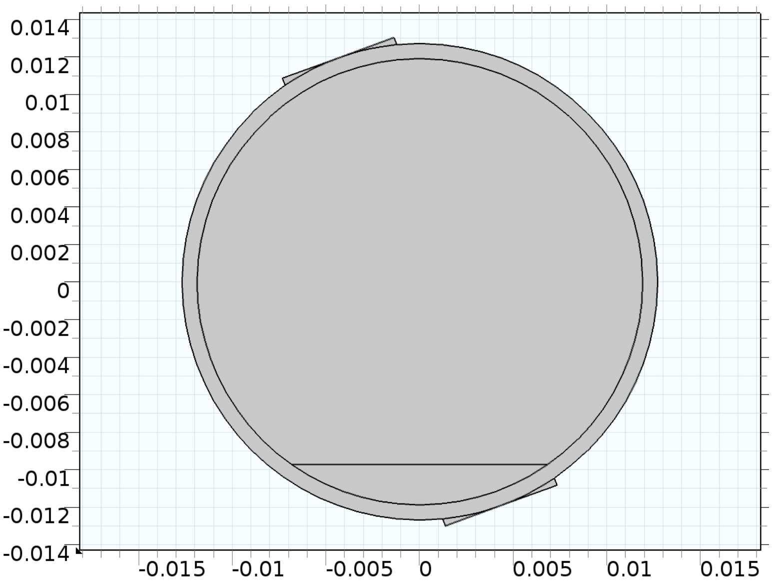

Figure B.8

Geometry 1.

Length unit	m
Angular unit	deg

Table B.18

Units.

Property	**Value**
Space dimension	2
Number of domains	7
Number of boundaries	25
Number of vertices	20

Table B.19

Geometry statistics.

B.2.2.1 Circle 1 (c1)

Name	**Value**
Position	{0, 0}
Radius	(25.4/2)[mm]

Table B.20

Position.

B.2.2.2 Circle 2 (c2)

Name	**Value**
Position	{0, 0}
Radius	((25.4 - 1.6)/2) [mm]

Table B.21

Position.

B.2.2.3 Square 1 (sq1)

Name	**Value**
Position	{-(0.25/2)[inch], -(25.4/2)[mm]}
Side length	0.25[inch]
Side length	0.25[inch]

Table B.22

Position.

B.2.2.4 Square 2 (sq2)

Name	**Value**
Position	{-(0.25/2)[inch], ((25.4/2))[mm] -(0.25)[inch]}
Side length	0.25[inch]
Side length	0.25[inch]

Table B.23

Position.

B.2.2.5 Circle 3 (c3)

Name	**Value**
Position	{0, 0}
Radius	(25.4/2)[mm]

Table B.24

Position.

B.2.2.6 Circle 4 (c4)

Name	**Value**
Position	{0, 0}
Radius	((25.4 - 1.6)/2) [mm]

Table B.25

Position.

B.2.2.7 Rotate 1 (rot1)

Name	**Value**
Rotation	20
Point on axis of rotation	{0, 0}

Table B.26

Selections of resulting entities.

B.2.2.8 Square 3 (sq3)

Name	**Value**
Position	{0, Sed[mm]}
Base	Center
Side length	(25.4 - 1.6)[mm]
Side length	(25.4 - 1.6)[mm]

Table B.27

Position.

B.2.2.9 Circle 5 (c5)

Name	**Value**
Position	{0, 0}
Radius	((25.4 - 1.6)/2) [mm]

Table B.28

Position.

B.2.3 Materials

B.2.3.1 Steel

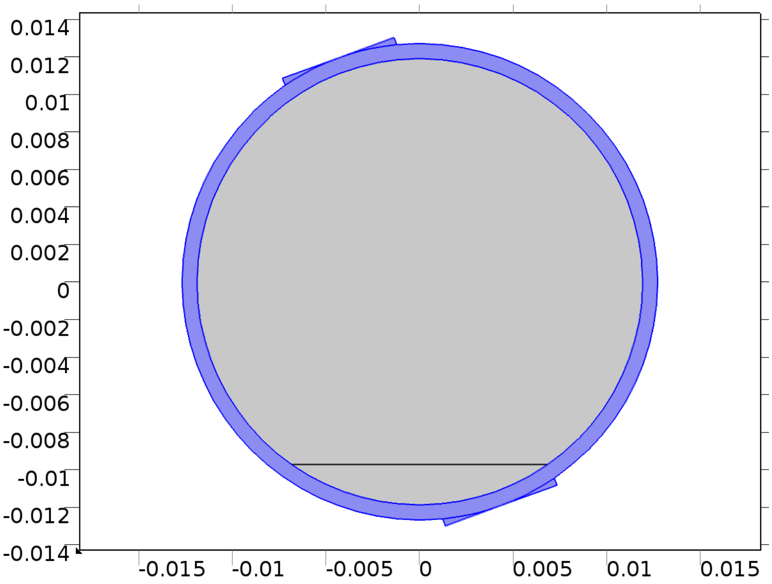

Figure B.9

Steel.

Geometric entity level	Domain
Selection	Domains 1, 4-7

Table B.29

Selection.

Name	**Value**	**Unit**
Density	8050	kg/m^3
Speed of sound	v_steel	m/s

Table B.30

Material parameters.

Description	**Value**
Density	8050
Speed of sound	v_steel

Table B.31

Basic Settings.

B.2.3.2 Water

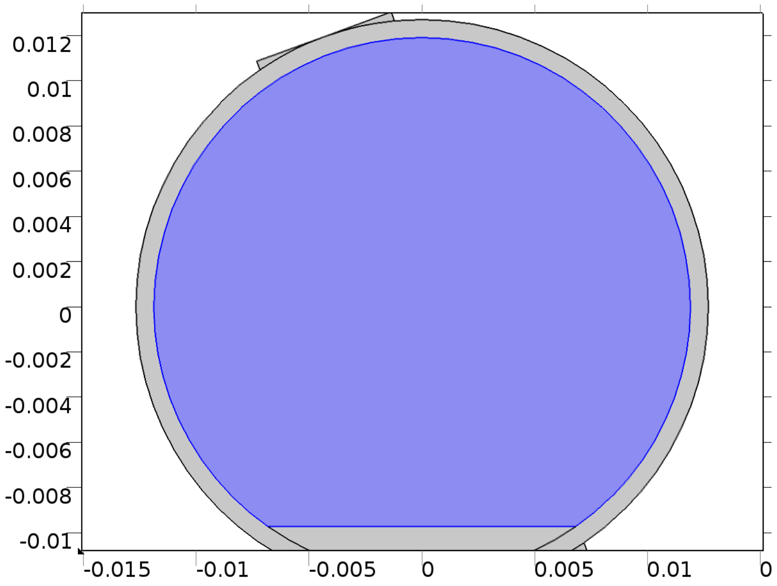

Figure B.10

Water.

Geometric entity level	Domain
Selection	Domain 2

Table B.32

Selection.

Name	**Value**	**Unit**
Density	997	kg/mˆ3
Speed of sound	v_water	m/s

Table B.33

Material parameters.

Description	Value
Density	997
Speed of sound	v_water

Table B.34

Basic Settings.

B.2.3.3 Silica

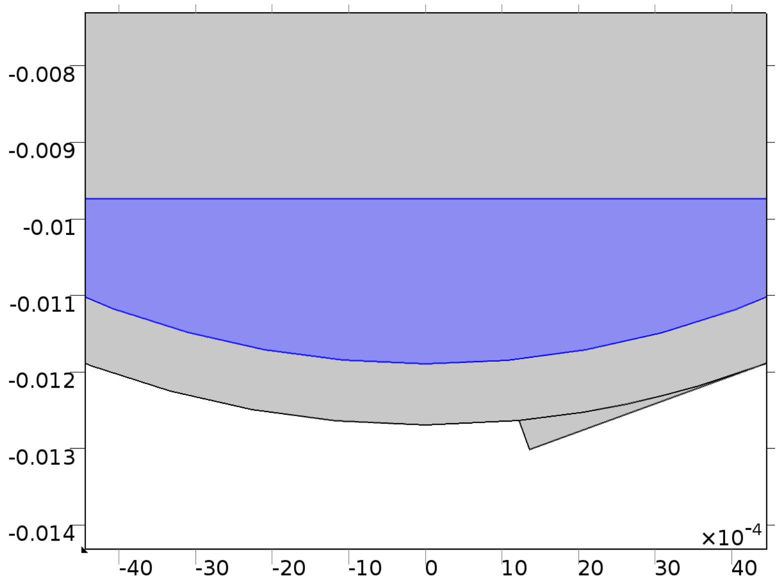

Figure B.11

Silica.

Geometric entity level	Domain
Selection	Domain 3

Table B.35

Selection.

Name	Value	Unit
Density	2650	kg/m^3
Speed of sound	v_silica	m/s

Table B.36

Material parameters.

Description	Value
Density	2650
Speed of sound	v_silica

Table B.37

Basic Settings.

B.2.4 Pressure Acoustics, Transient (actd)

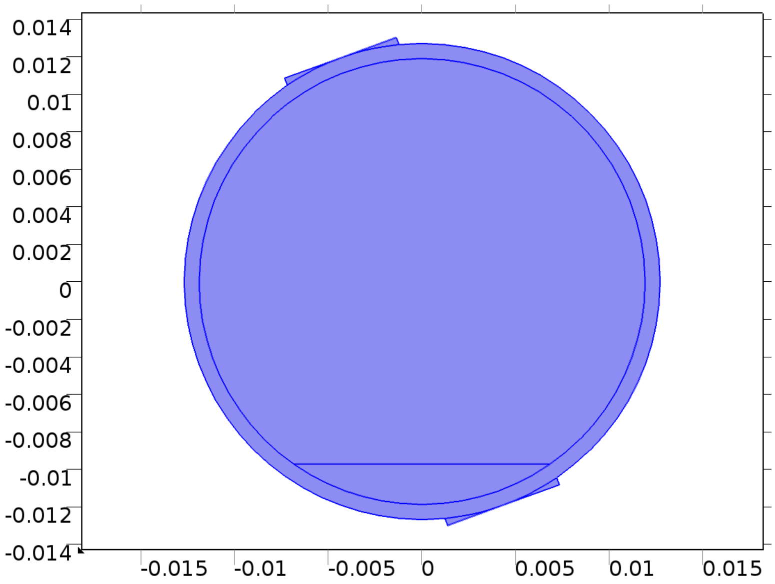

Figure B.12

Pressure Acoustics, Transient.

Geometric entity level	Domain
Selection	Domains 1-7

Table B.38

Selection.

Equations

$$\frac{1}{\rho c^2}\frac{\partial^2 p_t}{\partial t^2} + \nabla \cdot \left(-\frac{1}{\rho} \left(\nabla p_t - \mathbf{q}_d \right) \right) = Q_m, \tag{B.1}$$

$$p_t = p + p_b, \tag{B.2}$$

Description	**Value**
Pressure	Quadratic
Value type when using splitting of complex variables	Complex
Out-of-plane wave number	0
Reference pressure for the sound pressure level	Use reference pressure for air

Table B.39

Settings.

COMSOL Multiphysics
Acoustics Module

Table B.40

Used products.

Name	Expression	Unit	Description	Selection
actd.delta	1		Scaling factor	Domains 1-7
actd.pref_SPL	2.0E-5[Pa]	Pa	Reference pressure	Global
actd.nx	treatasconst(nx)	1	Normal vector, x component	Boundaries 3, 12-16, 19-20, 22-24
actd.ny	treatasconst(ny)	1	Normal vector, y component	Boundaries 3, 12-16, 19-20, 22-24
actd.nz	0	1	Normal vector, z component	Boundaries 3, 12-16, 19-20, 22-24
actd.nx	treatasconst(dnx)	1	Normal vector, x component	Boundaries 1-2, 4-11, 17-18, 21, 25
actd.ny	treatasconst(dny)	1	Normal vector, y component	Boundaries 1-2, 4-11, 17-18, 21, 25
actd.nz	0	1	Normal vector, z component	Boundaries 1-2, 4-11, 17-18, 21, 25
actd.nxmesh	treatasconst(root.nxmesh)	1	Normal vector (mesh), x component	Boundaries 3, 12-16, 19-20, 22-24
actd.nymesh	treatasconst(root.nymesh)	1	Normal vector (mesh), y component	Boundaries 3, 12-16, 19-20, 22-24
actd.nzmesh	0	1	Normal vector (mesh), z component	Boundaries 3, 12-16, 19-20, 22-24
actd.nxmesh	treatasconst(root.dnxmesh)	1	Normal vector (mesh), x component	Boundaries 1-2, 4-11, 17-18, 21, 25
actd.nymesh	treatasconst(root.dnymesh)	1	Normal vector (mesh), y component	Boundaries 1-2, 4-11, 17-18, 21, 25
actd.nzmesh	0	1	Normal vector (mesh), z component	Boundaries 1-2, 4-11, 17-18, 21, 25

Table B.41

Variables.

B.2.4.1 Transient Pressure Acoustics Model 1

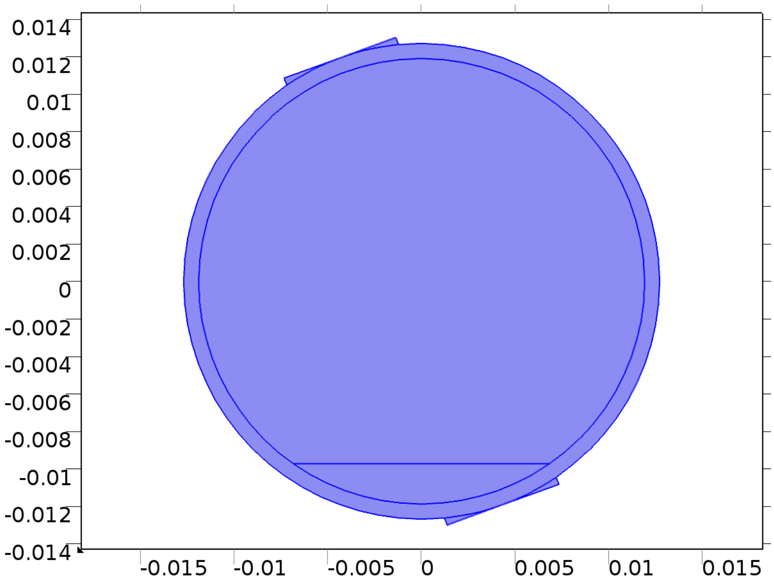

Figure B.13

Transient Pressure Acoustics Model 1.

Geometric entity level	Domain
Selection	Domains 1-7

Table B.42

Selection.

Equations (B.1) and (B.2).

Settings

Description	**Value**
Fluid model	Linear elastic
Density	From material
Speed of sound	From material

Table B.43

Settings.

Property	**Material**	**Property group**
Density	Steel	Basic
Speed of sound	Steel	Basic
Density	Water	Basic
Speed of sound	Water	Basic
Density	Silica	Basic
Speed of sound	Silica	Basic

Table B.44

Properties from material.

Table B.45

Variables.

Name	**Expression**	**Unit**	**Description**	**Selection**
actd.p_s	actd.p_t-actd.p_b	Pa	Scattered pressure field	Domains 1-7
actd.p_b	0	Pa	Background pressure field	Domains 1-7
actd.rho	model.input.rho	kg/m^3	Density	Domains 1, 4-7
actd.rho	model.input.rho	kg/m^3	Density	Domain 2
actd.rho	model.input.rho	kg/m^3	Density	Domain 3
actd.c	model.input.c	m/s	Speed of sound	Domains 1, 4-7
actd.c	model.input.c	m/s	Speed of sound	Domain 2
actd.c	model.input.c	m/s	Speed of sound	Domain 3
actd.Q	0	1/s^2	Monopole source	Domains 1-7
actd.qx	0	N/m^3	Dipole source, x component	Domains 1-7

Continued on next page

Table B.45 – *Continued from previous page*

Name	**Expression**	**Unit**	**Description**	**Selection**
actd.qy	0	N/m^3	Dipole source, y component	Domains 1-7
actd.qz	0	N/m^3	Dipole source, z component	Domains 1-7
actd.q_totx	actd.qx	N/m^3	Total dipole source, x component	Domains 1-7
actd.q_toty	actd.qy	N/m^3	Total dipole source, y component	Domains 1-7
actd.q_totz	actd.qz	N/m^3	Total dipole source, z component	Domains 1-7
actd.nacc	0	m/s^2	Inward acceleration	Boundaries 1-25
actd.FAcoPerAreax	actd.p_t*actd.nx	N/m^2	Acoustic load per unit area, x component	Boundaries 1-25
actd.FAcoPerAreay	actd.p_t*actd.ny	N/m^2	Acoustic load per unit area, y component	Boundaries 1-25
actd.FAcoPerAreaz	actd.p_t*actd.nz	N/m^2	Acoustic load per unit area, z component	Boundaries 1-25
actd.p_t	p+actd.p_b	Pa	Total acoustic pressure field	Domains 1-7
actd.c_c	actd.c	m/s	Complex speed of sound	Domains 1-7

Continued on next page

Table B.45 – *Continued from previous page*

Name	**Expression**	**Unit**	**Description**	**Selection**
actd.rho_c	actd.rho	kg/m^3	Complex density	Domains 1-7
actd.Z	actd.rho_c*actd.c_c	Pa*s/m	Characteristic acoustic impedance	Domains 1-7
actd.gradpx	d(actd.p_t,x)	N/m^3	Gradient of the total pressure, x component	Domains 1-7
actd.gradpy	d(actd.p_t,y)	N/m^3	Gradient of the total pressure, y component	Domains 1-7
actd.gradpz	0	N/m^3	Gradient of the total pressure, z component	Domains 1-7
actd.grad testpx	test(px)	N/m^3	Help variable for equations, x component	Domains 1-7
actd.grad testpy	test(py)	N/m^3	Help variable for equations, y component	Domains 1-7
actd.grad testpz	0	N/m^3	Help variable for equations, z component	Domains 1-7
actd.ax	-(actd.gradpx-actd.q_totx) /actd.rho_c	m/s^2	Local acceleration, x component	Domains 1-7
actd.ay	-(actd.gradpy-actd.q_toty) /actd.rho_c	m/s^2	Local acceleration, y component	Domains 1-7

Continued on next page

Table B.45 – *Continued from previous page*

Name	**Expression**	**Unit**	**Description**	**Selection**
actd.az	-(actd.gradpz-actd.q_totz) /actd.rho_c	m/s^2	Local acceleration, z component	Domains 1-7
actd.a_inst	sqrt(real(actd.ax)^2 +real(actd.ay)^2 +real(actd.az)^2)	m/s^2	Instantaneous local acceleration	Domains 1-7
actd.absp	sqrt(realdot(actd.p_t ,actd.p_t))	Pa	Absolute pressure	Domains 1-7
actd.aipx	actd.ax	m/s^2	In-plane acceleration, x component	Domains 1-7
actd.aipy	actd.ay	m/s^2	In-plane acceleration, y component	Domains 1-7
actd.aipz	0	m/s^2	In-plane acceleration, z component	Domains 1-7
actd.aopx	actd.ax	m/s^2	Out-of-plane acceleration, x component	Domains 1-7
actd.aopy	actd.ay	m/s^2	Out-of-plane acceleration, y component	Domains 1-7
actd.aopz	actd.az	m/s^2	Out-of-plane acceleration, z component	Domains 1-7
actd.aip_inst	sqrt(real(actd.aipx)^2 +real(actd.aipy)^2 +real(actd.aipz)^2)	m/s^2	Instantaneous in-plane acceleration	Domains 1-7

Continued on next page

Table B.45 – *Continued from previous page*

Name	**Expression**	**Unit**	**Description**	**Selection**
actd.aop _inst	sqrt(real(actd.aopx)^2 +real(actd.aopy)^2 +real(actd.aopz)^2)	m/s^2	Instantaneous out-of-plane acceleration	Domains 1-7
actd.diss _visc	0	W/m^3	Viscous power dissipation density	Domains 1-7
actd.diss _therm	0	W/m^3	Thermal power dissipation density	Domains 1-7
actd.diss _tot	actd.diss_visc +actd.diss_therm	W/m^3	Total thermo-viscous power dissipation density	Domains 1-7

Name	**Shape function**	**Unit**	**Description**	**Shape frame**	**Selection**
p	Lagrange (Quadratic)	Pa	Pressure	Material	Domains 1-7

Table B.46

Shape functions.

Weak expression	**Integration frame**	**Selection**
(-actd.gradpx*actd.gradtestpx-actd.gradpy*actd.gradtestpy-actd.gradpz*actd.gradtestpz-d(d(actd.p_t,t),t)*test(p)/actd.c_c^2)/actd.rho_c	Material	Domains 1-7
actd.delta*actd.Q*test(p)	Material	Domains 1-7
actd.delta*(actd.q_totx*actd.gradtestpx+actd.q_toty*actd.gradtestpy+actd.q_totz*actd.gradtestpz)/actd.rho_c	Material	Domains 1-7

Table B.47

Weak expressions.

B.2.4.2 Sound Hard Boundary (Wall) 1

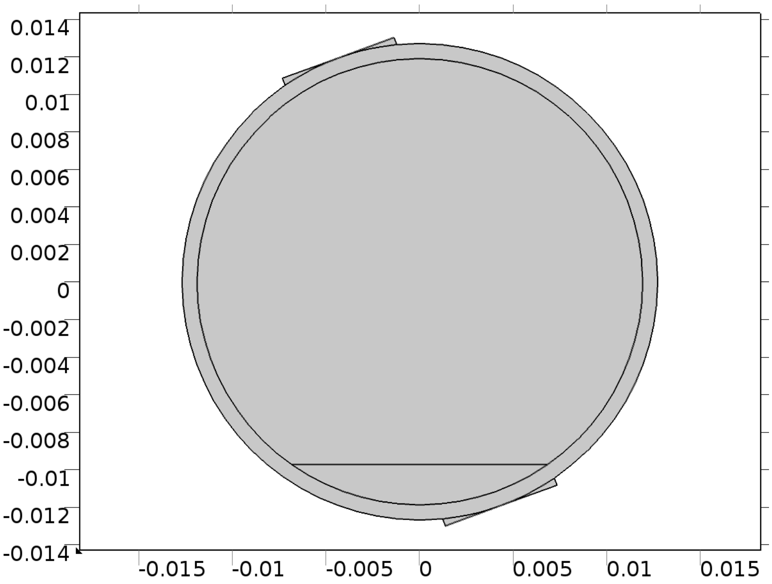

Figure B.14

Sound Hard Boundary (Wall) 1.

Geometric entity level	Boundary
Selection	No boundaries

Table B.48

Selection.

Equations

$$-\mathbf{n} \cdot \left(-\frac{1}{\rho} \left(\nabla p_t - \mathbf{q}_d \right) \right) = 0. \tag{B.3}$$

B.2.4.3 Initial Values 1

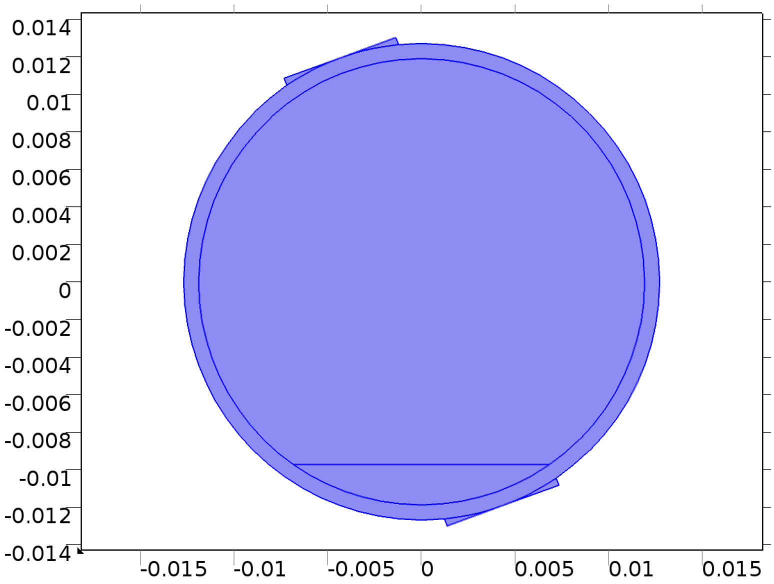

Figure B.15

Initial Values 1.

Geometric entity level	Domain
Selection	Domains 1-7

Table B.49

Selection.

Description	**Value**
Pressure	0
Pressure, first time derivative	0

Table B.50

Settings.

B.2.4.4 Plane Wave Radiation 1

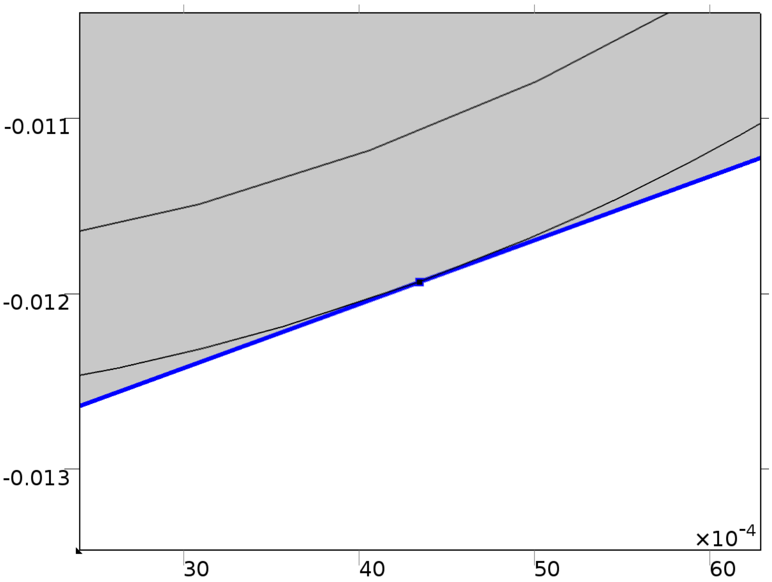

Figure B.16

Plane Wave Radiation 1.

Geometric entity level	Boundary
Selection	Boundaries 7-8

Table B.51

Selection.

Equations

$$-\mathbf{n} \cdot \left(-\frac{1}{\rho} \left(\nabla p_t - \mathbf{q}_d \right) \right) + \frac{1}{\rho} \left(\frac{1}{c} \frac{\partial p}{\partial t} \right) = Q_i. \tag{B.4}$$

Name	**Expression**	**Unit**	**Description**	**Selection**
actd.p_i	0	Pa	Incident pressure field	Boundaries 7-8

Table B.52

Variables.

Weak expression	**Integration frame**	**Selection**
test(p)*(-pt/actd.c+(d(actd.p_i,t) +actd.c*(actd.nx*d(actd.p_i,x) +actd.ny*d(actd.p_i,y)))/actd.c +actd.nx*mean(d(actd.p_b,x)) +actd.ny*mean(d(actd.p_b,y)) +actd.nz*mean(0))/actd.rho	Material	Boundaries 7-8

Table B.53

Weak expressions.

Incident Pressure Field 1

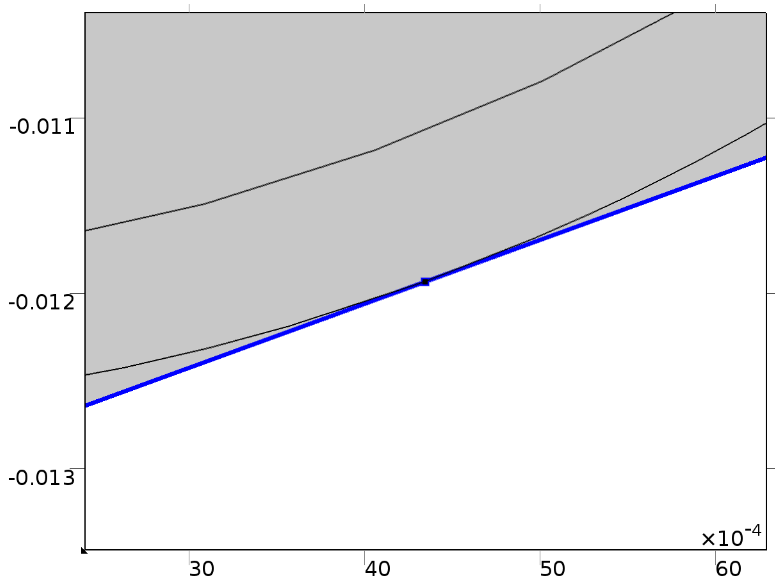

Figure B.17

Incident Pressure Field 1.

Geometric entity level	Boundary
Selection	Boundaries 7-8

Table B.54

Selection.

Equations (B.4) and

$$Q_i = \frac{1}{\rho}\left(\frac{1}{c}\frac{\partial p_i}{\partial t}\right) + \mathbf{n}\cdot\frac{1}{\rho}\nabla p_i. \tag{B.5}$$

Name	Expression	Unit	Description	Selection
actd.p_i	an1(t)	Pa	Incident pressure field	Boundaries 7-8

Table B.55

Variables.

B.2.4.5 Plane Wave Radiation 2

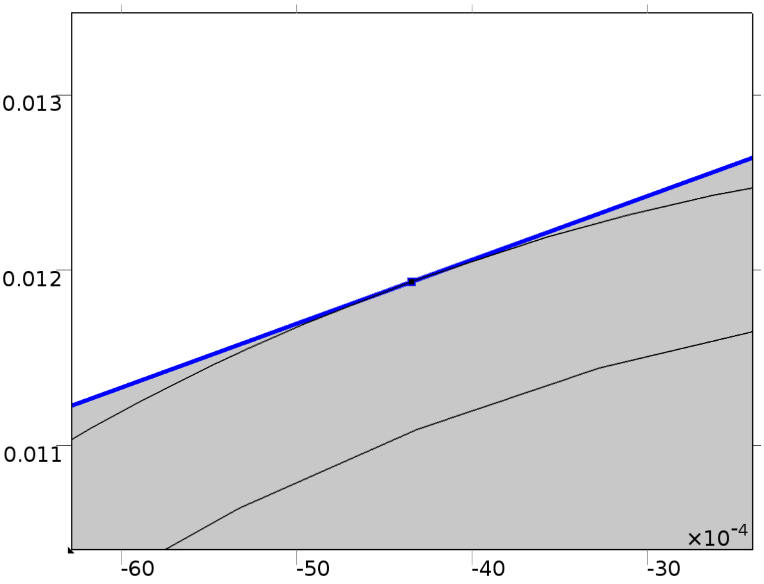

Figure B.18

Plane Wave Radiation 2.

Geometric entity level	Boundary
Selection	Boundaries 2, 4

Table B.56

Selection.

Equation (B.4).

Name	**Expression**	**Unit**	**Description**	**Selection**
actd.p_i	0	Pa	Incident pressure field	Boundaries 2, 4

Table B.57

Variables.

Weak expression	**Integration frame**	**Selection**
test(p)*(-pt/actd.c +(d(actd.p_i,t) +actd.c *(actd.nx*d(actd.p_i,x) +actd.ny*d(actd.p_i,y)))/actd.c +actd.nx*mean(d(actd.p_b,x)) +actd.ny*mean(d(actd.p_b,y)) +actd.nz*mean(0))/actd.rho	Material	Boundaries 2, 4

Table B.58

Weak expressions.

B.2.4.6 Impedance 1

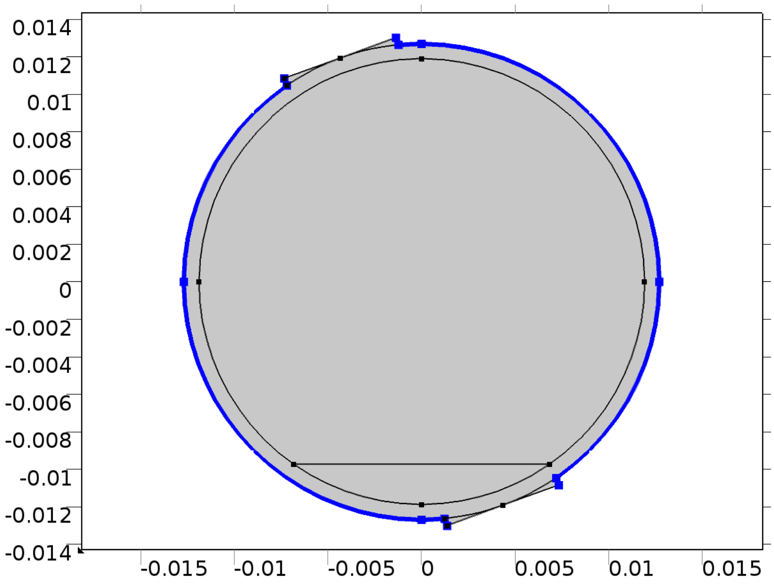

Figure B.19

Impedance 1.

Geometric entity level	Boundary
Selection	Boundaries 1, 5-6, 9-11, 17-18, 21, 25

Table B.59

Selection.

Equation

$$-\mathbf{n}\cdot\left(-\frac{1}{\rho}\left(\nabla p_t-\mathbf{q}_d\right)\right)=\frac{1}{Z_i}\frac{\partial p_t}{\partial t} \tag{B.6}$$

Name	Expression	Unit	Description	Selection
actd.Zi	1.2[kg/m^3]*343[m/s]	Pa*s/m	Impedance	Boundaries 1, 5-6, 9-11, 17-18, 21, 25

Table B.60

Variables.

Weak expression	Integration frame	Selection
-mean(d(actd.p_t,t))*test(p)/actd.Zi	Material	Boundaries 1, 5-6, 9-11, 17-18, 21, 25

Table B.61

Weak expressions.

B.2.5 Mesh 1

Property	Value
Minimum element quality	2.647E-5
Average element quality	0.9819
Triangular elements	154934
Edge elements	2604
Vertex elements	20

Table B.62

Mesh statistics.

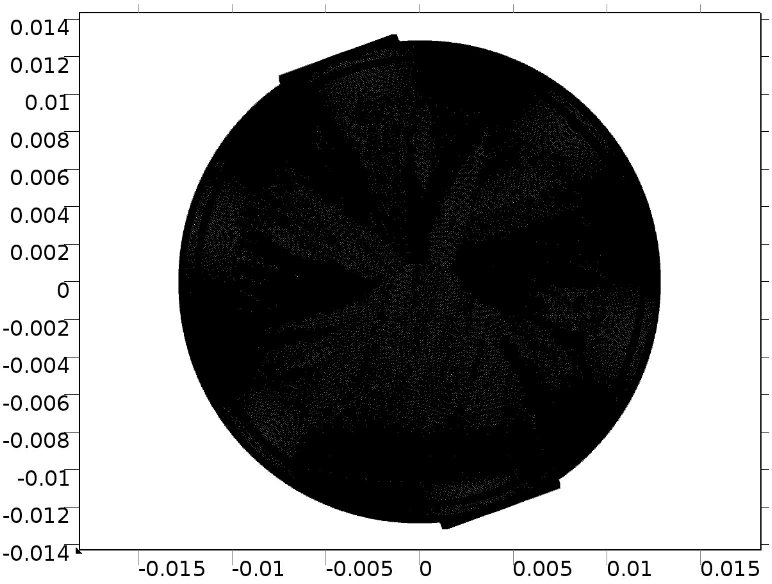

Figure B.20

Mesh 1.

B.2.5.1 Size (size)

Name	Value
Maximum element size	meshsize_water
Minimum element size	7.62E-6
Curvature factor	0.3
Maximum element growth rate	1.3
Custom element size	Custom

Table B.63

Settings.

B.2.5.2 Free Triangular 1 (auto_f1)

Geometric entity level	Remaining

Table B.64

Selection.

B.3 Study 1

B.3.1 Parametric Sweep

probeangle
Sed

Table B.65

Parameter names.

Parameter names	Parameter value list
probangle	range(0,10,90)
Sed	3.473758029929, 2.160241634627 , 0

Table B.66

Parameters.

B.3.2 Time Dependent

Property	Value
Include geometric nonlinearity	Off

Table B.67

Study settings.

Times: range(0,8.0e-5/14,8.0e-5)

Geometry	**Mesh**
Geometry 1 (geom1)	mesh1

Table B.68

Mesh selection.

Physics	**Discretization**
Pressure Acoustics, Transient (actd)	physics

Table B.69

Physics selection.

B.3.3 Solver Configurations

B.3.3.1 Solver 1

Compile Equations: Time Dependent (st1)

Name	**Value**
Use study	Study 1
Use study step	Time Dependent

Table B.70

Study and step.

Dependent Variables 1 (v1)

Name	**Value**
Defined by study step	Time Dependent

Table B.71

General.

Name	**Value**
Solution	Zero

Table B.72

Initial values of variables solved for.

Name	**Value**
Solution	Zero

Table B.73

Values of variables not solved for.

Pressure (comp1.p) (comp1_p)

Name	**Value**
Field components	comp1.p

Table B.74

General.

Time-Dependent Solver 1 (t1)

Name	Value
Defined by study step	Time Dependent
Time	{0, 5.7142857142857145E-6, 1.1428571428571429E-5, 1.7142857142857145E-5, 2.2857142857142858E-5, 2.857142857142857E-5, 3.428571428571429E-5, 4.0E-5, 4.5714285714285716E-5, 5.142857142857143E-5, 5.714285714285714E-5, 6.285714285714286E-5, 6.857142857142858E-5, 7.428571428571429E-5, 8.0E-5}
Relative tolerance	0.0001

Table B.75

General.

Name	Value
Method	Generalized alpha

Table B.76

Time stepping.

Fully Coupled 1 (fc1)

Name	Value
Linear solver	Direct

Table B.77

General.

B.4 Results

B.4.1 Data Sets

B.4.1.1 Solution 1

Name	Value
Solution	Solver 1
Component	Save Point Geometry 1

Table B.78

Solution.

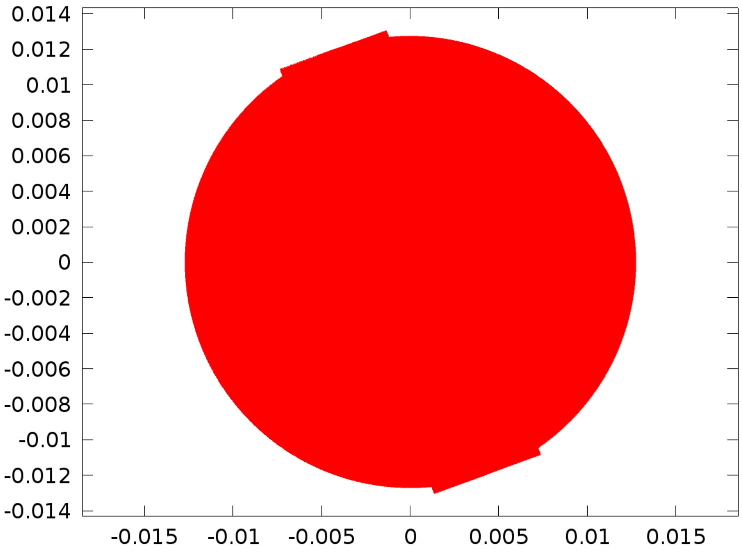

Figure B.21

Data set: Solution 1.

B.4.1.2 Probe Solution 2

Name	**Value**
Solution	Solver 1
Component	Save Point Geometry 1

Table B.79

Solution.

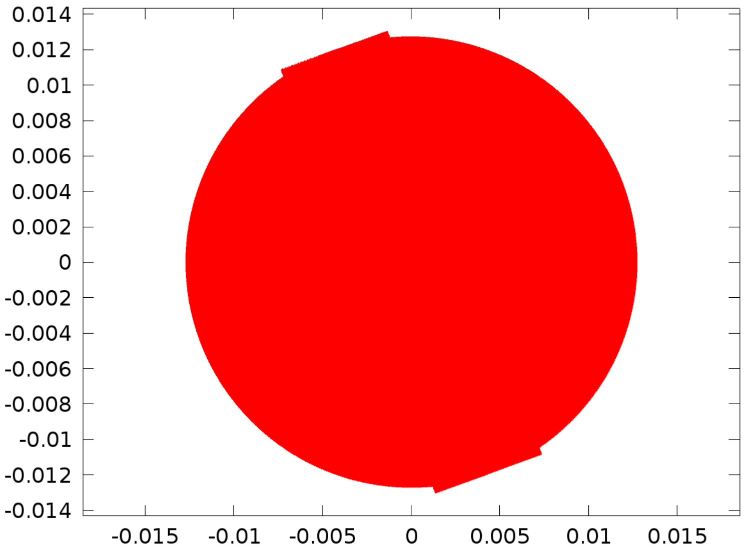

Figure B.22

Data set: Probe Solution 2.

B.4.1.3 Top Probe

Geometric entity level	Boundary
Selection	Boundaries 2, 4

Table B.80

Selection.

Name	**Value**
Data set	Probe Solution 2

Table B.81

Data.

Name	**Value**
Method	Integration
Integration order	4
Integration order	On

Table B.82

Settings.

B.4.1.4 Bottom Probe

Geometric entity level	Boundary
Selection	Boundaries 7-8

Table B.83

Selection.

Name	**Value**
Data set	Probe Solution 2

Table B.84

Data.

Name	Value
Method	Integration
Integration order	4
Integration order	On

Table B.85

Settings.

B.4.2 Plot Groups

B.4.2.1 Acoustic Pressure (actd)

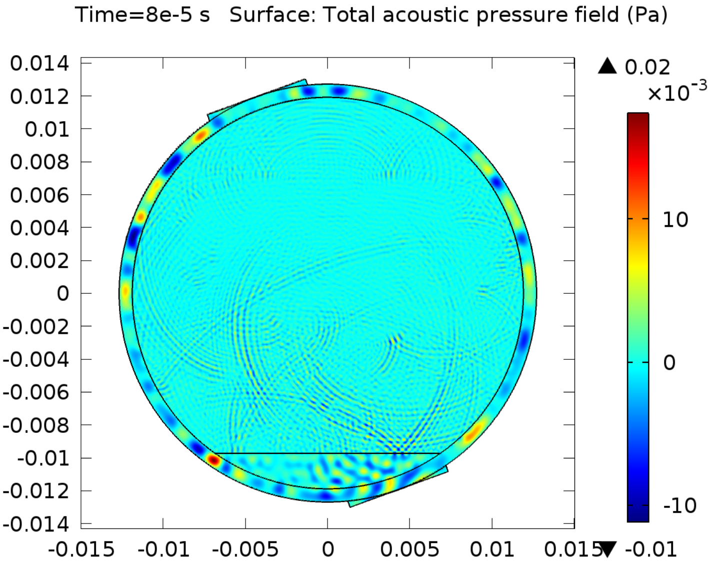

Figure B.23

Time=8e-5 s Surface: Total acoustic pressure field (Pa).

B.4.2.2 Probe 1D Plot Group 2

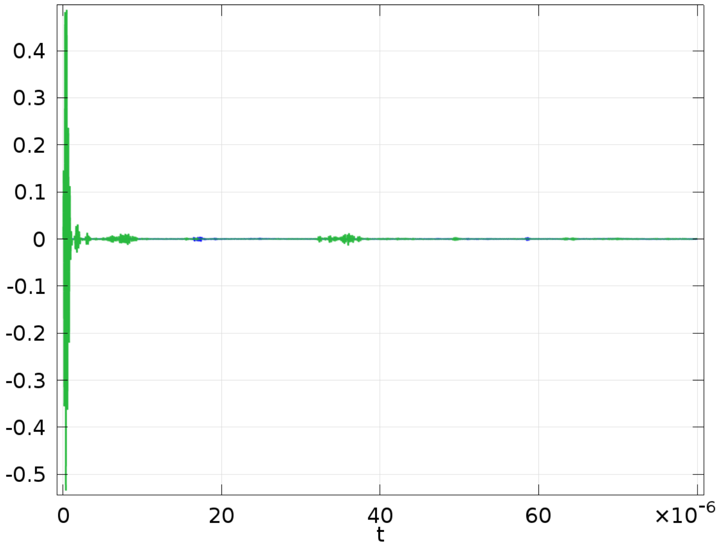

Figure B.24

Probe 1D Plot Group 2.

Bibliography

[1] R.H. Petrucci, W.S. Harwood, G.F. Herring, and J.D. Madura. *General Chemistry: Principles and Modern Applications*. Pearson Canada, Toronto, Canada, 10th edition, 2011.

[2] D.J. McClements and M.J.W. Povey. Scattering of ultrasound by emulsions. *Journal of Physics D: Applied Physics*, 22:38–47, 1989.

[3] F. Babick, M. Stintz, and A. Richter. Ultrasonic particle sizing of disperse systems with partly unknown properties. *Particle & Particle Systems Characterization*, 23:175–183, 2006.

[4] E. Dickinson, J.G. Ma, V.J. Pinfield, and M.J.W. Povey. Ultrasonic studies of the creaming of concentrated emulsions. In E Dickinson and D Lorient, editors, *Food Macromolecules and Colloids*, Special Publications, pages 223–234. The Royal Society of Chemistry, 1995.

[5] N. Herrmann, Y. Hemar, P. Lemarechal, and D.J. McClements. Probing particle-particle interactions in flocculated oil-in-water emulsions using ultrasonic attenuation spectrometry. *The European Physical Journal E*, 5:183–188, 2001.

[6] A.D. Pierce. *Acoustics: An Introduction to its Physical Principles and Applications*. McGraw-Hill, New York, 1981.

[7] R.B. Lindsay. *Acoustics: Historical and Philosphical Development*. Dowden, Hutchinson and Ross, Stroudsburg, 1973.

[8] M.J.W. Povey. *Ultrasonic Techniques for Fluids Characterization*. Academic Press, San Diego, USA, 1997.

[9] A.B. Wood. *A Textbook of Sound.* Bell and Sons, London, 2nd edition, 1941.

[10] R.J. Urick. A sound velocity method for determining the compressibility of finely divided substances. *Journal of Applied Physics*, (18):983–987, 1947.

[11] J.D. Colladon and J.C.F. Sturm. Memoir on the compression of liquids. *Annales de Chimie (Paris)*, (36):225–227, 1827.

[12] G. Kirchhoff. Ueber den einfluss der wärmeleitung in einem gas auf die schallbewegung. *Annalen der Physik (Leipzig)*, (134):177–193, 1868.

[13] J.W. (Lord Rayleigh) Strutt. *The Theory of Sound.* Macmillian, London, 2nd edition, 1896.

[14] G.W. Swift. *Thermoacoustics: A Unifying Perspective for some Engines and Refrigerators.* Acoustical Society of America Publications, Sewickley PA, 2002.

[15] P.D. Edmonds. *Ultrasonics*, volume 19 of *Methods of Experimental Physics:*. Acadmic Press, New York, 1981.

[16] M.J.W. Povey. Ultrasonics in food engineering, part i: Introduction and experimental methods. *Journal of Food Engineering*, (8):217–245, 1988.

[17] J.W. (Lord Rayleigh) Strutt. Investigation of the disturbance produced by a spherical obstacle on the waves of sound. *Proceedings of the London Mathematical Society*, 4:253–283, 1873.

[18] P.S. Epstein and R.R. Carhart. The absorption of sound in suspensions and emulsions i. water fog in air. *The Journal of the Acoustical Society of America*, 25(3):553–565, 1953.

[19] J.R. Allegra and S.A. Hawley. Attenuation of sound in suspensions and emulsions: Theory and experiments. *The Journal of the Acoustical Society of America*, 51(5B):1545–1564, 1972.

[20] V.J. Pinfield. Acoustic scattering in dispersions: Improvements in the calculation of single particle scattering coefficients. *The Journal of the Acoustical Society of America*, 122(1):205–221, 2007.

[21] D.S. Jones. *Acoustic and Electromagnetic Waves.* Oxford University Press, first edition, 1986.

[22] R.E. Challis, J.S. Tebbutt, and A.K. Holmes. Equivalence between three scattering formulations for ultrasonic wave propagation in particulate mixtures. *Journal of Physics D: Applied Physics*, (31):3481–97, 1998.

[23] O.G. Harlen, M.J. Homes, M.J.W. Povey, Y. Qiu, and B.D. Sleeman. A low frequency potential scattering description of acoustic propagation in dispersions. *SIAM Journal on Applied Mathematics*, 61(6):1906–1931, 2001.

[24] F.W.J. Olver, D.W. Lozier, R.F. Boisvert, and C.W. Clark. *NIST Handbook of Mathematical Functions.* Cambridge University Press, New York, NY, USA, 2010.

[25] R.E. Kleinmann. The Dirichlet problem for Helmholtz equation. *Archive for Rational Mechanics and Analysis*, (18):205–229, 1965.

[26] O.G. Harlen, M.J. Homes, M.J.W. Povey, and B.D. Sleeman. Acoustic propagation in dispersions and the geometric theory of diffraction. *SIAM Journal on Applied Mathematics*, 63(3):834–849, 2003.

[27] O.G. Harlen, M.J. Homes, V.J. Pinfield, M.J.W. Povey, and B.D. Sleeman. A perturbation solution for long wavelength thermoacoustic propagation in dispersions. *Journal of Computational and Applied Mathematics*, 234(6):1996–2002, 2010.

[28] V.J. Pinfield and M.J.W. Povey. A perturbation approach to acoustic scattering in dispersions. *The Journal of the Acoustical Society of America*, 120(2):719–732, 2006.

[29] V.J. Pinfield, O.G. Harlen, M.J.W. Povey, and B.D. Sleeman. Acoustic propagation in dispersions in the long wavelength limit. *SIAM Journal on Applied Mathematics*, 66(2):489–509, 2005.

[30] R.J. Urick and W.S. Ament. The propagation of sound in composite media. *The Journal of the Acoustical Society of America*, 21:115–119, 1949.

[31] P.C. Waterman and R. Truell. Multiple scattering of waves. *Journal of Mathematical Physics*, 2:512–537, 1961.

[32] J.G. Fikioris and P.C. Waterman. Multiple scattering of waves. ii "hole corrections" in the scalar case. *Journal of Mathematical Physics*, 51:1413–1420, 1964.

[33] P. Lloyd. Wave propagation through an assembly of spheres. ii. the density of single particle eigenstates. *Proceedings of the Physical Society, London*, 90:2107–215, 1967.

[34] P. Lloyd. Wave propagation through an assembly of spheres. iii. the density of states in a liquid. *Proceedings of the Physical Society, London*, 90:217–231, 1967.

[35] P. Lloyd and M.V. Berry. Wave propagation through an assembly of spheres. iv. relations between different multiple scatting theories. *Proceedings of the Physical Society, London*, 91:678–688, 1967.

[36] L.L. Foldy. The multiple scattering of waves. i. general theory of isotropic scattering by randomly distributed scatterers. *Physical Review*, 67:107–119, 1945.

[37] M. Lax. Multiple scattering of waves. *Reviews of Modern Physics*, 23:287–310, 1951.

[38] M. Lax. Multiple scattering of waves. ii. the effective field in dense systems. *Physical Review*, 85:621–629, 1952.

[39] C.M. Linton and P.A. Martin. Multiple scattering by multiple spheres: A new proof of the Lloyd-Berry formula for the effective wavenumber. *SIAM Journal on Applied Mathematics*, 66(5):1649–1668, 2006.

[40] V.J. Pinfield and M.J.W. Povey. Thermal scattering must be accounted for in the determination of adiabatic compressibility. *The Journal of Physical Chemistry B*, 101:1110–1112, 1997.

[41] V.J. Pinfield. *Studies of Creaming, Occulation and Crystallisation in Emulsions: Computer Modelling and Analysis of Ultrasound Propagation.* PhD thesis, Procter Department of Food Science, University of Leeds, 1996.

[42] V.J. Pinfield. Advances in ultrasonic monitoring of oil-in-water emulsions. *Food Hydrocolloids*, 42:48–55, 2014.

[43] V.J. Pinfield. Thermo-elasric multiple scattering in random dispersions of spherical scatterers. *The Journal of the Acoustical Society of America*, 136(6):3008–3017, 2014.

[44] F. Luppé, J.M. Conoir, and A.N. Norris. Effective wave numbers for the thermo-viscoelastic media containing random configurations of spherical scatters. *The Journal of the Acoustical Society of America*, 131(2):1113–1120, 2012.

[45] P.C. Waterman. New formulation of acoustic scattering. *The Journal of the Acoustical Society of America*, 60:567–580, 1976.

[46] G.C. Gaunaurd, H. Huang, and H.C. Strifors. Acoustic scattering by a pair of spheres. *The Journal of the Acoustical Society of America*, (98):495–507, 1995.

[47] L. Greengard and V. Rokhlin. *The rapid evaluation of potential field in three dimensions*, volume 1360 of *Lecture Notes in Mathematics*, chapter 2, pages 121–141. Springer, Heidelberg, 1988.

[48] D.J. McClements and J.N. Coupland. Theory of droplet size distribution measurements in emulsions using ultrasonic spectroscopy. *Colloids and Surfaces A: Physicochemical and Engineering Aspects*, (117):161–170, 1996.

[49] T.J. O'Neill. *Extended Computation of Ultrasonic Wavenumber in Particulate Dispersions.* PhD thesis, Keele University, Decemeber 1998.

[50] G.W.C. Kaye and T.H. Laby. *Tables of Physical and Chemical Constants.* Longman, Harlow, UK, 16th edition, 1995.

[51] D.E. Gray. *American Institute of Physics Handbook.* McGraw Hill, New York, 2nd edition, 1963.

[52] Malvern ltd. `http://www.malvern.com`.

[53] M.J. Holmes, N.G. Parker, and M.J.W. Povey. Temperature dependence of bulk viscosity in water using acoustic spectroscopy. *Journal of Physics: Conference Series*, (269):012011, 2011.

[54] M.J.W. Povey. Ultrasound partilce sizing: A review. *Particuology*, 110(2):135–147, 2013.

[55] P.V. Nelson, M.J.W. Povey, and Y. Wang. An ultrasound velocity and attenuation scanner for view the temporal evolution of a dispersed phase in fluids. *Review of Scientific Instruments*, 72(11):4234–4241, 2001.

[56] W. Marczak. Water as a standard in the measurments of speed of sound in liquids. *The Journal of the Acoustical Society of America*, 102(5):2776–2779, 1997.

[57] M.J. Holmes, T. Southworth, N.G. Watson, and M.J.W. Povey. Enzyme activity determination using ultrasound. *Journal of Physics: Conference Series*, 498:012003, 2014.

[58] Resoscan, TF Instruments Inc. `http://www.tf-instruments.com/`.

[59] N. Herrmann, P. Boltenhagen, and J. Lemarchal. Experimental study of sound attenuation in quasi-monodisperse emulsions. *Journal de Physique II*, 6(10):1389–1404, 1996.

[60] F. Eggers and T. Funck. Ultrasonic measurements with milliliter liquid samples in the 0.5-100 mhz range. *Review of Scientific Instruments*, 44(8):969–977, 1973.

[61] V.J. Pinfield, M.J.W. Povey, and E. Dickinson. Interpretation of ultrasound velocity creaming profiles. *Ultrasonics*, 34(6):695–698, 1996.

[62] V.J. Pinfield, M.J.W. Povey, and E. Dickinson. The application of modified forms of the urick equation to the interpretation of ultrasound velocity in scattering systems. *Ultrasonics*, 33(3):243–251, 1995.

[63] T.A. Hazlehurst, O.G. Harlen, M.J. Holmes, and M.J.W. Povey. Multiple scattering in dispersions, for long wavelength thermoacoustic solutions. *Journal of Physics: Conference Series*, 498:012005, 2014.

[64] P.M. Morse and H. Feshback. *Methods of Theoretical Physics*, volume I, II. McGraw-Hill, New York, 1953.

[65] J.F. Rico, R. López, I. Ema, and G Ramíres. Translation of real solid spherical harmonics. *International Journal of Quantum Chemistry*, (113):1544–1548, 2013.

[66] D.J. McClements and E.D. Dickinson. *Advances in Food Colloids.* Chapman & Hall, 1st edition, 1996.

[67] N. Choudhury and S.K. Ghosh. Density functional approach to the structure of homogeneous colloidal dispersion. *Physical Review E*, 53(4):3847–3853, 1996.

[68] J.-P. Hansen and I.R. McDonald. *Theory of Simple Liquids.* Academic Press, London, 2nd edition, 1986.

[69] P.A. Egelstaff. *An Introduction to the Liquid State.* Clarendon Press, Oxford, 2nd edition, 1992.

[70] W.B. Russel, D.A. Saville, and W.R. Schowalter. *Colloidal Dispersions.* Cambridge University Press, Cambridge, 1989.

[71] J. Mahanty and B.W. Ninham. *Dispersion Forces.* Academic Press, New York, 1976.

[72] L.S. Ornstein and F. Zernike. Accidental deviations of density and opalescence at the critial point of a single substance. *Proceedings of the Academy of Sciences of Amsterdam*, (17):793–806, 1914.

[73] J.K. Percus and G.J. Yevick. Analysis of classical statistical mechanics by means of collective coordinates. *Physical Review*, 110(10):1–13, 1958.

[74] M.S. Wertheim. Exact solution of the percus-yevick integral equation for hard spheres. *Physical Review Letters*, 10(8):321–323, 1963.

[75] S. Bravo Yuste and A. Santos. Radial distribution function for hard spheres. *Physical Review A*, 43(10):5418–5423, 1991.

[76] S. I. Sandler. *An Introduction to Applied Statistical Thermodynamics.* Wiley, Chichester, 1st edition, 2011.

[77] W.M. Qiao, Y. Song, S.-H. Yoon, Y. Korai, I. Mochida, and O. Katou. Preparation of PVC pitch from waste pipe. *Carbon*, 9(9):2022–2025, 2005.

[78] A. Demŏenko, R. Akkerman, P.B. Nagy, and R. Loendersloot. Non-collinear wave mixing for non-linear ultrasonic detection of physical ageing in PVC. *NDT & E International*, 49:34–39, 2012.

[79] S. Kim. Pyrolysis kinetics of waste PVC pipe. *Waste Management*, 21(7):609–616, 2001.

[80] R. Ranasiak. Hydraulic performance of sewer pipes with deposited sediments. *Water Science and Technology*, 57:1743–1748, 2008.

[81] L.C. Lynnworth. Industrial applications of ultrasound - a review ii. measurements, tests, and process control using low-intensity ultrasound. *IEEE Transactions on Sonics and Ultrasonics*, 2(22):71–101, 1975.

[82] H. Seo, K. Lee, and K-Y. Jhang. In-line ultrasonic monitoring for sediments stuck on inner wall of a polyvinyl chloride pipe. *The Scientific World Journal*, (Article ID 731621):8 pages, 2014.

[83] K.I. Lee. Ultrasonic technique for measuring the thickness of scale on the inner surfaces of pipes. *Journal of the Korean Physical Society*, 56(2):558–561, 2010.

[84] COMSOL Multiphysics. `http://www.comsol.com`.

[85] D.T. Blackstock. *Fundamentals of Physical Acoustics.* John Wiley & Sons, Inc., 1st edition, 2000.

[86] N. Watson, T.A. Hazlehurst, M.J.W. Povey, J. Vieira, R. Sundara, and J-P. Sandoz. Can airborne ultrasound monitor bubble size in chocolate? *Journal of Physics: Conference Series*, 498(1):012001, 2014.

[87] P.S.K. Mylavarapu and S. Boddapati. Numerical modeling of wave propagation in particulate composites. *Proceedings of the 2011 COMSOL Conference in Bangalore*, 2011.

[88] C. Pozrikidis. *Boundary Integral and Singularity Methods for Linearized Viscous Flow.* Cambridge University Press, 1992.

[89] A. Edmonds. *Angular Momentum in Quantum Mechanics.* Princeton U.P., London, 1957.